HAL
open science

On the role of relativistic effects on the structural, physical and chemical properties of molecules and materials

Rémi Maurice

To cite this version:

Rémi Maurice. On the role of relativistic effects on the structural, physical and chemical properties of molecules and materials. Theoretical and/or physical chemistry. Université de Nantes (UNAM), 2018. tel-02308305

HAL Id: tel-02308305

https://imt-atlantique.hal.science/tel-02308305

Submitted on 8 Oct 2019

HAL is a multi-disciplinary open access archive for the deposit and dissemination of scientific research documents, whether they are published or not. The documents may come from teaching and research institutions in France or abroad, or from public or private research centers.

L'archive ouverte pluridisciplinaire **HAL**, est destinée au dépôt et à la diffusion de documents scientifiques de niveau recherche, publiés ou non, émanant des établissements d'enseignement et de recherche français ou étrangers, des laboratoires publics ou privés.

On the role of relativistic effects on the structural, physical and chemical properties of molecules and materials

Rémi Maurice

Mémoire en vue de l'obtention d'une
Habilitation à Diriger des Recherches

31 octobre 2018

On the role of relativistic effects on the structural, physical and chemical properties of molecules and materials

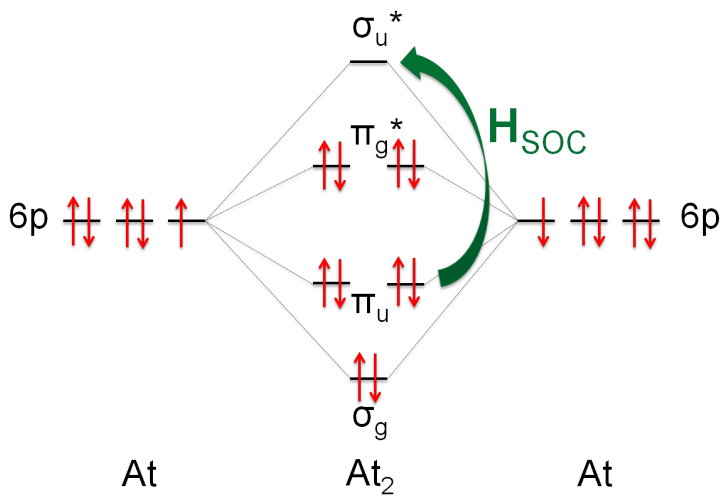

Rémi Maurice

2008–2018

Preface

This manuscript was prepared during the 2017-2018 academic year in view of obtaining the French *Habilitation à diriger des recherches* qualification. This qualification is required for being the full promotor of PhD students and is also a prerequisite for promotion in the French academic system. Therefore, it is clear that I had personal interest in preparing it, but it should also be mentioned that my host laboratory, Subatech, would also benefit from having one more bearer of this habilitation.

This exercice in style is expected to be based on (i) an extended curriculum vitae, (ii) a research report and (iii) a selection of representative publications. I have tried to follow these specifications, but of course with my own interpretation. For instance, I have chosen to detail only my research works that relate to one well-identified common theme: "Role of relativistic effects on the properties of molecules and materials". Therefore, only the publications for which the computed property vanishes in the absence at least one relativistic interaction, or the ones in which the role of at least one relativistic term on a given property is determined, will be discussed. The only exception to this rule concern one publication related to photophysics [article #22]. Although the introduction of the spin-orbit coupling is necessary to formally activate the main triplet population mechanism in photoexcited benzophenone, this work is out of the scope of the three main research topics that I have defined for organizing the manuscript, and thus, it will be skipped from the discussion. Anyway, the interested reader will find a complete list of my scientific production in the Curriculum vitae section, which is placed as a prelude to the main text. Note that this list concerns the 2008–2018 period, *i.e.* ten years of research.

In this manuscript, I have tried to put more emphasis on the concepts than on the results, in view of providing a comprehensive overview of my work. Hopefully, a few readers may find some useful advises or relevant explanations in this habilitation thesis.

Nantes, April 2018 Rémi Maurice

Curriculum vitae

Rémi Maurice

Born: April 19, 1985

Nationality: French

E-mail: remi.maurice@subatech.in2p3.fr

Google Scholar: Rémi Maurice

ResearchGate: Rémi Maurice

IdHAL: Rémi Maurice

CNRS researcher, Subatech, UMR CNRS 6457

IN2P3/IMT Atlantique/Université de Nantes

Education

During my university years, I progressively chose to focus on chemistry (*licence* and *maîtrise*) and then eventually in theoretical chemistry (master's degree and PhD). Therefore, I have notably acquired a decent level in molecular chemistry and in analytical chemistry, which later proved to be useful for efficiently interacting with experimental colleagues.

2006 **University of Toulouse**

Undergraduate degree in Molecular Chemistry (*licence*), with honours.

2007 **University of Toulouse**

Bachelor's degree in Chemistry (*maîtrise*), with honours, rank: 1/52.

2008 **University of Toulouse**

Master's degree in Physical and Theoretical Chemistry, with honours, rank: 1/51.

2011 **University of Toulouse**

PhD degree in Theoretical Chemistry.

2011 **University of Tarragona, Spain**

PhD degree in Chemical Sciences and Engineering, with *summa cum laude.*

Theses

Since I found myself particularly interested in the properties of transition metal complexes and in molecular orbital theory, I decided to do my master's project, and then, as a continuation to it, my PhD project, in the molecular magnetism field. We agreed with N. Guihéry, N. Suaud and C. de Graaf to focus on magnetic anisotropy, a challenging topic. It took quite a while to solve some complex issues, but in the end it led to several firsts in *ab initio* quantum chemistry, *i.e.* it ended up to be a very wise choice.

2008 **Master thesis, University of Toulouse**

Zero-field splitting: Ab initio calculations for Ni(II) mono- and bi-metallic complexes.

Supervisors: N. Guihéry and N. Suaud (Toulouse), C. de Graaf (Tarragona, Spain).

2011 **PhD thesis, University of Toulouse and University of Tarragona, Spain**

Zero-field anisotropic spin Hamiltonians in first-row transition metal complexes: Theory, models and applications.

Supervisors: N. Guihéry (Toulouse) and C. de Graaf (Tarragona, Spain).

Post-doctoral experiences

After my PhD, I decided to move to Groningen to learn more on the embedded cluster approach in the group of R. Broer. After a first succesful work on $LiCu_2O_2$, I chose to start working on a different topic, namely photophysics. After one year, the group was out of money for further paying me and I had also failed a couple of times to get funding from NWO to stay there. Therefore, I decided to move to the U.S., actually in the group of L. Gagliardi. This allowed me to work on other types of systems (actinides and metal-organic frameworks), as well as to learn more advanced density functional theory things by interacting with D. Truhlar and his students.

2011–2012 **Post-doctorate in the University of Groningen, The Netherlands**

Solid state magnetism and photophysics of organic systems.

2011–2012 **Post-doctorate in the University of Minnesota, United States**

Chemistry of the actinides and metal-organic frameworks.

Current position

It is hard to obtain a permanent position and even harder to find one that suits well one's skills and personnality. I have to admit that I have been lucky to find such a position within the radiochemistry group of Subatech. Indeed, I am surrounded by experimentalists, which allows me to make strong and direct interactions with them and also to feel quite free in my work since, anyway, they have little clues on what it consists in!

Since 2013 **CNRS researcher, Subatech laboratory, Nantes**
Theoretical radiochemistry.

Publications

1. R. Maurice*, R. Bastardis, C. de Graaf, N. Suaud, T. Mallah and N. Guihéry*, *Universal theoretical approach to extract anisotropic spin Hamiltonians*, J. Chem. Theory Comput. **5**, 2977–2984 (2009).

2. R. Maurice*, N. Guihéry, R. Bastardis and C. de Graaf*, *Rigorous extraction of the anisotropic multispin Hamiltonian in bimetallic complexes from the exact electronic Hamiltonian*, J. Chem. Theory Comput. **6**, 55–65 (2010).

3. R. Maurice, C. de Graaf and N. Guihéry*, *Magnetic anisotropy in binuclear complexes in the weak-exchange limit: From the multispin to the giant spin Hamiltonian*, Phys. Rev. B **81**, 214427 (2010).

4. R. Maurice*, C. de Graaf and N. Guihéry, *Magnetostructural relations from a combined ab initio and ligand field analysis for the nonintuitive zero-field splitting in Mn(III) complexes*, J. Chem. Phys. **133**, 084307 (2010).

5. R. Maurice, A. M. Pradipto, N. Guihéry*, R. Broer and C. de Graaf*, *Antisymmetric magnetic interactions in oxo-bridged copper(II) bimetallic systems*, J. Chem. Theory Comput. **6**, 3092–3010 (2010).

6. R. Maurice, K. Sivalingam, D.Ganyushin, N. Guihéry*, C. de Graaf and F. Neese, *Theoretical determination of the zero-field splitting in copper acetate monohydrate*, Inorg. Chem. **50**, 6229–6236 (2011).

7. R. Maurice*, L. Vendier and J.-P. Costes*, *Magnetic anisotropy in Ni^{II}-Y^{III} binuclear complexes: On the importance of both the first coordination sphere of the Ni^{II} ion and of the Y^{III} ion belonging to the second coordination sphere*, Inorg. Chem. **50**, 11075–11081 (2011).

8. L. J. Batchelor*, M. Sangalli, R. Guillot, N. Guihéry, R. Maurice, F. Tuna and T. Mallah*, *Pentanuclear cyanide-bridged complexes based on highly anisotropic Co^{II} seven-coordinate building blocks: Synthesis, structure and magnetic behavior*, Inorg. Chem. **50**, 12045–12052 (2011).

9. A.-M. Pradipto, R. Maurice, N. Guihéry, C. de Graaf and R. Broer*, *First-principles study of magnetic interactions in cupric oxide*, Phys. Rev. B **85**, 014409 (2012).

10. J.-P. Costes*, R. Maurice* and L. Vendier, *Pentacoordinate Ni^{II} complexes: Preparation, magnetic measurements and ab initio calculations of the magnetic anisotropy terms*, Chem. Eur. J. **18**, 4031–4040 (2012).

11. R. Maurice, A.-M. Pradipto, C. de Graaf and R. Broer*, *Magnetic interactions in $LiCu_2O_2$: Single-chain versus double chain models*, Phys. Rev. B **86**, 024411 (2012).

12. R. Ruamps, L. J. Batchelor, R. Maurice, N. Gogoi, P. Jiménez-Lozano, N. Guihéry*, C. de Graaf, A.-L. Barra, J.-P. Sutter and T. Mallah*, *Origin of the magnetic anisotropy in Ni(II) and Co(II) heptacoordinate complexes*, Chem. Eur. J. **19**, 950–956 (2013).

13. R. Ruamps, R. Maurice, L. Batchelor, M. Boggio-Pasqua, R. Guillot, A.-L. Barra, J. Liu, E.-E. Bendeif, S. Pillet, S. Hill*, T. Mallah* and N. Guihéry*, *Giant Ising-type magnetic anisotropy in trigonal bipyramidal Ni(II) complexes: Experiment and theory*, J. Am. Chem. Soc. **135**, 3017–3026 (2013).

14. N. A. Bogdanov, R. Maurice, I. Rousochatzakis, J. van den Brink and L. Hozoi, *Magnetic state of pyrochlore $Cd_2Os_2O_7$ emerging from strong competition of ligand distortion and longer-range crystalline anisotropy*, Phys. Rev. Lett. **110**, 127206 (2013).

15. R. Maurice, P. Verma, J. M. Zadrozny, S. Luo, J. Borycz, J. R. Long*, D. G. Truhlar* and L. Gagliardi*, *Single-ion magnetic anisotropy and isotropic magnetic couplings in Fe_2(dobdc)*, Inorg. Chem. **52**, 9379–9389 (2013).

16. C. C. L. Pereira, R. Maurice, A. F. Lucena, S. Hu, A. P. Gonçalves, J. Marçalo*, J. K. Gibson, L. Andrews and L. Gagliardi*, *Thorium and uranium carbide cluster cations in the gas phase: Similarities and differences between Th and U*, Inorg. Chem. **52**, 10968–10975 (2013).

17. R. Maurice, C. de Graaf* and N. Guihéry, *Theoretical determination of spin Hamiltonians with isotropic and anisotropic magnetic interactions in transition metal and lanthanide complexes*, Phys. Chem. Chem. Phys. **15**, 18784–18804 (2013).

18. S. J. Tereniak, R. K. Carlson, L. J. Clouston, V. G. Young, E. Bill*, R. Maurice, Y.-S. Chen, H. J. Kim, L. Gagliardi* and C. C. Lu*, *Role of the metal in the bonding and properties of*

bimetallic complexes involving manganese, iron and cobalt, J. Am. Chem. Soc. **136**, 1842–1855 (2014).

19. M. J. Polinski, E. B. Garner, R. Maurice, N. Planas, J. T. Stritzinger, T. Gannon Parker, J. N. Gross, T. D. Green, E. V. Alekseev, S. M. Van Cleve, W. Depmeier, L. Gagliardi, M. Shatruk, K. L. Knappenberger, L. Soderholm, D. A. Dixon and T. E. Albrecht-Schmitt*, *Unusual structure, bonding, and properties in a californium borate*, Nat. Chem. **6**, 387–392 (2014).

20. R. Ruamps, R. Maurice, C. de Graaf and N. Guihéry*, *Interplay between local anisotropies in binuclear complexes*, Inorg. Chem. **53**, 4508–4516 (2014).

21. J. Borycz, L.-C. Lin, E. D. Bloch, J. Kim, A. L. Dzubak, R. Maurice, D. Semrouni, K. Lee, B. Smit* and L. Gagliardi*, *CO_2 adsorption in Fe_2(dobdc): A classical force field parameterized from quantum mechanical calculations*, J. Phys. Chem. C **118**, 12230–12240 (2014).

22. D.-C. Sergentu, R. Maurice*, R. W. A. Havenith, R. Broer* and D. Roca-Sanjuán*, *Computational determination of the dominant triplet population mechanism in photoexcited benzophenone*, Phys. Chem. Chem. Phys. **16**, 25393–25403 (2014).

23. R. Maurice*, E. Renault, Y. Gong, P. X. Rutkowski and J. K. Gibson*, *Synthesis and structures of plutonyl nitrate complexes: Is plutonium heptavalent in $PuO_3(NO_3)_2^-$?*, Inorg. Chem. **54**, 2367–2373 (2015).

24. R. Maurice*, F. Réal, A. S. P. Gomes, V. Vallet, G. Montavon and N. Galland, *Effective bond orders from two-step spin-orbit coupling approaches: The I_2, At_2, IO^+ and AtO^+ case studies*, J. Chem. Phys. **142**, 094305 (2015).

25. D.-C. Sergentu, M. Amaouch, J. Pilmé, N. Galland* and R. Maurice*, *Electronic structures and geometries of the XF_3 (X = Cl, Br, I, At) fluorides*, J. Chem. Phys. **143**, 114306 (2015).

26. P. Verma, R. Maurice and D. G. Truhlar*, *Identifying the interactions that allow separation of O_2 from N_2 on the open iron sites of Fe_2(dobdc)*, J. Phys. Chem. C **119**, 28499–28511 (2015).

27. N. Guihéry, R. Ruamps, R. Maurice and C. de Graaf, *Synergy and destructive interferences between local magnetic anisotropies in binuclear complexes*, AIP Conf. Proc. **1702**, 090015 (2015).

28. D.-C. Sergentu, D. Teze, A. Sabatié-Gogova, C. Alliot, N. Guo, F. Bassal, I. Da Silva, D. Deniaud, R. Maurice, J. Champion, N. Galland* and G. Montavon*, *Advances on the determination of the astatine Pourbaix diagram: Predomination of $AtO(OH)_2^-$ over At^- in basic conditions*, Chem. Eur. J. **22**, 2964–2971 (2016).

29. T. Ayed, J. Pilmé, D. Teze, F. Bassal, J. Barbet, M. Chérel, J. Champion, R. Maurice, G. Montavon* and N. Galland*, *^{211}At-labeled agents for alpha-immunotherapy: On the in vivo stability of astatine-agent bonds*, Eur. J. Med. Chem. **116**, 156–164 (2016).

30. D.-C. Sergentu, G. David, G. Montavon, R. Maurice* and N. Galland*, *Scrutinizing "invisible" astatine: A challenge for modern density functionals*, J. Comput. Chem. **37**, 1345–1354 (2016).

31. P. Verma, R. Maurice and D. G. Truhlar*, *Adsorbate-induced changes in magnetic interactions in Fe_2(dobdc) with adsorbed hydrocarbon molecules*, J. Phys. Chem. C **120**, 9933–9948 (2016).

32. B. Cahier, R. Maurice, H. Bolvin, T. Mallah* and N. Guihéry*, *Tools for predicting the nature and magnitude of magnetic anisotropy in transition metal complexes: Application to Co(II) complexes*, Magnetochemistry **2**, 31 (2016).

33. P. D. Dau, R. Maurice*, E. Renault and J. K. Gibson*, *Heptavalent neptunium in a gas-phase complex: $(Np^{VII}O_3{}^+)(NO_3{}^-)_2$*, Inorg. Chem. **55**, 9830–9837 (2016).

34. D.-C. Sergentu, F. Réal, G. Montavon, N. Galland* and R. Maurice*, *Unravelling the hydration-induced ground-state change of AtO^+ with relativistic and multiconfigurational wave-function-based methods*, Phys. Chem. Chem. Phys. **18**, 32703–32712 (2016).

35. N. Guo, D.-C. Sergentu, D. Teze, J. Champion, G. Montavon, N. Galland* and R. Maurice*, *The heaviest possible ternary trihalogen species, $IAtBr^-$, evidenced in aqueous solution: An experimental performance driven by computations*, Angew. Chem. Int. Ed. **55**, 15393–15372 (2016).

36. D. Teze*, D.-C. Sergentu, V. Kalichuk, J. Barbet, D. Deniaud, N. Galland, R. Maurice* and G. Montavon, *Targeted radionuclide therapy with astatine-211: Oxidative dehalogenation of astatobenzoate conjugates*, Sci. Rep. **7**, 2579 (2017).

37. M. Amaouch, D.-C. Sergentu, D. Steinmetz, R. Maurice, N. Galland* and J. Pilmé*, *The bonding picture in hypervalent XF_3 (X = Cl, Br, I, At) fluorides revisited with quantum chemical topology*, J. Comput. Chem. **38**, 2753–2762 (2017).

38. N. Guo, R. Maurice, D. Teze, J. Graton, J. Champion, G. Montavon* and N. Galland*, *Experimental and computational evidence of halogen bonds involving astatine*, Nat. Chem. **10**, 428–434 (2018).

Book chapter

1. R. Maurice*, R. Broer, N. Guihéry and C. de Graaf, *Zero-field splitting in transition metal complexes: Ab initio calculations, effective Hamiltonians, model Hamiltonians, and crystal-field models*, in Handbook of Relativistic Quantum Chemistry, Ed. W. Liu, Springer-Verlag Berlin Heidelberg, 765–796 (2017).

NB: I have only reported hereafter the presentations for which I have been the actual speaker; furthermore, only the ones for which I was personnaly invited are mentioned as "invited" presentations.

Invited oral presentations

1. R. Maurice, *Studying the photophysics of benzphenone with quantum chemical methods*, CEICS Nobel Campus Chemistry for Life, Vila-seca, Spain, July 2012.

2. R. Maurice, A.-M. Pradipto, C. de Graaf, N. Guihéry and R. Broer, *Theoretical determination of magnetic interactions in ionic solids*, CSTCC 25, Guelph, Canada, July 2012.

3. R. Maurice, R. Broer, C. de Graaf and N. Guihéry, *Zero-field splitting in transition metal complexes: Ab initio calculations, effective Hamiltonians, and model Hamiltonians*, Conference on Modern Trends in Molecular Magnetism, Mumbai, India, May 2016.

4. R. Maurice, E. Renault, P. D. Dau, Y. Gong, P. X. Rutkowski and J. K. Gibson, *Synthesis, structures, and reactions of gas-phase actinide oxide complexes: Relative stabilities and An oxidation states in* $AnO_3(NO_3)_2^-$ *(An = U, Np, Pu)*, Pu Futures – The Science 2016, Baden-Baden, Germany, September 2016.

5. C. Gomez Pech, D.-C. Sergentu, N. Galland and R. Maurice, *Hunting invisible astatine: An excuse to study the role of spin-orbit coupling on chemical bonding?*, Theoretical Chemistry: Transition Metals, Excited States, and More, Groningen, The Netherlands, April 2017.

Contributed talks

1. R. Maurice, P. Verma, S. Luo, J. Borycz, X. Xu, D. G. Truhlar and L. Gagliardi, *Electronic structure of* Fe_2*(dobdc): Ligand field, magnetic interactions, and adsorption*, MWTCC 45, Urbana, United States, May 2013.

2. F. Bassal, F. Guillon Verne, R. Maurice, A. Sabatié-Gogova, J. Champion, G. Montavon and N. Galland, *Étude de la chimie de l'astate à l'aide de la modélisation moléculaire quantique*, XIVes Journées Nationales de Radiochimie et de Chimie Nuclaire, Orsay, September 2014.

3. R. Maurice, F. Réal, A. S. P. Gomes, G. Montavon, V. Vallet and N. Galland, *The role of spin-orbit coupling on the chemical bonding in At_2 and AtO^+: Analysis via effective bond orders*, WATOC 2014, Santiago, Chile, October 2014.

4. D.-C. Sergentu, F. Réal, N. Galland and R. Maurice, *Hydration-induced ground-state change of AtO^+: A relativistic and multiconfigurational wave function theory study*, TACC 2016, Seattle, United States, August 2016.

Other oral presentations

1. R. Maurice, *Can we understand magnetic anisotropy in mono- and bi-metallic complexes with symmetry, tensorial calculus and effective Hamiltonian theory?*, workshop Jujols IV, Zeegse, The Netherlands, May 2009.

2. R. Maurice, C. de Graaf and N. Guihéry, *Anisotropic magnétique dans la limite de l'échange faible: de l'hamiltonien multispin à l'hamiltonien de spin géant*, GDR-MCM annual meeting, Dourdan, December 2009.

3. R. Maurice, *The canting angle between local spins: Myth or reality?*, workshop Jujols V, la Horta de San Joan, Spain, November 2010.

4. R. Maurice, K. Sivalingam, D. Ganyushin, N. Guihéry, C. de Graaf and F. Neese, *Revisiting the zero-field splitting in copper acetate monohydrate*, workshop CECAM-FR-GSO, Toulouse, June 2011.

5. R. Maurice, *One-dimensional vs two-dimensional magnetic models in $LiCu_2O_2$: A final argument?*, workshop Jujols VI, Sevilla, Spain, February 2012.

6. D.-C. Sergentu and R. Maurice, *Pseudo Jahn-Teller effect, spin-orbit coupling, and electron correlation in the XF_3 (X = Cl, Br, I, At) series*, workshop Jujols VII, Mülheim an der Ruhr, Germany, January 2014.

7. R. Maurice, N. Galland and G. Montavon, *Investigation of astatine chemistry in solution*, 8th ICI, Chicago, United States, August 2014 (in replacement of G. Montavon, invited speaker).

8. R. Maurice, *Modélisation de molécules et matériaux d'intérêt en radiochimie*, Journée du pôle ouest du RFCT, Rennes, December 2014.

Posters

1. R. Maurice, C. de Graaf and N. Guihéry, *L'anisotropie magnétique dans les complexes binucléaires*, RCTF 2010, Namur, Belgium, July 2010.

2. R. Maurice, A. M. Pradipto, N. Guihéry, R. Broer and C. de Graaf, *Détermination rigoureuse de l'anisotropie magnétique antisymétrique dans les composés binucléaires*, CHITEL 2010, Anglet, September 2010.

3. R. Maurice, N. Guihéry and C. de Graaf, *Theoretical evaluation of the zero-field splitting in transition metal complexes*, CHAINS 2011, Maarssen, The Netherlands, November 2011.

4. R. Maurice, *Studying physical properties of molecules and materials with quantum chemical methods*, CEICS Nobel Campus Chemistry for Life, Vila-seca, Spain, July 2012.

5. D.-C. Sergentu, A. Sabatié-Gogova, J. Champion, J.-Y. Le Questel, G. Montavon, R. Maurice and N. Galland, *The role of water molecules of the first solvation shell in modeling ligand-exchange reactions leading to AtO^+ hydrolyzed species*, WATOC 2014, Santiago, Chile, October 2014.

6. R. Maurice, F. Réal, A. S. P. Gomes, V. Vallet, G. Montavon and N. Galland, *Effective bond orders from spin-orbit configuration approaches*, ICQC 2015 and workshop on New Frontiers of Relativistic Quantum Chemistry, Beijing, China, June 2015.

7. D.-C. Sergentu, N. Guo, D. Teze, J. Champion, G. Montavon, N. Galland and R. Maurice, *Relativistic calculations for identifying new chemical species at ultra-trace concentrations: $AtO(OH)_2^-$ and $IAtBr^-$ revealed*, WATOC 2017, Munich, Germany, August 2017 and workshop CNRS/PAN on Nuclear medicine and radiochemistry, Gif-sur-Yvette, France, December 2017.

Invited seminars

1. R. Maurice, *Anisotropic spin Hamiltonians in transition metal complexes*, Bonn, Germany, January 2010.

2. R. Maurice, *Anisotropic interactions in d^9-d^9 bimetallic systems*, Groningen, The Netherlands, June 2010.

3. R. Maurice, *Le défi du traitement théorique de l'anisotropie magnétique*, Paris, February 2012.

4. R. Maurice, *Étude théorique de propriétés magnétiques, ferroélectriques ou photophysiques: de la molécule au solide*, Lyon, March 2012.

5. R. Maurice, *Modélisation de propriétés physico-chimiques à l'aide de la chimie quantique relativiste*, Nantes, March 2013.

6. R. Maurice, *Spin-orbit coupling and physico-chemical properties of molecules and materials*, Lille, March 2014.

7. R. Maurice, *Electronic structure and reactivity of AtO^+: Gas-phase vs. aqueous solution*, Toulouse, May 2016.

NB: I have only reported hereafter the students that I have officially supervised or co-supervised.

Student supervisions

Master students:

1. Siddharta Omar, Top Master in Nanoscience, *Understanding ferroelectricity via first principles calculations*, bibliography project, University of Groningen, The Netherlands, 2012.
   Duration: 4 months.
   Supervision rate: 80 % (R. Broer: 20 %).

2. Aulia Sukma Hutama, Sandwich Program, *Theoretical study of magnetic properties of Fe/W(110) slabs*, research project, University of Groningen, The Netherlands, 2012.
   Duration: 6 months.
   Supervision rate: 100 %.

3. François Guillon Verne, *M1* A3M, *Vers une meilleure compréhension de la chimie de coordination de l'astate: étude par la modélisation moléculaire de l'interaction entre AtO^+ et des ligands phosphorés*, research project, University of Nantes, 2014.
   Duration: 4 months.
   Supervision rate: 100 %.

4. Ange Stoïanov, *M1* A3M, *Spectroscopie UV-visible de complexes du polonium et du bismuth en milieu chloré: modélisation moléculaire et expériences*, research project, University of Nantes, 2015.
   Duration: 4 months.
   Supervision rate: 100 %.
   Scientific production:
   - 1 article in preparation.

PhD students:

1. Dumitru-Claudiu Sergentu, *Geometries, electronic structures, physico-chemical properties of astatine species: An application of relativistic quantum mechanics*, University of Nantes, 2013–2016.

   Supervision rate: 20 % (N. Galland: 40 %, J.-Y. Le Questel: 40 %), informally: 40 %.

   Scientific production:

   - 5 articles [articles #25, #28, #30, #34, and #35].

   - 1 contributed talk [D.-C. Sergentu, N. Galland and R. Maurice, *Electronic structures of the XF_3 (X = Cl, Br, I, At) fluorides and topology of their potential energy surfaces*, DFT 2015, Debrecen, Hungary, September 2015].

2. Cecilia Gomez Pech, *Unravelling the role of spin-orbit coupling on chemical bonding*, University of Nantes, 2016–2019.

   Supervision rate: 40 % (T. Gousset: 40 %, N. Galland: 20 %).

   Scientific production:

   - 1 article in preparation.

3. Lu Liu, *Exploration de la chimie de l'astate et applications médicales*, IMT Atlantique, 2017–2020.

   Supervision rate: 10 % (G. Montavon: 40 %, J. Champion: 50 %).

Reviewer activities

Journals:

- Journal of the American Chemical Society (4 articles).
- Chemistry–A European Journal (2 articles).
- Theoreticals Chemistry Accounts (2 articles).
- Nature Communications (1 article).
- Journal of Chemical Theory and Computation (1 article).
- ChemistrySelect (1 article).
- Journal of Molecular Modeling (1 article).
- AIP Advances (1 proceeding of the 2016 MMM Conference).

Research proposals:

- U.S. Department of Energy (2 projects).

- Agence Nationale de la Recherche (2 projects).

PhD dissertations:

- Gerard Alcover Fortuny, "international doctor" distinction, University of Tarragona, Spain, 2016.

Committee memberships

PhD defense committees:

- Maxime Pouvreau, EMN Nantes, 2016.
- Iuliia Androniuk, IMT Atlantique, 2017.

Follow-up PhD committees:

- Iuliia Androniuk, IMT Atlantique, 2013–2017.
- Debashish Banerjee, IMT Atlantique, 2017–2020.

Scientific Councils:

- R. Maurice, *Production, extraction et interaction dans le milieu biologique des radioisotopes*, oral presentation at the "Radiochemistry" Scientific Council of IN2P3, Paris, October 2016.

Miscellaneous:

- elected member of the Subatech Laboratory Council, since 2017.
- Subatech new-direction Search Committee, 2017–2018.

NB: only the grants that I have deposited or the ones for which my name was associated with the proposal submission have been listed.

Grants

On-going:

1. POLLUSOLS, *Région Pays de la Loire*, *Dynamique Scientifique*, 1.2 M€, 2015–2020. This collaborative and interdisciplinary project focuses on the environmental impact of mining ac-

tivities. I am involved in the quantum mechanical modeling of polonium species for elucidating the polonium speciation. Project coordinator: T. Lebeau (LGPN, Nantes).
Involvement: 20 %.

2. ROASTA, *Agence Nationale de la Recherche*, *Projet de Recherche Collaborative*, 532 k€, 2017–2021. This collaborative and interdisciplinary project aims at designing specific ligands for retaining At^-, in view of preconcentrating At for medicinal applications. Project coordinator: J.-F. Gestin (CRCINA, Nantes).
Involvement: 10 %.

Pending applications:

1. TransForMed, *Initiative NExT*, "Integrative Research Cluster", 225 k€, 2018–2020. This cluster aims at strenghening the interactions between local research teams in the nuclear medicine field/context. I am the scientific leader for radiochemistry. Project coordinator: F. Haddad (Subatech & Arronax, Nantes).

Rejected applications:

1. Antisymmetric exchange in large polynuclear complexes, The Royal Society, Newton International Fellowship, 66 k£, 2011.

2. Singlet fission in organic systems, NWO, Rubicon, 59 k€, 2011.

3. Theoretical elucidation of singlet fission for optimising solar energy conversion into electricity, NWO, Veni, 250 k€, 2012.

4. Analysis of chemical bonding in systems containing heavy atoms, *Agence Nationale de la Recherche*, *Jeunes chercheuses – Jeunes chercheurs*, 190 k€, 2015.

5. Unravelling the role of spin-orbit coupling on chemical bonding, *Agence Nationale de la Recherche*, *Jeunes Chercheuses – Jeunes Chercheurs*, 180 k€, 2016.

6. eXoBond, *Agence Nationale de la Recherche*, *Projet de Recherche Collaborative*, 510 k€, 2017. Project coordinator: N. Galland (CEISAM, Nantes).

7. ExProFLAM, *Région Pays de la Loire*, *Paris Scientifique*, 150 k€, 2018. Project coordinator: F. Guérard (CRCINA, Nantes).

8. Quantum theory of astatine in molecules for targeted radionuclide therapy, European Research Council, Starting Grant, 1.2 M€, 2018.

Teaching activities

2008–2011 **University of Toulouse**

General chemistry for second-year students (20 hours)

Atomic structure and spectroscopy for third-year students (54 hours)

Kinetics and thermodynamics for third-year students (216 hours)

Magnetism for master students (2 hours)

2011–2012 **University of Groningen, The Netherlands**

Introduction to computational modeling for first-year students (10 hours)

Quantum chemistry for second-year students (22 hours)

Electronic structure for master students (3 hours)

2013–2017 **University of Nantes**

Chemical thermodynamics and kinetics for first-year students (54 hours)

Computer tools for chemistry for third-year students (39 hours)

Theoretical chemistry for third-year students (36 hours)

2016–2017 **Pôle ouest du RFCT**

Density functional theory for master and PhD students (3 hours)

Contents

1 Introduction and methods **1**

2 Magnetic properties of transition metal complexes and ionic solids **7**

2.1 Introduction . . . 7

2.2 Model Hamiltonians and their extraction from theoretical calculations . . . 8

2.2.1 Why model Hamiltonians are mandatory for describing magnetic systems? . 8

2.2.2 Theoretical tools for the extraction of model interactions . . . 8

2.3 Mononuclear compounds . . . 11

2.4 Polynuclear compounds . . . 15

2.4.1 The giant-spin approximation and its generalization to a block-spin model . . 16

2.4.2 The multispin model and its components . . . 18

2.5 Concluding remarks . . . 27

3 Structural and chemical properties of radioelement species **29**

3.1 Introduction . . . 29

3.2 Molecular geometries of 6p species and actinide species . . . 32

3.2.1 Astatine species . . . 32

3.2.2 The $[AnO_2(NO_3)_3]^-$ and $[AnO_3(NO_3)_2]^-$ complexes (An = U, Np, Pu) . . . 38

3.3 Absorption spectroscopy: The UV-Vis spectra of $[PoCl_6]^{2-}$ and $[Po(OH)Cl_4]^-$ . . . 40

3.4 Potential energy surfaces at the SOCI/NEVPT2 level . . . 42

3.4.1 Back to the AtF_3 hypothetical molecule . . . 42

3.4.2 The hydration-induced ground-state change of $[AtO]^+$ . . . 44

3.5 Transformation or reaction energies . . . 47

3.5.1 Ionization energies and electron affinities of astatine species . . . 47

3.5.2 Bond dissociation energies . . . 48

3.6 Concluding remarks . . . 50

4 Chemical bonding in heavy-(radio)element systems **51**

4.1 Introduction . . . 51

4.2 The SOC contribution to effective bond orders 53
4.2.1 The effective bond order concept 53
4.2.2 Homodiatomic molecules: The At_2 case study 54
4.2.3 Heterodiatomic molecules: The AtX (X = F–I) series 55
4.3 The role of the SOC revealed by topological analyses 57
4.3.1 A brief introduction to the quantum chemical topology 57
4.3.2 Analyses on top of one-component and two-component DFT calculations . . 58
4.3.3 Analyses on top of SA-CASSCF and SOCI/NEVPT2 calculations 60
4.4 Concluding remarks 61

5 Outlook **63**
5.1 Introduction 63
5.2 Molecular magnetism 64
5.3 Radiochemistry 64
5.4 Chemical bonding analysis 65
5.5 Epilogue 67

References **90**

Representative publications **91**
Universal theoretical approach to extract anisotropic spin Hamiltonians 93
Magnetic interactions in $LiCu_2O_2$: Single-chain versus double-chain models 105
Unravelling the hydration-induced ground-state change of AtO^+ by relativistic and multi-configurational wave-function-based methods 111
Targeted radionuclide therapy with astatine-211: Oxidative dehalogenation of astatobenzoate conjugates 123
Effective bond orders from two-step spin-orbit coupling approaches: The I_2, At_2, IO^+ and AtO^+ case studies 135

Chapter 1

Introduction and methods

Relativistic effects are at play in many situations, even in everyday life [1]. Of course, it is vain to make an exhaustive list of examples illustrating this; however, a few well-chosen cases are worth being reported. As often nicely stated by Pyykkö [1], "cars start because of relativity". Indeed, the electromotive force of the lead-acid battery, 2.017 V, cannot be explained without considering relativistic effects (an average non-relativistic value of 0.39 V was computed, while a fully relativistic one of 2.13 V was obtained [2]). One should already stress here that, in a similar way as electron correlation is defined, relativistic effects are usually defined and computed as the difference between two models, one more incomplete model (*e.g.* a nonrelativistic one) and one more complete one (*e.g.* a fully relativistic one) [3]. Note that in the remainder of this dissertation, relativistic effects will always be defined by following this governing principle. Another example concerns the color of gold: "nonrelativistic gold" is silver-like, *i.e.* white, while "relativistic gold" is yellow (the interband threshold energy being lowered from 3.5 to 1.35–1.85 eV by relativistic effects, leading to a drastic drop in the reflectivity in a significant part of the visible domain, instead of a constant and efficient reflectance in the entire visible domain [4]).

Within relativistic effects, one may distinguish the spin-free and the spin-dependent relativistic effects. The first ones do not formally depend on the spin degree of freedom, unlike the former ones, *e.g.* the spin-orbit coupling (SOC) term. The SOC is important for instance to explain the occurrence of spin-forbidden transformations, in which a spin-state change is observed. In such a case, the kinetics of the transformation relates to the magnitude of the SOC between the spin components of the two electronic states of interest in the region of interest, for instance in the vicinity of a crossing point [5]. In a similar way, the SOC can be responsible for spin-forbidden electronic transitions (see the discussion on the UV-Vis spectrum of the $[PoCl_6]^{2-}$ complex in Chapter 3). Another phenomenon associated with the SOC is the so-called zero-field splitting (ZFS) [6]. It concerns the degeneracy lift between the spin components (*i.e.* the M_S components) of one or of an ensemble of electronic states in the absence of any external perturbation such as a magnetic

field. The ZFS phenomenon will be at the core of Chapter 2, which hopefully will be somehow complementary to a review and to a book chapter that I have cosigned [7, 8].

In the previous paragraph, the SOC was fully responsible for the existence of the observed phenomena. However, other types of situations, in which the SOC still really matter, exist. For instance, the SOC can change chemical reactivity trends while it does not "activate" any reaction pathway, meaning that it plays the role of a troublemaker rather than a premier role. Nevertheless, obtaining qualitatively correct trends in this case clearly requires to consider the SOC in the quantum mechanical approach that is used to compute the reaction energies of interest. A few cases will be discussed in Chapter 3 to illustrate this possibility, with an example related to the nuclear medicine context [9]. Intuitively, for a chemist, if the SOC can affect reactivity trends, it means that it must be also capable of influencing chemical bonding. Although there is still the need for methodological developments and for further case studies, it is well-known that the SOC can affect chemical bonds [3]. In Chapter 4, a few cases will be reported together with recent developments to highlight the role of the SOC on chemical bonding, and then future developments will be proposed in Chapter 5. Note that at the time of writing this manuscript, the main achieved developments that were published concerned effective bond orders (EBOs) [10], but other chemical bonding analysis philosophies will be mentioned.

Actually, in most of this manuscript, the role of the SOC on structural, physical and chemical properties of molecules and materials will be discussed. From the viewpoint of a computational chemist, it means that the outcomes of calculations that does not account for this relativistic term and then the outcomes of calculations that does account for it will be analysed. Thus, a brief discussion on the main quantum mechanical methodologies that I have used over the years is necessary at this stage. Two main types of electronic structure calculations are available in the quantum chemistry community, formally differing by their working variables. The first class of methods is formally based on the wave function(s) of the quantum state(s) of interest. We call these methods the wave function theory (WFT) methods. The other class of methods formally deals with the electron density(ies) of the quantum state of interest, giving rise to the so-called density functional theory (DFT) methods. Various methods exist in both classes of methods, depending on the approximations that are made to obtain the wave function(s) or electron density(ies) of interest (*vide infra*). In WFT or DFT calculations, approximate solutions of the Schrödinger equation or of the Dirac equation are looked for. While in the former case relativistic effects are not considered (the exact solution to this equation thus corresponds to the exact nonrelativistic limit), all the relativistic effects are introduced in the four-component Dirac equation (the exact solution to this equation thus corresponds to the fully relativistic limit).

Interestingly, transformations and approximations may allow one to end up with the Schrödinger

equation while starting from the Dirac equation. Intermediate stages can be used to define relativistic levels. A first main step consists in reducing the four-component problem to a two-component one, for instance via the zero-order regular approximation (ZORA) [11, 12, 13], the Douglas-Kroll (DK) transformation [14, 15, 16] or a simple block diagonalization of the Dirac matrix [17], leading to the so-called exact two-component (X2C) formalism [18]. In the two-component formalisms, atomic or molecular spinors serve as a basis to expand the actual or the fictitious wave function(s) of interest (WFT or Kohn-Sham DFT [19], respectively). The resulting wave functions have the disadvantage of being less intuitive than the nonrelativistic ones. Furthermore, the two-component methods may be unnecessarily too accurate (!) and also too sophisticated/costly for solving given chemical problems. Therefore, it may be wise to further simplify the relativistic treatment.

Usually, one follows by separating the spin and the orbital (or space) variables in the Hamiltonian. This results in two parts in the Hamiltonian, the one that is formally spin-independent, which we usually refer to as a scalar-relativistic (SR) Hamiltonian, and the one that is formally spin-dependent, which includes the SOC and also other relativistic terms such as the spin-spin coupling (SSC) one [20]. From this, one can define two-step approaches, in which the spin-dependent effects are considered as a perturbation of the SR Hamiltonian. The second step of the calculation can typically be based on quasi-degenerate perturbation theory (QDPT) or on the diagonalization of a state-interaction (SI) matrix [21], expressed in the basis of the M_S components of a set of spin-orbit-free (SOF) states (which can reduce to a single SOF state if only the SSC term is introduced). Note that several implementations of such approaches are available have been reported in the literature (see for instance the ones of Malmqvist *et al.* [22] or the one of Ganyushin and Neese [23]). Also, the SOC may be introduced via the use of an actual operator such as the Breit-Pauli one or an approximation of it [24, 25], or alternatively via the use of spin-dependent (relativistic) pseudopotentials [26].

Another important part of the quantum mechanical treatment concerns the electron-electron interaction term. In Kohn-Sham DFT, it is represented by two terms, (i) the classical interelectronic repulsion and (ii) the exchange-correlation term, which, unlike what its name suggests, not only includes exchange and correlation, but also other "nonclassical" corrections (*e.g.* concerning the self-interaction error or the kinetic energy of the electrons). Although the exchange-correlation functionals can be classified by their levels of sophistication (local density approximation, LDA, generalized gradient approximation, GGA, *etc.*; "pure" *vs.* hydrid; *etc.*), it is hard to know *a priori* what to expect of a given exchange-correlation functional when it is applied to a brandnew chemical problem. Therefore, the successful application of DFT relies on prior benchmark studies that are specific to a property (or a set of properties) and to a type of chemical systems. Note that such a benchmark study will be mentioned in Chapter 3.

In WFT, the description of a given quantum state can be systematically improved by expanding

the basis on which the wave function is expanded. The simplest approach consists in representing it by a single Slater determinant, as it is done within the Hartree-Fock method (see [27] and references therein). Of course, this is way too simple to be generally accurate, and one needs to improve the quality of the wave function for expecting to reach the so-called "chemical accuracy". One way of doing this consists in optimizing both a set of molecular orbitals (MOs) and a set of configuration interaction (CI) coefficients [28]. This leads to the so-called multi-configurational self-consistent field (MCSCF) method. Various flavours of this approach exist, and these essentially differ by the way the CI space is defined. Schemes to facilitate the definition of the CI space for the user have been defined, for instance based on the concept of active space(s). An active space is defined by a number of electrons, n, and a number of MOs, m, and, when applicable, by further restrictions. In the complete active space self-consistent field (CASSCF) approach, a single active space is used and any single or multiple excitation, from the ground configuration state function (CSF), is allowed within the active space (*i.e.* a "full CI" is performed within the active space). Note that other schemes involve a set of active spaces and constraints on excitations or electron occupations, see for instance the restricted active space self-consistent field (RASSCF) approach of Roos and coworkers [29], the generalized active space self-consistent field (GASSCF) approach of Ma *et al.* [30], or even the SplitGAS method of Li Manni *et al.* [31].

Since in practice it is not often affordable to consider full-valence active spaces, methods to improve the quantum mechanical description of quantum states on top of CASSCF calculations have been developed, which can be referred to as "post-CASSCF" methods. These methods may be rely on perturbation theory or on CI theory. Usually, only single and double excitations are considered (see Figure 1.1). The excitation classes are characterized by a number of holes (h) and particles (p), corresponding to the number of electrons that can be withdrawed from the inactive orbitals and to the number of electrons that can be promoted to the virtual orbitals, respectively. Popular multireference perturbation theory (MRPT) approaches are for instance the complete active space second-order perturbation theory (CASPT2) of Roos and coworkers [32, 33, 34] or the second-order n-electron valence state perturbation theory (NEVPT2) of Angeli *et al.* [35, 36, 37]. The most important difference between these two methods relates to the choice of the zeroth-order Hamiltonian: an effective one-electron Fock-type operator is used in CASPT2 while the Dyall Hamiltonian [38], which notably includes the two-electron terms within the active space, is used in NEVPT2.

Alternatively, one can perform a multireference configuration interaction (MRCI) after a CASSCF calculation. If all the single and double excitations are introduced, an MRCISD calculation is performed. The MRCISD calculations are prohibitively expensive and usually suffer from important size-consistency errors. Therefore, it may be more practical and also paradoxally more accurate to restrict the excition list to a subset of the CAS+SD space (see Figure 1.1) when one specifically aims

at computing energy differences [39], especially between states belonging to a same orbital configuration. For instance, the DDCI3 list, usually simply referred to as the DDCI list, which includes all the single and double excitations except the 2h-2p ones, is considered as one of the standards to compute isotropic magnetic couplings in the molecular and solid state magnetism fields [40].

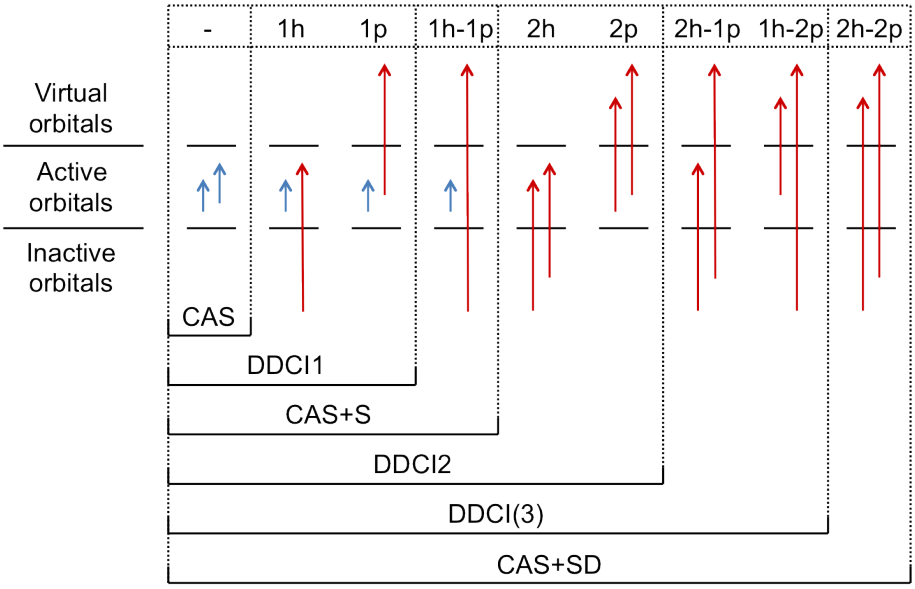

Figure 1.1: The single and double excitation classes at the post-CASSCF level and definition of multireference CI excitation lists. For instance, the CAS+S excitation list includes the DDCI1 list (1h and 1p excitations) plus the 1h-1p excitations, *i.e.* all the single excitations on top of the CAS.

The chapters have been defined according to research topics and not to the quantum mechanical methodologies that were followed. Chapter 2 focusses on molecular and solid state magnetism. Note that in all the studies that will be reported, spin-dependent relativistic effects were introduced *a posteriori*. Chapter 3 focusses mainly on "applied" theoretical radiochemistry, in the sense it essentially deals with the outcomes of quantum mechanical calculations that were performed to address experimental concerns, for interpretation and/or prediction purposes. Although two-step WFT approaches have also been used in this context, most of the reported results were based on DFT. A more fundamental aspect of theoretical radiochemistry concerns the development and application of chemical bonding analysis tools that are valid for heavy-(radio)element species, *i.e.* analysis tools applicable on top of DFT or WFT calculations that does include SOC, *a priori* or *a posteriori*. This will be the subject of Chapter 4 (results) and Chapter 5 (prospects). Interestingly, the two-step approach is the bridge between all the chapters, and I hope that this manuscript will convince the readers of the interest of using this approach in various contexts.

Chapter 2

Magnetic properties of transition metal complexes and ionic solids

2.1 Introduction

Remarkable properties of matter such as magnetism [41], magnetoresistive effects [42], molecular bistability [43], superconductivity [44], multiferroicity [45], *etc.* offer interesting prospects for technological applications in various fields. One may quote for instance magnetic levitation trains, energy storage with no loss, information storage and even quantum computing [46]. As they result from the quantum behavior of matter, they have also been the subject of fundamental research in quantum mechanics (quantum tunneling, quantum interferences, coherence/de-coherence phenomena, *etc.*) and solid-state chemistry and physics. Systems that house such properties have unpaired electrons and exhibit magnetic properties. They can be of different sizes ranging from mononuclear complexes (zero dimension, 0D) to nanoparticles and correlated materials (1D, 2D and 3D). Intense efforts have been devoted to the understanding of the microscopic origin of magnetic properties. This requires analyzing both the weak interactions due to relativistic effects, namely the SOC and/or the SSC, responsible for the single-molecule magnet (SMM) behavior for instance [47], and the interactions between the magnetic centres. As the theoretical description of such systems is usually particularly difficult, mononuclear and binuclear compounds are objects of choice for the study of these interactions. While for mononuclear species much has been done both experimentally and theoretically, only few experimental values are available for anisotropic binuclear compounds. This chapter focuses on the determination of the low-energy spectra and wave functions of mononuclear and binuclear compounds from which all significant interactions can be obtained. One of my objectives was to provide rationalization of complex properties from the understanding of what governs the magnitude and nature of microscopic interactions. Note this work on magnetism has lead to a few "firsts" in *ab initio* quantum chemistry and to some 20 publications in peer-review journals.

2.2 Model Hamiltonians and their extraction from theoretical calculations

2.2.1 Why model Hamiltonians are mandatory for describing magnetic systems?

The low-energy wave functions of highly correlated materials cannot be described using a single electronic configuration (*e.g.* with a single Slater determinant). The zeroth-order description of a magnetic system having N unpaired electrons (spins) in N orbitals must deal with all distributions of the spins in all the orbitals. As a consequence, for an infinite size system, an infinite space has to be considered. Moreover, as the low-energy spectrum of a magnetic system is quasi-degenerate, a good accuracy is required. To reach the suitable accuracy, theoretical descriptions should also account for the interaction among all the other electrons (core electrons of the magnetic centres and ligand electrons) and with the magnetic electrons, *i.e.* appropriate descriptions must treat dynamic electron correlation. Finally, as one is interested in anisotropic magnetic interactions, relativistic effects must be accounted for. For these reasons, both experimentalists in charge of the characterization of the magnetic properties and solid-state physicists who model the collective properties of magnetic materials consider Hamiltonians that are simpler than the exact electronic one. These Hamiltonians are called model Hamiltonians. The model space on which they are spanned only considers the most important electronic configurations and the interactions between these configurations are called model interactions. It is important to note that model interactions are effective interactions which, even if they appear as being simple interactions (such as hopping integrals or exchange integrals), result from much more complicated electronic mechanisms.

2.2.2 Theoretical tools for the extraction of model interactions

Theoretical calculations

Even if this chapter essentially focusses on the role of the SOC and/or the SSC on the low-energy spectra of magnetic systems, it is important to be able to describe them properly in the absence of these relativistic terms. Also, historically, the first important quantum mechanical calculations performed on magnetic systems concerned the isotropic couplings between magnetic centres, which already occurs in the absence of the SOC and of the SSC. As will be shown later, the isotropic couplings are effective interactions of the Heisenberg-Dirac-van Vleck (HDVV) model [48, 49, 50]. Once known, they permit one to reproduce the low-energy spectrum, *i.e.* the energy of all the spin states belonging to a given electronic configuration. Both DFT and WFT methods can be used to determine magnetic couplings. As will be rationalized later, the best available method up to date is the difference dedicated configuration interaction (DDCI) method [39]. Note that the values reported in this chapter have been computed with this method, implemented in either the ORCA

code [51] or the CASDI suite of programs [52].

The DDCI method is in practice restricted to finite-size systems, *i.e.* without the possibility for applying periodic boundary conditions (PBCs). Therefore, its use in the context of ionic solids deserves some more attention. Of course, isotropic couplings can be computed in the presence of PBCs with spin-unrestricted approaches [53], but my experience is clearly more toward molecular calculations. Due to the local character of the magnetic couplings in ionic solids, and due to the accuracy of the DDCI method for computing magnetic couplings, embedded cluster calculations at the DDCI level are capable of well reproducing experimental coupling values [54]. In embedded cluster calculations, a small fragment of the extended system is considered. Because one considers that most of the influence of the remaining part of the extended system is of electrostatic nature, a set of point charges is defined to reproduce the Madelung field within the cluster area. Since ionic solids are characterized by charge alternations, the combination of a small cluster and of point charges may excessively polarize the wave function(s) of the cluster. To prevent this, it is good practice to associate zero-electron model potentials, usually referred to as *ab initio* embedded model potentials (AIEMPs) [55], to the point charges that replace the neighboring atoms of the cluster. Another way of assessing the quality of the cluster approach consists in comparing magnetic couplings obtained with cluster and periodic calculations, such that no theory/experiment biais can alter the conclusion. This is the way we have checked the quality of the clusters in [56] and [57]. In the first paper, the calculations were performed by the PhD student A.-M. Pradipto, while they were actually performed by myself in the second one. Also, interestingly, it appears that in this second paper, we reported what I still consider as the worse agreement ever reported between cluster and periodic calculations! Note that I have also participated to a paper reporting MRCI coupling values based on a different CI list than the DDCI one [58] (the calculations were performed by the PhD student N. Bogdanov).

At low temperature, a degeneracy lift is observed between the various M_S components of the spin states in the absence of a magnetic field. This ZFS is due to relativistic effects [59]. Various methods have been developed in the last decades to compute or extract ZFS parameters from the outcomes of quantum mechanical calculations. Following the pioneering work of McWeeny and Mizuno on the so-called spin-spin coupling [20], various perturbative and linear response approaches have been designed to compute the ZFS parameters within DFT or WFT frameworks that does include spin-spin coupling and/or spin-orbit coupling terms [60, 61, 62, 23, 63, 64, 65]. One should note that the perturbative and linear response theory based DFT approaches do not lead to values in agreement with experimental results in the case of nickel(II) complexes [66], although satisfactory accuracy can be obtained in the case of other d^n configurations, *e.g.* in the case of high-spin manganese(II) or manganese(III) complexes (with d^5 and d^4 configurations respectively) [67, 68]. Therefore, WFT based approaches are recommended since, as shown many times by me and/or others, they usually

lead to accurate values in the case of any d^n configuration [67, 68, 69, 70, 71, 72, 73, 74, 75, 76]. Although one can use second-order perturbation theory to compute ZFS parameters [23], a more popular approach nowadays consists in performing spin-orbit configuration interaction (SOCI) calculations. Within the contracted scheme, the electronic energy plus SOC matrix is diagonalized in a second step [22, 21]. In order to obtain more accurate excitation energies on the diagonal of this matrix [77, 78], additional electron correlation is introduced after the MCSCF step, typically at an MRPT or at an MRCI level. After the SOCI step, the ZFS parameters and the magnetic anisotropy axes can be determined with the effective Hamiltonian theory (the method that I have developed in the first part of my PhD) [69], or with the pseudospin approach of Chiboratu and Ungur [79]. Values reported here have been computed using the SOCI method implemented in both the ORCA [51] and MOLCAS [80] codes and extracted using the effective Hamiltonian theory (see below).

The effective Hamiltonian theory

From the energies and the wave functions computed with (sophisticated) quantum chemistry methods, it is possible to extract in a rational way all the interactions of a model Hamiltonian by using the effective Hamiltonian theory. The basic idea consists in looking for an effective Hamiltonian that is spanned in a model space constituted of only the most important electron distributions and keeping only the most important interactions between these. This Hamiltonian is simpler than the exact electronic Hamiltonian, but must perfectly reproduce the low-energy spectrum [81]. In the des Cloizeaux formalism [82], it satisfies:

$$\hat{H}^{eff}\tilde{\Psi}_i = E_i\tilde{\Psi}_i \tag{2.1}$$

where E_i and $\tilde{\Psi}_i$ are respectively the energies and the symmetrically-orthonormalized projections onto the model space of the wave functions of the exact electronic Hamiltonian. As the energies and wavefunctions of the exact electronic Hamiltonian are determined by *ab initio* calculations, all the matrix elements of this effective Hamiltonian can be numerically computed via the following expression:

$$\hat{H}^{eff}_{jk} = \langle j|\sum_i E_i|\tilde{\Psi}_i\rangle\langle\tilde{\Psi}_i|k\rangle \tag{2.2}$$

The model Hamiltonian is then assimilated to the effective Hamiltonian. To perform the extraction, one writes down the analytical expression of all the matrix elements of the model Hamiltonian as functions of the model interactions. From the one-to-one correspondence between the numerical and analytical matrix elements, a numerical value can be attributed to all the model interactions. It is worthwhile to note that the projections of the wave functions onto the model space are actually calculated in the process. The validity of the model space can therefore be checked and the model

can be improved by introducing additional electron distributions in the model space when required. As all the matrix elements are numerically computed, additional operators (and therefore effective interactions) can be introduced if necessary. Such a method enables one to question the validity of any model Hamiltonian to extract in a rational way appropriate interactions and to refine existing models (and even helps in proposing new and adequate models).

Of course, the effective Hamiltonian theory was elaborated well before I was born. Moreover, it had been already used in various contexts before I started my PhD. However, under the initiative of N. Guihéry, I have been the first one to use it (let us template this by saying at least in the "Jujols community") after the introduction of the SOC, in other words with complex wave functions. This required me to adapt an existing effective Hamiltonian theory code that was working with real wave functions. This was the opportunity to do some little programming in FORTRAN (kind of a compulsory step for a quantum chemist apprentice...), and also to realize for instance that the usual expression for the Bloch effective Hamiltonian, *i.e.* $\sum_i |\tilde{\Psi}_i\rangle E_i S^{-1} \langle\tilde{\Psi}_i|$, was only correct for real wave functions (one should write $\sum_i |\tilde{\Psi}_i\rangle E_i \langle S^{-1}\tilde{\Psi}_i|$ instead for complex wave functions). Thus, changing the "double precision" declarations to "double complex" ones was necessary, but not salutary! Eventually, I managed to get my program working and delivering correct Bloch and des Cloizeaux effective Hamiltonians. Since all the model Hamiltonians were Hermitian, I then used only des Cloizeaux effective Hamiltonians, which are by construction Hermitian. This led to several firsts in *ab initio* quantum chemistry, and also gave me the opportunity to question and refine the general model Hamiltonians for binuclear complexes.

2.3 Mononuclear compounds

In mononuclear systems, such as mononuclear transition metal complexes, the M_S components of a non-degenerate state may split and mix in the absence of any external perturbation. This effect, referred to as ZFS, can only occur for states with $S > \frac{1}{2}$. It is well known that it can be observed in the presence of an anisotropic ligand field around the paramagnetic centre of interest, and relates to relativistic effects (essentially to the SOC). Derivations of ZFS parameters with simple Hamiltonians that include the ligand field and the SOC can be found in textbooks such as the one of Griffith [83] or the one of Abragam and Bleaney [84]. A typical configuration to illustrate such derivations is the d^8 one, *e.g.* the case of high-spin nickel(II) complexes. Within an octahedral ligand field, it can be easily shown that the spin components of the ground $^3A_{2g}$ state remain degenerate. If one considers an axially distorted field, the M_S components of this ground state (labeled $^3B_{1g}$ in the D_{4h} symmetry point group) are no longer three-fold degenerate. If one considers an appropriate coordinate frame (for which the quantization axis is oriented along the axial distortion), it can be shown that:

$$E(S=1, M_S=0) = -\frac{2\zeta^2}{\Delta_2} \tag{2.3}$$

and:

$$E(S=1, M_S=\pm 1) = -\frac{\zeta^2}{\Delta_1} - \frac{\zeta^2}{\Delta_2} \tag{2.4}$$

where ζ is the (effective) monoelectronic SOC constant of the nickel(II) ion, Δ_1 is the in-plane electronic excitation energy (corresponding to a $x^2-y^2 \rightarrow xy$ orbital excitation), and Δ_2 is the out-of-plane electronic excitation energy (corresponding to an appropriate combination of the $x^2-y^2 \rightarrow xz$ and $z^2 \rightarrow xz$ excitations or to a combination of the $x^2-y^2 \rightarrow yz$ and $z^2 \rightarrow yz$ excitations). The splitting between the $M_S = 0$ and the $|M_S| = 1$ components can be effectively described by the following model Hamiltonian:

$$\hat{H}_1 = D\left(\hat{S}_z^2 - \frac{1}{3}\hat{S}^2\right) \tag{2.5}$$

where D is the "axial" ZFS parameter. Thus, one can express this parameter in terms of both the electronic excitation energies and the ζ constant:

$$D = -\frac{\zeta^2}{\Delta_1} + \frac{\zeta^2}{\Delta_2} \tag{2.6}$$

If the symmetry of the field is further lowered, the $|M_S| = 1$ components of the ground orbital state split; appropriate linear combinations of these components are formed. As previously, one can recast the problem in terms of a simple model Hamiltonian:

$$\hat{H}_2 = \hat{H}_1 + E\left(\hat{S}_x^2 - \hat{S}_y^2\right) = D\left(\hat{S}_z^2 - \frac{1}{3}\hat{S}^2\right) + E\left(\hat{S}_x^2 - \hat{S}_y^2\right) = D\left(\hat{S}_z^2 - \frac{1}{3}\hat{S}^2\right) + \frac{E}{2}\left(\hat{S}_+^2 + \hat{S}_-^2\right) \tag{2.7}$$

where E is the "rhombic" ZFS parameter. Naturally, the D and E parameters can also be expressed in terms of electronic excitation energies and the ζ constant in such a situation, which I had actually done at the beginning of my PhD but eventually reported years after [8]. In the general case (*i.e.* in the absence of any particular symmetry element), the "natural" quantization axis is not known, and one needs to consider a symmetric second-rank ZFS tensor:

$$\hat{H}_3 = \hat{S}\overline{\overline{D}}\hat{S} \tag{2.8}$$

After having determined the $\overline{\overline{D}}$ tensor components in an arbitrary axis frame, diagonalization of this tensor gives access to its principal axes. The axial and rhombic ZFS parameters can be easily determined from the diagonal elements of this tensor in this frame (*i.e.* from its eigenvalues). By convention, the axial ZFS parameter is chosen to be at least three times larger than the rhombic

one in absolute value (such that $|\frac{E}{D}| \leq \frac{1}{3}$). This convention fixes the z anisotropy axis, while another convention must discriminate the x and y ones (note that two different conventions are commonly used in the literature, $E \geq 0$ or $\frac{E}{D} \geq 0$). If D is negative, z is the "easy" axis of magnetization, while it is the "hard" one if D is positive.

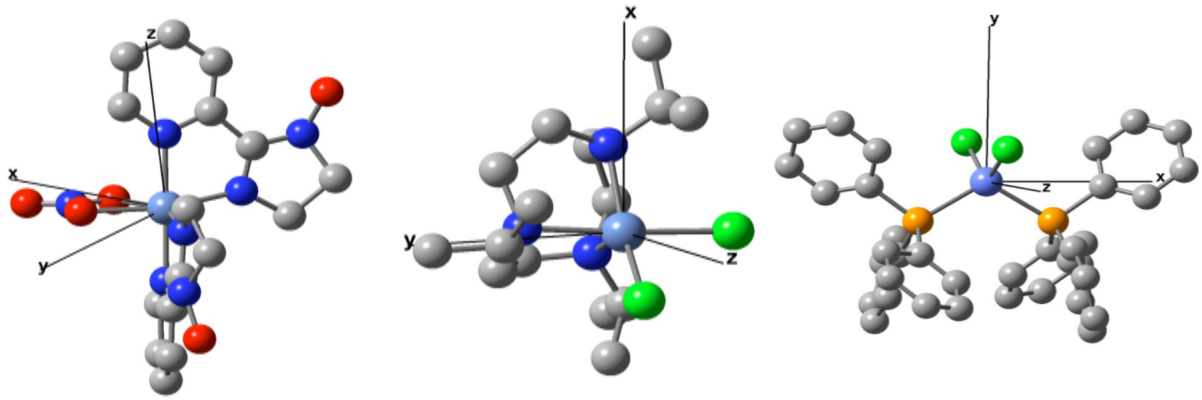

Figure 2.1: Representations of the $[Ni(HIM2\text{-}py)_2NO_3]^+$, $Ni(iPrtacn)Cl_2$, $CoCl_2(PPh_3)_2$ compounds, referred to as **1**, **2** and **3** in Table 2.1, respectively. The magnetic anisotropy axes are indicated [69].

Table 2.1: Computed and experimental values of the ZFS parameters for the Ni(II) and Co(II) complexes represented in Figure 2.1 [69].

Compound	Parameter	Comp. value (cm^{-1})	Expt. value (cm^{-1})
1	D	-10.60	-10.15 [85]
	E	0.76	0.10 [85]
2	D	$+16.45$	$+15.70$ [86]
	E	3.82	3.40 [86]
3	D	-14.86	-14.76 [87]
	E	0.54	1.14 [87]

This model Hamiltonian, $\hat{S}\overline{\overline{D}}\hat{S}$, also describes the ZFS in $S = \frac{3}{2}$ systems with non-degenerate ground states, such as nearly tetrahedral cobalt(II) complexes (d^7 configuration). Values of the ZFS parameters for the Ni(II) and Co(II) complexes that are represented in Figure 2.1 are compared to experimental ones in Table 2.1. I computed these values using the SOCI method [22, 21], as implemented in the MOLCAS code [80], and extracted with the effective Hamiltonian approach [69]. At that time, these were the first extractions of ZFS parameters based on the effective Hamiltonian theory, but note that my approach has become more popular after its independent implementation

in the ORCA code [51]. It is worth mentioning that the values for complex **3** were the first ones properly extracted at the SOCI level for an $S = \frac{3}{2}$ complex, *i.e.* after a variational SOC calculation and not with second-order perturbation theory. Indeed, determining the energy difference between the two Kramers doublet of interest after a variational calculation is not sufficient to extract the ZFS parameters [88], one must thus make use of the information contained in the wave functions. Also, the observed satisfactory agreement between theory and experiment kind of validates the methodology, as well as the choices that were made for the specific computational details (size of the active space, size of the state-averaging space, size of the SI matrix –usually chosen in correspondence with the state-averaging space –, *etc.*). For a more robust validation, one further needs to assess the dependence of the results with respect to these computational degrees of freedom, which was done in [69], but not reported here for the sake of simplicity. More importantly, the effective Hamiltonians, as expected (the contrary would have been really weird...), confirmed that $\hat{H}_3$ was perfectly suited to describe the ZFS in $S = 1$ and $S = \frac{3}{2}$ systems, and also that the effective $\overline{\overline{D}}$ matrix was indeed transforming as a true second-rank tensor with respect to a change in the coordinate frame, if reextracted after a new *ab initio* calculation in this new frame (I did this right from the beginning, but only mentioned it in my PhD dissertation and in [8]). Thus, not only it looked like a tensor, but it also behaved as a tensor, then it had to be a tensor!

For larger spin quantum numbers ($S \geq 2$), additional terms may have to be introduced in the model Hamiltonian to describe properly the energy levels and to ensure a good correspondence between the model vectors and the "true" wave functions:

$$\hat{H}_4 = \hat{H}_3 + \sum_{q=-k}^{k} \sum_{k=4}^{2S} B_k^q \hat{O}_k^q = \hat{S}\overline{\overline{D}}\hat{S} + \sum_{q=-k}^{k} \sum_{k=4}^{2S} B_k^q \hat{O}_k^q \tag{2.9}$$

where k is the rank of the spherical tensor and must be even, q may be odd, and $\hat{O}_k^q$ are extended Stevens operators [84, 89, 90, 91]. In the magnetic anisotropy axis frame, the model Hamiltonian reduces to:

$$\hat{H}_5 = \hat{H}_2 + \sum_{n=0}^{k} \sum_{k=4}^{2S} B_k^n \hat{O}_k^n = D\left(\hat{S}_z^2 - \frac{1}{3}\hat{S}^2\right) + \frac{E}{2}\left(\hat{S}_+^2 + \hat{S}_-^2\right) + \sum_{n=0}^{k} \sum_{k=4}^{2S} B_k^n \hat{O}_k^n \tag{2.10}$$

where n is even. I was the first one to compute *ab initio* the B_4^0, B_4^2 and B_4^4 parameters in mononuclear compounds [92], which were actually model complexes and not experimentally relevant ones. As I mentioned in a book chapter, I have already computed these terms in the [γ-Mn(acac)$_3$] complex [8]; however, as I had also shown with pain (the derivation was quite tedious), the values of these terms are proportional to the inverse of the degeneracy lift between the ground orbital states [92]. In other words, the Jahn-Teller effect causes there a large (axial) distortion that numerically "kills" the B_4^0, B_4^2 and B_4^4 parameters.

After having developed the theoretical tools to compute and understand the ZFS in mononuclear complexes, I started to collaborate with experimentalists, T. Mallah in Paris and J.-P. Costes in Toulouse, to guide them toward the synthesis of new systems with large anisotropies. I predicted for instance large and negative D values for heptacoordinate nickel(II) complexes and large and positive D values for analogous cobalt(II) complexes. The experiment was published before the *ab initio* calculations and the ligand-field theory based reasoning for the cobalt(II) case [93], but the reader of this manuscript should know that the theoretical prediction was done earlier, even if actually published after and together with the calculations and experiments on the nickel(II) system [75]. I also asked J.-P. Costes to synthesize new pentacoordinate nickel(II) complexes, but we only managed to obtain complexes with large positive D values, *i.e.* close to the square pyramid situation (in other words, these were not stricking D values, although this work was worthwhile on the synthesis side) [73]. Note that the reasoning that I developed during my PhD is still up-to-date, as attested for instance by a more recent publication that I have cosigned, dealing with pentacoordinate cobalt(II) complexes [94].

Concerning the single-ion anisotropies in solids, I started when I was in the Netherlands by guiding the PhD student N. Bogdanov from Dreden for computing the single-ion anisotropies of osmium(V) centres in the $Cd_2Os_2O_7$ pyrochlore, with the embedded cluster approach [58]. When I was in Minnesota, I focused extensively on the Fe_2(dobc) metal-organic framework. By means of cluster calculations (with no embedding this time), I showed that the iron(II) centres in this system, of unusual coordination sphere (with one "empty" coordination site), were highly anisotropic [95], and that this anisotropy was subject to changes by gas adsorption [96]. This ends up the present discussion on mononuclear compounds; however, the interested reader is encouraged to refer to the corresponding publications for more details.

2.4 Polynuclear compounds

In polynuclear compounds, two different approaches can be used. In the first one, referred to as the giant spin approximation (GSA), only the degeneracy lift of the M_S components of the ground spin state is described. Nevertheless, a more general definition of it will be presented here to deal with a set of spin states. It is expected to be appropriate only when the ground spin state is enough separated in energy from the first excited spin state, *i.e.* for strongly coupled spins. The other approach aims at describing all the states resulting from the coupling of the local ground states of the paramagnetic ions via a multispin model. In this model, both isotropic and anisotropic interactions between the magnetic centres are at play. Also, it is important to stress already here that when I started my work on binuclear complexes in 2008, only one publication was available in the literature concerning an *ab initio* calculation of the energy levels of a binuclear complex (*i.e.* in the presence

of the SOC) [97]. This publication concerned the coupling of two $S = \frac{1}{2}$ spins. Therefore, almost everything had to be done concerning the methodological aspects, the model Hamiltonians and the rationalization of the natures and magnitudes of the anisotropic exchange parameters. Even worse, there were some confusions and controversies concerning the models for the so-called 'weak-exchange limit', independently from the choice of the model Hamiltonian. Therefore, I had the opportunity to make a few more "firsts" in *ab initio* quantum chemistry and also to refine the standard model Hamiltonians for binuclear complexes and, as a consequence, for other polynuclear complexes.

2.4.1 The giant-spin approximation and its generalization to a block-spin model

Anisotropic interactions can substantially modify a low-energy spectrum by splitting and mixing the M_S components of the spin states that arise from the previously described isotropic interaction, as well as by mixing components or linear combinations of components that belong to different spin "states". The mixing of components belonging to different spin states is usually referred to as 'spin mixing' or 'S mixing' [98, 99]. This spin mixing originates from the SOC and some types of mixings can be symmetry forbidden. Two main types of couplings between different spin-state components can occur, namely couplings between (i) M_S components belonging to S and S+1 states, and (ii) M_S components belonging to S and S+2 states, which is somehow less documented (it may be considered though in the fitting of experimental data without necessarily being explicitly mentioned). In the former case, this coupling may be dominated by the "direct", *i.e.* first-order, SOC between these components [56, 100]. If the system of interest possesses a symmetry centre, these terms vanish (by symmetry). In the latter case, the interaction is "indirect", *i.e.* at second order of perturbation, that is, involves spin components of states that do not belong to the model space that is spanned by the M_S components of all the spin states generated by the isotropic interaction(s) (*e.g.* components which are not the M_S components of the lowest quintet, triplet and singlet states of a nickel(II)-nickel(II) binuclear complex) [101, 102]. Note that these two types of couplings will be attributed later to different types of effective interactions in terms of the multispin model.

If these couplings are negligible with respect to the isotropic interaction(s), *i.e.* in the 'strong-exchange limit', one can consider a block-diagonal model matrix [6, 103], which can be referred to as the 'block-spin model' [7, 8]. In this case, the different spin blocks can be independently dealt with and each spin block effectively described as if it were belonging to a mononuclear system, *i.e.* by applying $\hat{H}_4$, in the case of an arbitrary coordinate frame, or alternatively $\hat{H}_5$, if the magnetic anisotropy axis frame of the spin block of interest is considered. For a full block-spin picture, one must then also account for the splitting between the various spin states, and thus, introduce the isotropic coupling terms on the diagonal elements of the block-diagonal model matrix.

If the spin mixing can be considered as a perturbation of the block-spin picture, which may

be seen as an "intermediate-exchange regime", I confirmed with pen and paper that additional operators must be introduced to correctly describe the energy levels of the block spin of interest, and that, contrary to the common thought, these must be distinct from the extended/standard Stevens operators. For this, I took the example of the $S = 2$ block of a centrosymmetric nickel(II)-nickel(II) binuclear complex [102]. This approach in principle also gives access to the effective stabilization or destabilization of the $S = 0$ level that is due to the mixing with spin components of the $S = 2$ block (in the case of antiferromagnetic or ferromagnetic coupling, respectively –*vide infra*–). If the spin mixing and the block-spin terms are of the same orders of magnitude, as is the case in the 'weak-exchange limit', one should stress that the uses of the GSA or of the block-spin model are problematic, and that no systematic studies have been performed to discuss the consequences of these approximations on the parameter values that are extracted from experiments.

Concerning the computations of giant-spin or block-spin parameter values, a wide range of examples, including the "classical" Mn_{12} SMM [61], has been reported in the literature based on DFT and perturbation theory. These works usually lead to D values in good agreement with experimental ones [61, 104, 105, 106, 107, 108, 109, 110]. However, since, as mentioned previously, current DFT implementations to compute ZFS parameters seem to be largely off for the local anisotropy of nickel(II) paramagnetic centres [66], it would be interesting to see which values would be computed for nickel based SMMs such as Ni_4 ones [111].

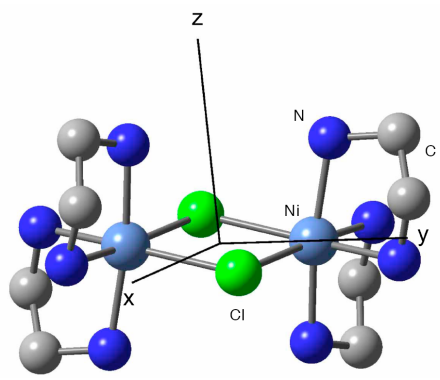

Figure 2.2: Representation of the $[Ni_2(en)_4Cl_2]^{2+}$ complex. The magnetic anisotropy axes are indicated [101, 102].

Concerning WFT, only a few studies have been reported, which include the pioneering work of Webb and Gordon [97], my work on the $[Ni_2(en)_4Cl_2]^{2+}$ (en=ethylenediamine) complex [101, 102] (see Figure 2.2) and also the study of model nickel(II)-nickel(II) binuclear complexes performed by R. Ruamps [112, 113], the PhD student who pursued my work in Toulouse and in Tarragona, and with whom I was still in contact after my defense. Concerning the $[Ni_2(en)_4Cl_2]^{2+}$ complex, the comparison of reliable computational and experimental data is problematic since no rhombic param-

eters were introduced in the latest experimental parameter determination [114], while calculations showed significant rhombic parameter values for the $S = 2$ and $S = 1$ blocks. For the $S = 2$ block, the computed D value, -3.0 cm^{-1}, is a bit larger in absolute value than the experimental one, -1.8 cm^{-1}, although still in reasonable agreement with it. Therefore, it can be seen as a successful application of WFT to the giant-spin problem. Concerning the study of the model systems and the D and E parameters and the $S = 2$ and $S = 1$ blocks, it appeared that the corresponding D parameters tend to have opposite signs, although no strong correlation between these two parameters was found [112], as I intuited a couple of years before the publication of this work. Moreover, the D parameter of the $S = 1$ block seems to be always larger in absolute value than the one of the $S = 2$ block by a factor that ranges from 2 to 5 [112], this interval notably including the factor 3 that can be obtained by further simplifying the equations reported by Boča based on a multispin picture [6, 103]. Last but not least, I should mention that my work on the copper acetate monohydrate molecule (see Figure 2.3), which was originally presented in the frame of the giant-spin model for the $S = 1$ spin block [71]. However, a strict proportionality occurs in this case between the giant-spin and multispin parameters, and thus, I have chosen to present this in the multispin part.

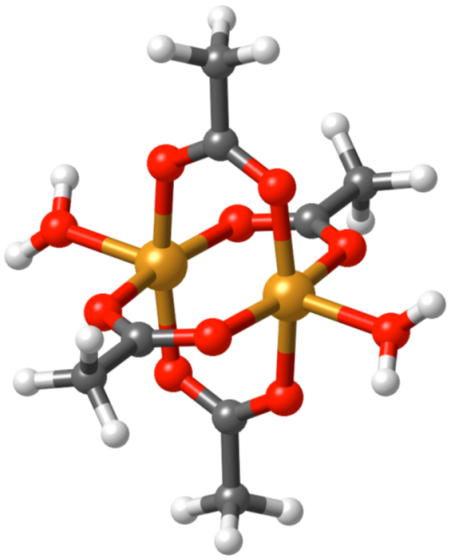

Figure 2.3: Representation of the copper acetate monohydrate molecule. The z anisotropy axis almost coincides with the Cu–Cu orientation [71].

2.4.2 The multispin model and its components

In the multispin picture, the model space is constituted of all the products of the atomic ground-state M_S components. As a consequence, diagonalization of a model matrix gives access to the M_S components of all the states of the configuration, and not only to those of a single spin state, contrary to the giant-spin model. For instance, considering a complex constituted of two high-spin Ni(II)

ions ($S = 1$), the coupling between the local (uncoupled) spin triplets will generate nine coupled states, forming the quintuplet, triplet and singlet spin states in the classical isotropic picture. In the next paragraphs, isotropic and anisotropic interactions will be step-by-step introduced by following an intended increase in complexity.

The zeroth-rank isotropic exchange

The HDVV model is an isotropic spin Hamiltonian [48, 49, 50]. It is relevant for the description of magnetic systems for which a large gap exists between each (local) electronic ground state and the corresponding local excited or ionized states. Thus, the model space can be restricted to the products of the local ground spin states. One should note that the spatial part of the wave function can be omitted to define the model space since all the spin states are assumed to have the same or very close ones; thus, the model space is actually constituted of pure spin functions and the only degrees of freedom are the M_S components of the spins of the magnetic centres. This spin Hamiltonian has the following expression for a binuclear system constituted of two magnetic centres, denoted a and b, respectively:

$$\hat{H}_6 = J\hat{S}^a \cdot \hat{S}^b = J\left(\hat{S}^a_x\hat{S}^b_x + \hat{S}^a_y\hat{S}^b_y + \hat{S}^a_z\hat{S}^b_z\right) = J\hat{S}^a_z\hat{S}^b_z + \frac{J}{2}\left(\hat{S}^a_-\hat{S}^b_+ + \hat{S}^a_+\hat{S}^b_-\right) \tag{2.11}$$

where J is the isotropic exchange effective integral, often called the magnetic coupling. Depending on the J sign, this coupling is said ferromagnetic ($J < 0$) meaning that the ground state has the largest possible S quantum number, or antiferromagnetic ($J > 0$) when the ground state has the smallest possible S. Let us recall that the coupling is said 'ferrimagnetic' when the spins to be coupled are of different values and if the coupling is antiferromagnetic, *i.e.* if $S_{min} > 0$.

For a binuclear system having only one unpaired electron per centre ($S^a = S^b = \frac{1}{2}$), the spin operators couple the two opposite-spin distributions $|\frac{1}{2}, -\frac{1}{2}\rangle$ and $|-\frac{1}{2}, \frac{1}{2}\rangle$, *i.e.* exchanges the M_S components of a and b, respectively, and the J sign determines whether the singlet or the triplet spin-coupled state will be the ground spin state since the energy difference between these two states, $\Delta E = E[S = 1] - E[S = 0]$, is simply J. This exchange goes through intermediate ionic electronic configurations in which one electron has jumped on the other centre according to the so-called Anderson mechanism [115, 116]. When the magnetic centres are connected through a bridging ligand, the generalized Anderson mechanism applies [117]. The electrons and the orbitals of the ligand mediates this coupling and metal-to-ligand charge transfer (MLCT) and ligand-to-metal charge transfer (LMCT) configurations are involved in the process.

This Hamiltonian is applicable to systems having more than one unpaired electron per centre. The model space is still constituted of the products of the ground spin states of the magnetic centres. As shown in various papers, the physical content of the magnetic coupling at second order

of perturbation is actually given by the direct exchange and the kinetic exchange [118, 119, 120]. One should however note that deviations to the Heisenberg spectrum may be observed. These are due to local excited states which may play a non-negligible role [121]. These effects may be effectively accounted for by additional interactions in the model Hamiltonian [122]. Note that N-body operators must sometimes be used for N-metallic compounds.

From a theoretical chemistry point of view an accurate calculation of the magnetic coupling requires accounting for various effects such as charge and spin polarization effects and a correct evaluation of the energy of the LMCT and MLCT intermediate configurations of the generalized Anderson mechanism. As it accounts well for all these effects, the DDCI method provides very precise values of magnetic couplings in transition metal complexes [40]. To reach the same accuracy in organic compounds, it is often required to determine accurate magnetic orbitals upstream, as the spins can be spread over several centres and an adequate description of their delocalization is crucial for obtaining precise magnetic couplings [123].

A long-standing experience on the computation and interpretation of isotropic couplings had been acquired in Toulouse and Tarragona well before I started my PhD [40]. Therefore, I have not brought much novelty on the isotropic coupling side. Of course, I have computed J values at the DDCI level, but this was essentially a necessary step prior to introducing and modeling the anisotropy, and thus, not a goal in itself. Only two points may be worth being mentioned, (i) I have shown that the SOC can slightly affect extracted J values [100, 101] and (ii) I computed the J values of orbitally-excited states of the copper acatate monohydrate molecule (see Figure 2.3) at the DDCI level [71], which was not only very costly, but also truly original at that time.

This discussion was essentially focused on WFT calculations. Of course, it is possible to compute J values with DFT, within the spin-broken-symmetry framework. Without entering into details, various extraction schemes are available, depending on the coupling regime that actually occurs or that is assumed (weak, intermediate or strong). Note that I have computed J values with DFT for the $LiCu_2O_2$ ionic solid (the Ising values reported in [57]) and for the $[PuO_3(NO_3)_2]^-$ gas-phase exotic complex [124], and that I have guided two PhD students for doing so when I was a post-doc in Minnesota, P. Verma from the Truhlar Group, who computed the J values for Fe_2(dobc) before [95] and after gas adsorption [96, 125], and R. K. Carlson, who computed the J values of various bimetallic complexes that were synthesized by the Lu Group [126].

The second-rank symmetric exchange

When the binuclear system is centrosymmetric and consists of magnetic centres having a single unpaired electron ($S^a = S^b = \frac{1}{2}$), the only anisotropic interaction that is spin and symmetry allowed is the symmetric anisotropic exchange [127]. As an interesting example of such anisotropic system,

one may quote the copper acetate monohydrate molecule (see Figure 2.3), which raised a series of fundamental questions. At first, copper acetate was assumed to be mononuclear, *i.e.* to contain only one Cu(II) ion per molecule. However, the unexpected decrease of the magnetic susceptibility at low temperature, first measured by Guha in 1951 (see Figure 2.4) [128], attracted the attention of Bleaney and Bowers who performed an electron paramagnetic resonance (EPR) study in 1952 [129]. Perhaps the more stricking indication for the occurence of a binuclear complex was the famous Christmas tree associated with the hyperfine coupling interaction, which could not be explained without considering two equivalent $I = \frac{3}{2}$ nucleus spins (see Figure 2.5). Since they also observed a small ZFS in the first excited state (a spin-triplet one), they strongly suggested the existence of interacting pairs of cupric ions, before the crystal structure of this molecule was even known. Several debates followed these studies concerning both the nature of the magnetic interactions (either metal-metal or through ligand) and the sign of the axial ZFS parameter. A last EPR study, performed in 2008 [130], definitly showed that the axial ZFS parameter is negative in this system.

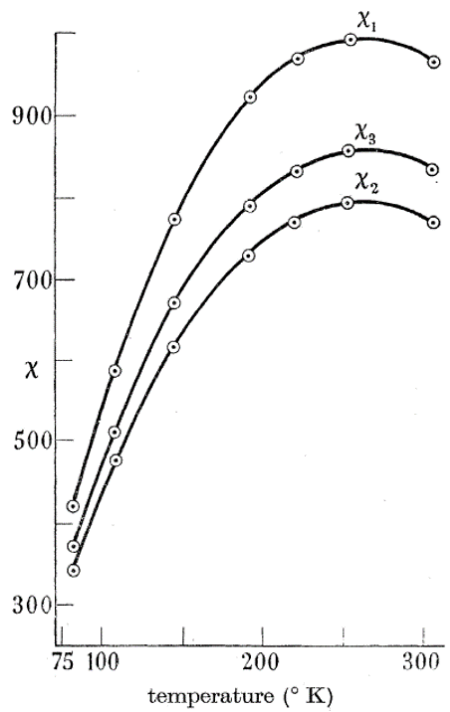

Figure 2.4: Magnetic susceptibility curves of copper acetate monohydrate, 1, 2 and 3 being the three orientations in space that correspond to the principal magnetic axes [128].

For such a simple binuclear system having one unpaired electron per centre, the multispin Hamiltonian writes:

$$\hat{H}_7 = \hat{H}_6 + S^a \overline{\overline{D^{ab}}} \hat{S}^b = J\hat{S}^a \cdot \hat{S}^b + \hat{S}^a \overline{\overline{D^{ab}}} \hat{S}^b \tag{2.12}$$

where $\overline{\overline{D^{ab}}}$ is the symmetric anisotropic exchange tensor. In the $S^a = S^b = \frac{1}{2}$ situation and in the

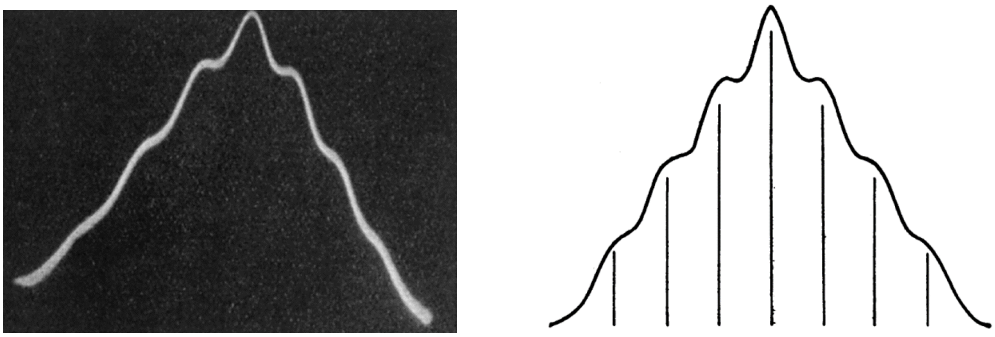

Figure 2.5: Oscillogram showing the hyperfine structure of copper acetate monohydrate with the magnetic field parallel to the z axis (left) and calculated hyperfine structure assuming two equivalent $I = \frac{3}{2}$ nucleus spins (right) [129].

absence of any antisymmetric term, the symmetric exchange tensor can be easily obtained from the giant-spin ZFS tensor of the $S = 1$ spin block [6, 8, 41, 71, 103]:

$$\overline{\overline{D^{ab}}} = 2\overline{\overline{D}} \tag{2.13}$$

Thus, the ZFS of the copper acetate monohydrate molecule could have been equally presented in the giant-spin part or in the multispin part of the discussion. Since I have chosen to present this with the multispin perspective, all the expressions and numerical values of the original publications [71, 130] have been multiplied by a factor of 2.

It is quite straightforward to derive analytical expressions for the SOC contributions to the D^{ab} and E^{ab} parameters [71]:

$$D^{ab} = 4\frac{\zeta^2 J_{x^2-y^2,xy}}{\Delta E^2_{x^2-y^2,xy}} - \frac{1}{2}\frac{\zeta^2 J_{x^2-y^2,xz}}{\Delta E^2_{x^2-y^2,xz}} - \frac{1}{2}\frac{\zeta^2 J_{x^2-y^2,yz}}{\Delta E^2_{x^2-y^2,yz}} \tag{2.14}$$

and:

$$E^{ab} = \frac{1}{2}\frac{\zeta^2 J_{x^2-y^2,yz}}{\Delta E^2_{x^2-y^2,yz}} - \frac{1}{2}\frac{\zeta^2 J_{x^2-y^2,xz}}{\Delta E^2_{x^2-y^2,xz}} \tag{2.15}$$

where $\Delta E^2_{x^2-y^2,n}$ are the squares of the geometric means of the excitation energies corresponding to the same local single excitations ($x^2 - y^2 \rightarrow n$) and $J_{x^2-y^2,n}$ are the magnetic couplings in these single-excited states.

Since it is crucial to get the $J_{x^2-y^2,n}$ magnetic couplings right for obtaining accurate SOC contributions to the symmetric exchange parameters for the right reason, I computed all these excite-state magnetic couplings at the DDCI level prior to performing various CI calculation *a posteriori*, (i) with the sole SSC term, (ii) with the sole SOC term and (iii) with both the SSC and SOC terms (referred to as SSC+SOC in Table 2.2). This was the first time that the DDCI method

Table 2.2: Symmetric exchange parameters computed at various CI levels for the copper acetate monohydrate molecule [71]. The values have been obtained by multiplying by a factor of 2 the values of the original publication ($D^{ab} = 2D$ and $E^{ab} = 2E$) and are compared with experiment.

Parameter	D^{ab} (cm^{-1})	E^{ab} (cm^{-1})
SSC	−0.24	0.00
SOC	−0.40	0.01
SSC+SOC	−0.64	0.01
Expt. [130]	−0.67	0.02

was used to compute the energies of orbitally-excited states for further SOCI calculations, and the first detailed and correlated study of the symmetric exchange in a binuclear complex. My work solved previous controversies also by expliciting how previous indirect determinations of the sign of the axial ZFS parameter in this molecule led to a wrong D sign. For instance, Bleaney and Bowers [129] assumed that all the excited-state magnetic couplings were equal to the one of the ground orbital configuration, which is clearly not the case [71]. I chose to collaborate with the group of F. Neese for this work, which was located in Bonn at that time. I should mention that when I arrived there for a month, a few minor bugs were present in the SSC and SOC parts of the ORCA code [51] and that I have thus stimulated a few corrections of this code.

The second-rank antisymmetric exchange: the Dzyaloshinskii-Moryia pseudo-vector

In the absence of some symmetry elements, such as for instance a symmetry centre, a mixing between the $S = 0$ and $S = 1$ spin blocks occurs in binuclear copper(II)-copper(II) complexes. It can be described via antisymmetric components of a second-rank exchange tensor, which can be mathematically reduced to pseudo-vector components, and added to the previous model Hamiltonian:

$$\hat{H}_8 = \hat{H}_7 + \overline{d^{ab}}\hat{S}^a \times \hat{S}^b = J\hat{S}^a \cdot \hat{S}^b + \hat{S}^a\overline{\overline{D^{ab}}}\hat{S}^b + \overline{d^{ab}}\hat{S}^a \times \hat{S}^b \tag{2.16}$$

where $\overline{d^{ab}}$ corresponds to the antisymmetric exchange, usually referred to as the Dzyaloshinsky-Moriya (DM) pseudo-vector [131, 132]. While the isotropic coupling term J acts in a same way on the diagonal elements of the three components of the $S = 1$ block in the coupled basis, the $\overline{\overline{D^{ab}}}$ tensor components are related to the splitting and mixing of these components, and the $\overline{d^{ab}}$ pseudo-vector mixes these components with the $S = 0$ state (spin mixing between S and S+1 blocks). Concerning the mechanisms, Moskvin carefully discussed them in 2007 in the case of copper oxides, highlighting potential contributions from the bridging oxygens [133]. Note that in the general case,

too many effective parameters are introduced to allow simple extractions from experiment. Indeed, many techniques are essentially sensitive to energy levels, and not to spin mixing. Moreover, it is crucial to determine the angles of the magnetic anisotropy axes (determined by the symmetric tensor) and the pseudo-vector to get the full multispin picture. Therefore, it is hard to get any reliable data from experiments concerning the DM pseudo-vector, unless the symmetric exchange components can be considered as negligible compared to the antisymmetric ones, which would in principle allow one to get the pseudo-vector norm even from powder samples.

From a computational perspective, it is straightforward to distinguish the symmetric and antisymmetric exchange terms as soon as an (effective) interaction matrix between the $S = 1$ and $S = 0$ blocks is determined. Since most of the perturbative approaches to compute ZFS were originally designed only to describe one spin block, they do not allow one to determine the DM pseudo-vector. One way of tackling the problem consists in using the effective Hamiltonian theory on top of SOCI calculations that consider both the $S = 1$ and $S = 0$ spin components. This is what I showed for the first time in a study of model copper(II)-copper(II) binuclear complexes [100], which notably confirmed the hypothesis of Moskvin that bridging oxygens contribute to the antisymmetric exchange. A couple of years later, I applied this approach to the $LiCu_2O_2$ ionic solid within the embedded cluster approach [57] and also guided in the meanwhile two PhD students, A.-M. Pradipto from Groningen, and N. Bogdanov from Dresden, to perform similar studies [56, 58]. Actually, my collaboration with Groningen was initiated by R. Broer during a workshop that was held there in 2009, and we decided that A.-M. Pradipto would join me in Tarragona for a couple of months the year after. Therefore, the first work on embedded clusters was done by this student under my guidance. From a methodological point of view, since the DM components are essentially governed by the direct SOC between the S and S+1 blocks, it is not necessary to compute local or delocalized ligand-field excited states to obtain good semi-quantitative estimates of them (unlike the symmetric exchange components or to the single-ion anisotropies) [56, 100]. After my pioneering work, Atanasov *et al.* reported a study of "real" copper(II)-copper(II) complexes based on a ligand-field theory based analysis [134].

The second-rank single-ion anisotropies

When two unpaired electrons are present on a paramagnetic centre, its single-ion anisotropy must also be introduced in the model Hamiltonian. Therefore, when the two magnetic centres trigger two unpaired electrons, it appeared natural from a phenomenological point of view to simply add their single ion anisotropies to the model Hamiltonian [6, 103, 41], such that:

$$\hat{H}_8 = \hat{H}_7 + \hat{S}^a\overline{\overline{D^a}}\hat{S}^a + \hat{S}^b\overline{\overline{D^b}}\hat{S}^b = J\hat{S}^a \cdot \hat{S}^b + \hat{S}^a\overline{\overline{D^{ab}}}\hat{S}^b + \overline{d^{ab}}\hat{S}^a \times \hat{S}^b + \hat{S}^a\overline{\overline{D^a}}\hat{S}^a + \hat{S}^b\overline{\overline{D^b}}\hat{S}^b \quad (2.17)$$

where $\overline{\overline{D^a}}$ and $\overline{\overline{D^b}}$ are the local anisotropy tensors of the a and b centres, respectively, while the other terms keep their previously mentioned meanings. This model Hamiltonian is often considered in the literature, *e.g.* in experimental studies of the $[Ni_2(en)_4Cl_2]^{2+}$ complex [130, 135, 136, 137].

From a computational perspective, it is common to compute the single-ion anisotropy tensors. For this, while not treating the full complexity associated with the low-energy levels, one can (i) mimic the effect one of the paramagnetic ions by an AIEMP [101], (ii) replace one of the paramagnetic ions by a diamagnetic one with a similar effective charge and a similar ionic radius [95, 101], (iii) consider one of the ions in its lowest-energy closed-shell excited configuration [112], or, as was done by others, (iv) consider the ground and excited configurations of the ion of interest while keeping the other paramagnetic centre in its high-spin configuration [138]. Although one may expect to obtain similar values with all these approaches, the fourth one is meant to be the most reliable one. However, even if the determination of the local anisotropy tensors can provide useful information to interpret magnetic data, the isotropic and local anisotropic terms are not sufficient to properly describe the energy levels and to obtain model vectors in good correspondence with the actual ones after diagonalization of the model interaction matrix. More importantly, I showed that $\hat{H}_8$ is not a sophisticated enough model Hamiltonian for describing the low-nergy spectra of binuclear nickel(II)-nickel(II) complexes [101]. Therefore, the previously mentioned experimental studies of the $[Ni_2(en)_4Cl_2]^{2+}$ complex were based on a too simple model Hamiltonian, and thus, the resulting parameters cannot actually have the physical meaning than the one they phenomenologically bear in $\hat{H}_8$. In other words, it would be vain in this case to compare the experimental values to properly extracted computational ones.

The fourth-rank symmetric exchange

Having noticed that $\hat{H}_8$ was not sufficient to describe the full complexity of the model interaction matrix that I had obtained for the $[Ni_2(en)_4Cl_2]^{2+}$ complex, I was wondering what could be actually missing in this model Hamiltonian. In mononuclear complexes, fourth-rank Stevens terms were appearing in the model Hamiltonian starting in the $S = 2$ case, *i.e.* when four unpaired electrons were in the game. In $S^a = S^b = \frac{1}{2}$ binuclear complexes, two electrons are effectively coupled, and this generates a second-rank exchange tensor. In the $S^a = S^b = 1$ situation under study, four unpaired electrons were at play and only a second-rank exchange tensor was sought to occur. By reading a textbook on tensors and their properties in physics [139], I realized that fourth-rank tensors were way more frequent than encounters of the third kind, *e.g.* the well-known fourth-rank elasticity tensor. Then, I intuited the occurence of a fourth-rank symmetric exchange tensor, $\overline{\overline{\overline{\overline{D^{ab}}}}}$, to be added to $\hat{H}_8$, leading to a refined multispin model Hamiltonian:

$$\hat{H}_9 = \hat{H}_8 + \hat{S}^a \otimes \hat{S}^a \overline{\overline{\overline{\overline{D^{ab}}}}} \hat{S}^b \otimes \hat{S}^b = J\hat{S}^a \cdot \hat{S}^b + \hat{S}^a \overline{\overline{D^{ab}}} \hat{S}^b + \overline{d^{ab}} \hat{S}^a \times \hat{S}^b + \hat{S}^a \overline{\overline{D^a}} \hat{S}^a + \hat{S}^b \overline{\overline{D^b}} \hat{S}^b + \hat{S}^a \otimes \hat{S}^a \overline{\overline{\overline{\overline{D^{ab}}}}} \hat{S}^b \otimes \hat{S}^b \tag{2.18}$$

When all these terms are introduced in the model Hamiltonian, their direct extraction with the effective Hamiltonian theory is practically impossible if one does not consider *ad hoc* relations between fourth-rank tensor components, due to a lack of information [101]. Moreover, this is a typical situation for which the initial motivation for using model Hamiltonians breaks down: if the model Hamiltonian appears as complex as the exact electronic one, one may legitimately wonder what is the practical interest of considering such a model! However, I took the time and energy to show that the effective interaction matrix was perfectly compatible with the one that I built with $\hat{H}_9$, in the magnetic anisotropy axis frame or in an arbitrary frame (for this, I derived the full model interaction matrix in an arbitrary frame with pen and paper, which took me a couple of weeks and quite some A3 and A4 pages).

How to deal with complexity

My PhD being soon over, and our curiosity with N. Guihéry still not fully satisfied, further efforts were still necessary to properly extract the parameters introduced in $\hat{H}_9$. To deal with the complexity of this model Hamiltonian, two actions were undertaken late 2010, (i) involve a new PhD student with a stronger mathematical/physical background than mine, and (ii) figure out some relations between parameters to reduce the number of independent parameters. Both actions were salutary, and R. Ruamps eventually managed to properly extract all the relevant terms of $\hat{H}_9$ in the case of two model nickel(II)-nickel(II) complexes of varying geometries [112]. Since I helped him to start with this problem and since I also gave him some feedback once in a while after my defense, I have cosigned the resulting publication. Two important conclusions arose from this work (i) the local $D^{a,b}$ and $E^{a,b}$ ZFS parameters obtained from a full treatment are in good agreement with those computed from simple schemes that aims only at computing solely local terms and (ii) the fourth-rank symmetric exchange tensor components have a stronger impact on the effective Hamiltonian matrix than the second-rank symmetric exchange ones. Also, it was nice to see that despite the complexity of the model, very intuitive molecular anisotropies were obtained. By imposing specific distortions around each magnetic ion, the synergy and interferences between the local anisotropies were studied in various cases. If the symmetric exchange tensors are neglected and in the case of a centrosymmetric complex, the ZFS parameters of the $S = 2$ spin block can be obtained from the local anisotropy ones by simple relations, *i.e.* $D_{S=2} = \frac{1}{3}\, D^a$ and $E_{S=2} = \frac{1}{3}\, E^a$. Therefore, synergistic effect are occuring if the resulting molecular anisotropy terms are larger (in absolute values) than the thirds of the local ones. Such a situation was obtained for the simpler studied model, of D_{4h}

molecular symmetry, for which the local z anisotropy axes were by construction oriented along the Ni-Ni orientation ($D_{S=2} = -2.4$ cm^{-1} while $D^a = D^b = -2.2$ cm^{-1}). When a mismatch appears between the local anisotropy tensors, it is crucial to consider it in the construction of a model interaction matrix, that obviously has to be done in a single frame. As I showed in a very simple case (C_{2v} symmetry point group, with "exchangeable" ions), such a mismatch also contributes to the spin mixings between the S and $S+1$ blocks [8]. This was further confirmed by R. Ruamps and many other (interesting) situations were reported in the resulting publication [112].

2.5 Concluding remarks

My work on molecular magnetism was essentially devoted to the study of magnetic interactions in mononuclear and binuclear complexes. While the EPR spectroscopy has clearly provided reliable experimental information regarding the ZFS of mononuclear species [140], the complexity of the models describing binuclear compounds prevents one from having such insights from experiment. Theoretical calculations thus constitutes a good alternative to elucidate the low-temperature properties of such complexes. Through various examples of increasing complexity, and as far as binuclear complexes are concerned, I have showed that:

1. The giant spin approximation is appropriate in the strong- and intermediate- exchange regimes.

2. The multispin model involving only a second-rank tensor is reliable for centrosymmetric compounds having a single unpaired electron per centre. In such a simple case analytical formulae for both the D^{ab} and E^{ab} parameters can be derived, providing rationalization of the magnitudes and signs of these ZFS parameters.

3. The DM pseudo-vector correctly describes the antisymmetric contribution to the ZFS.

4. For systems containing two unpaired electrons per magnetic centre, a fourth-rank tensor must be introduced to accurately describe the exchange anisotropy. Its elements are by far larger (in absolute values) than those of the second-rank exchange tensor.

5. Simple schemes can be used to compute the single-ion anisotropies without dealing with the full complexity of the multispin model Hamiltonian. By comparing the molecular anisotropies of the S blocks to what should have been obtained solely based on the local anisotropies (and by considering the Euler angles between the principal axes of the local anisotropy tensors, when applicable), one may evidence destructive or synergistic effects between the local anisotropies.

It is worthwhile noticing that operators involving six spins may appear in the the multispin model Hamiltonian for systems having three unpaired electrons per centre, and so on. This remains to be

checked (I attempted to do so, but unfortunately stopped because of an unfortunate computational issue). Also, further studies of giant spin models should be performed. I have notably attempted to compute the giant spin ZFS of a Ni_4 complex [111] with WFT, based on the RASSCF/RASPT2 approach for the electronic wave functions/energies, which I had validated first on the $[Ni_2(en)_4Cl_2]^{2+}$ complex (unpublished result). However, another computational issue prevented me to do so. It is clear that these two direct perspectives of my work are still topical. Other perspectives that I mentioned at the end of my PhD dissertation concerned the determination of model Hamiltonians that do include the orbital degree of freedom, for instance for describing the low-temperature magnetic behaviour of peculiar transition metal complexes [141] or of lanthanide-based single-ion magnets (SIMs) [142]. Usually, it is hard to work on the perspectives of one's own PhD work since the beginning of a scientific career is usually driven by the constraint of finding a job, then another job, and then hopefully a permanent position. I am no exception to this rule and currently not that active in the molecular magnetism field, theoretical radiochemistry keeping me busy enough.

Chapter 3

Structural and chemical properties of radioelement species

3.1 Introduction

Although one may consider that quantum chemistry was born in 1933 with the creation of *The Journal of Chemical Physics* [143], "modern" quantum chemistry required the development of computers. Perhaps one can thus similarly associate the creation of the *International Journal of Quantum Chemistry* in 1967 with the emergence of quantum chemistry as we know it nowadays. In the opening editorial of this journal written by Löwdin [144], the importance for writing programs in spread languages such as FORTRAN instead of "machine language" was stated and the connection between theory and experiment was highlighted (see Figure 3.1). Clearly, the initial "interpretation" to convert an experimental situation into a set of postulates and axioms, *i.e* to start defining a theoretical approach, should be done with care, otherwise, the final interpretation(s) or the resulting prediction(s) may be formally wrong, no matter the appearances. Thus, a good connection requires a good understanding of the experimental situation from the quantum chemist in charge of the theoretical study and I consider that most of the art of connecting theory and experiment lie in this initial step, even if it may not be explicited in publications.

In this chapter, most of the systems that will be described have been the subject of joint theory/experiment studies or somehow have an interest within a given experimental context. Therefore, they may have been suggested by experimental collaborators or colleagues, or sometimes have emerged from the discussions between theorists and experimentalits that I have participated to. Since this chapter focusses more specifically on the role of relativistic effects on molecular properties, the experimental contexts may only be briefly mentioned. Actually, I started to work on radioelement species when I was a post-doctoral associate in Minnesota. The Gagliardi Group, which I belonged to, was collaborating with various experimentalists from the actinide chemistry

community, and I ended up being involved in these, which is attested by two publications, one in collaboration with J. K. Gibson from Berkeley [145] and one in collaboration with the Albrecht-Schmitt Group [146]. This allowed me to start working on the chemistry of heavy-element species.

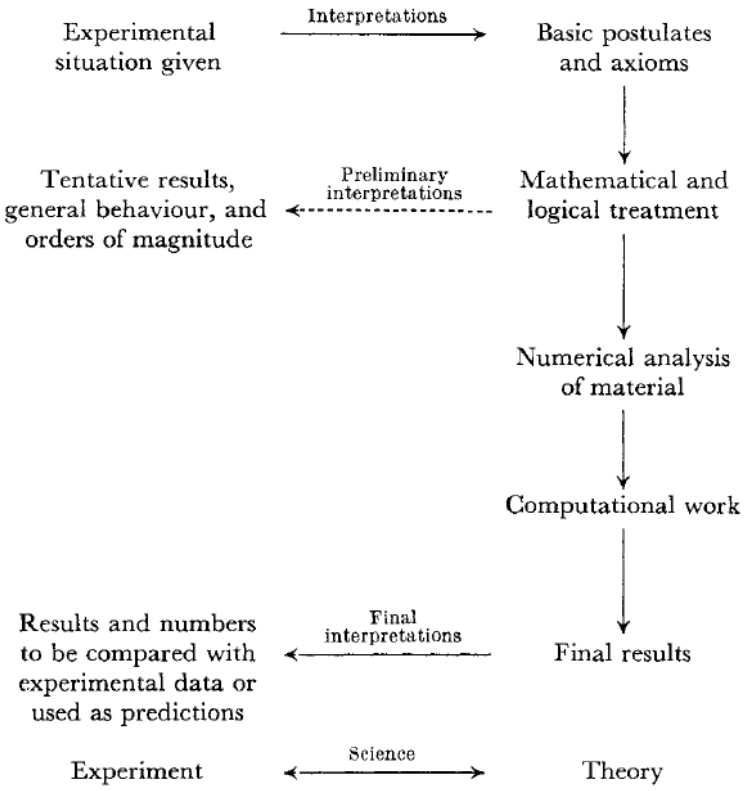

Figure 3.1: Connection between theory and experiment in science, as presented by Löwdin in the opening editorial for the *International Journal of Quantum Chemistry* in 1967 [144].

Quantum chemistry calculations may be quite crucial when little information is experimentally known. This is typically the case when one is obliged to work at "ultra-trace" concentrations, as it is done to study the chemistry of the astatine element (At, $Z = 85$). Note that such chemical studies may be of interest for nuclear medicine, since its 211 radioisotope (astatine-211) has favorable properties for targeted therapy. The idea is to bind the At-211 radioisotope to a specific biological vector, which may be done in three conceptual steps (see Figure 3.2). Because so little is known about the basic chemistry of At [147], G. Montavon (from the radiochemistry group of Subatech) and N. Galland (from the CEISAM laboratory in Nantes) offered J. Champion to devote her PhD studies to this element. This was the start of the locally famous "astatine project" in the Subatech and CEISAM laboratories. To convincingly identify new chemical species, it was necessary to combine quantum chemistry calculations and indirect experimental probes (*e.g.* from distribution measurements). The computational strategy [148], designed by N. Galland, was based on the SODFT method as implemented in NWChem [149] and on an implicit solvation model [150, 151].

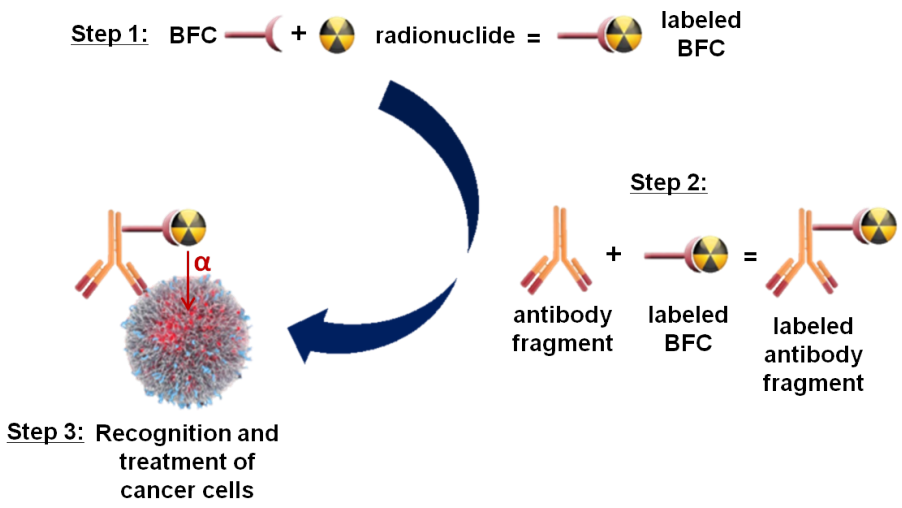

Figure 3.2: The three (conceptual) steps of targeted radionuclide therapy involving a bifunctional chelating agent (BFC).

When I arrived at Subatech in 2013, a couple of successful theory/experiment studies had been already performed [152, 153]. My main contribution to this already working theory/experiment collaboration has been to take profit of predictions based on quantum chemical calculations and thermodynamical models prior to performing the experiments, in view of judiciously choosing the experimental conditions. This new strategy notably allowed us to evidence the exotic $[BrAtI]^-$ triatomic anion [154], while the initial experimental study had failed to do so. Furthermore, I have started to play a central role on the interpretation of experimental data, notably concerning the first experimental characterization of halogen-bonded adducts involving astatine [155]. Also, note that I have participated in making this project more visible by making our theory/experiment studies published in more prestigious chemistry journals than was done before. From a quantum chemistry perspective, I have brought to Nantes my expertise on multiconfigurational WFT calculations, and thus included them in the computational toolkit of the astatine project, by performing myself calculations and also by training and guiding the PhD student D.-C. Sergentu, whom I was coadvising together with N. Galland, to such methodologies. This training and guidance has been fruitful since it has directly led to two publications in specialized journals [156, 157].

To be in full adequation with the scope of my new group, I decided late 2013 to focus my research essentially on the chemistry of radioelement species by (i) bringing to Nantes my collaboration with J. K. Gibson from Berkeley, (ii) involving myself in the astatine project, as mentioned before, and (iii) starting to work on the spectroscopy of polonium(IV) complexes, at the initiative of my experimental colleague J. Champion. Of course, calculations with other radioelements may be of interest (*e.g.* technetium, $Z = 43$ [158, 159]), but so far, my work in "applied" theoretical radiochemistry has been restricted to polonium, astatine or actinide species.

3.2 Molecular geometries of 6p species and actinide species

3.2.1 Astatine species

Diatomics

The AtX (X = At–F) series is a nice one to highlight the role of relativistic effects or the role of the SOC on molecular geometries since significant effects can be observed. Although the At_2 molecule is quite emblematic [10, 160, 161, 162, 163, 164, 165], no evidence for the existence of this species has been acquired, while the first unsuccessful trial to form it was reported in 1966 [166]. However, it is clear that the AtI, AtBr and AtCl molecules are of experimental interest [148, 154, 155, 166, 167]. The AtX (X = At–F) series had been already studied by N. Galland and coworkers before my involvement in the astatine project [164] (see Table 3.1 for DFT results based on the B3LYP exchange-correlation functional [168]). However, since these systems are quite small (in terms of the number of atoms and also of the number of correlated electrons), they can be studied with a wide range of methods and, thus, I have performed and also motivated further quantum chemical calculations on these systems, in collaboration with F. Réal, A. S. P. Gomes and V. Vallet (PhLAM laboratory, Villeneuve d'Ascq) for the At_2 molecule, and with A. Borschevsky (University of Groningen, The Netherlands) for the full series (the NR-CCSD(T) and X2C-CCSD(T) calculations being performed by her PhD student, P. Haase).

Table 3.1: Computed bond distances (Å) for various diatomic molecules. The differences between the non-relativistic (NR) and exact two-component (X2C) CCSD(T) calculations define the whole role of the relativistic effects on these distances.

Method	SRDFT [164]	SODFT [164]	NR-CCSD(T)	X2C-CCSD(T)
At_2	$2.88^{a,b}$	3.05^{c}	2.88	2.97^{c}
AtI	2.79^{b}	2.88	2.77	2.82
AtBr	2.60^{b}	2.67	2.57	2.61
AtCl	2.45^{b}	2.52	2.42	2.47
AtF	2.03^{b}	2.08	1.98	1.99

[a]This value may be compared with the NEVPT2 one that we reported (2.85 Å) [10].

[b]These values may be compared with the CP-CCSD(T)-F12b/VTZ-F12 ones of Hill and Hu (2.86, 2.77, 2.57, 2.42 and 2.01 Å, respectively) [163].

[c]These values may be compared with the fully-relativistic CCSD(T) values of Visscher and Dyall (3.05 Å) [160] and of Höfener *et al.* (3.01 Å) [161], and with the SOCI/NEVPT2 ones that we reported (2.96 Å at the contracted SOCI level and 2.97 Å at the uncontracted SOCI one) [10].

As can be seen in Table 3.1, relativistic effects play a significant role on the AtX bond distances, the SOC causing an enlargement of them, which, naturally, tend to decrease within the series. If one arbitrarily considers that an effect of the order of 0.05 Å is significant, it is clear that the SOC should not be neglected when one wants to accurately compute AtX bond distances. The bond enlargement induced by the SOC can be easily understood by looking at the ground SOF configuration and at the main single excitation that is generated from it by the SOC operator (see Figure 3.3). In the centrosymmetric At_2 molecule, the $\pi \rightarrow \sigma^*$ excitation "weakens" the bond. Indeed, it is necessary to reduce the energy difference between the π MOs and the σ^* one for the SOC to lower more the total energy of the system, which causes an enlargement of the bond distance. A similar mechanism is at play in the non-centrosymmetric AtX systems, with an additional subtlety: two single excitations are there at play, the previously mentioned $\pi \rightarrow \sigma^*$ one plus the $\pi^* \rightarrow \sigma^*$ one (which was symmetry forbidden in the At_2 case).

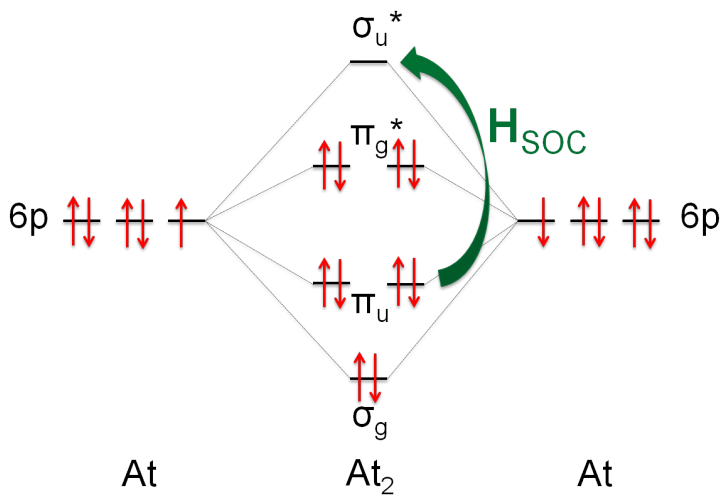

Figure 3.3: MO diagram and ground spin-orbit-free configuration of the At_2 molecule. The main single excitation that is triggered by the SOC is depicted by a green arrow.

Triatomic anions

It is known that the reaction of AtX with another halogen anion can lead to the formation of $[XAtY]^-$ triatomic anions, for instance, the $[IAtI]^-$ anion [154, 167] or the $[BrAtBr]^-$ one [148, 154]. These systems are valence isoelectronic with the famous $[I_3]^-$ triodide anion [169, 170]. As for the other analogous trihalogen anions (apart from $[F_3]^-$ which is even more subtle [171]), the bonding in the $[XAtY]^-$ systems is dominated by two Lewis structures, X–At Y^- and X^- At–Y, with also a minor contribution from the fully ionic X^- At^+ Y^- structure. To show this, I asked D.-C. Sergentu to perform complete active space configuration interaction (CASCI) calculations after localizing the orbitals resulting from a first CASSCF calculation. In this way, it was possible to confirm the

dominant Lewis structures from a standard WFT calculation, without the necessity for performing a true valence-bond (VB) study with a dedicated VB code (nothing very original there!). Since we have reported the experimental evidence for the existence of the ternary $[BrAtI]^-$ anion in aqueous solution [155], we have also assessed the importance of the SOC on the bond distances of the binary $[BrAtBr]^-$ and $[IAtI]^-$ species and also of the newly discovered ternary $[BrAtI]^-$ one, still with the B3LYP exchange-correlation functional [168] (see Table 3.2, the calculations having been performed by D.-C. Sergentu). Without surprise, similar effects as the ones observed in the AtBr and AtI species were found, but naturally attenuated by the presence of the third halogen (+0.05 Å for the At–Br bonds instead of +0.07 and +0.07 Å for the At–I bonds instead of +0.11).

Table 3.2: Computed bond distances (Å) in the gas phase for selected $[XAtY]^-$ triatomic anions of experimental relevance [154].

X	Y	Method	d(X–At) (Å)	d(At–Y) (Å)
Br	Br	SRDFT	2.86	2.86[a]
		SODFT	2.91	2.91[a]
I	I	SRDFT	3.08	3.08[a]
		SODFT	3.15	3.15[a]
Br	I	SRDFT	2.87	3.07
		SODFT	2.92	3.14

[a]These values are, by symmetry, equal to the corresponding d(X–At) ones.

Halogen-bonded adducts

Since the bonding in the $[XAtY]^-$ systems is dominated by the X–At Y^- and X^- At–Y Lewis structures, one may consider that a given X–At or At–Y bond is a kind of intermediate between a covalent bond and a halogen one. Naturally, it was interesting to go one step further and study true halogen-bonded complexes. One may recall here that a halogen bond is characterized by the alignment or near alignement between three atoms, two of them belonging to the halogen-bond donor R–X, and one belonging to the Lewis base, *i.e.* to the halogen-bond acceptor [172]. A halogen bond may thus be depicted as R–X$\cdots$B, and that the propensities of Lewis bases to form halogen bonds may be described by the basicity scale with a reference halogen-bond donor, for instance I_2 [173]. The idea of studying halogen-bonded complexes involving the At element was first formulated by J. Graton and N. Galland (both from the CEISAM laboratory, Nantes). We managed to experimentally evidence the occurence of such bonds for the first time [155], my contribution being essentially focussed on the definition of the experimental conditions to be applied

and on the interpretation of the experimental data. We reported halogen-bonded adducts with the AtI halogen-bond donor and selected Lewis bases, in order to facilitate the experimental study. The calculations reported in the article were performed by N. Galland, based on both the B3LYP [168] and the PW6B95 [174] exchange-correlation functionals. For justifying the necessity of including the SOC in the calculations, SRDFT and SODFT calculations were performed on the IAt$\cdots$NH$_3$ system (see Table 3.3), since reference SR geometries were available for AtI and for the IAt$\cdots$NH$_3$ system [163]. Both the I–At and At–N bond distances were found to be significantly enlarged by the SOC (by about 0.05 Å), meaning that the SOC can play a non-negligible role on the geometries of halogen-bonded adducts that involve the astatine element. Note that additional calculations were reported in another publication [165], which I have not been part of. However, these is still room for more detailed explanations concerning the SOC mechanism that is at play to enlarge the At$\cdots$B bond distance.

Table 3.3: Computed bond distances (Å) for the IAt$\cdots$NH$_3$ halogen-bonded adduct [155]. The d(N–H) distances are not reported, but these are not that susceptible for changes upon formation of the halogen-bonded adduct [163].

Method	d(I–At) (Å)	d(At$\cdots$N) (Å)
SRDFT	2.86^a	2.71^a
SODFT	2.92	2.76

^{a}These values may be compared with the CP-CCSD(T)-F12b/VTZ-F12 ones of Hill and Hu (2.82 and 2.74 Å, respectively) [163] or with the previously reported ones for AtI (see Table 3.1) for assessing the change in d(I–At) upon formation of the halogen-bonded adduct.

The AtF$_3$ hypothetical molecule

Although it is known that the ClF$_3$ [175, 176] and BrF$_3$ [177] molecules can be observed in the gas phase, or even IF$_3$ in the solid state [178], the only reported attempt to form astatine fluorides was unsuccessful [166]. Therefore, the AtF$_3$ molecule is still a hypothetical one, which does not prevent computational chemists to perform calculations on this system [179, 180, 181, 182], in particular, for discussing trends within the halogen series. N. Galland (CEISAM laboratory, Nantes) and J. Pilmé (LCT laboratory, Paris) started to lead topological analyses on this system, in particular to undertand the occurence of two stable structures (see Figure 3.4), one T-shaped C_{2v} one (as for the lighter valence isoelectronic XF$_3$ systems), and one planar D_{3h} (as for the heavier (117)F$_3$ system, now referred to as TsF$_3$). Because I was disagreeing with some conclusions of the last available publication for this system [182], I asked the PhD student D.-C. Sergentu to perform further DFT

calculations (see Table 3.4, the reported results being based on the PBE0 exchange-correlation functional [183, 184]) and also to study the potential energy surfaces (PESs) of a set of quantum states for this system at the SOCI level (*vide infra*). Note that preliminary DFT calculations and topological analyses had been performed by the master student D. Steinmetz at the LCT laboratory, which were to be followed by the final calculations and topological analyses of the PhD student M. Amaouch (see Chapter 4). In accord with previous studies [180, 181, 182], we found that the SOC was playing a non-negligible role on the bond distances (+0.04 Å in average) and on the characteristic bond angle for the T-shaped C_{2v} structure (+5°). Although nothing new was found there, it was worth mentioning this result here since more discussions concerning the AtF_3 molecule will appear later in this manuscript.

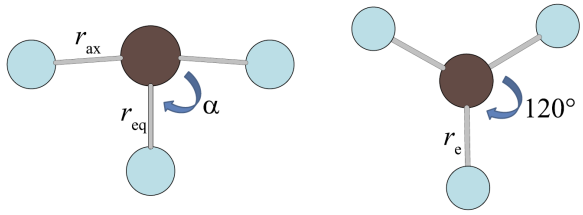

Figure 3.4: Representations of the T-shaped (C_{2v}, left) and planar (D_{3h}, right) AtF_3 molecular structures [156].

Table 3.4: Computed bond distances (Å) and bond angles (°) for the AtF_3 molecular structures that are depicted in Figure 3.4 [156, 185].

Method	r_{eq} (Å)	r_{ax} (Å)	α (°)	r_e (Å)
SRDFT	1.96	2.04	85.7	2.04
SODFT	2.01	2.07	91.0	2.07

Miscellaneous

The previous examples aimed at illustrating the potentially important role of the SOC on the molecular geometries of astatine species (in particular on bond distances and angles). Perhaps it is nice to introduce now a system for which the SOC effect on the bond distance is negligible, and of course, explain why it is so. The $[AtO]^+$ cation is the perfect candidate for this. It is valence isoelectronic with the chalcogen diatomics and also have a similar SOF ground state (a spin-triplet state, dominated by the $[...]\sigma^2\pi^4\pi^{*2}$ electronic configuration) [10, 186, 187, 188, 189]. As for the AtX systems, it is nice to describe the role of the SOC within a two-step based reasoning. Unlike

the AtX systems (spin-singlet ground SOF states), the ground spin-orbit free configuration triggers three spin components (spin-triplet ground SOF state). From the $|M_S| = 0$ component, the main single excitation that is induced by the SOC mixes this component of the $^3\Sigma^-$ state with the $^1\Sigma^+$ one [10]. This latter state wave function is essentially constituted of the two closed-shell configurations belonging to the $[...]\sigma^2\pi^4\pi^{*2}$ electronic configuration, *i.e.* the SOC does not trigger any drastic change in the electronic configuration of the ground state (it essentially mixes components of the same electronic configuration). As a consequence, little effect of the SOC on the bond distance is obtained (see Table 3.5). Note the calculations reported in this Table 3.5 have been performed at my initiative by collaborators (F. Réal, A. S. P. Gomes and V. Vallet for the PhLAM laboratory, Villeneuve d'Ascq). Both the contracted (c) and uncontracted (uc) [190] types of SOCI calculations were there performed.

Table 3.5: Computed bond distances (Å) in the gas phase for the $[AtO]^+$ cation [10] at various relativistic levels. Contracted (c) and uncontracted (uc) SOCI values are reported and a reference fully relativistic value ("DC-CCSD(T)") is also given for comparison.

Method	NEVPT2	c-SOCI/NEVPT2	uc-SOCI/NEVPT2	DC-CCSD(T)
r_e	1.89	1.90	1.89	1.93 [189]

Perhaps it is worth mentioning here that a benchmark study concerning the molecular geometries of a few astatine species with the SODFT method has been performed by D.-C. Sergentu [191], at the initiative of N. Galland, his other coadvisor. It is important to stress that at the time of performing the study, reference geometries were available for only a few systems, namely the previouly mentioned At_2, AtF_3 and $[AtO]^+$ system, plus the AtH one [192]. Because of the two possible structures for AtF_3, six bond distances were considered in this benchmark study. Obviously, this is insufficient to lead to statistically relevant conclusions, but, out of this work, a few exchange-correlation functionals were highlighted, as for instance PBE0 [183, 184], PW6B95 [174] and HSE06 [193]. All the tested LDA and GGA exchange-correlation functionals plus two meta-GGA exchange-correlation functionals failed to obtain a minimum energy structure of T-shaped type for AtF_3. Moreover, the three other meta-GGA exchange-correlation functionals, which succeeded in obtaining a T-shaped minimum for AtF_3, can lead in some cases to large deviations with respect to the reference values. Thus, the actual conclusion of this benchmark study is perhaps that hybrid exchange-correlation functionals should be used to compute molecular geometries of astatine species, for reasons that have not been yet explicited.

As a conclusion to this astatine part, I would say that the SOC may really matter for determining the geometries of astatine species and that its effect can be assessed by the difference between

the parameter values obtained with SRDFT and SODFT, or alternatively with the NEVPT2 and SOCI/NEVPT2 methods. To keep the discussion at the property level and not entering too deep in the computational details, I have said no word about basis sets, all-electron *vs.* pseudopotential calculations (of course, with compatible basis sets), *etc.* However, it is clear that basis set effects can be significant, especially if one expects to obtain "spectroscopic accuracy" (see for instance [10] for a comparison of results obtained with SARC [194, 195] and ANO-RCC [196] basis sets). Therefore, the reader is meant to assume that decent enough basis sets were used in the reported results, as in the remainder of the manuscript. Note that it is also the case for the sizes of the active spaces, when applicable, as well as for other computational degrees of freedom.

3.2.2 The $[AnO_2(NO_3)_3]^-$ and $[AnO_3(NO_3)_2]^-$ complexes (An = U, Np, Pu)

Because things are not always simple, the differences between the results of standard SRDFT and SODFT calculations cannot be always attributed to the sole SOC effect. For illustrating this, it is nice to introduce the $[AnO_2(NO_3)_3]^-$ and $[AnO_3(NO_3)_2]^-$ complexes (An = U, Np, Pu) and, in particular, the $[PuO_3(NO_3)_2]^-$ one (see Figure 3.5). While it is known that the $[UO_2(NO_3)_3]^-$ complex can be formed in solution [197], the $[AnO_3(NO_3)_2]^-$ complexes are more exotic in the sense that they can only be formed in the gas phase under specific conditions, for instance by infrared multiple photon dissociation (IRMPD) for the An = U case [198]. In a collaboration with J. K. Gibson from Berkeley, E. Renault (from the CEISAM laboratory, Nantes) and I have performed DFT calculations with the PBE0 exchange-correlation functional [183, 184] on the $[AnO_2(NO_3)_3]^-$ and $[AnO_3(NO_3)_2]^-$ complexes (An = U, Np, Pu) [124, 199], in particular to confirm the oxidation numbers of the actinides in the $[AnO_3(NO_3)_2]^-$ systems (the +VI oxidation number is obvious in the $[AnO_2(NO_3)_3]^-$ ones). Since the SOC is a local interaction, I do not expect it to change oxidation number assignements, and thus, most of our study was based on SRDFT. From the experimental side, the $[AnO_3(NO_3)_2]^-$ complexes (An = U, Np, Pu) were formed by collision induced dissociation (CID) and evidenced by their masses. For the An = U and An = Np complexes, only SRDFT calculations were performed. Since the correponding geometries may be of interest for comparison with the An = Pu ones, relevant geometrical parameters are reported in Table 3.6. The oxidation numbers of the actinides in two of the $[AnO_3(NO_3)_2]^-$ complexes can be directly assigned at this stage: +VI for $[UO_3(NO_3)_2]^-$, as expected, and +VII for $[NpO_3(NO_3)_2]^-$, as hoped.

The case of the $[PuO_3(NO_3)_2]^-$ complex is more complicated: three low-energy SRDFT solutions of different nature can be obtained: a high-spin (HS) $M_S = \frac{3}{2}$ solution and two "low-spin" (LS) ones (see Table 3.6). The ground one, with an $<S^2>$ value of 1.74, may be associated with the HS solution to define a magnetic coupling constant: these two solutions are characterized by three unpaired electrons, two on the plutonium atom and one on the equatorial oxygen atom [124], and

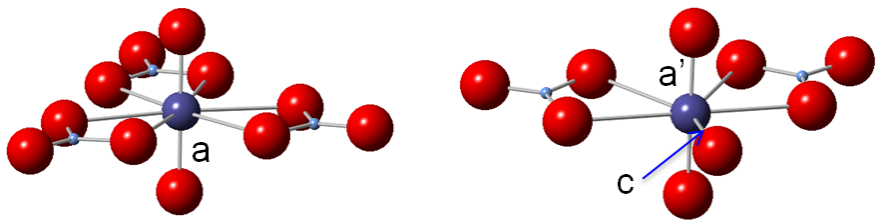

Figure 3.5: Computed structures of the $[AnO_2(NO_3)_3]^-$ and $[AnO_3(NO_3)_2]^-$ complexes (An = U, Np, Pu). The a, a', and c bond distances are given Table 3.6 [124, 199].

Table 3.6: Computed $<S^2>$ values and bond distances (Å) for the complexes that are depicted in Figure 3.5 [124, 199]. Three SRDFT spin-unrestricted solutions were obtained for the $[PuO_3(NO_3)_2]^-$ complex, a high-spin (HS) one and two "low-spin" (LS) ones; the adiabatic energy differences (kJ·mol^{-1}) between them are also given.

An	Method	$[AnO_2(NO_3)_3]^-$		$[AnO_3(NO_3)_2]^-$			
		$<S^2>$	a	$<S^2>$	a'	c	ΔE
U	SRDFT	0	1.75	0.76	1.76	2.12	–
Np	SRDFT	0.76	1.74	0	1.74	1.82	–
Pu	SRDFT	2.00	1.74	3.78	1.72	2.12	14.0
				0.86[a]	1.73	1.83	10.6
				1.74	1.72	2.08	0.0
	SODFT	–	1.71	–	1.72	2.05	–

[a]This solution was not reported in [124] and [199].

the energy difference between the HS and this spin-broken symmetry is proportinal to J, at a given geometry, within the weak-coupling scheme (it is directly equal to J with equation 2.11; the spin-broken symmetry solution is assumed to be an ideal mixture of the two spin states, here $\frac{1}{3}$ of the $S = \frac{3}{2}$ state and $\frac{2}{3}$ of the $S = \frac{1}{2}$ one, leading to an ideal $<S^2>$ value of 1.75). Note that the +VI oxidation state may be assigned for the plutonium atom in these two solutions. A metastable state, intermediate between the two other solutions in terms of energy (see Table 3.6), is more in line with a +VII oxidation state for the plutonium center. Comparing the SRDFT and SODFT molecular geometries is a bit tricky: the differences between the spin-broken-symmetry solution at the SRDFT level and the SODFT one may be affected by two types of spin-symmetry (un)breaking (i) the removal of the artificial spin-symmetry breaking that occurs in the spin-broken-symmetry solution and then (ii) the physical spin-symmetry breaking that is triggered by the SOC. Therefore, in this case, to avoid using specific spin-projection geometry optimization tools [200], it would be

interesting to perform NEVPT2 and SOCI/NEVPT2 calculations to clearly avoid spurious spin-symmetry breakings and also track the natures of the low-lying quantum states along the potential energy curve (PEC), with the bond distance between the plutonium atom and the equatorial oxygen as the transformation coordinate. Therefore, the comparison of NEVPT2 and SOCI/NEVPT2 calculations appears in principle as a more universal recipee for assessing the role of the SOC on molecular properties than the comparison of SRDFT and SODFT ones (which does not mean that the relativistic and multiconfigurational approach is always easy nor affordable; also, note that no geometry optimization algorithm at the SOCI level is available in quantum chemistry codes).

3.3 Absorption spectroscopy: The UV-Vis spectra of $[PoCl_6]^{2-}$ and $[Po(OH)Cl_4]^-$

Polonium(IV) complexes are somehow interesting in the sense that the SOC is not expected to drastically affect their ground-state properties, while it is expected to do so for excited-state properties. Indeed, the free Po^{4+} ion is characterized by the [...]$6s^2$ electronic structure and thus the populations of the valence 6p of the polonium(IV) ions are not meant to be that large in the ground SOF state (of course, these should be non-zero in complexes due to some electron donation from the ligand(s)). From the experimental side, it is hard to identify the nature of polonium species. For instance, UV-Vis spectra of polonium(IV) complexes in HCl media could not lead to a complete identification of the observed species [201]. Out of this pioneering work, at least two species emerged, (at least) one characterized by a maximum of absorption at 418 nm for large concentrations in HCl (the only one observed above 0.5 mol·L^{-1}), and (at least) one characterized by a maximum of absorption at 344 nm (observed for concentrations in HCl within the 0.15–0.5 mol·L^{-1} range). As a conclusion to the study, which also included an analysis of the pH dependence of the $\frac{A_{418}}{A_{344}}$ ratio, it was concluded that the speciation change observed by enlarging the HCl concentration could be modeled by the occurence of the $[PoOHCl_x]^{3-x} + 2\ Cl^- \rightarrow [PoCl_{x+2}]^{2-x} + [OH]^-$ reaction. Thus, the $[PoOHCl_x]^{3-x}/[PoCl_{x+2}]^{2-x}$ couple remained to be identified. My experimental colleague J. Champion was interested in studying polonium(IV) complexes in view of performing at some point extended X-ray absorption fine structure (EXAFS) experiments to determine the structures of such complexes. In a first study related to the polonium speciation, my colleague and coworkers showed that the $[PoCl_6]^{2-}$ complex predominated in highly concentrated HCl solutions (for concentrations in HCl above 7 mol·L^{-1}) [202]. Therefore, the $[PoCl_{x+2}]^{2-x}$ complex could actually be the $[PoCl_6]^{2-}$ one. To obtain a further indirect identification of the $[PoCl_{x+2}]^{2-x}$ complex, and thus, of the $[PoOHCl_x]^{3-x}/[PoCl_{x+2}]^{2-x}$ couple observed by Moyer decades ago, I started to perform calculations related to the UV-Vis spectrum of polonium(IV) complexes, and then, decided to supervise a master student, A. Stoïanov, for continuing this work.

Since the $[PoCl_6]^{2-}$ complex is meant to predominate above 7 mol·L^{-1} in HCl [202], x should not be larger than 4; also, it would be weird if it would be smaller than 2 (one can assume that, otherwise, a cationic polonium(IV) complex would further interact with chloride ions at such large HCl concentrations). Therefore, we have only retained the $[PoOHCl_4]^-/[PoCl_6]^{2-}$, $PoOHCl_3/[PoCl_5]^-$ and $[PoOHCl_2]^+/PoCl_4$ couples as potential candidates to explain the data reported by Moyer. First, geometry optimizations were performed at a given SRDFT level (with the B3LYP exchange-correlation functional [168]). To assess the role of solvation on the geometries of these complexes, an implicit solvation model was employed [150, 151]. For the polonium radius, the value proposed by Ayala *et al.* [203] and further used by the same authors to study hydrolyzed complexes [204] was employed. Notable changes were induced by solvation, for instance, $[PoCl_5]^-$ has a D_{3h} symmetry (trigonal bipyramid) in the gaz phase and a C_{4v} one (square pyramid) in the condensed one. Also, the geometry of $PoCl_4$, close to tetrahedral in the gas phase (C_{2v} symmetry), is much more distorted in the condensed one ("seesaw" structure, still of C_{2v} symmetry). Therefore, it is clear that the condensed-phase geometries should be used for performing single-point calculations.

For computing the excitation energies, the SOCI/NEVPT2 method was used. Actually, the SOC must be included in the calculations to obtain electronic transitions in the correct energy domain. For explaining this, it is simpler to discuss the case of the $[PoCl_6]^{2-}$ complex. The important electronic transition(s) correspond to the excitation from the highest-occupied (HO) MO (bearing some 6s character) to the essentially 6p orbitals, leading to two triply-degenerate SOF excited states, one of spin-triplet character and one of spin-singlet one (see Figure 3.6). In the absence of the SOC, only the $^1A_{1g} \rightarrow {}^1T_{1u}$ excitation is spin allowed. However, after introducing the SOC at the SOCI level, $^1T_{1u}$ and $^3T_{1u}$ components significantly mix, leading to two "active" transitions, the newly active transition being the one that, at least according to the SOCI/NEVPT2 calculations, corresponds to an excitation energy around 3 eV, *i.e.* that could explain a maximum of absorption at 418 nm (the other excitation being above 5 eV at the SOCI/NEVPT2 level, it should correspond to another range of wavelength –below 250 nm–). The SOCI/NEVPT2 calculations were performed at the condensed-phase geometries, but without including the effect of an implicit solvation model on the excitation energies. One should note that test time-dependent (TD) DFT calculations showed that the inclusion of the implicit solvation model affect the SOF excitation energies by at most 0.2 eV. Furthermore, in all the cases, solvation pushes up in a similar way all the SOF excitation energies of interest (leading to both the spin-triplet and the spin-singlet SOF states), and thus, no strong differential effect on the singlet–triplet energy differences of interest nor between compared $[PoCl_{x+2}]^{2-x}$ or $[PoOHCl_x]^{3-x}$ cases is expected.

According to all the performed calculations, the 418 nm peak was found more likely to be due to the $[PoCl_6]^{2-}$ complex, while the 344 nm one can be explained by the occurence of the

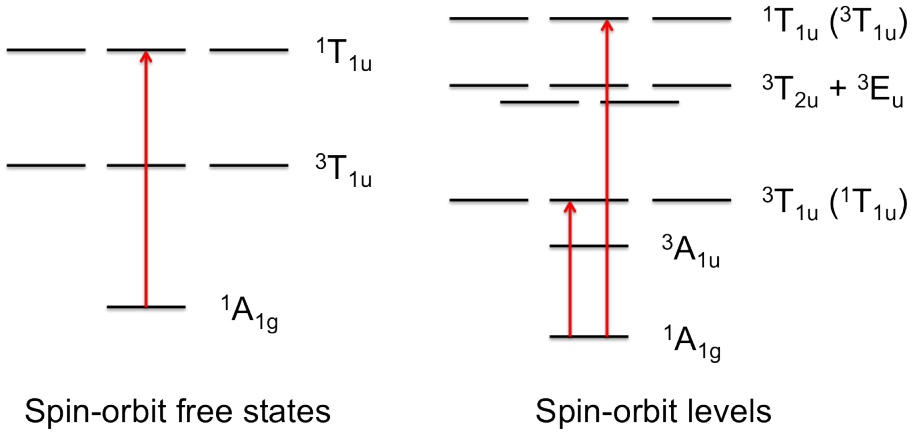

Figure 3.6: Ground and single-excited spin-orbit-free states and spin-orbit levels of the $[PoCl_6]^{2-}$ complex (O_h symmetry point group). Significant but not major components are given in parentheses. Spin-allowed transitions from the ground state/level are indicated by red arrows.

$[PoOHCl_4]^-$ complex. Due to the approximations that were introduced in the computational study and, of course, the initial hypotheses, one cannot completely exclude at this stage the possibility for another scenario that would alternatively and satisfactorily explain the UV-Vis data reported by Moyer [201]. Therefore, there is still the need for further studies, in particular with the EXAFS technique, to get more direct structural information and thus a more convincing determination of the polonium(IV) speciation in HCl solution as well as in other media. Concerning the already performed DFT and SOCI/NEVPT2 study, an article is still in preparation (this article not being a priority, I regularly postpone the actual writing of the main text). I consider that this is a nice example of the crucial role that the SOC can have on absorption spectroscopy, although of course, this idea belongs for long to the "public domain".

3.4 Potential energy surfaces at the SOCI/NEVPT2 level

3.4.1 Back to the AtF_3 hypothetical molecule

As mentioned before, I have guided D.-C. Sergentu for performing DFT and WFT calculations concerning the ground-state PES of the AtF_3 hypothetical molecule, in the absence and in the presence of the SOC. From a computational point of view, reporting the ground-state PES of this system at the SOCI/NEPT2 level was quite original, and by comparing it with the NEVPT2 one, it allowed us to highlight the role of the SOC on this ground-state PES [156]. Before commenting on these PESs, it is worth mentioning the important particular points that belong to this surface. Unlike the lighter XF_3 systems (X = Cl–I) [179], the *pseudo* Jahn–Teller effect (PJTE) [205] is inhibited in the AtF_3 system since the highly-symmetric D_{3h} structure is a local minimum [181, 182]. For connecting this D_{3h} structure to one of the three equivalent T-shaped C_{2v} structures,

one needs to pass a small energy barrier via a Y-shaped C_{2v} transition-state (TS) structure [156, 182]. For connecting two equivalent T-shaped C_{2v} structures, D.-C. Sergentu figured out with DFT calculations that a C_s TS structure should be invoked [156]. Therefore, two types of minima and two types of TSs are important in the ground-state PES of this system (see Figure 3.7). Also, by means of single-point non-relativistic (NR) and SR Hartree-Fock (HF) and NEVPT2 calculations, he showed that the D_{3h} structure only becomes a local minimum when the electron correlation and the scalar relativistic effects are introduced. In other words, the PJTE was active at the NR-HF, SR-HF and NR-NEVPT2 levels, while it was not the case at the SR-NEVPT2 one and also after the introduction of the SOC (*i.e.* at the SOCI/SR-NEVPT2 level).

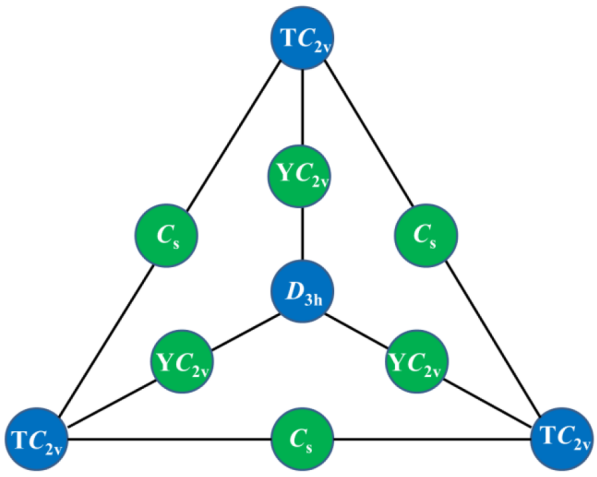

Figure 3.7: Connectivity map between the important critical points of the AtF_3 PES [156]. Color code: blue = minimum, green = transition state.

After the work of Yang and Wang [182], one question remained to be clearly answered: is the SOC in favour or against the PJTE in AtF_3? This was actually one of the facts that motivated me to work on this system, even if I was aware that it clearly looked like a nerd question! With single-point NEVPT2 and SOCI/NEVPT2 calculations performed at retained DFT structures, the SOC was slightly enhancing the energy difference between the Y-shaped C_{2v} TS structures and the D_{3h} one, meaning that it was definitly killing the idea of an active PJTE in AtF_3. Also, as correctly pointed out before by Yang and Wang [182], it also clearly reduces the energy difference between the T-shaped C_{2v} minima and the D_{3h} one, meaning that the SOC really had something against the PJTE. Actually, it may not be that simple, and it was necessary to go beyong single-point SOCI/NEVPT2 calculations to be definitly convinced of something regarding this point. This is why I asked D.-C. Sergentu to built the NEVPT2 and SOCI/NEVPT2 ground-state PESs. As suggested before, three geometrical parameters are at play: two bond distances (r_{eq} and r_{ax} in Table 3.4) and one bond angle (α in Table 3.4). Obviously, we had a representation problem if we wanted to independently vary all these parameters and put all the information into a single graph.

Therefore, we made vary the r_{ax} parameter together with the r_{eq} one, and plotted the ground-state energy as a function of the r_{eq} and α parameters (see Figure 3.8). As can be seen, the main effect of the SOC is to "flatten" the ground-state PES, which means that the SOC better stabilizes the ground state in the more symmetric D_{3h} structure than it does it in the less symmetric C_{2v} ones. By this flattening effect, the SOC is meant to decrease the energy difference between the Y-shaped C_{2v} TS structures and the D_{3h} one, *i.e.* it cannot actually act against the PJTE. Anyway, the true conclusion regarding this question ended up to be that the SOC cannot play any important role concerning the non-occurence of the PJTE in AtF_3 [156].

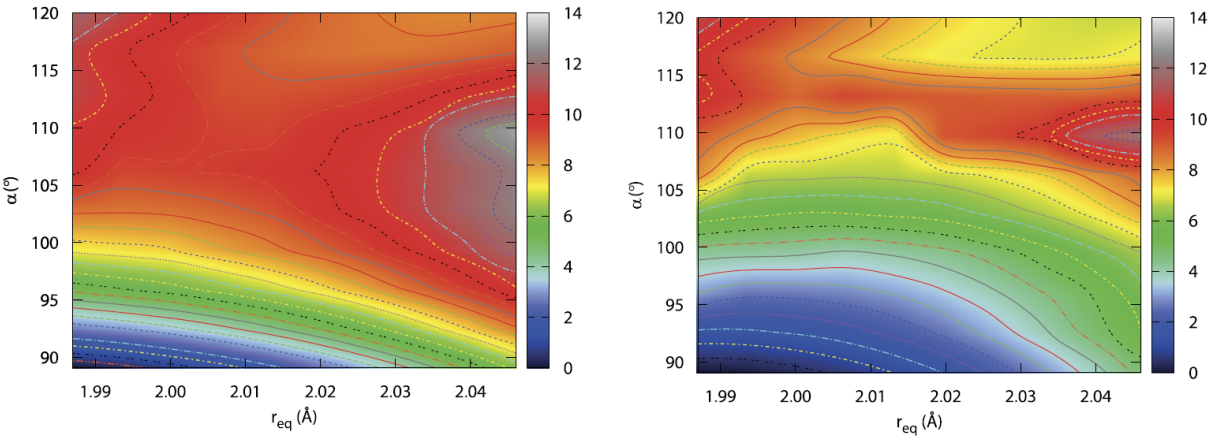

Figure 3.8: Representation of the NEVPT2 (left) and SOCI/NEVPT2 (right) ground state PESs of AtF_3. The energy scale is expressed in kJ·mol^{-1} and the energies of the T-shaped C_{2v} structures are chosen as the zeroes of energy [156].

3.4.2 The hydration-induced ground-state change of $[AtO]^+$

In the previous example, the SOC was not triggering any important change in the topology of the PES of interest. However, this is something that may happen, as will be illustrated here by the first hydrated configuration of the $[AtO]^+$ cation. The main motivation for studying the stepwise hydration of $[AtO]^+$ with SOCI/NEVPT2 was to confirm or infirm the occurence of a hydration-induced ground-state change in this system, and also track the nature of the quantum states involved in this change as a function of relevant geometrical parameters. The possibility for the occurence of a hydration-induced ground-state change was first formulated by N. Galland (CEISAM laboratory, Nantes) and supported by DFT calculations [187, 188], before my actual involvement in the astatine project. These calculations suffered from a couple of biaises, (i) the use of a single-determinental approach may lead to an incorrect nature of the quantum state of interest and (ii) the choice that was made of using the M06-2X exchange-correlation functional [206] was probably not the wisest one that could be done, as correcly stated shortly after [187] and [188] by Gomes *et al.* [189].

Therefore, I asked D.-C. to further study the hydration of the $[AtO]^+$ cation at the SOCI/NEVPT2 level. Note that the $[AtO]^+$ cation is one of the stable forms of astatine that may occur in solution [152], and that it may further lead to two hydrolyzed forms of it in solution, namely AtO(OH) [153] and $[AtO(OH)_2]^-$ [207].

As mentioned before, the ground SOF ground state of the free $[AtO]^+$ cation is dominated by the $[...]\sigma^2\pi^4\pi^{*2}$ configuration [10, 187, 188, 189]. The π^{*2} manifold generates three SOF states, $^3\Sigma^-$, $^1\Delta$ (with one open-shell component and one closed-shell one, the latter resulting from the combination of the two closed-shell configurations) and $^1\Sigma^+$ (resulting from the other combination of the two closed-shell configurations). With the first hydration, which leads to the $[AtO]^+$–(H_2O) system, the molecular symmetry is of course lowered. The PESs of the SOF states correlating with the $^3\Sigma^-$, $^1\Delta$ and $^1\Sigma^+$ of the free $[AtO]^+$ cation were determined as a function of two main geometrical parameters, namely the $[AtO]^+$–(H_2O) bond distance (defined as the distance between the At atom and the water O atom) and the O–At–O bond angle, in such a way that for a straight O–At–O bond angle, the system has a C_{2v} symmetry, while for any other value of this bond angle the system has a C_s symmetry. Naturally, it is important to correctly describe the multiconfigurational nature of the two closed-shell SOF states that correlate with $^1\Delta$ to obtain accurate PESs for these states (note that large geometrical deformations may lead to two essentially-single-configurational SOF states; thus, it does not mean that single-configurational geometry optimizations are here irrelevant). As can be seen in Figure 3.9, the ground SOF state, which correlates with $^3\Sigma^-$, has a C_{2v} geometry, in accord with the previous studies [188, 189]. A local minimum, corresponding to a C_s structure and to a spin-singlet state, can be observed in Figure 3.9 and perhaps more clearly in Figure 3.10.

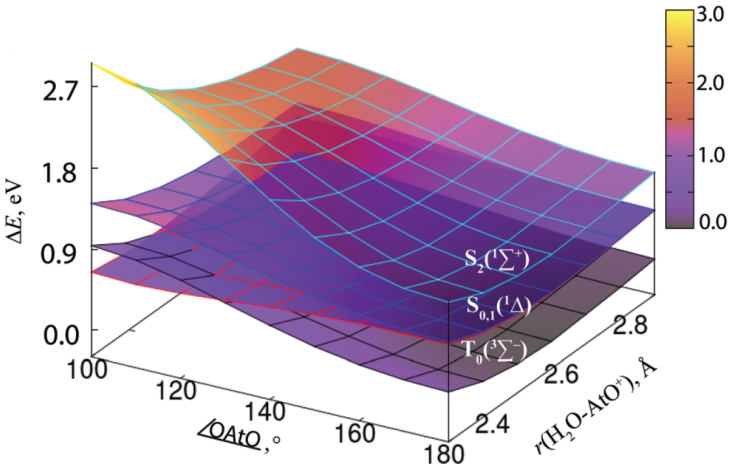

Figure 3.9: Representation of NEVPT2 PESs of the $[AtO]^+$–(H_2O) system. The energy of the global minimum C_{2v} structure is chosen as the zero of energy [157].

Three low-energy energy levels emerge in the free $[AtO]^+$ cation after the introduction of the SOC, $X0^+$ and the two doubly-degenerate **a**1 and **a**2 levels [10, 189]. The $X0^+$ and **a**1 energy levels

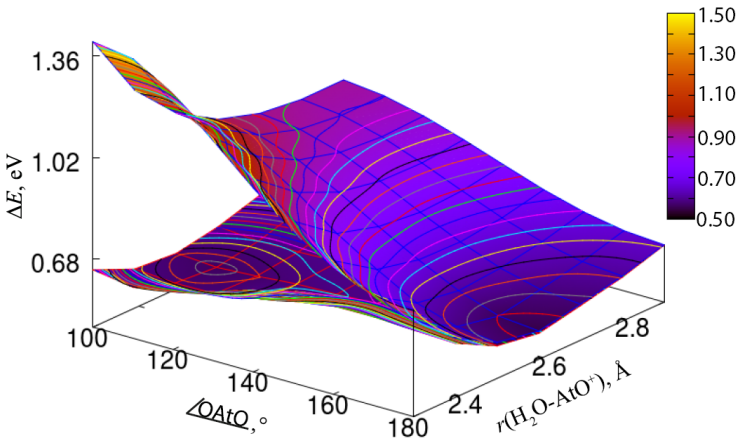

Figure 3.10: Representation of the $S_0(^1\Delta)$ and $S_1(^1\Delta)$ NEVPT2 PESs of the $[AtO]^+$–(H_2O) system. The energy of the global minimum C_{2v} structure is chosen as the zero of energy [157].

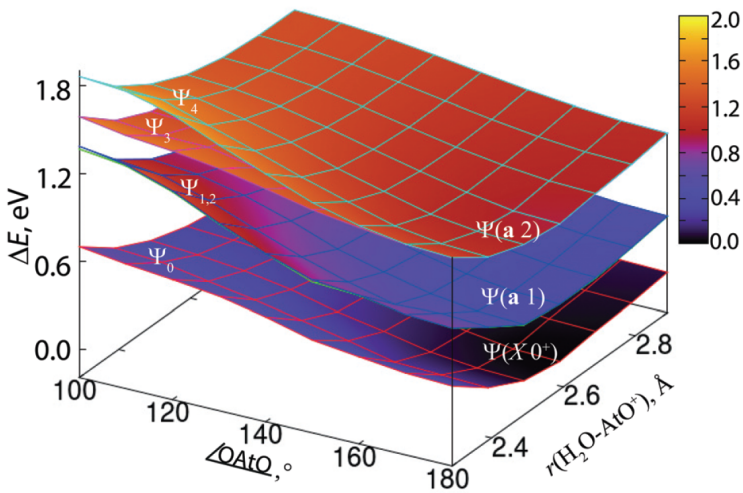

Figure 3.11: Representation of SOCI/NEVPT2 PESs of the $[AtO]^+$–(H_2O) system. The energy of the global minimum C_{2v} structure is chosen as the zero of energy [157].

are dominated by the $M_S = 0$ and $M_S = \pm 1$ components of $^3\Sigma^-$, respectively, while the **a**2 levels essentially match with the two components of $^1\Delta$. Therefore, in the $[AtO]^+$–(H_2O) system, at least five energy levels must be tracked down, *i.e.* five PESs may be determined and plotted (see Figure 3.11). Clearly, no local minimum does appear in the PESs of the two states which correlate with the $^1\Delta$ SOF state of the free $[AtO]^+$ cation. Therefore, the SOC is responsible for the removal of the local minimum that was observed at the SRDFT [188] and NEVPT2 [157] levels. This shows, probably for the nth time, that the SOC is capable of changing the topology of PESs. When further water molecules are considered, an essentially spin-singlet minimum appears [157, 188], and this minimum ends up to be the global one with four or five water molecules, depending on the level

of theory [157, 188]. Consequently, the work of D.-C. Sergentu definitly supported the hydration-induced ground-state change of $[AtO]^+$ and the natures of the involved energy levels were eventually revealed by relativistic and multiconfigurational calculations [157]. Note that ground-state reversals were reported for CUO and UO_2 in argon matrices [208, 209, 210, 211]. Therefore, even it is not the first reported case of a ground-state reversal, it is quite spectacular since the energy difference between the two swapped states is significantly larger than in the previous examples (∼1 eV instead of ∼0.2 eV, *i.e.* it is larger by almost one order of magnitude).

3.5 Transformation or reaction energies

3.5.1 Ionization energies and electron affinities of astatine species

Monoatomic astatine

Before ending this chapter, it is worth briefly discussing the role of the SOC on transformation or reaction energies. The simplest transformations perhaps correspond to the loss or gain of an electron for monoatomic astatine, *i.e.* to the first ionization potential (IP_1) and to the electron affinity (EA) of free astatine. Reference values are available for these quantities, either coming from experiment [212] or from state-of-the-art fully relativistic calculations [213] (see Table 3.7). If one defines the electronegativity as $\chi = \frac{1}{2}(IP_1+EA)$ (Mulliken scale), this leads to a reference electronegativity value of 5.86, which may convert into a 1.82 value in the Pauling scale [214]. Note that this 1.82 value is not inconsistent with the 2.2 value that is usually reported [215] (it was initially described as being inferior or equal to the one of the H atom, *i.e.* it should be read as inferior or equal to 2.2 in the revised Pauling scale [216]). Anyway, from the results of Table 3.7, obtained by D.-C. Sergentu by considering electron transfer reactions between At and I^+ and I^- and At, respectively and with the B3LYP exchange-correlation functional [168]), it is clear that the SOC plays a non-negligible role on the IP_1 and EA of At, as expected.

Table 3.7: First ionization potential (IP_1) and electron affinity (EA) of At (eV) [191]. Reference values from experiment (IP_1) or from fully relativistic CCSD(T) calculations (EA) are also given.

Method	IP_1	EA
SRDFT	9.90	2.89
SODFT	9.29	2.41
Reference	9.32 [212]	2.41 [213]

Astatobenzoate derivatives

In a work aiming at explaining the difference of the *in vivo* behaviours of astatine and iodine compounds [217], the first IP_1 of an astatobenzoate compound and its analogous iodine species were computed by the post-doctoral associate D. Tézé with the B3LYP exchange-correlation functional [168] (see Table 3.8) [9]. As can be seen in this table, the SOC makes the astatobenzoate compound more sensitive to a first oxidation than its iodine counterpart. Therefore, it is clear that the correct trend in reactivity can only be obtained after the inclusion of the SOC. In other words, the SOC is capable of changing chemical reactivity trends. For further commenting on the difference between the behaviours of astatobenzoate and iodobenzoate compounds, note that bond dissociation energies (BDEs) were also computed, in the starting compounds, and also after a probable oxidation of the halogen (*vide infra*).

Table 3.8: First ionization potentials (IP_1) of an astatobenzoate compound ("astatobenzoate") and its iodine analogue ("iodobenzoate") (eV) [9].

Method	Astatobenzoate	Iodobenzoate
SRDFT	9.03	8.56
SODFT	8.06	8.51

3.5.2 Bond dissociation energies

Diatomics

It is well know that the SOC affect the BDEs of diatomic molecules, typically by reducing them since the SOC stabilizations of the ground states of the fragments are stronger than the SOC stabilization of the ground state of the bound system. Astatine diatomics are no exception to this rule, as can be seen for instance in Table 3.9. In the At_2 hypothetical molecule, it reduces the BDE by more than half according to the calculations performed by my collaborators F. Réal, A. S. P. Gomes and V. Vallet (PhLAM laboratory, Villeneuve d'Ascq). Also, significant differences appear between the c-SOCI/NEVPT2 and uc-SOCI/NEVPT2 results, meaning that the polarization of the "in-CAS" electron correlation by the SOC matters for computing these quantities. However, in both cases, most of the observed difference lies in the fragments. For instance, in the At_2 case, the effect of this polarization on the sum of the SOC stabilizations of the fragments at dissociation is 0.23 eV (for the interested reader, it accounts for twice the third of the SOC splitting between the $^2P_{\frac{3}{2}}$ and $^2P_{\frac{1}{2}}$ levels of monoatomic astatine), while the difference between the c-SOCI/NEVPT2 and uc-SOCI/NEVPT2 result is 0.21 eV (see Table 3.9) [10]. In other words, the effect of the polarization that is introduced

by the uc-SOCI/NEVPT2 method stabilizes by only 0.02 eV the bound system at equilibrium, and thus, the c-SOCI/NEVPT2 method is well suited for describing this bound system, while it is clearly more accurate to use the uc-SOCI/NEVPT2 one for monoatomic astatine.

Table 3.9: Bond dissociation energies (BDEs) of astatine diatomics (eV) [10]. Contracted (c) and uncontracted (uc) SOCI results are reported to highlight the role of the polarization of the "in-CAS" electron correlation by the SOC.

Method	NEVPT2	c-SOCI/NEVPT2	uc-SOCI/NEVPT2
At_2	1.86	0.85	0.64
AtO^+	3.15	2.43	2.30

Astatobenzene *vs.* iodobenzene

To show results concerning larger molecules (*i.e.* not diatomics), B3LYP [168] SRDFT and SODFT BDEs for the astatobenzene and iodobenzene molecules are reported in Table 3.10 [9]. In this case, the astatine *vs.* iodine trend is not reversed by the SOC, although it is clear that the effect of the SOC is stronger in the astatine case than in the iodine one. In other words, the At–C bond in astatobenzene is significantly less stable than its iodinated counterpart, which is partly due to the SOC. The BDEs of the previouly mentioned astatobenzoate and iodobenzoate compounds were not computed at the SRDFT level; however, it is worth mentioning the SODFT results for showing the interest of the performed computational study in the biological context. As previouly mentioned, it is easier to oxidize At in astatobenzoates than it is to oxidize I in iodobenzoates. Furthermore, in [9], we showed that once At is oxidized, the At–C bond remain significantly less stable than the analogous I–C one after I is also oxidized. Therefore, we proposed to attribute the dehalogenation mechanism that is observed *in vivo* to oxidative dehalogenation. I believe that this is a nice example of a relativistic quantum chemistry study aiming at identifying a mechanism of biological interest.

Table 3.10: Bond dissociation energies (BDEs) of astatobenzene and iodobenzene (eV) [9]. Experimental values are also given for comparison (derived from bond enthalpies).

Method	Astatobenzene	Iodobenzene
SRDFT	2.61	2.92
SODFT	1.93	2.58
Expt.	1.95 [218]	2.82 [219]

3.6 Concluding remarks

There is no need to deeply insist on the fact that relativistic quantum chemistry calculations may be of interest for studying the chemistry of heavy-(radio)element species, in complement or even before experiments. Via selected examples, I have illustrated again the fact that relativistic effects and in particular the SOC can significantly affect the structural and chemical properties of heavy-(radio)element species. Also, I have shown that the SOCI/NEVPT2 approach is capable of well describing the properties of bound systems, even in the case of astatine molecules. The next logical step is to attempt using the outcomes of such calculations to analyse chemical bonds, which will be the main scope of the next chapter.

Chapter 4

Chemical bonding in heavy-(radio)element systems

4.1 Introduction

In molecular and materials chemistry, the rational design of new systems with desired properties is a goal in itself. In bottom-up approaches, it requires a good "chemical intuition" on the reactivity and properties of building blocks, and on the assembly between these. For instance, in transition metal chemistry, the low-temperature magnetic behaviour is essentially driven by the choice of the diamagnetic ion(s) and by the nature and the positions of the atoms belonging to the first coordination sphere(s) of the ion(s) and, to a lesser extent, by the atoms belonging to the second coordination sphere [58, 72]. By playing with these factors based on theoretical arguments or experience, it is possible to successfully design complexes with large magnetic anisotropies [73, 76]. Because a lot of experience has been acquired during several decades on transition metal chemistry, theory is not there mandatory, although it is of course of good help. However, when little is known on the basic chemistry of the element of interest, no "chemical intuition" can be invoked, and one has to rely on serendipity or on chemical analogies, which of course, is not always the key to success!

As mentioned in Chapter 3, this is typically the case in the field of astatine chemistry [147]. Because this naturally occurring element is extremely rare in nature, its chemistry can only be studied after production in cyclotrons. All the At isotopes should be considered as short-lived (their half-life time being at most 8.1 h) and the obtained quantities of matter are much too weak to obtain any structural information by spectroscopy. Therefore, computational chemistry tools are crucial for identifying or evidencing new astatine species [154, 207], as well as for determining the nature of the chemical bonds in them. To understand better the chemistry of this element, I became interested in chemical bonding analyses of astatine species performed on top of relativistic calculations that do include the SOC term, *i.e.* from hopefully qualitatively correct wave functions/densities.

Actually, most of the chemical bonding analysis tools that are currently available have been developed in the absence of the SOC. Because of the lack of adequate tools and/or because of a lack of knowledge on the importance of the SOC on chemical bonding, some researchers have been or are even still tempted to analyse chemical bonds involving heavy atoms in the absence of the SOC [220, 221, 222]. Therefore, it is quite important to develop and apply chemical bonding analysis tools on top of SODFT and/or SOCI/NEVPT2 calculations, *i.e.* on top of "routine" SOC calculations. Concerning the former case, my current collaborators J. Pilmé (LCT laboratory, Paris) and N. Galland (CEISAM laboratory, Nantes), together with coworkers, had already implemented topological analyses on top of SODFT calculations before I started to work in this field [162, 164]. However, these analyses of the electron density (quantum theory of atoms in molecules, QTAIM, fashion [223]) and of the electron localization function (ELF) [224] may not be valid in the general case because of both the theory behind the calculations and its implementation: since a single-determinant approach is used, the quantum state of interest should be dominated by a single determinant; furthermore, since a collinear approximation is used for determining the spin density, this determinant must be closed-shell (in terms of an MO picture) [225]. Alternatively, an implementation of the ELF topological analysis is available within the Dirac code [226], with analyses which can be performed for instance on top of fully relativistic CCSD(T) calculations (of both the X2C and Dirac-Coulomb types) [227]. However, fully relativistic calculations may be too expensive for treating medium- to large-size systems. Therefore, these implementations were not necessarily capable of properly treating all the chemical bonds that I wanted to; this is one of the reasons that made me initiate the will of performing chemical bonding analyses on top of SOCI/NEVPT2 calculations.

Analysing chemical bonds on top of SOCI/NEVPT2 calculations may have more advantages, *e.g.* (i) many chemical bonding analysis tools must be possible since any tool that is applicable at the CI level must be also applicable at the SOCI/NEVPT2 level and (ii) the SOCI/NEVPT2 wave functions can be directly interpreted in a somehow more intuitive way than the fully relativistic ones since since they are expressed in terms of linear combinations of the M_S components of SOF states, which are themselves expressed in terms of CI coefficients and real MOs (instead of molecular spinors). Also, note that performing topological analyses at various state average (SA) CASSCF levels or at various SOCI/NEVPT2 levels, based on different SA spaces, may lead to a nice and original way to reveal the importance of SA effects (the CI coefficients of SA-CASSCF wave functions may be very close to the state specific (SS) CASSCF ones and thus, the sole analysis of the CI coefficients is not sufficient to discuss SA effects). I started with a first work [10] on effective bond orders (EBOs) [228], independently from the work of Gendron *et al.* [229], which I was not aware of. To go further on EBOs at the SOCI/NEVPT2 level and to interface a topological analysis program with the outcomes of SOCI/NEVPT2 calculations, I enrolled in 2016 a PhD student, C. Gomez-Pech.

4.2 The SOC contribution to effective bond orders

4.2.1 The effective bond order concept

The EBOs were defined by Roos *et al.* in 2007 in the framework of SS-CASSCF calculations [228]. The idea beyond the EBO concept is to define a bond order (BO) that depends on the wave function in such a way that (i) it is neither an integer nor a half-integer and that (ii) it gradually tends to zero towards dissociation. It was clear that the analysis of a multiconfigurational wave function, such as the CASSCF one, could readily satisfy such requirements if one computes the occupation numbers of the bonding and antibonding orbitals, and define the EBO from them as:

$$\mathrm{EBO} = \frac{\sum_b \eta_b - \sum_a \eta_a}{2} \tag{4.1}$$

where b and a are the bonding and antibonding orbitals within the active space, respectively, and η_b and η_a are the occupation numbers of the bonding and antibonding orbitals, respectively. In the examples that were treated in this article, the occurrence of a symmetry centre imposed (by symmetry!) a clear bonding or antibonding character for any of the natural orbitals (NOs). The NOs are, by definition, the orbitals that make the one-electron density matrix diagonal [230]. Therefore, even if it is obvious that the NOs are good choices for defining EBOs in homodiatomic systems, the case of non-centrosymmetric molecules may be less clear. Although it was claimed that "This measure of the bond multiplicity is based on very well defined and stable quantities: the occupation numbers of the natural orbitals (NOs)" [228], this may lead to some (little) contradiction: yes, the occupation numbers of the NOs are well defined and stable quantities, but these NOs may not have strong bonding or antibonding characters, while such a character is supposed for defining the EBO. This relates to a pure interpretation of the wave function problem, and not to a problem lying in the quantum chemical calculation itself: one may think of fixing this issue by a transformation of the active MOs, which must keep invariant the electron density. Note that it may happen to obtain active orbitals with moderate bonding/antibonding characters, as was done for instance in a work I co-signed [126], in which "partially delocalized" NOs were used to define the EBO in a non-centrosymmetric dicobalt complex. Another, perhaps more important, issue concerns the rounding-up rule: "The EBO is non-integer and in naming the multiplicity of a bond one may then use the lowest integer value larger than the EBO" [228]. This rule is in my opinion clearly inconsistent with the EBO concept itself and I only see it as a way to artificially claim higher bond multiplicities than should be done (*e.g.* the reported quintuple bond in U_2 despite an EBO value of 4.2 [220, 228]). Instead, I recommend, if rounding-up is required, to do it with the closest integer or half-integer value, for instance referring to no more than a quadruple bond in U_2. Since the SOC is susceptible to affect the EBOs of heavy-element systems, I started to be interested in EBOs.

4.2.2 Homodiatomic molecules: The At_2 case study

In homodiatomic molecules, symmetry imposes the active orbitals to have pure $\sigma/\pi/etc.$ characters and also pure bonding/antibonding characters (if one performs the calculation/reasoning in the actual symmetry point group of the system, $D_{\infty h}$, or in the D_{2h} subgroup of it). Moreover, the NOs of the SA-CASSCF calculations are also NOs of all the SOF states that are considered in the SA space and, as a consequence, of each energy level obtained at the SOCI level. As a consequence, no ambiguity can arise from the nature of the active orbitals for computing the EBOs. To illustrate the case of homodiatomic molecules, it is nice to discuss again the case of the At_2 hypothetical molecule. As mentioned in Chapter 3, the ground SOF configuration in this system is $[...]\sigma^2\pi^4\pi^{*4}$. From this configuration, two main effects at at play, (i) the electron correlation triggers the $\sigma^2 \rightarrow \sigma^{*2}$ double excitation and (ii) the SOC leads to the $\pi^4 \rightarrow \pi^3\sigma^{*1}$ single excitations (two possible orbital excitations times two possible spins results in four excitated SOC components –in terms of M_S components of SOF configurations–). Therefore, both effects are expected to reduce the σ contribution (EBO_σ) to the total EBO (EBO_{tot}), while the SOC is also expected to reduce the π contribution (EBO_π) to EBO_{tot}. Naturally, things may be a little more subtle if one deals with multiconfigurational wave functions, as is done within the CASSCF and SOCI/NEVPT2 frameworks; this is why it is still important to look at actual data. In collaboration with F. Réal, A. S. P. Gomes and V. Vallet (PhLAM laboratory, Villeneuve d'Ascq), we computed at my initiative EBO values for the ground-state of At_2 at various levels of theory and at the equilibrium geometry of each method or with single-point calculations [10].

Table 4.1: Ground-state SOF and SOC EBOs of At_2 computed with various methods at the corresponding equilibrium geometries [10].

Method	EBO_σ	EBO_π	EBO_{tot}
NEVPT2	0.93	0.00	0.93
c-SOCI/NEVPT2	0.82	−0.04	0.78
uc-SOCI/NEVPT2	0.75	−0.08	0.66

In Table 4.1, the equilibrium geometry of each method was considered to determine the EBOs. As can be seen in this table, the SOC plays a more important role on EBO_σ, on EBO_π, and thus, on EBO_{tot} than the "in-CAS" electron correlation. Therefore, it is clear that the SOC contribution to the EBOs should not be neglected in the case of heavy-(radio)element species, apart from particular cases (*e.g.* the $[AtO]^+$ cation, for which the SOC does not lead to a drastic change in the electronic structure, as mentioned in Chapter 3, and also discussed in [10]). Clearly, a significant π antibonding

character is evidenced for At_2 and, *in fine*, the chemical bond in this system seems closer to a half bond than it is of an ideal single one or even to a typical single bond (EBO_{tot} ~0.9). It is important to stress that at the uc-SOCI/NEVPT2 level, the effect of the SOC is strengthened as compared to the one observed at the c-SOCI/NEVPT2 level, which is not really surprising. However, since an EBO is only a rough probe of the nature of a chemical bond, one may consider that determining EBOs at the c-SOCI/NEVPT2 level already leads to good semi-quantitative estimates of these quantitites. Also, similar EBOs can be obtained for At_2 with the SOCI approach at the equilibrium geometries or at a fixed (reference) geometry [10], meaning that single-point calculations can alternatively be used for computing EBOs, although of course the numerical values may slightly differ. Indeed, the ground-state SOF and SOC wave functions of At_2 do not drastically change with moderate changes in the molecular geometry, which is in line with the fact that no ground-state change is observed for this system in the range of probed geometries (with the bond distance within the ~2.8 Å to ~3.1 Å range, and with an equilibrium bond distance of 2.96 Å at the c-SOCI/NEVPT2 level [10]). Therefore, apart from specific pathological cases, one can safely compute c-SOCI/NEVPT2 EBOs at a fixed geometry, for instance at a reference fully relativistic one.

4.2.3 Heterodiatomic molecules: The AtX (X = F–I) series

In heterodiatomic molecules, although symmetry imposes the active orbitals to have pure $\sigma/\pi/etc.$ characters (if one performs the calculation/reasoning in the actual symmetry point group of the system, $C_{\infty v}$, or in the C_{2v} subgroup of it), it is not the case for the bonding/antibonding characters. As a consequence, the bonding and antibonding orbitals of the same type may rotate and the NOs an SA-CASSCF calculation may not be NOs of any of the SOF states that are considered in the SA space and, thus, of any of the energy levels obtained at the SOCI level. Therefore, it may be necessary to make a specific transformation of the SA-CASSCF NOs to obtain the NOs of a given SOF state, and in a similar way for a given energy level obtained at the SOCI level [231]. In two-electron systems [230], the NOs not only diagonalize the one-electron density matrix, by definition, but they also extremize the occupation numbers. However, since the NOs may not always lead to the most optimal expansion of the wave function [232], I found interesting to numerically check at the SA-CASSCF and SOCI/NEVPT2 levels if the NOs of a given SOF state or energy level maximize the absolute values of the $\sigma/\pi/etc.$ contributions to EBO_{tot}. Therefore, I asked C. Gomez-Pech, the second PhD student that I co-advise with N. Galland (CEISAM laboratory, Nantes), to study the EBOs of the AtX series (X = I–F) at the SA-CASSCF and SOCI/NEVPT2 levels and at the X2C-CCSD(T) reference geometries provided by my collaborators from the University of Groningen (A. Borschevsky and her PhD student P. Haase). As mentioned before, the NOs may not be the active MOs that have the most bonding/antibonding characters. Therefore, N. Galland also suggested

to C. Gomez-Pech to determine the EBOs with the most bonding/antibonding (B/AB) σ and π "rotated" active MOs, obtained after rotating the SA-CASSCF orbitals to maximize the absolute values of the interatomic overlaps, defined as:

$$S_k = \sum_{i \in I} \sum_{j \in J} c_{ki} c_{kj} S_{ij} \tag{4.2}$$

where k is an active orbital, i an atomic orbital (AO) of atom I, j an AO of atom J, c_{ki} and c_{kj} are the linear combinations of atomic orbital (LCAO) coefficients of the basis functions i and j, respectively, of orbital k, and S_{ij} is an element of the overlap matrix between the basis functions.

Table 4.2: Ground-state SOF and SOC EBOs of the AtX (X = I–F) systems computed at reference X2C-CCSD(T) geometries (see Table 3.1), with the ground-state natural orbitals or with the most bonding/antibonding (B/AB) σ and π "rotated" active MOs.

		Natural orbitals			Most B/AB orbitals		
X	Method	EBO_σ	EBO_π	EBO_{tot}	EBO_σ	EBO_π	EBO_{tot}
I	SA-CASSCF	0.92	0.00	0.93	0.91	0.00	0.91
	SOCI/NEVPT2	0.87	0.00	0.87	0.85	0.00	0.85
Br	SA-CASSCF	0.93	0.00	0.93	0.85	0.00	0.85
	SOCI/NEVPT2	0.87	0.03	0.90	0.80	0.03	0.83
Cl	SA-CASSCF	0.93	0.00	0.94	0.79	0.00	0.79
	SOCI/NEVPT2	0.87	0.06	0.93	0.74	0.05	0.79
F	SA-CASSCF	0.93	0.00	0.94	0.82	0.00	0.82
	SOCI/NEVPT2	0.87	0.07	0.94	0.77	0.04	0.81

The first result of C. Gomez-Pech has been to confirm that the NOs of the quantum state of interest indeed maximize the absolute values of EBO_σ and EBO_π, meaning that the NOs lead to well-grounded contributions to EBO_{tot}. Therefore, one can indeed safely use the NOs to discuss EBO trends. Note that Gendron *et al.* directly used the NOs obtained at the SOCI level to compute their EBOs at the SOCI level [229], while I did not so in the first heterodiatomic compound that I studied, namely $[AtO]^+$. However, note that this subtlety is not meant to change the conclusions that we reported in [10]. If one looks at the SOF and SOC EBOs that are reported in Table 4.2 based on NOs (left part of the table) and of the values that were previouly mentioned for At_2 (see Table 4.1), a trend clearly emerges: by going from X = At to X = F, the SOC reduces in all the cases EBO_σ, while its contribution to EBO_π gradually increases (from -0.04 in At_2 to 0.07 in AtF). This is due to the fact that in the At_2 case, the SOC only triggers the $\pi \rightarrow \sigma^*$ single excitation

from the ground SOF configuration, while in the heterodiatomic cases two excitations are allowed, the $\pi \rightarrow \sigma^*$ one, as in the homodiatomic dihalogens, and also the $\pi^* \rightarrow \sigma^*$ one, as mentioned in Chapter 3. These two excitations have opposite-sign contributions to EBO_π, and the latter one becomes more and more important in the series. Thus, in this series, the role of the SOC on EBO_π is not trivial, and one should be careful in attempting to transfer the conclusions obtained on one system to another one, even if they may look chemically quite close (all the studied AtX systems are valence isoelectronic). By comparing the left and right parts of Table 4.2, one can see the influence of the choice of the "rotated" active MOs on the determined EBOs. Although the same trend is observed (the SOC contribution to EBO_π increases in the series), the difference with the results based on the NOs ends up to be quite significant for the more ionic systems within the series (AtCl and AtF). This difference being clearly a sign of symmetry beaking (as mentioned before, both sets of active MOs are by symmetry identical in homodiatomic molecules), perhaps one can interpret it as a sign of ionicity of the At–X bonds. Of course, for highly ionic systems, the EBOs may not be the most natural probes of the chemical bonds, and thus, maybe one should restrict the usage of the EBOs to the systems for which the two sets or active MOs lead to very close values. Note that one publication is currently in preparation concerning this work and that more details and discussions will be given in this forthcoming publication.

4.3 The role of the SOC revealed by topological analyses

4.3.1 A brief introduction to the quantum chemical topology

Another way of analysing chemical bonds relies on the topological analyses of one-density functions. Two main one-density functions can be used, the electron density, giving rise to the QTAIM of Bader [223], and the ELF [233], which can be used to reveal atomic shell structures [234], the nature of chemical bonds [224], and even electron delocalization via fluctuation analysis [235]. The QTAIM approach can be used to definite atomic charges (one has just to integrate the electron density over the atomic basins to get the number of electrons associated with the atoms, and thus, the atomic charges). Also, the indicators defined at a bond critical point (BCP), a special point of the interatomic zero-flux surface, such as the value of the density ρ and of its Laplacian $\nabla^2\rho$, or the position of the BCP (the deviation of the BCP from the middle of the bond can be characterized by the R_{BCP}/R_{eq} value) can be used to classify the bonding types [236]. The topology of the ELF is a more complex one in the sense that basins of different types may arise in molecules, typically core basins, denoted C(X), non-bonding valence basins (corresponding to "lone-pair" regions), denoted V(X) and disynaptic valence basins, *i.e.* bonding basins, denoted V(X,Y), where X and Y are atoms. The electron population of a bonding basin can be obtained by integrating the electron density ρ

over the whole basin [235]. In this way, it is thus possible to define the number of core electrons and of non-bonding electrons of each atom, as well as the number of electrons that are involved in the bond between two atoms. This latter indicator is important for classifying the nature of the bond, *e.g.* a population of *ca.* 2.0 electrons would correspond to an ideal single bond. Also, the presence of a bonding basin associated with a non-negligible electron population discards the idea of an ionic bond, while a population of about one electron plus a large population variance, σ^2, may be indicative of a "charge-shift" (CS) bond [237]. However, one should note that the identification of CS bonds, for which an effective resonance between two opposite-polarized ionic structures occurs ($X^-\ Y^+ \longleftrightarrow X^+\ Y^-$), is more natural within the VB framework [238], even if it can obviously be alternatively done within an MO theory framework [239].

4.3.2 Analyses on top of one-component and two-component DFT calculations

By collaborating with N. Galland (CEISAM laboratory, Nantes) and J. Pilmé (LCT laboratory, Paris), I have been involved in two publications related to topological analyses performed on top of DFT calculations [185, 240]. Although I have not performed any calculation in these studies (I was involved though in the interpretation of the results and also of course in correcting the drafts of the manuscripts), some results will be presented here to examplify a few things that can be highlighted by topological analyses. Note that my main contribution to the field of topological analysis has actually been to push for performing topological analyses on top of SOCI/NEVPT2 calculations, which is the main objective that I gave to the PhD student C. Gomez-Pech (*vide infra*).

Differences between an emblematic At–C bond and a relevant At–B one

In a work aiming at expliciting the differences between an emblematic At–C bond and a relevant At–B one, with the perspective of explaining their different *in vivo* behaviours (the At–B one is more stable when the labeled biological vector is internalized –into cells–), topological properties of these bonds were studied [240]. As can be seen in Table 4.3, the At atom in the *N*-succinimidylastatobenzoate (SAB) compound has an opposite-sign atomic charge than it has in a labeled closo-decaborate, which indicates that the At–C and At–B bonds of interest are opposite-polarized. Furthermore, it appears that the At–C bond under study has a stronger covalent character than the At–B one (which is attested by a larger electron population associated with the disynaptic V(At,X) basin, the basins being depicted in Figure 4.1), despite the more favorable bond enthalpy in the At–B case. Note a tentative explanation for the different *in vivo* behaviours of these bonds was proposed [240]: "the difference in *in vivo* stabilities may be related to the different stabilities of the At–C and At–B bonds of interest with respect to oxidation". So far, we have shown via the study of a model compound that the At–C bond of the SAB is sensitive to oxidation [9], but the

stability of the At–B bonds of labeled closo-decaborates toward oxidative conditions remains to be studied, to support or infirm this first explanation (but not to prove it, which would require even more experimental studies). Concerning the role of the SOC on the topological properties, little differences appears in Table 4.3. The observed differences in the At atomic charges should not be interpreted as a "direct" consequence of the SOC, but rather as an "indirect" one associted with geometry relaxation, since the SRDFT and SODFT calculations were performed at the corresponding equilibrium geometries, and since the local SOC interaction is not meant to trigger any significant "electron transfer" at a given geometry.

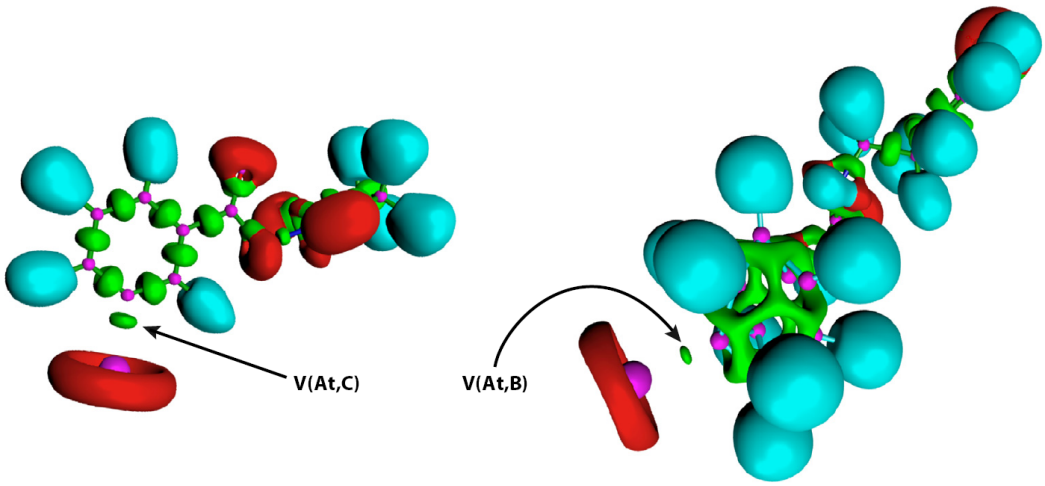

Figure 4.1: ELF localization domains (isosurface = 0.87) of the SAB (left) and of a labeled closo-decaborate (right) obtained on top of SODFT calculations. Color code: magenta = core basin, red = non-bonding basin, green = bonding basin (with no H atom involved), cyan = bonding basin (with an H atom involved) [240].

Table 4.3: Electron populations of the ELF disynaptic V(At,X) basins involving the At atom of the N-succinimidylastatobenzoate (SAB) and of a labeled closo-decaborate and At atomic charges [240], all obtained on top of DFT calculations with the M06-2X exchange-correlation functional [206].

Compound	Method	V(At,X)	q(At)
SAB	SRDFT	1.44	+0.16
	SODFT	1.50	+0.22
Closo-decaborate	SRDFT	1.14	−0.46
	SODFT	1.15	−0.45

Back again to the AtF_3 hypothetical molecule

In another work [185], we reported topological properties of the chemical bonds in the AtF_3 hypothetical system. Clearly, no significant change triggered by the SOC was observed, and thus, a complete description of this work would be a bit off-topic here. I would just mention that since the goal of article was to provide an explanation regarding the relative stabilities of the T-shaped C_{2v} structures and the planar D_{3h} one (these structures were mentioned in Chapter 3), a multipole expansion analysis was performed at the SODFT level, to study the Coulomb repulsions between the two lone pairs of the At atom and between the lone pairs of the At atom and the ones of the F atoms, revealing similar Coulomb repulsions in the two structures of AtF_3, unlike the ligher XF_3 (X = I–Cl) fluorides, for which the T-shaped C_{2v} situation is clearly more favorable [185].

4.3.3 Analyses on top of SA-CASSCF and SOCI/NEVPT2 calculations

As previouly mentioned, I have initiated and I lead the project of performing topological analyses at the SA-CASSCF and SOCI/NEVPT2 levels. For this, I have enrolled the PhD student C. Gomez-Pech and chosen to collaborate with N. Galland (CEISAM laboratory, Nantes, coadvisor of her) and also J. Pilmé (LCT laboratory, Paris). To have her efficiently trained on topological analyses, I have sent her for one month to Paris, in the first year of her PhD, for working with J. Pilmé. She is in charge of developing the necessary code and also of performing the actual analyses.

The plan

The SOCI calculations are performed with the Molpro program package [241] since this program allows expressing the MOs from Cartesian AOs, which is required by the TopMod program [242] to be used for the topological analyses. While the definition of the electron density at the SOCI level is straightforward, one also needs to define the ELF within a multiconfigurational framework. Actually, the ELF is usually defined within single-determinant approaches such as HF or Kohn-Sham DFT. For this project, I proposed to follow what was done for defining the ELF at multiconfigurational non-relativistic levels [243, 244], such that in practice, only a simple interface between the SOCI code and the topological analysis one had to be made. This interface had to include the computation of the updated fractional occupation numbers of the NOs after the inclusion of the SOC, which required determining the NOs at the SOCI level [231]. Since this had already been done by C. Gomez-Pech for instance for computing some of the EBOs that are reported in Table 4.2, no major difficulty was expected. Naturally, as often, things ended up to be more complex than we expected and it took quite some efforts to have the correct interface. For instance, the generation of .wfn files, compatible with the TopMod program from the outputs of Molpro calculations with Cartesian AOs, ended up to be quite tricky (because of the AO ordering and normalization factors).

The first results

The first topological analysis results obtained by C. Gomez-Pech concern the AtX (X = I–F) systems (see Table 4.4), *i.e.* the ones that she has already studied with the EBO perspective (see Table 4.2). As can be seen in Table 4.4, the computed At atomic charges are not changed by the SOC in these systems, which is due to the fact that the SA-CASSCF and SOCI/NEVPT2 calculations were performed at the same geometry for each system. In the X = I–Cl cases, the SOC reduces the population of the disynaptic V(At,X) basins, which is in line with the DFT results of Pilmé *et al.* performed at SRDFT and SODFT equilibrium geometries [164] and also with previous discussions in this manuscript. In the AtF case, no disynaptic basin was found at both the SA-CASSCF and SOCI/NEVPT2 levels, which is also in line with the previous DFT study [164]. Overall, nothing very surprising was obtained, which is not problematic since these results were essentially reported to show that the interface between the Molpro [241] and Topmod [242] programs is now effective.

Table 4.4: Electron populations of the ELF bonding basins of the AtX (X = I–F) systems and At atomic charges obtained on top of SA-CASSCF and SOCI/NEVPT2 calculations performed at reference X2C-CCSD(T) geometries (see Table 3.1).

X	Method	V(At,X)	q(At)
I	SA-CASSCF	0.78	0.08
	SOCI/NEVPT2	0.67	0.08
Br	SA-CASSCF	0.67	0.22
	SOCI/NEVPT2	0.54	0.22
Cl	SA-CASSCF	0.56	0.33
	SOCI/NEVPT2	0.34	0.33
F	SA-CASSCF	–	0.62
	SOCI/NEVPT2	–	0.62

4.4 Concluding remarks

Bond indicators coming from two different perspectives, namely the EBO concept and quantum chemical topology, can be now in principle obtained at the same exact levels of theory with both the SA-CASSCF and SOCI/NEVPT2 methods, notably thanks to the work the PhD student C. Gomez-Pech, performed under my guidance. Therefore, the effect of the SOC on chemical bonding can be now assessed at these SOF and SOC levels with different chemical bonding analysis tools. Naturally, I have more developments and applications in mind, which I will explicit in Chapter 5.

Chapter 5

Outlook

5.1 Introduction

In ten years of research, I have tackled problems of different natures and from various fields, namely molecular magnetism, theoretical radiochemistry and more recently chemical bonding analysis. Since I am currently working within a radiochemistry group, it is clear that I find important to focuss on chemical species of radioelements, especially since in some cases the molecular quantum chemistry perspective is really helpful, if not mandatory, to interpret or guide experiments. With this in mind, I would like to push a bit concepts and ideas in these three identified research themes and also find more connections between these. Perhaps the actinides present the most suited situations for this, and this is why I plan dedicate more and more of my time to the study of actinide systems. Concerning less "transversal" activities for me (in the sense of the three identified themes), I would say that I have three main objectives in mind, still based on the quantum study of stationary states:

1. Unambiguously evidencing CS bonds in heavy-element species by means of VB calculations, which I associate with the development and implementation of a "VBSOCI" method.

2. Establishing rules to anticipate the importance of the SOC on chemical bonding and its consequences on the properties of any system, *a priori* based on the least possible information on the electronic structure the system.

3. Performing calculations in the support of new spectroscopy experiments of heavy-element species, in particular to elucidate the speciation of such elements in given media.

Also, knowing that radiochemists tend to specialize on the chemistry of one or few radioelements, I would like to stimulate and support the start of chemical studies of new or relatively new radioelements for my group, notably concerning the actinides (*e.g.* Ac, Pa or Np), and also to strengthen emerging research, as for instance the one associated to the "polonium project" of my colleague J. Champion, for which a couple of successful studies have already been published [202, 245, 246].

5.2 Molecular magnetism

In my opinion, there is still some room for the derivation of model Hamiltonians for describing the low-temperature magnetic behaviour of the f elements, in particular concerning the effective coupling of two magnetic centers with one of the two being an ion of an f element (the typical case of f–d binuclear complexes or of lanthanide/actinide–radical complexes). In this case, one must consider the crystal-field splitting of the f ion, plus the magnetic coupling(s) between the f ion and the other magnetic centre. In the simplest situation, let us say the coupling of an f^1 ion and a d^1 one, with a system displaying an axial symmetry, the crystal field of the f^1 ion results in a splitting of the ground $J = \frac{5}{2}$ term in such a was that the components having different $|M_J|$ values are split, which results in three distinct energy levels: $|M_J| = \frac{5}{2}$, $|M_J| = \frac{3}{2}$ and $|M_J| = \frac{1}{2}$. If the crystal field splits these terms, it is because they differ in terms of the orbital part of their associated wave functions. Therefore, attributing a single isotropic coupling J value between the f ion and the d one may be too simplistic, even if it is usually done in the interpretation of experiments, while a simple and intuitive model to describe such a situation is yet to be defined (there already exists one model for this [247], which I personally do not find that intuitive). I believe that considering the crystal-field splitting of the f ion plus three distinct isotropic coupling values $J^{ab}_{M^a_J}$ (with the first "J" referring to the magnetic coupling constant between the a and b centers and the M^a_J index referring to the f ion, denoted a) should already provide a satisfactory model, without the necessity for formally introducing the "anisotropy" of the interaction (*i.e.* without a D^{ab} term –with the nomenclature of Chapter 2–). Alternatively, one may also consider the crystal-field splitting of the f ions plus four distinct isotropic coupling values $J^{ab}_{M^a_L}$ (the M^a_L index referring to the f ion), which would perhaps be even more intuitive. Of course, this is of the typical type of nerd question I like to tackle, but it is also clear that it would not generate a revolution in the field, especially if one considers the energy range it may concern (at most one or a few cm^{-1}). However, I would be pleased to extend my PhD work, *i.e.* the rigorous determination of model Hamiltonians to binuclear complexes containing one or two f ions, in particular actinide ones. Of course, as for my PhD work, I would perform or lead the study on a series of examples of increasing complexity, yet to be defined.

5.3 Radiochemistry

In radiochemistry, it is not always possible to perform spectroscopy experiments. It is often the case in the frame of my collaboration with J. K. Gibson from Berkeley, for which we may only have access to the molecular masses (from the m/z ratios) and also to reactivity information, as in some studies that I have already mentioned in this manuscript [124, 199]. Because I find very nice this collaboration, I plan to continue it, and one current project concern the study of mixed-

valence $[(UO_2)_2(C_{2+n}O_4H_{2n})_2]^-$ complexes (of the U(V)–U(VI) or the $U^{5.5+}$–$U^{5.5+}$ character, with n = 3–8), for which the mixed-valence class can only be determined from the quantum chemistry calculations that I perform together with E. Renault (CEISAM laboratory, Nantes). Our objective is to determine the structures and mixed-valence classes of the complexes, in view of explaining their different reactivities toward O_2 and H_2O. At this stage, we are fully convinced of the non-occurrence of "class III" complexes [248], but sill need to confirm our first potential explanation concerning the differences in the observed reactivities of these complexes. Another work, still done in collaboration with J. K. Gibson and E. Renault, concerns the IRMPD spectra of uranium oxide complexes with nitrates, which is kind of a direct follow-up to our previous studies [124, 199]. The confrontation of theoretical and experimental data will surely help us identifying new exotic uranium species (with the IRMPD technique, quite unstable species, usually not observed, may be formed and characterized, and these may in principle differ from the ones that can be formed by CID).

Sometimes, experiments are not only "blurred" (knowing the m/z ratio of the species of interest is already quite informative), but rather "blind", which is for instance the case when competition between two phases experiments are performed. There, calculations are also needed to support the experiments, not only for the identification of the observed species, but also for defining *a priori* well-suited experimental conditions for identifying a given species, in the spirit of what I have first proposed for the $[BrAtI]^-$ species [154]. I plan to follow a similar approach, together with my experimental colleague J. Champion, to make progress on the determination of the polonium speciation. However, we plan at her initiative not to stay stuck with "blind" experiments, but also to perform the first spectroscopy experiments devoted to polonium species, in collaboration with C. den Auwer (ICN laboratory, Nice). In this context, I also plan to perform calculations related to the EXAFS study of polonium species, naturally geometry and electronic structure calculations, but not exclusively. In particular, I would like to compute the X-ray absorption near edge structure (XANES) part of the spectrum with *ab initio* calculations. For this, I would like to collaborate with specialists of such types of calculations, although I have not yet taken any contact since I decided at the beginning to wait for enough experimental progress before starting to work on this.

5.4 Chemical bonding analysis

In the field of chemical bonding analysis, I first propose to trigger some progress on two main aspects, in particular on the definition of rules of thumb for defining EBOs in polynuclear systems (even when no symmetry element is of help –C_1 symmetry point group–) and on the develpment of a "VBSOCI" method. Also, I plan to lead a significant study on the chemical bonding of a wide range of heavy-element systems, with the aim of establishing general rules concerning the role and importance of the SOC on chemical bonding and on molecular properties, as previously mentioned.

Naturally, it is vain to make an extensive list of systems when describing a project, but the idea will be to tackle a wide range of situations in terms of the electronic structures of both the fragments and of the bound systems, different enough for safely deriving general rules.

To properly define the EBO between two atoms A and B of polynuclear systems (of course with more than two atoms, to go further than what was aleary reported in Chapter 4), one must ensure quite some requirements, (i) that a subset of the active orbitals do not delocalize too much on other atoms of the molecule, (ii) that a reasonable separation of the σ, π, *etc.* characters is done, and (iii) that net bonding and antibonding characters are obtained for the orbitals of interest. For (ii), a simple rule may do the job: if one chooses the coordinate frame in such a way that the z Cartesian axis corresponds to the A–B axis, the separation between the σ and π orbitals can be done based on the basis functions (*e.g.* s and p_Z for σ, p_X and p_Y for π, *etc.*). Furthermore, for (iii) one can make use of the "most B/AB orbitals" of Chapter 4. Therefore, the only main difficulty comes from (i). For this, I propose to perform exploratory trials for finding ways to "pair localize" a subset of the active orbitals, for instance by first localizing the orbitals and then allowing the orbitals localized on A and B to mutually delocalize. However, it is not guaranteed that any proper rule will be easy to be put in practice. Anyway, I also propose to define proper EBOs in polynuclear molecules with adequate symmetries (*e.g.* $AtCH_3$, which belongs to the C_{3v} symmetry point group), for which less ambiguity is expected. Thus, I plan to lead the generation of further robust EBO data, for comparison with indicators coming from other perspectives (for instance based on quantum chemical topology), in view of obtaining a database of various bond indicators for various systems.

CS bonding may occur for instance in At_2. As previously mentioned, I have shown that the SOC largely affects its ground-state wave function, mainly by coupling the $[...]\sigma^2\pi^4\pi^{*4}$ ground configuration to the $[...]\sigma^2\pi^3\pi^{*4}\sigma^{*1}$ one. If one omits the π system for the sake of simplicity, the σ system of this excited configuration, characterized by the $\sigma^2\sigma^{*1}$ electronic configuration, corresponds to the prototype of a two-center/three-electron σ half-bond [249]; thus, the SOC must enhance the charge fluctuation in the ground-state wave function of At_2, as B. Braïda (LCT laboratory, Paris) pointed out to me. In order to know if we should rather classify this system as a covalent or a CS one after the inclusion of the SOC, methodological development is required for introducing the SOC into a VB code. I am aware that I do not have the knowledge to lead this methodological development by myself, and thus, I have taken some contacts to ensure the feasibility of the project. Therefore, I have discussed with B. Braïda (LCT laboratory) and Z. Chen (Xiamen University, Xiamen, China) of the possibility of implmenting a "VBSOCI" approach in the XMVB code [250]. When this approach will be implemented, I expect to be able to unambiguously determine the CS character of chemical bonds of heavy-element systems, in particular in the case of species of radioelements for which little information can be experimentally obtained, *e.g.* in the case of a (new) polonium species.

5.5 Epilogue

In my ten years of research, I think that I have shown several times that I am capable of performing or leading original research, based on the quantum study of stationary states, in quite distinct fields. I believe that the life of a scientist, which consists in regularly learning and understanding new things and tackling new problems, requires quite some independence for being interesting, which is unfortunately not always fully compatible with the current game of building a successful scientific career in academia. In this context, I hope that obtaining the *Habilitation à diriger des recherches* qualification will allow me to become more visible as an independent scientist in the French community. Also, with this qualification in my portfolio, I plan to continue performing and leading original research, notably via the full guidance of PhD students. Hopefully, I will eventually manage to obtain funding on my own name, which is still probably one of the most lacking arguments in my curriculum vitae.

References

[1] P. Pyykkö. Relativistic effects in chemistry: More common than you thought. *Annu. Rev. Phys. Chem.* **63**, 45–64 (2012).

[2] R. Ahuja, A. Blomqvist, P. Larsson, P. Pyykkö, and P. Zaleski-Ejgierd. Relativity and the lead-acid battery. *Phys. Rev. Lett.* **106**, 018301 (2011).

[3] K. G. Dyall and K. Faegri Jr. *Introduction to relativistic quantum chemistry.* Oxford University Press, New York (2007).

[4] K. Glantschnig and C. Ambrosch-Draxl. Relativistic effects on the linear optical properties of Au, Pt, Pb and W. *New J. Phys.* **12**, 103048 (2010).

[5] J. N. Harvey. Understanding the kinetics of spin-forbidden chemical reactions. *Phys. Chem. Chem. Phys.* **9**, 331–343 (2007).

[6] R. Boča. Zero-field splitting in metal complexes. *Coord. Chem. Rev.* **248**, 757–815 (2004).

[7] R. Maurice, C. de Graaf, and N. Guihéry. Theoretical determination of spin hamiltonians with isotropic and anisotropic magnetic interactions in transition metal and lanthanide complexes. *Phys. Chem. Chem. Phys.* **15**, 18784–18804 (2013).

[8] R. Maurice, R. Broer, N. Guihéry, and C. de Graaf. *Zero-field splitting in transition metal complexes: Ab initio calculations, effective Hamiltonians, model Hamiltonians, and crystal-Field Models.* In Handbook of Relativistic Quantum Chemistry, Ed. W. Liu, Springer-Verlag Berlin Heidelberg, 765–796 (2017).

[9] D. Teze, D.-C. Sergentu, V. Kalichuk, J. Barbet, D. Deniaud, N. Galland, R. Maurice, and G. Montavon. Targeted radionuclide therapy with astatine-211: Oxidative dehalogenation of astatobenzoate conjugates. *Sci. Rep.* **7**, 2579 (2017).

[10] R. Maurice, F. Réal, A. S. P. Gomes, V. Vallet, G. Montavon, and N. Galland. Effective bond orders from two-step spin-orbit coupling approaches: The I_2, At_2, IO^+, and AtO^+ case studies. *J. Chem. Phys.* **142**, 094305 (2015).

[11] C. Chang, M. Pelissier, and P. Durand. Regular two-component Pauli-like effective Hamiltonians in Dirac theory. *Phys. Scripta* **34**, 394–404 (1986).

[12] J.-L. Heully, I. Lindgren, E. Lindroth, S. Lundqvist, and A.-M. Martensson-Pendrill. Diagonalisation of the Dirac Hamiltonian as a basis for a relativistic many-body procedure. *J. Phys. B* **19**, 2799–2815 (1986).

[13] E. van Lenthe, E. J. Baerends, and J. G. Snijders. Relativistic regular two-component Hamiltonians. *J. Chem. Phys.* **99**, 4597–4610 (1993).

[14] M. Douglas and N. M. Kroll. Quantum electrodynamical corrections to the fine structure of helium. *Ann. Phys.* **82**, 89–155 (1974).

[15] B. A. Hess. Relativistic electronic-structure calculations employing a two-component no-pair formalism with external-field projection operators. *Phys. Rev. A* **33**, 3742–3748 (1986).

[16] G. Jansen and B. A. Hess. Revision of the Douglas-Kroll transformation. *Phys. Rev. A* **39**, 6016–6017 (1989).

[17] M. Iliaš and T. Saue. An infinite-order two-component relativistic hamiltonian by a simple one-step transformation. *J. Chem. Phys.* **126**, 064102 (2007).

[18] W. Liu and D. Peng. Exact two-component Hamiltonians revisited. *J. Chem. Phys.* **131**, 031104 (2009).

[19] W. Kohn and L. J. Sham. Self-consistent equations including exchange and correlation effects. *Phys. Rev.* **140**, A1133–A1138 (1965).

[20] R. McWeeny and Y. Mizuno. The density matrix in many-electron quantum mechanics II. Separation of space and spin variables; spin coupling problems. *Proc. R. Soc. A* **259**, 554–577 (1961).

[21] B. O. Roos and P.-Å. Malmqvist. Relativistic quantum chemistry: the multiconfigurational approach. *Phys. Chem. Chem. Phys.* **6**, 2919–2927 (2004).

[22] P.-Å. Malmqvist, B. O. Roos, and B. Schimmelpfennig. The restricted active space (RAS) state interaction approach with spin-orbit coupling. *Chem. Phys. Lett.* **357**, 230–240 (2002).

[23] D. Ganyushin and F. Neese. First-principles calculations of zero-field splitting parameters. *J. Chem. Phys.* **125**, 024103 (2006).

[24] B. A. Hess, C. M. Marian, U. Wahlgren, and O. Gropen. A mean-field spin-orbit method applicable to correlated wavefunctions. *Chem. Phys. Lett.* **251**, 365–371 (1996).

[25] F. Neese. Efficient and accurate approximations to the molecular spin-orbit coupling operator and their use in molecular g-tensor calculations. *J. Chem. Phys.* **122**, 034107 (2005).

[26] M. Dolg and X. Cao. Relativistic pseudopotentials: Their development and scope of applications. *Chem. Rev.* **112**, 403–480 (2012).

[27] J. C. Slater. A simplification of the Hartree-Fock method. *Phys. Rev.* **81**, 385–390 (1951).

[28] R. McWeeny. On the basis of orbital theories. *Proc. R. Soc. A* **232**, 114–135 (1955).

[29] P.-Å. Malmqvist, A. Rendell, and B. O. Roos. The restricted active space self-consistent-field method, implemented with a split graph unitary group approach. *J. Phys. Chem.* **94**, 5477–5482 (1990).

[30] D. Ma, G. L. Manni, and L. Gagliardi. The generalized active space concept in multiconfigurational self-consistent field methods. *J. Chem. Phys.* **135**, 044128 (2011).

[31] G. Li Manni, D. Ma, F. Aquilante, J. Olsen, and L. Gagliardi. SplitGAS method for strong correlation and the challenging case of Cr_2. *J. Chem. Theory Comput.* **9**, 3375–3384 (2013).

[32] B. O. Roos, P. Linse, P. E. M. Siegbahn, and M. R. A. Blomberg. A simple method for the evaluation of the second-order-perturbation energy from external double-excitations with a CASSCF reference wavefunction. *Chem. Phys.* **66**, 197–207 (1982).

[33] K. Andersson, P.-A. Malmqvist, B. O. Roos, A. J. Sadlej, and K. Wolinski. Second-order perturbation theory with a CASSCF reference function. *J. Phys. Chem.* **94**, 5483–5488 (1990).

[34] K. Andersson, P. Malmqvist, and B. O. Roos. Second-order perturbation theory with a complete active space self-consistent field reference function. *J. Chem. Phys.* **96**, 1218–1226 (1992).

[35] C. Angeli, R. Cimiraglia, S. Evangelisti, T. Leininger, and J.-P. Malrieu. Introduction of n-electron valence states for multireference perturbation theory. *J. Chem. Phys.* **114**, 10252–10264 (2001).

[36] C. Angeli, R. Cimiraglia, and J.-P. Malrieu. N-electron valence state perturbation theory: a fast implementation of the strongly contracted variant. *Chem. Phys. Lett.* **350**, 297–305 (2001).

[37] C. Angeli, R. Cimiraglia, and J.-P. Malrieu. N-electron valence state perturbation theory: A spinless formulation and an efficient implementation of the strongly contracted and of the partially contracted variants. *J. Chem. Phys.* **117**, 9138–9153 (2002).

[38] K. G. Dyall. The choice of a zeroth-order Hamiltonian for second-order perturbation theory with a complete active space self-consistent-field reference function. *J. Chem. Phys.* **102**, 4909–4918 (1995).

[39] J. Miralles, O. Castell, R. Caballol, and J.-P. Malrieu. Specific CI calculation of energy differences: Transition energies and bond energies. *Chem. Phys.* **172**, 33–43 (1993).

[40] J.-P. Malrieu, R. Caballol, C. J. Calzado, C. de Graaf, and N. Guihéry. Magnetic interactions in molecules and highly correlated materials: Physical content, analytical derivation, and rigorous extraction of magnetic Hamiltonians. *Chem. Rev.* **114**, 429–492 (2014).

[41] K. O. *Molecular magnetism.* VCH, New York (1993).

[42] A. B. Pippard. *Magnetoresistance in metals.* Cambridge University Press, Cambridge (1989).

[43] A. Hauser. *Light-induced spin crossover and the high-spin→low-spin relaxation.* In Spin-Crossover in Transition Metal Compounds II, Eds. P. Gütlich and H. A. Goodwin, Springer, Berlin, Heidelberg, 155–198 (2004).

[44] J. Bardeen, L. N. Cooper, and J. R. Schrieffer. Theory of superconductivity. *Phys. Rev.* **108**, 1175–1204 (1957).

[45] C. Ederer and N. A. Spaldin. Magnetoelectrics: A new route to magnetic ferroelectrics. *Nat. Mater.* **3**, 849–851 (2004).

[46] M. N. Leuenberger and D. Loss. Quantum computing in molecular magnets. *Nature* **410**, 789–793 (2001).

[47] D. Gatteschi and R. Sessoli. Quantum tunneling of magnetization and related phenomena in molecular materials. *Angew. Chem. Int. Ed.* **42**, 268–297 (2003).

[48] W. Heisenberg. Zur theorie des ferromagnetismus. *Z. Phys.* **49**, 619–636 (1928).

[49] P. A. M. Dirac. Quantum mechanics of many-electron systems. *Proc. R. Soc. A* **123**, 714–733 (1929).

[50] J. H. Van Vleck. A survey of the theory of ferromagnetism. *Rev. Mod. Phys.* **17**, 27–47 (1945).

[51] F. Neese. ORCA – An ab initio, DFT and semiempirical SCF-MO package, Max-Planck-Institut für Bioanorganische Chemie, Mülheim an der Ruhr.

[52] D. Maynaud and N. Ben Amor, CASDI suite of programs, Toulouse.

[53] I. d. P. R. Moreira and F. Illas. A unified view of the theoretical description of magnetic coupling in molecular chemistry and solid state physics. *Phys. Chem. Chem. Phys.* **8**, 1645–1659 (2006).

[54] I. d. P. R. Moreira, F. Illas, C. J. Calzado, J. F. Sanz, J.-P. Malrieu, N. B. Amor, and D. Maynau. Local character of magnetic coupling in ionic solids. *Phys. Rev. B* **59**, R6593–R6596 (1999).

[55] Z. Barandiarán and L. Seijo. The *ab initio* model potential representation of the crystalline environment. Theoretical study of the local distortion on NaCl:Cu^+. *J. Chem. Phys.* **89**, 5739–5746 (1988).

[56] A.-M. Pradipto, R. Maurice, N. Guihéry, C. de Graaf, and R. Broer. First-principles study of magnetic interactions in cupric oxide. *Phys. Rev. B* **85**, 014409 (2012).

[57] R. Maurice, A.-M. Pradipto, C. de Graaf, and R. Broer. Magnetic interactions in $LiCu_2O_2$: Single-chain versus double-chain models. *Phys. Rev. B* **86**, 024411 (2012).

[58] N. A. Bogdanov, R. Maurice, I. Rousochatzakis, J. van den Brink, and L. Hozoi. Magnetic state of pyrochlore $Cd_2Os_2O_7$ emerging from strong competition of ligand distortions and longer-range crystalline anisotropy. *Phys. Rev. Lett.* **110**, 127206 (2013).

[59] R. McWeeny. On the origin of spin-Hamiltonian parameters. *J. Chem. Phys.* **42**, 1717–1725 (1965).

[60] F. Neese and E. I. Solomon. Calculation of zero-field splittings, g-values, and the relativistic nephelauxetic effect in transition metal complexes. Application to high-spin ferric complexes. *Inorg. Chem.* **37**, 6568–6582 (1998).

[61] M. R. Pederson and S. N. Khanna. Magnetic anisotropy barrier for spin tunneling in $Mn_{12}O_{12}$ molecules. *Phys. Rev. B* **60**, 9566–9572 (1999).

[62] F. Aquino and J. H. Rodriguez. First-principle computation of zero-field splittings: Application to a high valent Fe(IV)-oxo model of nonheme iron proteins. *J. Chem. Phys.* **123**, 204902 (2005).

[63] F. Neese. Importance of direct spin-spin coupling and spin-flip excitations for the zero-field splittings of transition metal complexes: A case study. *J. Am. Chem. Soc.* **128**, 10213–10222 (2006).

[64] F. Neese. Calculation of the zero-field splitting tensor on the basis of hybrid density functional and Hartree-Fock theory. *J. Chem. Phys.* **127**, 164112 (2007).

[65] S. Schmitt, P. Jost, and C. van Wüllen. Zero-field splittings from density functional calculations: Analysis and improvement of known methods. *J. Chem. Phys.* **134**, 194113 (2011).

[66] A. Kubica, J. Kowalewski, D. Kruk, and M. Odelius. Zero-field splitting in nickel(II) complexes: A comparison of DFT and multi-configurational wavefunction calculations. *J. Chem. Phys.* **138**, 064304 (2013).

[67] S. Zein and F. Neese. Ab initio and coupled-perturbed density functional theory estimation of zero-field splittings in Mn^{II} transition metal complexes. *J. Phys. Chem. A* **112**, 7976–7983 (2008).

[68] C. Duboc, D. Ganyushin, K. Sivalingam, M.-N. Collomb, and F. Neese. Systematic theoretical study of the zero-field splitting in coordination complexes of Mn(III). Density functional theory versus multireference wave function approaches. *J. Phys. Chem. A* **114**, 10750–10758 (2010).

[69] R. Maurice, R. Bastardis, C. d. Graaf, N. Suaud, T. Mallah, and N. Guihéry. Universal theoretical approach to extract anisotropic spin Hamiltonians. *J. Chem. Theory Comput.* **5**, 2977–2984 (2009).

[70] M. Atanasov, D. Ganyushin, D. A. Pantazis, K. Sivalingam, and F. Neese. Detailed ab initio first-principles study of the magnetic anisotropy in a family of trigonal pyramidal iron(II) pyrrolide complexes. *Inorg. Chem.* **50**, 7460–7477 (2011).

[71] R. Maurice, K. Sivalingam, D. Ganyushin, N. Guihéry, C. de Graaf, and F. Neese. Theoretical determination of the zero-field splitting in copper acetate monohydrate. *Inorg. Chem.* **50**, 6229–6236 (2011).

[72] R. Maurice, L. Vendier, and J.-P. Costes. Magnetic anisotropy in Ni^{II}–Y^{III} binuclear complexes: On the importance of both the first coordination sphere of the Ni^{II} ion and the Y^{III} ion belonging to the second coordination sphere. *Inorg. Chem.* **50**, 11075–11081 (2011).

[73] J.-P. Costes, R. Maurice, and L. Vendier. Pentacoordinate Ni^{II} complexes: Preparation, magnetic measurements, and *ab initio* calculations of the magnetic anisotropy terms. *Chem. Eur. J.* **18**, 4031–4040 (2012).

[74] S. Gomez-Coca, E. Cremades, N. Aliaga-Alcalde, and E. Ruiz. Mononuclear single-molecule magnets: Tailoring the magnetic anisotropy of first-row transition-metal complexes. *J. Am. Chem. Soc.* **135**, 7010–7018 (2013).

[75] R. Ruamps, L. J. Batchelor, R. Maurice, N. Gogoi, P. Jiménez-Lozano, N. Guihéry, C. de Graaf, A.-L. Barra, J.-P. Sutter, and T. Mallah. Origin of the magnetic anisotropy in heptacoordinate Ni^{II} and Co^{II} complexes. *Chem. Eur. J.* **19**, 950–956 (2013).

[76] R. Ruamps, R. Maurice, L. Batchelor, M. Boggio-Pasqua, R. Guillot, A. L. Barra, J. Liu, E.-E. Bendeif, S. Pillet, S. Hill, T. Mallah, and N. Guihéry. Giant Ising-type magnetic anisotropy in trigonal bipyramidal Ni(II) complexes: Experiment and theory. *J. Am. Chem. Soc.* **135**, 3017–3026 (2013).

[77] C. Teichteil, M. Pélissier, and F. Spiegelmann. Ab initio molecular calculations including spin-orbit coupling. I. Method and atomic tests. *Chem. Phys.* **81**, 273–282 (1983).

[78] R. Llusar, M. Casarrubios, Z. Barandiarán, and L. Seijo. *Ab initio* model potential calculations on the electronic spectrum of Ni^{2+}-doped MgO including correlation, spin-orbit and embedding effects. *J. Chem. Phys.* **105**, 5321–5330 (1996).

[79] L. F. Chibotaru and L. Ungur. *Ab initio* calculation of anisotropic magnetic properties of complexes. I. Unique definition of pseudospin Hamiltonians and their derivation. *J. Chem. Phys.* **137**, 064112 (2012).

[80] F. Aquilante, L. De Vico, N. Ferré, G. Ghigo, P.-Å. Malmqvist, P. Neogrády, T. B. Pedersen, M. Pitoňák, M. Reiher, B. O. Roos, L. Serrano-Andrés, M. Urban, V. Veryazov, and R. Lindh. MOLCAS 7: The next generation. *J. Comput. Chem.* **31**, 224–247 (2010).

[81] C. Bloch. Sur la théorie des perturbations des états liés. *Nucl. Phys.* **6**, 329–347 (1958).

[82] J. des Cloizeaux. Extension d'une formule de Lagrange à des problèmes de valeurs propres. *Nuclear Physics* **20**, 321–346 (1960).

[83] J. S. Griffith. *The theory of transition metal ions.* Cambridge University Press, Cambridge (1961).

[84] A. Abragam and B. Bleaney. *Electron paramagnetic resonance of transition ions.* Dover Publications, New York (1986).

[85] G. Rogez, J.-N. Rebilly, A.-L. Barra, L. Sorace, G. Blondin, N. Kirchner, M. Duran, J. van Slageren, S. Parsons, L. Ricard, A. Marvilliers, and T. Mallah. Very large Ising-type magnetic anisotropy in a mononuclear Ni^{II} complex. *Angew. Chem. Int. Ed.* **44**, 1876–1879 (2005).

[86] J.-N. Rebilly, G. Charron, E. Rivière, R. Guillot, A.-L. Barra, M. Serrano, J. van Slageren, and T. Mallah. Large magnetic anisotropy in pentacoordinate Ni^{II} complexes. *Chem. Eur. J.* **14**, 1169–1177 (2008).

[87] J. Krzystek, S. A. Zvyagin, A. Ozarowski, A. T. Fiedler, T. C. Brunold, and J. Telser. Definitive spectroscopic determination of zero-field splitting in high-spin cobalt(II). *J. Am. Chem. Soc.* **126**, 2148–2155 (2004).

[88] C. de Graaf and C. Sousa. Assessing the zero-field splitting in magnetic molecules by wave function-based methods. *Int. J. Quantum Chem.* **106**, 2470–2478 (2006).

[89] K. W. H. Stevens. Matrix elements and operator equivalents connected with the magnetic properties of rare earth ions. *Proc. Phys. Soc. A* **65**, 209–215 (1952).

[90] S. A. Altshuler and B. M. Kozyrev. *Electron paramagnetic resonance in compounds of transition elements.* John Wiley and Sons, New York (1976).

[91] C. Rudowicz and C. Y. Chung. The generalization of the extended Stevens operators to higher ranks and spins, and a systematic review of the tables of the tensor operators and their matrix elements. *J. Phys.: Condens. Matter* **16**, 5825–5847 (2004).

[92] R. Maurice, C. de Graaf, and N. Guihéry. Magnetostructural relations from a combined ab initio and ligand field analysis for the nonintuitive zero-field splitting in Mn(III) complexes. *J. Chem. Phys.* **133**, 084307 (2010).

[93] L. J. Batchelor, M. Sangalli, R. Guillot, N. Guihéry, R. Maurice, F. Tuna, and T. Mallah. Pentanuclear cyanide-bridged complexes based on highly anisotropic Co^{II} seven-coordinate building blocks: Synthesis, structure, and magnetic behavior. *Inorg. Chem.* **50**, 12045–12052 (2011).

[94] B. Cahier, R. Maurice, H. Bolvin, T. Mallah, and N. Guihéry. Tools for predicting the nature and magnitude of magnetic anisotropy in transition metal complexes: Application to Co(II) complexes. *Magnetochemistry* **2**, 31 (2016).

[95] R. Maurice, P. Verma, J. M. Zadrozny, S. Luo, J. Borycz, J. R. Long, D. G. Truhlar, and L. Gagliardi. Single-ion magnetic anisotropy and isotropic magnetic couplings in the metal-organic framework Fe_2(dobdc). *Inorg. Chem.* **52**, 9379–9389 (2013).

[96] P. Verma, R. Maurice, and D. G. Truhlar. Adsorbate-induced changes in magnetic interactions in Fe_2(dobdc) with adsorbed hydrocarbon molecules. *J. Phys. Chem. C* **120**, 9933–9948 (2016).

[97] S. P. Webb and M. S. Gordon. The effect of spin-orbit coupling on the magnetic properties of $H_2Ti(\mu\text{–}H)_2TiH_2$. *J. Chem. Phys.* **109**, 919–927 (1998).

[98] E. Liviotti, S. Carretta, and G. Amoretti. S-mixing contributions to the high-order anisotropy terms in the effective spin Hamiltonian for magnetic clusters. *J. Chem. Phys.* **117**, 3361–3368 (2002).

[99] S. Carretta, E. Liviotti, N. Magnani, P. Santini, and G. Amoretti. S mixing and quantum tunneling of the magnetization in molecular nanomagnets. *Phys. Rev. Lett.* **92**, 207205 (2004).

[100] R. Maurice, A. M. Pradipto, N. Guihéry, R. Broer, and C. de Graaf. Antisymmetric magnetic interactions in oxo-bridged copper(II) bimetallic systems. *J. Chem. Theory Comput.* **6**, 3092–3101 (2010).

[101] R. Maurice, N. Guihéry, R. Bastardis, and C. de Graaf. Rigorous extraction of the anisotropic multispin Hamiltonian in bimetallic complexes from the exact electronic Hamiltonian. *J. Chem. Theory Comput.* **6**, 55–65 (2010).

[102] R. Maurice, C. de Graaf, and N. Guihéry. Magnetic anisotropy in binuclear complexes in the weak-exchange limit: From the multispin to the giant-spin Hamiltonian. *Phys. Rev. B* **81**, 214427 (2010).

[103] R. Boča. *Theoretical foundations of molecular magnetism.* Elsevier, Amsterdam (1999).

[104] J. Kortus, T. Baruah, N. Bernstein, and M. R. Pederson. Magnetic ordering, electronic structure, and magnetic anisotropy energy in the high-spin Mn_{10} single molecule magnet. *Phys. Rev. B* **66**, 092403 (2002).

[105] T. Baruah and M. R. Pederson. Density functional study of the conformers of Co_4-based single-molecule magnet. *Int. J. Quant. Chem.* **93**(5), 324–331 (2003).

[106] J. Kortus, M. R. Pederson, T. Baruah, N. Bernstein, and C. Hellberg. Density functional studies of single molecule magnets. *Polyhedron* **22**, 1871–1876 (2003).

[107] K. Park, M. R. Pederson, and C. S. Hellberg. Properties of low-lying excited manifolds in Mn_{12} acetate. *Phys. Rev. B* **69**, 014416 (2004).

[108] J. Ribas-Arino, T. Baruah, and M. R. Pederson. Density-functional study of two Fe_4-based single-molecule magnets. *J. Chem. Phys.* **123**, 044303 (2005).

[109] J. Ribas-Arino, T. Baruah, and M. R. Pederson. Toward the control of the magnetic anisotropy of Fe^{II} cubes: A DFT study. *J. Am. Chem. Soc.* **128**, 9497–9505 (2006).

[110] E. Ruiz, J. Cirera, J. Cano, S. Alvarez, C. Loose, and J. Kortus. Can large magnetic anisotropy and high spin really coexist? *Chem. Commun.* , 52–54 (2008).

[111] M. Moragues-Cánovas, M. Helliwell, L. Ricard, E. Rivière, W. Wernsdorfer, E. Brechin, and T. Mallah. An Ni_4 single-molecule magnet: Synthesis, structure and low-temperature magnetic behavior. *Eur. J. Inorg. Chem.* **2004**, 2219–2222 (2004).

[112] R. Ruamps, R. Maurice, C. de Graaf, and N. Guihéry. Interplay between local anisotropies in binuclear complexes. *Inorg. Chem.* **53**, 4508–4516 (2014).

[113] N. Guihéry, R. Ruamps, R. Maurice, and C. de Graaf. Synergy and destructive interferences between local magnetic anisotropies in binuclear complexes. *AIP Conf. Proc.* **1702**, 090015 (2015).

[114] R. Herchel, R. Boča, J. Krzystek, A. Ozarowski, M. Durán, and J. van Slageren. Definitive determination of zero-field splitting and exchange interactions in a Ni(II) dimer: Investigation of $[Ni_2(en)_4Cl_2]Cl_2$ using magnetization and tunable-frequency high-field electron paramagnetic resonance. *J. Am. Chem. Soc.* **129**, 10306–10307 (2007).

[115] P. W. Anderson. Antiferromagnetism. Theory of superexchange interaction. *Phys. Rev.* **79**, 350–356 (1950).

[116] P. W. Anderson. New approach to the theory of superexchange interactions. *Phys. Rev.* **115**, 2–13 (1959).

[117] P. W. Anderson. *Theory of magnetic exchange interactions: Exchange in insulators and semiconductors.* In Solid State Physics, Eds. F. Seitz and D. Turnbull, Academic Press, New York and London, 99–214 (1963).

[118] C. J. Calzado, J. Cabrero, J.-P. Malrieu, and R. Caballol. Analysis of the magnetic coupling in binuclear complexes. I. Physics of the coupling. *J. Chem. Phys.* **116**, 2728–2747 (2002).

[119] C. J. Calzado, J. Cabrero, J.-P. Malrieu, and R. Caballol. Analysis of the magnetic coupling in binuclear complexes. II. Derivation of valence effective Hamiltonians from *ab initio* CI and DFT calculations. *J. Chem. Phys.* **116**, 3985–4000 (2002).

[120] C. J. Calzado, C. Angeli, D. Taratiel, R. Caballol, and J.-P. Malrieu. Analysis of the magnetic coupling in binuclear systems. III. The role of the ligand to metal charge transfer excitations revisited. *J. Chem. Phys.* **131**, 044327 (2009).

[121] R. Bastardis, N. Guihéry, and C. de Graaf. Isotropic non-Heisenberg terms in the magnetic coupling of transition metal complexes. *J. Chem. Phys.* **129**, 104102 (2008).

[122] R. Bastardis, N. Guihéry, and C. de Graaf. Microscopic origin of isotropic non-Heisenberg behavior in $S = 1$ magnetic systems. *Phys. Rev. B* **76**, 132412 (2007).

[123] N. Suaud, R. Ruamps, N. Guihéry, and J.-P. Malrieu. A strategy to determine appropriate active orbitals and accurate magnetic couplings in organic magnetic systems. *J. Chem. Theory Comput.* **8**, 4127–4137 (2012).

[124] R. Maurice, E. Renault, Y. Gong, P. X. Rutkowski, and J. K. Gibson. Synthesis and structures of plutonyl nitrate complexes: Is plutonium heptavalent in $PuO_3(NO_3)_2^-$? *Inorg. Chem.* **54**, 2367–2373 (2015).

[125] P. Verma, R. Maurice, and D. G. Truhlar. Identifying the interactions that allow separation of O_2 from N_2 on the open iron sites of Fe_2(dobdc). *J. Phys. Chem. C* **119**, 28499–28511 (2015).

[126] S. J. Tereniak, R. K. Carlson, L. J. Clouston, V. G. Young, E. Bill, R. Maurice, Y.-S. Chen, H. J. Kim, L. Gagliardi, and C. C. Lu. Role of the metal in the bonding and properties of bimetallic complexes involving manganese, iron, and cobalt. *J. Am. Chem. Soc.* **136**, 1842–1855 (2014).

[127] A. D. Buckingham, P. Pyykkö, J. B. Robert, and L. Wiesenfeld. Symmetry rules for the indirect nuclear spin-spin coupling tensor revisited. *Mol. Phys.* **46**, 177–182 (1982).

[128] B. C. Guha. Magnetic properties of some paramagnetic crystals at low temperatures. *Proc. R. Soc. A* **206**, 353–373 (1951).

[129] B. Bleaney and K. D. Bowers. Anomalous paramagnetism of copper acetate. *Proc. R. Soc. A* **214**, 451–465 (1952).

[130] A. Ozarowski. The zero-field-splitting parameter D in binuclear copper(II) carboxylates is negative. *Inorg. Chem.* **47**, 9760–9762 (2008).

[131] I. Dzyaloshinsky. A thermodynamic theory of weak ferromagnetism of antiferromagnetics. *J. Phys. Chem. Solids* **4**, 241–255 (1958).

[132] T. Moriya. Anisotropic superexchange interaction and weak ferromagnetism. *Phys. Rev.* **120**, 91–98 (1960).

[133] A. S. Moskvin. Dzyaloshinsky-Moriya antisymmetric exchange coupling in cuprates: Oxygen effects. *J. Exp. Th. Phys.* **104**, 913–927 (2007).

[134] M. Atanasov, P. Comba, G. R. Hanson, S. Hausberg, S. Helmle, and H. Wadepohl. Cyano-bridged homodinuclear copper(II) complexes. *Inorg. Chem.* **50**, 6890–6901 (2011).

[135] A. P. Ginsberg, R. L. Martin, R. W. Brookes, and R. C. Sherwood. Magnetic exchange in transition metal complexes. IX. Dimeric nickel(II)-ethylenediamine complexes. *Inorg. Chem.* **11**, 2884–2889 (1972).

[136] Y. Journaux, O. Kahn, B. Chevalier, J. Etourneau, R. Claude, and A. Dworkin. Evidence for a low temperature phase transition in DI-μ-chloro-tetrakis (ethylene diamine) dinickel(II) chloride. *Chem. Phys. Lett.* **55**, 140–143 (1978).

[137] K. O. Joung, C. J. O'Connor, E. Sinn, and R. L. Carlin. Structural and magnetic properties of dimeric $[Ni_2(en)_4Cl_2]Cl_2$. *Inorg. Chem.* **18**, 804–808 (1979).

[138] M. Retegan, N. Cox, D. A. Pantazis, and F. Neese. A first-principles approach to the calculation of the on-site zero-field splitting in polynuclear transition metal complexes. *Inorg. Chem.* **53**, 11785–11793 (2014).

[139] J. F. Nye. *Physical properties of crystals.* Clarendon Press, Oxford (1985).

[140] J. Telser, A. Ozarowski, and J. Krzystek. *High-frequency and -field electron paramagnetic resonance of transition metal ion (d block) coordination complexes.* In Electron Paramagnetic Resonance: Volume 23, Eds. B. C. Gilbert, D. M. Murphy and V. Chechik, The Royal Society of Chemistry, Cambridge, 209–263 (2013).

[141] G. Juhász, R. Matsuda, S. Kanegawa, K. Inoue, O. Sato, and K. Yoshizawa. Bistability of magnetization without spin-transition in a high-spin cobalt(II) complex due to angular momentum quenching. *J. Am. Chem. Soc.* **131**, 4560–4561 (2009).

[142] N. Ishikawa, M. Sugita, and W. Wernsdorfer. Quantum tunneling of magnetization in lanthanide single-molecule magnets: Bis(phthalocyaninato)terbium and bis(phthalocyaninato)dysprosium anions. *Angew. Chem. Int. Ed.* **44**, 2931–2935 (2005).

[143] M.-D. Droin-Oger. *La thérie des orbitales moléculaires et l'émergence de la chimie quantique.* PhD thesis (2003).

[144] P.-O. Löwdin. Nature of quantum chemistry. *Int. J. Quantum Chem.* **1**, 7–12 (1967).

[145] C. C. L. Pereira, R. Maurice, A. F. Lucena, S. Hu, A. P. Gonçalves, J. Marçalo, J. K. Gibson, L. Andrews, and L. Gagliardi. Thorium and uranium carbide cluster cations in the gas phase: Similarities and differences between thorium and uranium. *Inorg. Chem.* **52**, 10968–10975 (2013).

[146] M. J. Polinski, E. B. Garner, R. Maurice, N. Planas, J. T. Stritzinger, T. G. Parker, J. N. Cross, T. D. Green, E. V. Alekseev, S. M. V. Cleve, W. Depmeier, L. Gagliardi, M. Shatruk, K. L. Knappenberger, G. Liu, S. Skanthakumar, L. Soderholm, D. A. Dixon, and T. E. Albrecht-Schmitt. Unusual structure, bonding and properties in a californium borate. *Nat. Chem.* **6**, 387–392 (2014).

[147] D. S. Wilbur. Enigmatic astatine. *Nat. Chem.* **5**, 246 (2013).

[148] J. Champion, M. Seydou, A. Sabatié-Gogova, E. Renault, G. Montavon, and N. Galland. Assessment of an effective quasirelativistic methodology designed to study astatine chemistry in aqueous solution. *Phys. Chem. Chem. Phys.* **13**, 14984–14992 (2011).

[149] M. Valiev, E. J. Bylaska, N. Govind, K. Kowalski, T. P. Straatsma, H. J. J. Van Dam, D. Wang, J. Nieplocha, E. Apra, T. L. Windus, and W. A. de Jong. NWChem: A comprehensive and scalable open-source solution for large scale molecular simulations. *Comput. Phys. Commun.* **181**, 1477–1489 (2010).

[150] V. Barone, M. Cossi, and J. Tomasi. A new definition of cavities for the computation of solvation free energies by the polarizable continuum model. *J. Chem. Phys.* **107**, 3210–3221 (1997).

[151] M. Cossi, N. Rega, G. Scalmani, and V. Barone. Energies, structures, and electronic properties of molecules in solution with the C-PCM solvation model. *J. Comput. Chem.* **24**, 669–681 (2003).

[152] J. Champion, C. Alliot, E. Renault, B. M. Mokili, M. Chérel, N. Galland, and G. Montavon. Astatine standard redox potentials and speciation in acidic medium. *J. Phys. Chem. A* **114**, 576–582 (2010).

[153] J. Champion, A. Sabatié-Gogova, F. Bassal, T. Ayed, C. Alliot, N. Galland, and G. Montavon. Investigation of astatine(III) hydrolyzed species: Experiments and relativistic calculations. *J. Phys. Chem. A* **117**, 1983–1990 (2013).

[154] N. Guo, D.-C. Sergentu, D. Teze, J. Champion, G. Montavon, N. Galland, and R. Maurice. The heaviest possible ternary trihalogen species, $IAtBr^-$, evidenced in aqueous solution: An experimental performance driven by computations. *Angew. Chem. Int. Ed.* **55**, 15369–15372 (2016).

[155] N. Guo, R. Maurice, D. Teze, J. Graton, J. Champion, G. Montavon, and N. Galland. Experimental and computational evidence of halogen bonds involving astatine. *Nat. Chem.* **10**, 428–434 (2018).

[156] D.-C. Sergentu, M. Amaouch, J. Pilmé, N. Galland, and R. Maurice. Electronic structures and geometries of the XF_3 (X = Cl, Br, I, At) fluorides. *J. Chem. Phys.* **143**, 114306 (2015).

[157] D.-C. Sergentu, F. Réal, G. Montavon, N. Galland, and R. Maurice. Unraveling the hydration-induced ground-state change of AtO^+ by relativistic and multiconfigurational wave-function-based methods. *Phys. Chem. Chem. Phys.* **18**, 32703–32712 (2016).

[158] I. Denden, F. Poineau, M. L. Schlegel, J. Roques, P. L. Solari, G. Blain, K. R. Czerwinski, R. Essehli, J. Barbet, and M. Fattahi. Behavior of heptavalent technetium in sulfuric acid under α-irradiation: Structural determination of technetium sulfate complexes by X-ray ab-

sorption spectroscopy and first principles calculations. *J. Phys. Chem. A* **118**, 1568–1575 (2014).

[159] M. Ferrier, J. Roques, F. Poineau, A. P. Sattelberger, J. Unger, Czerwinski, and K. R. Speciation of technetium in sulfuric acid/hydrogen sulfide solutions. *Eur. J. Inorg. Chem.* **2014**, 2046–2052 (2014).

[160] L. Visscher and K. G. Dyall. Relativistic and correlation effects on molecular properties. I. the dihalogens F_2, Cl_2, Br_2, I_2, and At_2. *J. Chem. Phys.* **104**, 9040–9046 (1996).

[161] S. Höfener, R. Ahlrichs, S. Knecht, and L. Visscher. Relativistic and non-relativistic electronic molecular-structure calculations for dimers of 4p-, 5p-, and 6p-block elements. *ChemPhysChem* **13**, 3952–3957 (2012).

[162] J. Pilmé, E. Renault, T. Ayed, G. Montavon, and N. Galland. Introducing the ELF topological analysis in the field of quasirelativistic quantum calculations. *J. Chem. Theory Comput.* **8**, 2985–2990 (2012).

[163] J. G. Hill and X. Hu. Theoretical insights into the nature of halogen bonding in prereactive complexes. *Chem. Eur. J.* **19**, 3620–3628 (2013).

[164] J. Pilmé, E. Renault, F. Bassal, M. Amaouch, G. Montavon, and N. Galland. QTAIM analysis in the context of quasirelativistic quantum calculations. *J. Chem. Theory Comput.* **10**, 4830–4841 (2014).

[165] N. Galland, G. Montavon, J.-Y. Le Questel, and J. Graton. Quantum calculations of At-mediated halogen bonds: on the influence of relativistic effects. *New J. Chem.* **42**, Advance Article, DOI: 10.1039/C8NJ00484F (2018).

[166] E. H. Appelman, E. N. Sloth, and M. H. Studier. Observation of astatine compounds by time-of-flight mass spectrometry. *Inorg. Chem.* **5**, 766–769 (1966).

[167] R. Ludwig, S. Fischer, H. Hussein, M. Frind, and R. Dreyer. Stability constants of At(I)-complexes with thiourea, iodide and mixed ligands in ethanol and water. *J. Radioanal. Nucl. Chem.* **134**, 141–149 (1989).

[168] P. J. Stephens, F. J. Devlin, C. F. Chabalowski, and M. J. Frisch. *Ab initio* calculation of vibrational absorption and circular dichroism spectra using density functional force fields. *J. Phys. Chem.* **98**, 11623–11627 (1994).

[169] K. R. Loos and A. C. Jones. Structure of triiodide ion in solution. Raman evidence for the existence of higher polyiodide species. *J. Phys. Chem.* **78**, 2306–2307 (1974).

[170] B. Braïda and P. C. Hiberty. Application of the valence bond mixing configuration diagrams to hypervalency in trihalide anions: A challenge to the Rundle–Pimentel model. *J. Phys. Chem. A* **112**, 13045–13052 (2008).

[171] B. Braïda and P. C. Hiberty. What makes the trifluoride anion F_3^- so special? A breathing-orbital valence bond ab initio study. *J. Am. Chem. Soc.* **126**, 14890–14898 (2004).

[172] G. Cavallo, P. Metrangolo, R. Milani, T. Pilati, A. Priimagi, G. Resnati, and G. Terraneo. The halogen bond. *Chem. Rev.* **116**, 2478–2601 (2016).

[173] C. Laurence, J. Graton, M. Berthelot, and M. J. El Ghomari. The diiodine basicity scale: Toward a general halogen-bond basicity scale. *Chem. Eur. J.* **17**, 10431–10444 (2011).

[174] Y. Zhao and D. G. Truhlar. Design of density functionals that are broadly accurate for thermochemistry, thermochemical kinetics, and nonbonded interactions. *J. Phys. Chem. A* **109**, 5656–5667 (2005).

[175] D. F. Smith. The microwave spectrum and structure of chlorine trifluoride. *J. Chem. Phys.* **21**, 609–614 (1953).

[176] H. S. P. Muller. The rotational spectrum of chlorine trifluoride, ClF_3. Centrifugal distortion analysis, Cl nuclear magnetic shielding tensor, structure, and the harmonic force field. *Phys. Chem. Chem. Phys.* **3**, 1570–1575 (2001).

[177] D. W. Magnuson. Microwave spectrum and molecular structure of bromine trifluoride. *J. Chem. Phys.* **27**, 223–226 (1957).

[178] S. Hoyer and K. Seppelt. The structure of IF_3. *Angew. Chem. Int. Ed.* **39**, 1448–1449 (2000).

[179] P. Schwerdtfeger. Second-order Jahn–Teller distortions in group 17 fluorides EF_3 (E = Cl, Br, I, and At). Large relativistic bond angle changes in AtF_3. *J. Chem. Phys.* **100**, 2968–2973 (1996).

[180] C. Bae, Y.-K. Han, and Y. S. Lee. Spin–orbit and relativistic effects on structures and stabilities of group 17 fluorides EF_3 (E = I, At, and element 117): Relativity induced stability for the D_{3h} structure of $(117)F_3$. *J. Phys. Chem. A* **107**, 852–858 (2003).

[181] H. Kim, Y. J. Choi, and Y. S. Lee. Spin–orbit and electron correlation effects on the structure of EF_3 (E = I, At, and element 117). *J. Phys. Chem. B* **112**, 16021–16029 (2008).

[182] D.-D. Yang and F. Wang. Structures and stabilities of group 17 fluorides EF_3 (E = I, At, and element 117) with spin-orbit coupling. *Phys. Chem. Chem. Phys.* **14**, 15816–15825 (2012).

[183] J. P. Perdew, M. Ernzerhof, and K. Burke. Rationale for mixing exact exchange with density functional approximations. *J. Chem. Phys.* **105**, 9982–9985 (1996).

[184] C. Adamo and V. Barone. Toward reliable density functional methods without adjustable parameters: The PBE0 model. *J. Chem. Phys.* **110**, 6158–6170 (1999).

[185] M. Amaouch, D.-C. Sergentu, D. Steinmetz, R. Maurice, N. Galland, and J. Pilmé. The bonding picture in hypervalent XF_3 (X = Cl, Br, I, At) fluorides revisited with quantum chemical topology. *J. Comput. Chem.* **38**, 2753–2762 (2017).

[186] J.-B. Rota, S. Knecht, T. Fleig, D. Ganyushin, T. Saue, F. Neese, and H. Bolvin. Zero field splitting of the chalcogen diatomics using relativistic correlated wave-function methods. *J. Chem. Phys.* **135**, 114106 (2011).

[187] T. Ayed, M. Seydou, F. Réal, G. Montavon, and N. Galland. How does the solvation unveil AtO^+ reactivity? *J. Phys. Chem. B* **117**, 5206–5211 (2013).

[188] T. Ayed, F. Réal, G. Montavon, and N. Galland. Rationalization of the solvation effects on the AtO^+ ground-state change. *J. Phys. Chem. B* **117**, 10589–10595 (2013).

[189] A. S. P. Gomes, F. Réal, N. Galland, C. Angeli, R. Cimiraglia, and V. Vallet. Electronic structure investigation of the evanescent AtO^+ ion. *Phys. Chem. Chem. Phys.* **16**, 9238–9248 (2014).

[190] V. Vallet, L. Maron, C. Teichteil, and J.-P. Flament. A two-step uncontracted determinantal effective Hamiltonian-based SO–CI method. *J. Chem. Phys.* **113**, 1391–1402 (2000).

[191] D.-C. Sergentu, G. David, G. Montavon, R. Maurice, and N. Galland. Scrutinizing "invisible" astatine: A challenge for modern density functionals. *J. Comput. Chem.* **37**, 1345–1354 (2016).

[192] A. S. P. Gomes and L. Visscher. The influence of core correlation on the spectroscopic constants of HAt. *Chem. Phys. Lett.* **399**, 1–6 (2004).

[193] J. Heyd, G. E. Scuseria, and M. Ernzerhof. Hybrid functionals based on a screened Coulomb potential. *J. Chem. Phys.* **118**, 8207–8215 (2003).

[194] D. A. Pantazis, X.-Y. Chen, C. R. Landis, and F. Neese. All-electron scalar relativistic basis sets for third-row transition metal atoms. *J. Chem. Theory Comput.* **4**, 908–919 (2008).

[195] D. A. Pantazis and F. Neese. All-electron scalar relativistic basis sets for the 6p elements. *Theor. Chem. Acc.* **131**, 1292 (2012).

[196] B. O. Roos, R. Lindh, P.-Å. Malmqvist, V. Veryazov, and P.-O. Widmark. Main group atoms and dimers studied with a new relativistic ANO basis set. *J. Phys. Chem. A* **108**, 2851–2858 (2004).

[197] A. Ikeda-Ohno, C. Hennig, S. Tsushima, A. C. Scheinost, G. Bernhard, and T. Yaita. Speciation and structural study of U(IV) and -(VI) in perchloric and nitric acid solutions. *Inorg. Chem.* **48**, 7201–7210 (2009).

[198] G. S. Groenewold, J. Oomens, W. A. de Jong, G. L. Gresham, M. E. McIlwain, and M. J. Van Stipdonk. Vibrational spectroscopy of anionic nitrate complexes of UO_2^{2+} and Eu^{3+} isolated in the gas phase. *Phys. Chem. Chem. Phys.* **10**, 1192–1202 (2008).

[199] P. D. Dau, R. Maurice, E. Renault, and J. K. Gibson. Heptavalent neptunium in a gas-phase complex: $(Np^{VII}O_3^+)(NO_3^-)_2$. *Inorg. Chem.* **55**, 9830–9837 (2016).

[200] T. Saito, Y. Kitagawa, M. Shoji, Y. Nakanishi, M. Ito, T. Kawakami, M. Okumura, and K. Yamaguchi. Theoretical studies on the structure and effective exchange integral (J_{ab}) of an active site in oxyhemocyanin (oxyHc) by using approximately spin-projected geometry optimization (AP-opt) method. *Chem. Phys. Lett.* **456**, 76–79 (2008).

[201] H. V. Moyer. *Chemical properties of polonium.* In Polonium, Ed. H. V. Moyer, United States Atomic Energy Commission, Oak Ridge, Tenessee, 33–96 (1956).

[202] A. Younes, C. Alliot, B. Mokili, D. Deniaud, G. Montavon, and J. Champion. Solvent extraction of polonium(IV) with tributylphosphate (TBP). *Solvent Extr. Ion Exch.* **35**, 77–90 (2017).

[203] R. Ayala, J. M. Martinez, R. R. Pappalardo, A. Muñoz Paez, and E. S. Marcos. Po(IV) hydration: A quantum chemical study. *J. Phys. Chem. B* **112**, 5416–5422 (2008).

[204] R. Ayala, J. M. Martinez, R. R. Pappalardo, A. Muñoz Paez, and E. S. Marcos. General quantum-mechanical study on the hydrolysis equilibria for a tetravalent aquaion: The extreme case of the Po(IV) in water. *J. Phys. Chem. B* **113**, 487–496 (2009).

[205] I. B. Bersuker. Pseudo-Jahn–Teller effect—A two-state paradigm in formation, deformation, and transformation of molecular systems and solids. *Chem. Rev.* **113**, 1351–1390 (2013).

[206] Y. Zhao and D. G. Truhlar. The M06 suite of density functionals for main group thermochemistry, thermochemical kinetics, noncovalent interactions, excited states, and transition elements: two new functionals and systematic testing of four M06-class functionals and 12 other functionals. *Theor. Chem. Acc.* **120**, 215–241 (2008).

[207] D.-C. Sergentu, D. Teze, A. Sabatié-Gogova, C. Alliot, N. Guo, F. Bassal, I. Da Silva, D. Deniaud, R. Maurice, J. Champion, N. Galland, and G. Montavon. Advances on the determination of the astatine pourbaix diagram: Predomination of $AtO(OH)_2^-$ over At^- in basic conditions. *Chem. Eur. J.* **22**, 2964–2971 (2016).

[208] L. Andrews, B. Liang, J. Li, and B. E. Bursten. Ground-state reversal by matrix interaction: Electronic states and vibrational frequencies of CUO in solid argon and neon. *Angew. Chem. Int. Ed.* **39**, 4565–4567 (2010).

[209] J. Li, B. E. Bursten, B. Liang, and L. Andrews. Noble gas-actinide compounds: Complexation of the CUO molecule by Ar, Kr, and Xe atoms in noble gas matrices. *Science* **295**, 2242–2245 (2002).

[210] J. Li, B. E. Bursten, L. Andrews, and C. J. Marsden. On the electronic structure of molecular UO_2 in the presence of Ar atoms: Evidence for direct U–Ar bonding. *J. Am. Chem. Soc.* **126**, 3424–3425 (2004).

[211] I. Infante, L. Andrews, X. Wang, and L. Gagliardi. Noble gas matrices may change the electronic structure of trapped molecules: The $UO_2(Ng)_4$ [Ng=Ne, Ar] case. *Chem. Eur. J.* **16**, 12804–12807 (2010).

[212] S. Rothe, A. N. Andreyev, S. Antalic, A. Borschevsky, L. Capponi, T. E. Cocolios, H. De Witte, E. Eliav, D. V. Fedorov, V. N. Fedosseev, D. A. Fink, S. Fritzche, L. Ghys, M. Huyse, N. Imai, U. Kaldor, Y. Kudryavtsev, U. Köster, J. F. W. Lane, J. Lassen, V. Liberati, K. M. Lynch, B. A. Marsh, K. Nishio, D. Pauwels, V. Pershina, L. Popescu, T. J. Procter, D. Radulov, S. Raeder, M. M. Rajabali, E. Rapisarda, R. E. Rossel, K. Sandhu, M. D. Seliverstov, A. M. Sjödin, P. Van den Bergh, P. Van Duppen, M. Venhart, Y. Wakabayashi, and K. D. A. Wendt. Measurement of the first ionization potential of astatine by laser ionization spectroscopy. *Nat. Commun.* **4**, 1835 (2013).

[213] A. Borschevsky, L. F. Pašteka, V. Pershina, E. Eliav, and U. Kaldor. Ionization potentials and electron affinities of the superheavy elements 115–117 and their sixth-row homologues Bi, Po, and At. *Phys. Rev. A* **91**, 020501 (2015).

[214] D. R. Herrick. Connecting Pauling and Mulliken electronegativities. *J. Chem. Theory Comput.* **1**, 255–260 (2005).

[215] R. E. Vernon. Which elements are metalloids? *J. Chem. Edu.* **90**, 1703–1707 (2013).

[216] A. Allred. Electronegativity values from thermochemical data. *J. Inorg. Nucl. Chem.* **17**, 215–221 (1961).

[217] S. W. Hadley, D. S. Wilbur, M. A. Gray, and R. W. Atcher. Astatine-211 labeling of an antimelanoma antibody and its Fab fragment using *N*-succinimidyl *p*-astatobenzoate: Comparisons in vivo with the p-[^{125}I]iodobenzoyl conjugate. *Bioconjugate Chem.* **2**, 171–179 (1991).

[218] L. Vasharosh, Y. V. Norseev, and V. A. Khalkin. Determination of carbon-astatine chemical bond breaking energy. *Dokl. Akad. Nauk SSSR* **263**, 119–123 (1982).

[219] J. B. Pedley, R. D. Naylor, and S. P. Kirby. *Thermodynamic data of organic compounds.* Chapmand and Hall, New York (1986).

[220] L. Gagliardi and B. O. Roos. Quantum chemical calculations show that the uranium molecule U_2 has a quintuple bond. *Nature* **433**, 848–851 (2005).

[221] A. P. Sattelberger and M. J. A. Johnson. Uncovering the uranium-nitrogen triple bond. *Science* **337**, 652–653 (2012).

[222] X. Li. Metalophilic interaction in gold halide: Quantum chemical study of AuX (X=F–At). *J. Comput. Chem.* **35**, 923–931 (2014).

[223] R. F. W. Bader. A quantum theory of molecular structure and its applications. *Chem. Rev.* **91**, 893–928 (1991).

[224] B. Silvi and A. Savin. Classification of chemical bonds based on topological analysis of electron localization functions. *Nature* **371**, 683–686 (1994).

[225] C. van Wüllen. Spin densities in two-component relativistic density functional calculations: Noncollinear versus collinear approach. *J. Comput. Chem.* **23**, 779–785 (2002).

[226] L. Visscher, H. J. Aa. Jensen, R. Bast, and T. Saue, with contributions from V. Bakken, K. G. Dyall, S. Dubillard, U. Ekström, E. Eliav, T. Enevoldsen, E. Faßhauer, T. Fleig, O. Fossgaard, A. S. P. Gomes, E. D. Hedegård, T. Helgaker, J. Henriksson, M. Iliaš, Ch. R. Jacob, S. Knecht, S. Komorovský, O. Kullie, J. K. Lærdahl, C. V. Larsen, Y. S. Lee, H. S. Nataraj, M. K. Nayak, P. Norman, G. Olejniczak, J. Olsen, J. M. H. Olsen, Y. C. Park, J. K. Pedersen, M. Pernpointner, R. di Remigio, K. Ruud, P. Sałek, B. Schimmelpfennig, A. Shee, J. Sikkema, A. J. Thorvaldsen, J. Thyssen, J. van Stralen, S. Villaume, O. Visser, T. Winther, and S. Yamamoto. DIRAC, a relativistic ab initio electronic structure program.

[227] P. Jerabek, B. Schuetrumpf, P. Schwerdtfeger, and W. Nazarewicz. Electron and nucleon localization functions of oganesson: Approaching the Thomas-Fermi limit. *Phys. Rev. Lett.* **120**, 053001 (2018).

[228] B. O. Roos, A. C. Borin, and L. Gagliardi. Reaching the maximum multiplicity of the covalent chemical bond. *Angew. Chem. Int. Ed.* **46**, 1469–1472 (2007).

[229] F. Gendron, B. Le Guennic, and J. Autschbach. Magnetic properties and electronic structures of Ar_3U^{IV}–L complexes with Ar = $C_5(CH_3)_4H^-$ or $C_5H_5{}^-$ and L = CH_3, NO, and Cl. *Inorg. Chem.* **53**, 13174–13187 (2014).

[230] P.-O. Löwdin and H. Shull. Natural orbitals in the quantum theory of two-electron systems. *Phys. Rev.* **101**, 1730–1739 (1956).

[231] F. Gendron, D. Páez-Hernández, F.-P. Notter, B. Pritchard, H. Bolvin, and J. Autschbach. Magnetic properties and electronic structure of neptunyl(VI) complexes: Wavefunctions, orbitals, and crystal-field models. *Chem. Eur. J.* **20**, 7994–8011 (2014).

[232] K. Giesbertz. Are natural orbitals useful for generating an efficient expansion of the wave function? *Chem. Phys. Lett.* **591**, 220–226 (2014).

[233] A. D. Becke and K. E. Edgecombe. A simple measure of electron localization in atomic and molecular systems. *J. Chem. Phys.* **92**, 5397–5403 (1990).

[234] M. Kohout and A. Savin. Atomic shell structure and electron numbers. *Int. J. Quantum Chem.* **60**, 875–882 (1996).

[235] A. Savin, B. Silvi, and F. Colonna. Topological analysis of the electron localization function applied to delocalized bonds. *Can. J. Chem.* **74**, 1088–1096 (1996).

[236] L. Zhang, F. Ying, W. Wu, P. C. Hiberty, and S. Shaik. Topology of electron charge density for chemical bonds from valence bond theory: A probe of bonding types. *Chem. Eur. J.* **15**, 2979–2989 (2009).

[237] S. Shaik, D. Danovich, B. Silvi, D. L. Lauvergnat, and P. C. Hiberty. Charge-shift bonding—A class of electron-pair bonds that emerges from valence bond theory and is supported by the electron localization function approach. *Chem. Eur. J.* **11**, 6358–6371 (2005).

[238] S. Shaik, D. Danovich, W. Wu, and P. C. Hiberty. Charge-shift bonding and its manifestations in chemistry. *Nat. Chem.* **1**, 443–449 (2009).

[239] H. Zhang, D. Danovich, W. Wu, B. Braïda, P. C. Hiberty, and S. Shaik. Charge-shift bonding emerges as a distinct electron-pair bonding family from both valence bond and molecular orbital theories. *J. Chem. Theory Comput.* **10**, 2410–2418 (2014).

[240] T. Ayed, J. Pilmé, D. Tézé, F. Bassal, J. Barbet, M. Chérel, J. Champion, R. Maurice, G. Montavon, and N. Galland. ^{211}At-labeled agents for alpha-immunotherapy: On the *in vivo* stability of astatine-agent bonds. *Eur. J. Med. Chem.* **116**, 156–164 (2016).

[241] H. J. Werner, P. J. Knowles, R. Lindh, F. R. Manby, M. Schtz, P. Celani, T. Korona, A. Mitrushenkov, G. Rauhut, T. B. Adler, R. D. Amos, A. Bernhardsson, A. Berning, D. L. Cooper, M. J. O. Deegan, A. J. Dobbyn, F. Eckert, E. Goll, C. Hampel, G. Hetzer, T. Hrenar, G. Knizia, C. Kppl, Y. Liu, A. W. Lloyd, R. A. Mata, A. J. May, S. J. McNicholas, W. Meyer, M. E. Mura, A. Nicklass, P. Palmieri, K. Pflger, R. Pitzer, M. Reiher, U. Schumann, H. Stoll, A. J. Stone, R. Tarroni, T. Thorsteinsson, M. Wang, and A. Wolf. MOLPRO, A package of ab initio programs.

[242] S. Noury, X. Krokidis, F. Fuster, and B. Silvi. Computational tools for the electron localization function topological analysis. *Comput. Chem.* **23**, 597–604 (1999).

[243] E. Matito, B. Silvi, M. Duran, and M. Solà. Electron localization function at the correlated level. *J. Chem. Phys.* **125**, 024301 (2006).

[244] F. Feixas, E. Matito, M. Duran, M. Solà, and B. Silvi. Electron localization function at the correlated level: A natural orbital formulation. *J. Chem. Theory Comput.* **6**, 2736–2742 (2010).

[245] A. Younes, G. Montavon, C. Alliot, M. Mokili, F. Haddad, D. Deniaud, and J. Champion. A route for polonium 210 production from alpha-particle irradiated bismuth-209 target. *Radiochim. Acta* **102**, 681–689 (2014).

[246] A. Younes, G. Montavon, S. G. Gouin, E. Andre-Joyaux, R. Peumery, T. Chalopin, C. Alliot, M. Mokili, J. Champion, and D. Deniaud. Investigation of a new "$N_2S_2O_2$" chelating agent with high Po(IV) affinity. *Chem. Commun.* **53**, 6492–6495 (2017).

[247] N. Iwahara and L. F. Chibotaru. Exchange interaction between J multiplets. *Phys. Rev. B* **91**, 174438 (2015).

[248] M. B. Robin and P. Day. *Mixed Valence Chemistry-A Survey and Classification.* In Advances in Inorganic Chemistry and Radiochemistry, Eds. von H. J. Enieldus and A. G. Sharpe, Academic Press, 247–422 (1968).

[249] P. C. Hiberty, S. Humbel, D. Danovich, and S. Shaik. What is physically wrong with the description of odd-electron bonding by Hartree-Fock theory? A simple nonempirical remedy. *J. Am. Chem. Soc.* **117**, 9003–9011 (1995).

[250] L. Song, Y. Mo, Q. Zhang, and W. Wu. XMVB: A program for *ab initio* nonorthogonal valence bond computations. *J. Comput. Chem.* **26**, 514–521 (2005).

Representative publications

In this part, five representative publications are reported to illustrate various aspects of my work on the role of relativistic effects on the properties of molecules and materials. These publications are not necessarily the ones belonging to the most prestigious journals in which I have published. Instead, they correspond to publications in which I have had a key role such as being the first author, the last author and/or (co-)corresponding author and they display important differences in the followed methodologies.

The first key publication illustrates the use of the effective Hamiltonian theory to extract anisotropic spin Hamiltonians. This publication, which is actually my very first one, opened the way for all the work that I have done in molecular magnetism.

The second one is a nice example of the application of this methodology to solid state problems via the embedded cluster approach. By computing all the relevant effective interactions, this publication allowed to discreminate between two envisaged models for describing the low-temperature magnetic behavior of the $LiCu_2O_2$ ionic solid.

The third one is one of the pioneering works that I have led on the exploration of potential energy surfaces with the SOCI approach by guiding my first officially co-advised PhD student, D.-C. Sergentu. This publication is fundamentally interesting for the radiochemistry community since it definitly justifies the occurence of an environment-induced ground-state change that occurs when AtO^+ is hydrated.

The fourth key publication relates to the reactivity of astatobenzoate compounds. It was shown with DFT calculations that the SOC must be introduced to obtain the correct trend in the relative stabilities of iodobenzoate and astatobenzoate compounds. Note that this publication is of interest in the context of nuclear medicine with astatine-211 and that most of the actual work was performed by the post-doctoral associate D. Tézé, with whom I was regularly in interaction.

The last reported publication is the first of my publications related to the used of spin-orbit configuration interaction wave functions for describing chemical bonding. This approach notably allows to readily determine the influence of the SOC on chemical bonds.

Magnetic properties of transition metal complexes and ionic solids:

1. R. Maurice*, R. Bastardis, C. de Graaf, N. Suaud, T. Mallah and N. Guihéry*, *Universal theoretical approach to extract anisotropic spin Hamiltonians*, J. Chem. Theo. Comput. **5**, 2977–2984 (2009).

   http://dx.doi.org/10.1021/ct900326e

2. R. Maurice, A.-M. Pradipto, C. de Graaf and R. Broer*, *Magnetic interactions in $LiCu_2O_2$: Single-chain versus double-chain models*, Phys. Rev. B **86**, 024411 (2012).

   http://dx.doi.org/10.1103/PhysRevB.86.024411

Structural and chemical properties of radioelement species:

3. D.-C. Sergentu, F. Réal, G. Montavon, N. Galland* and R. Maurice*, *Unravelling the hydration-induced ground-state change of AtO^+ by relativistic and multiconfigurational wave-function-based methods*, Phys. Chem. Chem. Phys. **18**, 32703–32712 (2016).

   http://dx.doi.org/10.1039/C6CP05028J

4. D. Teze*, D.-C. Sergentu, V. Kalichuk, J. Barbet, D. Deniaud, N. Galland, R. Maurice* and G. Montavon, *Targeted radionuclide therapy with astatine-211: Oxidative dehalogenation of astatobenzoate conjugates*, Sci. Rep. **7**, 2579 (2017).

   http://dx.doi.org/10.1038/s41598-017-02614-2

Chemical bonding in heavy-(radio)element systems:

5. R. Maurice*, F. Réal, A. S. P. Gomes, V. Vallet, G. Montavon and N. Galland, *Effective bond orders from two-step spin-orbit coupling approaches: The I_2, At_2, IO^+ and AtO^+ case studies*, J. Chem. Phys. **142**, 094305 (2015).

   http://dx.doi.org/10.1063/1.4913738

JCTC Journal of Chemical Theory and Computation

Universal Theoretical Approach to Extract Anisotropic Spin Hamiltonians

Rémi Maurice,*,†,§ Roland Bastardis,‡ Coen de Graaf,§,⊥ Nicolas Suaud,† Talal Mallah,‖ and Nathalie Guihéry*,†

Laboratoire de Chimie et Physique Quantiques, IRSAMC/UMR5626, Université de Toulouse III, 118 route de Narbonne, F-31062 Toulouse Cédex 4, France, Laboratoire de Mathématiques, Physiques et Systemes, Université de Perpignan Via Domitia, 52 Avenue Paul Alduy, 66860 Perpignan, France, Departament de Química Física i Inorganica, Universitat Rovira i Virgili, Marcel lí Domingo s/n, 43007 Tarragona, Spain, Institut de Chimie Moléculaire et des Matériaux d'Orsay, Université Paris sud 11, 91405 Orsay, France, and Institució Catalana de Recerca i Estudis Avançats (ICREA), Passeig Lluis Companys 23, 08010, Barcelona, Spain

Received June 27, 2009

Abstract: Monometallic Ni(II) and Co(II) complexes with large magnetic anisotropy are studied using correlated wave function based ab initio calculations. Based on the effective Hamiltonian theory, we propose a scheme to extract both the parameters of the zero-field splitting (ZFS) tensor and the magnetic anisotropy axes. Contrarily to the usual theoretical procedure of extraction, the method presented here determines the sign and the magnitude of the ZFS parameters in any circumstances. While the energy levels provide enough information to extract the ZFS parameters in Ni(II) complexes, additional information contained in the wave functions must be used to extract the ZFS parameters of Co(II) complexes. The effective Hamiltonian procedure also enables us to confirm the validity of the standard model Hamiltonian to produce the magnetic anisotropy of monometallic complexes. The calculated ZFS parameters are in good agreement with high-field, high-frequency electron paramagnetic resonance spectroscopy and frequency domain magnetic resonance spectroscopy data. A methodological analysis of the results shows that the ligand-to-metal charge transfer configurations must be introduced in the reference space to obtain quantitative agreement with the experimental estimates of the ZFS parameters.

1. Introduction

The recent interest for information storage at the molecular scale motivates both experimental and theoretical studies of molecules presenting a bistability. Among the different bistable chemical systems, single molecule magnets (SMMs)[1−5] are the smallest species that have been conceived. Their remarkable properties come from their intrinsic feature to present two high spin states of different magnetization $+M_S$ and $-M_S$ separated by an energy barrier. From a fundamental point of view, works on these systems have opened new perspectives in the study of quantum mechanics effects such as tunnelling, coherence, and interference. Magnetic anisotropy is responsible for both the existence of the energy barrier and the dominant factor of the tunnelling, and hence, it determines the magnetic behavior of these systems. A crucial landmark for chemistry, for technological devices as well as for fundamental investigations, would be the control and tuning of the magnetic anisotropy.

From a theoretical point of view, the understanding of the electronic and the structural factors governing the anisotropy

* Corresponding author. Telephone: +33561556488. E-mail: rmaurice@irsamc.ups-tlse.fr.
† Université de Toulouse III.
§ Universitat Rovira i Virgili.
‡ Université de Perpignan Via Domitia.
⊥ Institució Catalana de Recerca i Estudis Avançats (ICREA).
‖ Université Paris.

10.1021/ct900326e CCC: $40.75 © 2009 American Chemical Society
Published on Web 10/02/2009

is of primary importance. The first attempts to calculate anisotropy parameters from first principles are less than 10 years old. Most of the studies concern one component density functional theory (DFT) based calculations with a perturbative inclusion of spin−orbit (SO) coupling (see the ORCA[6−11] and NRLMOL[12−16] code). Very recently, a two-component DFT method[17] has been implemented in the ReSpect code[18] and used to study the zero field splittings (ZFS) of several mononuclear complexes. For polynuclear systems, good agreement with experimental values was obtained using the NRLMOL method for the calculated D and E ZFS parameters of the Fe_4, Mn_{12}, and Mn_6-based SMMs.[19,20] Nevertheless, only the global ZFS parameters of the SMMs in its ground spin states (i.e., the parameters of the giant spin Hamiltonian) were accessible within the DFT scheme. The understanding and control of the property requires studying the local anisotropies of each metal ion and the anisotropies of their interactions. To extract such quantities, the multideterminantal descriptions are mandatory, and the excited spin states should be calculated. Wave function based calculations can provide this accurate description of the multideterminantal character of SMMs wave functions, but only few works dealt with the extraction of ZFS parameters using wave function based computational schemes. One can mention the pioneering work of Michl[21] involving a perturbative treatment of spin dependent terms and the work done by Ågren et al.[22] based on the linear response theory. Among the most popular methods, we quote the ones implemented in the ORCA[6] and MOLCAS[23] codes. Both codes provide accurate results on the mono- and polynuclear nuclear complexes.[7−11,24−28]

In the present paper, spin-orbit restricted active space state interaction (SO-RASSI) calculations on mononuclear species are performed in order to determine the energies and wave functions of the lowest electronic states. These solutions are then used to build and to calculate the matrix elements of the effective Hamiltonian that best fits the ab initio results. Since this Hamiltonian matrix can be compared to the commonly used model Hamiltonian matrix, the procedure provides a rational way to check (and eventually to improve) the ability of the phenomenological Hamiltonian to describe accurately the magnetic anisotropy. The same philosophy has been applied to many magnetic systems in order to measure the different contributions to the magnetic exchange integral[29,30] and to rationally parametrize t-J models,[31,32] double exchange models,[33−39] and spin Hamiltonians.[40] In all cases, the procedure has shown the validity and the application limits of the phenomenological Hamiltonians that are commonly used to interpret the experimental data or to understand the physics of the system under study. The comparison has led to different improvements of the model Hamiltonians, such as the inclusion of a priori neglected exchange interactions,[31] and the three- or four-body operators[41,42] that are crucial for the reproduction of the magnetic properties of the systems. Concerning the study of magnetic anisotropy, the effective Hamiltonian theory is particularly promising for polynuclear species given the uncertainties in the proper definition of the model Hamiltonian for these systems.[43−45] In this work, we use the effective Hamiltonian theory to extract the anisotropic spin Hamiltonian from the first principles for mononuclear species, laying in this way, the foundation for the study of the more complicated polynuclear systems. We show how the magnetic anisotropy axes can be determined, and that the rigorous computational extraction of the anisotropy parameters for the high spin d^7 configuration requires the construction of an effective Hamiltonian.

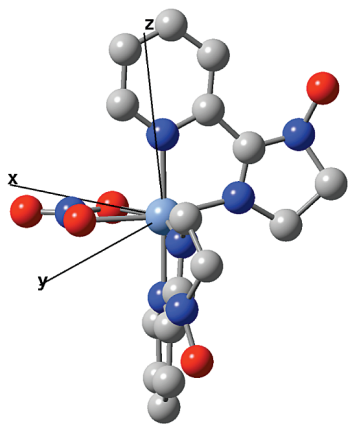

Figure 1. The $[Ni(HIM2-Py)_2NO_3]^+]$ complex (**1**) and its proper magnetic axes. The magnetic *z*-axis has an angle of 12.7° with the normal of the plane formed by Ni and by the NO_3^- ligand.

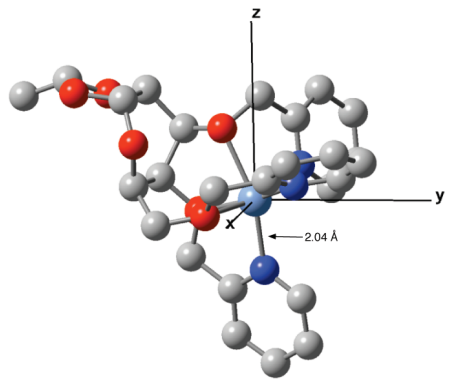

Figure 2. The $[Ni(glycoligand)]^{2+}]$ complex (**2**) and its proper magnetic axes. The magnetic *z*-axis has an angle of 9.5° with the 2.04 Å Ni−N bond.

2. Methodological Study

2.1. Description of the Compounds and Computational Information. Three Ni(II) complexes and one Co(II) complex were studied. $[Ni(HIM2-Py)_2\ NO_3]^+$ (**1**, see Figure 1) and $[Ni(glycoligand)]^{2+}$ (**2**, see Figure 2) show a quasi-octahedral coordination of Ni(II), while $[Ni(iPrtacn)Cl_2]$ (**3**, see Figure 3) has a pentacoordinated Ni(II) ion in an arrangement of the ligands that is intermediate between a trigonal bipyramid and a square pyramid. The geometries have been taken from crystallographic data and experimental information about the structure, high-field, high-frequency electron paramagnetic resonance (HF-HFEPR) and frequency domain magnetic resonance spectroscopy (FDMRS) data can be found in refs 46−48 for each compound, respectively. In order to reduce the computational cost for **1**, the CH_3 groups, which are geometrically distant from the metal ion, have been modeled

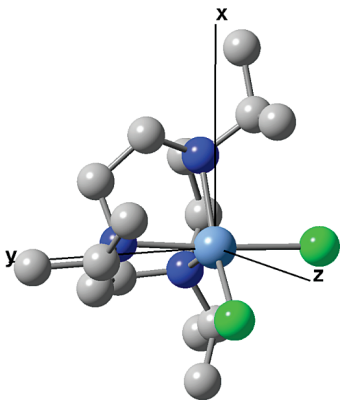

Figure 3. The [Ni(*i*Prtacn)Cl_2] complex (**3**) and its proper magnetic axes. The magnetic *z*-axis has an angle of 26.0° with the Cl−N−Cl plane.

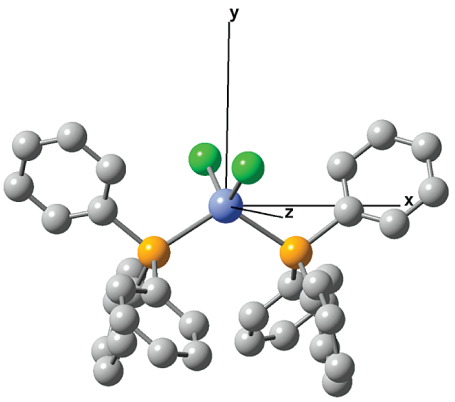

Figure 4. The [Co(PPh_3)$_2$$Cl_2$] (Ph = phenyl) complex (**4**) and its proper magnetic axes.

by H atoms. Owing to the local character of the ZFS property, this simplification should not affect the results. The local geometry of Co(II) in [Co(PPh_3)$_2$$Cl_2$][49,50] (**4**, see Figure 4), is a distorted tetrahedron.

The electronic structure of the complexes have been studied using the SO-RASSI method[51,52] implemented in MOLCAS 7. The scalar relativistic effects are included through the use of the Douglas−Kroll−Hess Hamiltonian,[53,54] and the SO effects are treated within the one-component formalism through the so-called spin-orbit state interaction (SO-SI) technique using the atomic mean-field approximation (AMFI). The method is a two-step procedure based on the idea that electron−correlation and SO effects are largely decoupled. The first step involves a complete active space self-consistent field (CASSCF) calculation to treat nondynamic correlations followed by the introduction of dynamic correlation effects through the evaluation of the single and double excitation contributions in a second-order perturbative manner (CASPT2). The second step calculates the SO interactions between the CASSCF states. The CASSCF diagonal elements of the so-obtained SO-SI matrix are substituted by the CASPT2 energies in order to take into account the main dynamic correlation effects.[55,56] In this method, the dipole-spin coupling is neglected. Contrarily to what was assumed for several decades, it has recently been shown that for Mn(III) complexes, the spin−spin part is not negligible for a quantitative description of the anisotropy.[22,10] In the considered Ni(II) and Co(II) complexes, the contribution of the SO interaction to the anisotropy is relatively important, and the number of unpaired electrons is small. Hence, the spin−spin part is expected to bring a minor contribution to the overall anisotropy.

Two different active spaces have been considered in the CASSCF calculations. The minimal active space has five TM-3d (TM = Ni,Co) orbitals and an extra set of five TM-d′ orbitals to accurately describe the radial electron correlation. This gives a CAS(8,10) and CAS(7,10) for the Ni- and Co-based compounds, respectively. The second, extended active space also includes some doubly occupied σ ligand−metal bonding orbitals. These orbitals essentially represent the nonbonding pairs of the atoms coordinated to the metal ion. Adding the orbitals with the strongest TM−ligand interaction leads to CAS(12,12) and CAS(13,13) for Ni- and Co-based compounds, respectively. Molecular orbitals have been optimized in an average way for all states belonging to a given spin multiplicity. The following all-electron ANO-RCC basis sets[57] are used: Ni and Co (6s 5p 4d 2f), Cl and P (5s 4p 1d), coordinated N (4s 3p 1d), other N (3s 2p 1d), O (4s 3p 1d), C (3s 2p), and H (2s).

The IP-EA shift has been set to zero for the nickel complexes since the states which are strongly coupled through the SO interaction are the lowest triplets, which have the same number of unpaired electrons, and to 0.25 for the cobalt one for which the excited doublets were suspected to play an important role. The minimal imaginary shift necessary in order to remove intruder states has been introduced in all cases (0.05 for **1** and **2**, 0.10 for **3,** and 0.20 au for **4**).

2.2. Dependence of the Zero-Field Splitting on the Computational Degrees of Freedom of the SO-RASSI Method. In addition to the usual computational degrees of freedom, such as the number of basis functions and the size of the active space, the outcomes of the SO-RASSI calculations also depend on the number of states included in the state interaction and the choice of the diagonal elements in the SO matrix: CASSCF or CASPT2 energies. To establish the precision of the SO-RASSI method, we explored these computational degrees of freedom in **1** and **4**. We concentrated on three aspects: (i) the number of excited states, which are included in the SO-SI space. Here a balance should be found between the computational cost of calculating many excited states and the influence of the matrix elements on the final result; (ii) The size of the active space, i.e. the effect of the inclusion of the ligand-to-metal charge transfer excitations in the CASSCF wave function affect the low-energy spectrum; and (iii) the comparison of the results using CASSCF or CASPT2 energies on the diagonal of the SO-SI matrix.

The dependence of the results to the number of states considered in the SO-SI calculations is studied for compounds **1** and **4**. The number of states has progressively been reduced starting from the complete TM-3d^n manifold to finally four states only. The selection of the states is based on an energy criterion, and states which are close in energy are removed from the SO-SI space simultaneously. In both cases, the smallest calculations (four states) couples the ground state with the first three excited states. These three states correspond to the three degenerate spatial components

Table 1. Energy Differences (in cm^{-1}) of the Spin−Orbit Splitted States Arising from the Fundamental Triplet State of **1** as Function of the Number of Spin−Orbit Coupled States[a]

		ΔE_1		ΔE_2	
number of states in SI	active space	CASSCF	CASPT2	CASSCF	CASPT2
10T, 14S	(8,10)	15.1	11.6	13.2	10.1
10T, 9S	(8,10)	17.1	14.2	14.5	11.7
7T, 2S	(8,10)	14.1	10.7	12.4	9.3
4T	(8,10)	14.8	13.0	13.0	11.3
4T	(12,12)	12.9	11.4	11.3	9.8
FDMRS[46]		10.3 ± 0.1		9.7 ± 0.1	

[a] $\Delta E_1 = E(|1,0\rangle) - E(|1,1\rangle - |1,-1\rangle)$ and $\Delta E_2 = E(|1,0\rangle) - E(|1,1\rangle + |1,-1\rangle)$. The number and spin multiplicity of the coupled states are indicated as *n*T(triplets) and *m*S(singlets).

Table 2. Energy Differences (in cm^{-1}) of the Spin−Orbit Splitted States Arising from the Fundamental Quartet State of **4** as Function of the Number of Spin−Orbit Coupled States[a]

		ΔE	
number of states in SI	active space	CASSCF	CASPT2
10Q, 40D	(7,10)	36.0	42.6
7Q	(7,10)	29.0	35.8
7Q	(13,13)	22.7	29.7
4Q	(7,10)	17.9	26.0
4Q	(13,13)	14.4	21.6
HF-HFEPR[49,50]		29.8	

[a] ΔE is the absolute value of $E(|3/2,\pm3/2\rangle) - E(|3/2,\pm1/2)$. The number and spin multiplicity of the coupled states are indicated as *n*Q (quartets) and *m*D (doublets).

of the first excited state in an ideal octahedral (Ni) or tetrahedral (Co) coordination. A further reduction of the SO-SI space is physically not grounded and has not been performed.

The d^8 configuration of the Ni(II) ion contains 25 spin free states, 10 triplets, and 15 singlets. Due to an intruder state problem, the CASPT2 energy of the highest singlet state could not be obtained with a high enough precision, hence 14 singlets have been considered in the SO calculation. Since this last singlet is very high in energy, its neglect is not expected to have any significant influence on the ZFS parameters. The Co(II)-d^7 configuration contains 10 quadruplets and 40 doublets. In this case, the energetic decomposition is not trivial since, except for the seven first quadruplet states which are well separated in energy from the others, all the other excited states are close in energy. We have, therefore, only compared the results obtained for the four and seven quadruplets and the complete collection of the 50 states of the configuration.

Table 1 compares the computed relative energies of the M_S components (or their combinations) of the ground state of **1** to the experimental ones for different SO-SI spaces. Table 2 lists the energy difference of the lowest two Kramers doublets for **4**. In all cases, the states are labelled using the main M_S components (or their combinations) appearing in the SO wave functions computed in the proper magnetic axes frame (the determination of this frame is discussed in Section 3). FDMRS transition energies are available for compound **1**, while the transition energy has been calculated from the ZFS parameters derived from the EPR data for **4**.

From the results reported in Tables 1 and 2, several conclusions can be inferred:

(i) In the Ni compounds, the lowest excited states of the same spin multiplicity as the ground state, i.e., the three lowest excited triplets, make the main contribution to ZFS. The analysis of the physical content of the wave functions of these SO excited states rationalizes their predominant role. They all result from a single electron replacement in the TM-3d orbitals with respect to the fundamental state. These excited states are, therefore, not only low in energy but also strongly coupled through SO coupling with the ground state. For the quasi-tetrahedrally coordinated Co complex, the SO-SI space cannot be restricted to the lowest four quartet states, which arise from the $^4A_2$ and $^4T_2$ states of the perfect tetrahedron. The three excited states arising from the $^4T_1$ state are so low in energy that they have a non-negligible interaction via the SO operator with the ground state, notwithstanding the marked contribution of the doubly excited configurations in the wave functions of these states.

(ii) At first sight, it may be surprising that the best agreement with experiment is obtained for the smaller SO-SI spaces (4T for **1** and 7Q for **4**), and that the inclusion of more states does not improve the result or even worsen it. However, the use of the state-average CASSCF orbitals to obtain the higher excited states affects the description of the lowest states. Indeed, in these averaged orbital sets, these states are less precisely described than in a set of orbitals optimized for the lowest states only. Hence, the precision that is gained by enlarging the SO-SI space is lost by the more approximate description of the lowest excited states. This is a limitation of the CASPT2/SO-SI methodology, enlarging the SI space does not guarantee a convergence of the results. Hence, we would recommend to optimize the orbitals in an average way for only those states that strongly interact through the SO coupling with the ground state.

(iii) Reasonable results can be obtained with a relatively small computational effort. Qualitative agreement with experiment is observed for the CASSCF wave functions and the energies calculated with the smaller active space, averaging for the lowest electronic states only. The incorporation of dynamic correlation effects (CASPT2) moderately modifies the obtained results. For a quantitative agreement with experiment, it is necessary to extend the active space to those ligand orbitals that have sizable tails on the metal center. This shows that the ligand-to-metal charge transfer (LMCT) configurations can play an important role in the magnetic anisotropy and should be variationally described. The active space should be chosen in such a way that it does not only include the radial electron correlation (smaller active space) but also the nondynamical correlation effects associated to the LMCT configurations.

3. Theory and Results

3.1. General Approach. The model spin Hamiltonian of a mononuclear anisotropic complex in the absence of a magnetic field is given by the following expression:

$$\hat{H}^{\mathrm{mod}} = \hat{S} \cdot \bar{\bar{D}} \cdot \hat{S} \tag{1}$$

where $\hat{S}$ is the spin operator, and $\bar{\bar{D}}$ is the second-order anisotropy tensor. For more than three unpaired electrons, even higher-order terms can be considered in the model Hamiltonian.[43] These higher-order terms will not be considered here since the complexes studied are limited to two or three unpaired electrons only. The projections of the lowest SO states onto the $|S,M_S\rangle$ states constitute the basis functions of the model space S_0 on which this model Hamiltonian is spanned. The SO coupling results in a mixing of the M_S components and, therefore, in a removal of their degeneracy. The procedure to extract the ZFS tensor, which is proposed here, uses the effective Hamiltonian theory.[58,59] This theory is based on the existence of a biunivocal relation between a model space S_0 and a target space S constituted of those eigenstates Ψ_i of the all-electron Hamiltonian that should be accurately reproduced by the model Hamiltonian. The effective Hamiltonian (which will be later compared to the model Hamiltonian) may be written as

$$\hat{H}^{\mathrm{eff}} = \sum_i |\tilde{\Psi}_i\rangle E_i \langle\tilde{\Psi}_i| \tag{2}$$

where $|\tilde{\Psi}_i\rangle$ are the orthogonalized projections of the $|\Psi_i\rangle$ states onto S_0, and E_i are their ab initio energies. The projections were orthogonalized by an $S^{-1/2}$ orthonormalization (where S is the overlap matrix) as proposed by des Cloizeaux.[59] This formalism guarantees that the eigenvalues of the model Hamiltonian are the eigenvalues of the all-electron Hamiltonian, and that its eigenfunctions are the orthogonalized projections $|\tilde{\Psi}_i\rangle$ of the eigenfunctions of the all-electron Hamiltonian onto the model space, such that:

$$\hat{H}^{\mathrm{eff}}|\tilde{\Psi}_i\rangle = E_i|\tilde{\Psi}_i\rangle \tag{3}$$

The norm of these projections provides a rational way to check the relevance of the model Hamiltonian to be extracted. If the norm of the projection is small, then important physics are missing in the model space, and one should reconsider the definition of the model Hamiltonian. Therefore, the method provides a rigorous and controlled way to extract the model Hamiltonian. Another advantage of the use of the effective Hamiltonian theory resides in the possibility to determine the principal axes of the ZFS tensor. Indeed, the expressions of both the eigenfunctions of the all-electron Hamiltonian and the matrix elements of the effective Hamiltonian defined in eq 2 depend on the axes frame. An identification of these terms with those of the analytical matrix of the model Hamiltonian expressed in the general case of a nondiagonal tensor leads to a complete determination of the $\bar{\bar{D}}$ components in an arbitrary frame. The proper magnetic axes are then determined from the diagonalization of the ZFS tensor. In comparison to the perturbative approach of calculating the ZFS tensor components, the effective Hamiltonian theory enables one to identify as high-order terms as required, since the interactions of the model Hamiltonian (and therefore its operators) are not guessed a priori. To recover the results of the effective Hamiltonian theory, one should expand the perturbation until an infinite order.

3.2. Extraction of the ZFS Parameters from the Effective Hamiltonian Theory. The ZFS tensor is only diagonal in the magnetic anisotropy axes frame. In the following development, its matrix representation in an arbitrary frame will be denoted as

$$\mathbf{D} = \begin{pmatrix} D_{11} & D_{12} & D_{13} \\ D_{12} & D_{22} & D_{23} \\ D_{13} & D_{23} & D_{33} \end{pmatrix} \tag{4}$$

The elements of the analytical matrix of $\hat{H}^{\mathrm{mod}}$ (eq 1) are functions of the different components D_{ij}, including the extradiagonal elements of the ZFS tensor. Using $|1,-1\rangle$, $|1,0\rangle$, and $|1,1\rangle$ as basis functions, the matrix elements $\langle S,M_S|\hat{H}^{\mathrm{mod}}|S,M'_S\rangle$ for the high spin d^8 configuration are

$$\begin{array}{lccc} \hat{H}_{\mathrm{mod}} & |1,-1\rangle & |1,0\rangle & |1,1\rangle \\ \langle 1,-1| & \frac{1}{2}(D_{11}+D_{22})+D_{33} & -\frac{\sqrt{2}}{2}(D_{13}+iD_{23}) & \frac{1}{2}(D_{11}-D_{22}+2iD_{12}) \\ \langle 1,0| & -\frac{\sqrt{2}}{2}(D_{13}-iD_{23}) & D_{11}+D_{22} & \frac{\sqrt{2}}{2}(D_{13}+iD_{23}) \\ \langle 1,1| & \frac{1}{2}(D_{11}-D_{22}-2iD_{12}) & \frac{\sqrt{2}}{2}(D_{13}-iD_{23}) & \frac{1}{2}(D_{11}+D_{22})+D_{33} \end{array} \tag{5}$$

The next step is the construction of the effective Hamiltonian based on the ab initio calculations. We take here, as an example, the CAS(12,12)PT2 results of **1** with the 4T SO-SI space (one but last row in Table 1). The projections of the eigenfunctions all electron Hamiltonian on the model space at this level of calculation are

$$|\Psi_1\rangle = (0.045 + 0.092i)|1,-1\rangle + (-0.668 + 0.724i)|1,0\rangle + (0.096 + 0.037i)|1,1\rangle$$
$$|\Psi_2\rangle = (-0.395 + 0.578i)|1,-1\rangle + (0.062 + 0.088i)|1,0\rangle + (-0.678 + 0.173i)|1,1\rangle$$
$$|\Psi_3\rangle = (0.701 + 0.026i)|1,-1\rangle + (-0.090 - 0.037i)|1,0\rangle + (-0.519 - 0.472i)|1,1\rangle$$

Using these projections and the corresponding energy eigenvalues ($E_1 = 0.000$, $E_2 = 1.529$, $E_3 = 11.369$ cm^{-1}), the application of eq 2 leads to the following numerical effective Hamiltonian:

$$\begin{array}{lccc} & |1,-1\rangle & |1,0\rangle & |1,1\rangle \\ \langle 1,-1| & 6.386 & -0.690 + 0.376i & -3.734 + 3.134i \\ \langle 1,0| & -0.690 - 0.376i & 0.125 & 0.690 - 0.376i \\ \langle 1,1| & -3.734 - 3.134i & 0.690 + 0.376i & 6.386 \end{array} \tag{6}$$

Before calculating the ZFS tensor **D**, we observe that there is a perfect one-to-one correspondence of the matrix elements of the effective Hamiltonian derived from the ab initio calculations and those of the model Hamiltonian of eq 5. The effective Hamiltonian does not present extra interaction to those expected from the model Hamiltonian. Combined with the large norm of the projections, we conclude that the model Hamiltonian (eq 1) perfectly describes the ZFS in this case. The same behavior is found for the other Ni(II) compounds. The comparison of eqs 5 and 6 leads to six linear independent equations in terms of the D_{ij}, which determine uniquely the ZFS tensor. The full expression of the numerical effective Hamiltonians for **2** and **3** can be found in the

Supporting Information. From eqs 5 and 6 we derive the values of the **D** tensor of **1** in the original coordinates frame.

$$\mathbf{D} = \begin{pmatrix} -3.671 & 3.134 & 0.976 \\ 3.134 & 3.797 & -0.532 \\ 0.976 & -0.532 & 6.323 \end{pmatrix} \tag{7}$$

The **D** tensors for **2** and **3** are given in the Supporting Information. The diagonalization of **D** gives us the transformation matrix to rotate the coordinates frame such that the axes coincide with the magnetic one. These axes are indicated in the Figures 1−3 for the complexes studied here. Note that the orientation of the magnetic axes is almost independent of the computational degrees of freedom, unlike the energy differences between the lowest spin−orbit states, as shown in the previous section. Furthermore, it allows us to determine the commonly used ZFS parameters for the axial ($D = (3/2)D_{zz}$) and the rhombic ($E = (1/2)(D_{xx} - D_{yy}) > 0$) anisotropy. In the general case presented here, (Tr $\mathbf{D} \neq 0$), D and E can be derived from

$$\begin{aligned} D &= D_{33} - \frac{1}{2}(D_{11} + D_{22}) \\ E &= \frac{1}{2}(D_{11} - D_{22}) > 0 \end{aligned} \tag{8}$$

In practice, D_{33} is chosen as the diagonal element that maximizes the spacing with respect to the other two diagonal elements. D_{11} and D_{22} are identified by the convention that E is always positive. The resulting anisotropy parameters for **1**−**3** are listed in Table 3 and will be discussed in the next section.

For the Ni(II) complexes, the ZFS parameters can, of course, also be extracted from the spectrum only without going through the construction of the effective Hamiltonian. One should notice, however, that the magnetic anisotropy axes could not be determined, and that no information about the character of the wave functions can be used.

3.3. Extraction of ZFS Parameters for the d^7 Configuration. Spin−orbit interaction splits the quartet ground state of the high spin d^7 configuration into two Kramers doublets. Hence, the information from the spectrum is obviously not enough to determine the ZFS parameters D and E. It is not even possible to determine the sign of the axial anisotropy, except for the case when the magnetic axes are known and the wave function is available. This is, however, generally not the case, and the construction of an effective Hamiltonian is the preferred route toward a full description of the ZFS. Following the previously outlined procedure, we first calculate the matrix elements of the model Hamiltonian in the $|S,M_S\rangle$ basis for the d^7 configuration:

$$\begin{array}{c|cccc} \hat{H}_{\mathrm{mod}} & \left|\frac{3}{2},-\frac{3}{2}\right\rangle & \left|\frac{3}{2}-\frac{1}{2}\right\rangle & \left|\frac{3}{2},\frac{1}{2}\right\rangle & \left|\frac{3}{2},\frac{3}{2}\right\rangle \\ \hline \left\langle\frac{3}{2},-\frac{3}{2}\right| & \frac{3}{4}(D_{11}+D_{22})+\frac{9}{4}D_{33} & -\sqrt{3}(D_{13}+iD_{23}) & \frac{\sqrt{3}}{2}(D_{11}-D_{22}+2iD_{12}) & 0 \\ \left\langle\frac{3}{2},-\frac{1}{2}\right| & -\sqrt{3}(D_{13}-iD_{23}) & \frac{7}{4}(D_{11}+D_{22})+\frac{1}{4}D_{33} & 0 & \frac{\sqrt{3}}{2}(D_{11}-D_{22}+2iD_{12}) \\ \left\langle\frac{3}{2},\frac{1}{2}\right| & \frac{\sqrt{3}}{2}(D_{11}-D_{22}-2iD_{12}) & 0 & \frac{7}{4}(D_{11}+D_{22})+\frac{1}{4}D_{33} & \sqrt{3}(D_{13}+iD_{23}) \\ \left\langle\frac{3}{2},\frac{3}{2}\right| & 0 & \frac{\sqrt{3}}{2}(D_{11}-D_{22}-2iD_{12}) & \sqrt{3}(D_{13}-iD_{23}) & \frac{3}{4}(D_{11}+D_{22})+\frac{9}{4}D_{33} \end{array} \tag{9}$$

Subsequently, the effective Hamiltonian is constructed from the ab initio energies and wave functions. The numerical expression of this Hamiltonian can be found in the Supporting Information. We note again that the model Hamiltonian perfectly fits the effective Hamiltonian, and hence, the full **D** tensor can be extracted. The magnetic axes are shown in Figure 4, and the ZFS parameters are listed in Table 3. The appearance of off-diagonal terms in the effective Hamiltonian suggests that the eigenfunctions can have contributions from determinants with different M_S values. This implies that M_S is not a good quantum number anymore. Nevertheless, the off-diagonal terms that cause the interaction between the determinants with different M_S values are strictly zero in the proper magnetic frame under the condition of no rhombic distortion. In the case of **4**, the rhombic distortions are small ($E/|D| = 0.08$), and the wave functions that describe the four lowest states have almost pure $M_S = \pm 1/2$ or $M_S = \pm 3/2$ character.

3.4. Magneto-Structural Relations for *D* and *E*. Table 3 compares the calculated anisotropy parameters with the experimental values of these parameters extracted from HF-HFEPR data.[46−49] While the agreement with experiment is excellent for **1**, **3**, and **4**, the calculated D-value for **2** deviates by approximately 4 cm^{-1}. The smallness of the anisotropy of this complex may be the origin of the difference between theory and experiment. The SO-SI methodology may have reached its numerical precision for this complex. This is subject to further study on other complexes with small anisotropy.

A less equally important question is whether it can be established why **1** has a large negative D, **2** a very small D, and **3** a large positive D. For this purpose, we study the effect of different distortions on the anisotropy in the three Ni(II) complexes using CASSCF energies and the 4T SO-SI space. The starting point for the decomposition is the isotropic, perfect octahedron of the model compound $[Ni(NCH)_6]^{2+}$. The first coordination sphere of complex **1** shows two major distortions in the xy-plane. The first distortion is a cis elongation, and the second is an angular distortion in which one N−Ni−N angle increases to

Table 3. SO-SI Axial and Rhombic Anisotropy Parameters D and E (in cm^{-1}) for Three Ni(II) Complexes (**1**−**3**) and One Co(II) Complex (**4**)[a]

	SO-SI		exptl	
complex	D	E	D	E
1	−10.60	0.76	−10.15	0.10
2	8.10	0.58	4.40	0.75
3	16.45	3.82	15.70	3.40
4	−14.86	0.54	−14.76	1.14

[a] Calculations were performed with the extended CAS and the 4T or 7Q SO-SI space for **1**−**3** and **4**, respectively. The energies of the spin-free states are calculated with CASPT2.

100° and the opposite angle reduces to 60°. Other smaller distortions complete the route from perfect octahedron to real geometry. The subsequent application of these three distortions gives $D = +0.2$ cm^{-1} (xy-plane elongation), $D = -4.9$ cm^{-1} (after adding the angular distortion), and $D = -9.6$ cm^{-1} for the complete distortion. Hence, the largest effect on the anisotropy is found to be the xy-plane angular distortion, while the combination of the smaller angular distortions significantly enhances the D parameter.

The geometry of **2** is close to octahedral, showing an elongation along the positive z-axis and an angular distortion of both axial ligands in cis mode. Applying these distortions on the model complex gives $D = +3.0$ cm^{-1} for the elongation and $D = -4.5$ cm^{-1} for the axial distortion. The application of both distortions simultaneously gives $D = +6.1$ cm^{-1}, close to the value calculated for the real complex.

Complex **3** is pentacoordinated. Hence, the first obvious distortion is the removal of one of the ligands from the model complex. The resulting square pyramid leads to a large positive D of $+16.3$ cm^{-1}, while the trigonal bypiramid leads to a first-order angular momentum in the ground state, and the model Hamiltonian, which only contains spin operators, no longer applies. On the way to the real geometry, we apply an elongation of two equatorial cis ligands on the square pyramid, reducing the D-value to $+11.2$ cm^{-1}. The next distortion that should be applied is an angular out-of-plane distortion of 60° from one the equatorial ligands. This causes, again, a near degeneracy and an appearance of a first-order angular momentum. Alternatively, we constructed a $[Ni(NCH)_5]^{2+}$ model with the same geometry as the first coordination sphere as the real complex **3**. This resulted in a D-value of $+24.4$ cm^{-1}. After replacing two NCH groups by Cl ligands, as in the real complex, D further increases to $+27.7$ cm^{-1}. The only remaining difference with the real complex is the replacement of the three NCH ligands with *i*Prtacn, which reduces the anisotropy to $D = +20$ cm^{-1}. This demonstrates the important interplay between the geometry and the σ-donating character of the ligands in the anisotropy of the complex, whose character is mainly determined by its resemblance to the square pyramid.

4. Conclusions

From the wave functions and the energies of the all-electron Hamiltonian, effective Hamiltonian theory rigorously determines the anisotropic spin Hamiltonian of anisotropic monometallic compounds. The method gives access to all the components of the ZFS tensor and, therefore, leads to the extraction of both the axial D and the rhombic E anisotropy parameters and to the proper magnetic axes frame.

The advantages of the proposed method of extraction are most obvious for the high spin Co(II) compound for which the anisotropy parameters cannot be extracted from the relative energies of the lowest spin−orbit states.

The extracted D and E parameters are in good agreement with the HF-HFEPR data for large magnetic parameters, establishing the precision of the SO-SI method to describe single-ion anisotropy. The main conclusions of the methodological study are that the best results are obtained with wave functions and energies obtained from an enlarged active space that includes ligand orbitals.

Finally, the effective Hamiltonian theory permits the accuracy of the model Hamiltonian to reproduce the physics of the studied systems to be checked. In the present case, the validity of the usual Hamiltonian is confirmed for the d^7 and the d^8 configurations of monometallic complexes. The procedure is now being applied to other d^n configurations and to polymetallic systems in order to extract the interactions of both multispin and giant spin Hamiltonians.

Acknowledgment. We thank Carmen J. Calzado for providing us the basis for the effective Hamiltonian program. Financial support has been provided by the Spanish Ministry of Science and Innovation (Project CTQ2008-06644-C02-01) and the Generalitat de Catalunya (Project 2009SGR462 and Xarxa d'R+D+I en Química Teorica i Computacional, XRQTC). This work was supported by the French Centre National de la Recherche Scientifique (CNRS), Université de Toulouse.

Supporting Information Available: Numerical expression of the effective Hamiltonians for **1**, **2**, and **4**, **D**-tensors for **2**, **3**, and **4**, and orthogonalized projections of the ab initio wave function of **1** on the model space. This material is available free of charge via the Internet at http://pubs.acs.org.

References

(1) Caneschi, A.; Gatteschi, D.; Sessoli, R.; Barra, A. L.; Brunel, L. C.; Guillot, M. *J. Am. Chem. Soc.* **1991**, *113*, 5873.

(2) Friedman, J. R.; Sarachik, M. P.; Tejada, J.; Ziolo, R. *Phys. Rev. Lett.* **1996**, *76*, 3830.

(3) Thomas, C.; Lionti, F.; Ballou, R.; Gatteschi, D.; Sessoli, R.; Barbara, B. *Nature* **1996**, *383*, 145.

(4) Gatteschi, D.; Sessoli, R. *Angew. Chem., Int. Ed.* **2003**, *42*, 246.

(5) Gatteschi, D.; Sessoli R.; Villain J. *Molecular Nanomagnets*; Oxford University Press: Oxford, U.K., 2006.

(6) Neese, F. *ORCA*, Version 2.6; an ab initio, density functional and semiempirical program package; University of Bonn: Bonn, Germany, 2008.

(7) Sinnecker, S.; Neese, F.; Noodleman, L.; Lubitz, W. *J. Am. Chem. Soc.* **2004**, *126*, 2613.

(8) Neese, F.; Solomon, E. I. *Inorg. Chem.* **1998**, *37*, 6568.

(9) Ganyushin, D.; Neese, F. *J. Chem. Phys.* **2006**, *125*, 024103.

(10) Neese, F. *J. Am. Chem. Soc.* **2006**, *128*, 10213.

(11) Neese, F. *J. Chem. Phys.* **2007**, *127*, 164112.

(12) Pederson, M. R.; Khanna, S. N. *Phys. Rev. B: Condens. Matter* **1999**, *60*, 9566.

(13) Kortus, J.; Pederson, M. R.; Baruah, T.; Bernstein, N.; Hellberg, C. S. *Polyhedron* **2003**, *22*, 1871.

(14) Postnikov, A. V.; Kortus, J.; Pederson, M. R. *Phys. Status Solidi B* **2006**, *128*, 9497.

(15) Jackson, K. A.; Pederson, M. R. *Phys. Rev. B: Condens. Matter* **1990**, *42*, 3276.

(16) Pederson, M. R.; Jackson, K. A. *Phys. Rev. B: Condens. Matter* **1990**, *41*, 7453 (see also: http://cst-www.nrl.navy.mil/users/nrlmol).

(17) Reviakine, R.; Arbuznikov, A.; Tremblay, J. C.; Remenyi, C.; Malkina, O.; Malkin, V. G.; Kaupp, M. *J. Phys. Chem.* **2006**, *125*, 054110.

(18) Malkin, V. G.; Malkina, O. L.; Reviakine, R. *RESPECT Program*, Version 2.1, 2005. The property part of the code (MAG-ReSpect) is freely available as binary for LINUX PCs from the authors (vladimir.malkin@savba.sk).

(19) Ruiz, E.; Cirera, J.; Cano, J.; Alvarez, S.; Loose, C.; Kortus, J. *Chem. Commun.* **2008**, *1*, 52.

(20) Loose, C.; Ruiz, E.; Kersting, B.; Kortus, J. *Chem. Phys. Lett.* **2008**, *452*, 38.

(21) Havlas, Z.; Downing, J. W.; Michl, J. *J. Phys. Chem. A* **1998**, *102*, 5681.

(22) Engström, M.; Vahtras, O.; Ågren, H. *Chem. Phys. Lett.* **2000**, *328*, 483.

(23) Karlström, G.; Lindh, R.; Malmqvist, P.-Å.; Roos, B. O.; Ryde, U.; Veryazov, V.; Widmark, P.-O.; Cossi, M.; Schimmelpfennig, B.; Neogrady, P.; Seijo, L. *Comput. Mater. Sci.* **2003**, *28*, 222.

(24) Chibotaru, L.; Ungur, L.; Soncini, A. *Angew. Chem., Int. Ed.* **2008**, *120*, 4194.

(25) Petit, S.; Pilet, G.; Luneau, D.; Chibotaru, L. F.; Ungur, L. *Dalton Trans.* **2007**, 4582.

(26) Soncini, A.; Chibotaru, L. F. *Phys. Rev. B: Condens. Matter* **2008**, *77*, 220406.

(27) Chibotaru, L. F.; Ungur, L.; Aronica, C.; Elmoll, H.; Pilet, G.; Luneau, D. *J. Am. Chem. Soc.* **2008**, *130*, 12445.

(28) Sousa, C.; de Graaf, C. *Int. J. Quantum Chem.* **2006**, *106*, 2470.

(29) Calzado, C. J.; Cabrero, J.; Malrieu, J. P.; Caballol, R. *J. Chem. Phys.* **2002**, *116*, 2728.

(30) Calzado, C. J.; Cabrero, J.; Malrieu, J. P.; Caballol, R. *J. Chem. Phys.* **2002**, *116*, 3985.

(31) Calzado, C. J.; Malrieu, J. P. *Phys. Rev. B: Condens. Matter* **2001**, *63*, 214520.

(32) Bordas, E.; de Graaf, C.; Caballol, R.; Calzado, C. J. *Phys. Rev. B: Condens. Matter* **2005**, *71*, 045108.

(33) Guihéry, N.; Malrieu, J. P. *J. Chem. Phys.* **2003**, *119*, 8956.

(34) Taratiel, D.; Guihéry, N. *J. Chem. Phys.* **2004**, *121*, 7127.

(35) Bastardis, R.; Guihéry, N.; de Graaf, C. *Phys. Rev. B: Condens. Matter* **2006**, *74*, 014432.

(36) Guihéry, N. *Theor. Chem. Acc.* **2006**, *116*, 576.

(37) Bastardis, R.; Guihéry, N.; Suaud, N.; de Graaf, C. *J. Chem. Phys.* **2006**, *125*, 194708.

(38) Bastardis, R.; Guihéry, N.; Suaud, N. *Phys. Rev. B: Condens. Matter* **2007**, *75*, 132403.

(39) Bastardis, R.; Guihéry, N.; de Graaf, C. *Phys. Rev. B: Condens. Matter* **2008**, *77*, 054426.

(40) de P. R. Moreira, I.; Suaud, N.; Guihéry, N.; Malrieu, J. P.; Caballol, R.; Bofill, J. M.; Illas, F. *Phys. Rev. B: Condens. Matter* **2002**, *66*, 134430.

(41) Bastardis, R.; Guihéry, N.; de Graaf, C. *Phys. Rev. B: Condens. Matter* **2007**, *76*, 132412.

(42) Calzado, C. J.; de Graaf, C.; Bordas, E.; Caballol, R.; Malrieu, J. P. *Phys. Rev. B: Condens. Matter* **2003**, *67*, 132409.

(43) Boča, R. *Theoretical Foundations of Molecular Magnetism*; Elsevier: Amsterdam, The Netherlands, 1999, 642−680.

(44) Boča, R. *Coord. Chem. Rev.* **2004**, *248*, 757.

(45) Park, K. N.; Pederson, M. R.; Richardson, S. L.; Aliaga-Alcalde, N.; Christou, G. *Phys. Rev. B: Condens. Matter* **2003**, *68*, 020405.

(46) Rogez, G.; Rebilly, J. N.; Barra, A. L.; Sorace, L.; Blondin, G.; Kirchner, N.; Duran, M.; Van Slageren, J.; Parsons, S.; Ricard, L.; Marvilliers, A.; Mallah, T. *Angew. Chem., Int. Ed.* **2005**, *44*, 1876.

(47) Charron, G.; Bellot, F.; Cisnetti, F.; Pelosi, G.; Rebilly, J. N.; Riviere, E.; Barra, A. L.; Mallah, T.; Policar, C. *Chem. Eur. J.* **2007**, *13*, 2774.

(48) Rebilly, J. N.; Charron, G.; Riviere, E.; Guillot, R.; Barra, A. L.; Serrano, M. D.; Van Slageren, J.; Mallah, T. *Chem. Eur. J.* **2008**, *14*, 1169.

(49) Krzystek, J.; Zvyagin, S. A.; Ozarowski, A.; Fiedler, A. T.; Brunold, T. C.; Tesler, J. *J. Am. Chem. Soc.* **2004**, *126*, 2148.

(50) Carlin, R. L.; Chirico, R. D.; Sinn, E.; Mennenga, G.; de Jongh, L. J. *Inorg. Chem.* **1982**, *21*, 2218.

(51) Malmqvist, P.-Å.; Roos, B. O. *Chem. Phys. Lett.* **1989**, *155*, 189.

(52) Malmqvist, P.-Å.; Roos, B. O.; Schimmelpfennig, B. *Chem. Phys. Lett.* **2002**, *357*, 230.

(53) Douglas, N.; Kroll, N. M. *Ann. Phys.* **1974**, *82*, 89.

(54) Hess, B. *Phys. Rev. A: At., Mol., Opt. Phys.* **1986**, *33*, 3742.

(55) Llusar, R.; Casarrubios, M.; Barandiarán, Z.; Seijo, L. *J. Chem. Phys.* **1996**, *105*, 5321.

(56) Baradiarán, Z.; Seijo, L. *J. Chem. Phys.* **2003**, *118*, 7439.

(57) Roos, B. O.; Lindh, R.; -Å.; Malmqvist, P.; Veryazov, V.; Widmark, P. O. *J. Phys. Chem. A* **2005**, *109*, 6575.

(58) Bloch, C. *Nucl. Phys.* **1958**, *6*, 329.

(59) des Cloizeaux, J. *Nucl. Phys.* **1960**, *20*, 321.

CT900326E

Supporting Information

Universal theoretical approach to extract anisotropic spin Hamiltonians

Rémi Maurice,[a,c] Roland Bastardis,[b] Coen de Graaf,[c,e] Nicolas Suaud, [a]
Talal Mallah,[d] and Nathalie Guihéry[a]

[a] Laboratoire de Chimie et Physique Quantiques, IRSAMC/UMR5626 Université Paul Sabatier, 118 route de Narbonne, F-31062 Toulouse Cédex 4, France.

[b] Laboratoire de Mathématiques, Physiques et Systèmes, Université de Perpignan Via Domitia, 52 avenue Paul Alduy, 66860 Perpignan, France.

[c] Departament de Química Física i Inorgànica, Universitat Rovira i Virgili, Marcel·lí Domingo s/n, 43007 Tarragona, Spain.

[d] Institut de Chimie Moléculaire et des Matériaux d'Orsay, Université Paris sud 11, 91405 Orsay, France.

[e] Institució Catalana de Recerca i Estudis Avançats (ICREA), Passeig Lluis Companys 23, 08010, Barcelona, Spain

Contents:

- Numerical expression of the effective Hamiltonian for **2**, **3**, and **4**
- D-tensors for **2**, **3**, and **4**
- Orthogonalized projections of the *ab initio* wave function of **1** on the model space

Effective Hamiltonian for **2**

	$\|1,-1\rangle$	$\|1,0\rangle$	$\|1,1\rangle$
$\langle 1,-1\|$	5.741	$-2.181+1.894i$	$-0.533-2.210i$
$\langle 1,0\|$	$-2.181-1.894i$	4.716	$2.181-1.894i$
$\langle 1,1\|$	$-0.533+2.210i$	$2.181+1.894i$	5.741

Effective Hamiltonian for **3**

	$\|1,-1\rangle$	$\|1,0\rangle$	$\|1,1\rangle$
$\langle 1,-1\|$	12.069	$-3.667+5.134i$	$3.613-2.926i$
$\langle 1,0\|$	$-3.667-5.134i$	8.767	$3.667-5.134i$
$\langle 1,1\|$	$3.613+2.926i$	$3.667+5.134i$	12.069

Effective Hamiltonian for **4**

	$\|\frac{3}{2},-\frac{3}{2}\rangle$	$\|\frac{1}{2},-\frac{1}{2}\rangle$	$\|\frac{1}{2},\frac{1}{2}\rangle$	$\|\frac{3}{2},\frac{3}{2}\rangle$
$\|\frac{3}{2},-\frac{3}{2}\rangle$	0.203	2.282	-0.889	0.000
$\|\frac{1}{2},-\frac{1}{2}\rangle$	2.282	29.549	0.000	-0.889
$\|\frac{1}{2},\frac{1}{2}\rangle$	-0.889	0.000	29.549	-2.282
$\|\frac{3}{2},\frac{3}{2}\rangle$	0.000	-0.889	-2.282	0.203

D-tensor for **2**:

$$\begin{pmatrix} 1.825 & -2.210 & 3.084 \\ -2.210 & 2.891 & -2.679 \\ 3.084 & -2.679 & 3.383 \end{pmatrix}$$

Diagonalized D-tensor for **2**:

$$\begin{pmatrix} 8.099 & 0.0 & 0.0 \\ 0.0 & -0.583 & 0.0 \\ 0.0 & 0.0 & 0.583 \end{pmatrix}$$

D-tensor for **3**:

$$\begin{pmatrix} 7.997 & -2.926 & 5.186 \\ -2.926 & 0.772 & -7.261 \\ 5.186 & -7.261 & 7.684 \end{pmatrix}$$

Diagonalized D-tensor for **3**:

$$\begin{pmatrix} 16.454 & 0.0 & 0.0 \\ 0.0 & 3.822 & 0.0 \\ 0.0 & 0.0 & -3.822 \end{pmatrix}$$

D-tensor for **4**:

$$\begin{pmatrix} 8.255 & 0.0 & -1.317 \\ 0.0 & 9.461 & 0.0 \\ -1.317 & 0.0 & -5.815 \end{pmatrix}$$

Diagonalized D-tensor for **4**:

$$\begin{pmatrix} 9.461 & 0.0 & 0.0 \\ 0.0 & 8.377 & 0.0 \\ 0.0 & 0.0 & -5.937 \end{pmatrix}$$

Orthonormalized projections of the *ab initio* wave functions of **1** on the model space:

$$\widetilde{\Psi}_1 = (0.0447 + i0.0928)|1,-1\rangle + (-0.6709 + i0.7271)|1,0\rangle + (0.0960 + i0.0371)|1,1\rangle$$

$$\widetilde{\Psi}_2 = (-0.3962 + i0.5806)|1,-1\rangle + (0.0621 + i0.0887)|1,0\rangle - (0.6813 - i0.1733)|1,1\rangle$$

$$\widetilde{\Psi}_3 = (0.7033 + i0.0262)|1,-1\rangle - (0.0901) + i0.0369)|1,0\rangle - (0.5203 + i0.4739)|1,1\rangle$$

Magnetic interactions in $LiCu_2O_2$: Single-chain versus double-chain models

Rémi Maurice,[1] Abdul-Muizz Pradipto,[1] Coen de Graaf,[1,2,3] and Ria Broer[1,*]
[1]*Zernike Institute for Advanced Materials, University of Groningen, Groningen 9747AG, The Netherlands*
[2]*Departament de Química Física i Inorgànica, Universitat Rovira i Virgili, Marcel·lí Domingo s/n, 43007 Tarragona, Spain*
[3]*Institució Catalana de Recerca i Estudis Avançats (ICREA), Passeig Lluis Companys 23, 08010 Barcelona, Spain*
(Received 29 February 2012; revised manuscript received 8 May 2012; published 10 July 2012)

The possible origin of the spiral spin structure in multiferroic $LiCu_2O_2$ is studied by calculating all relevant isotropic and anisotropic magnetic interactions in the material. The coupling constants are extracted from accurate *ab initio* quantum chemical calculations with an effective Hamiltonian theory. First, the anisotropic or Dzyaloshinskii-Moriya interactions are found to be negligible. Secondly, we obtain small isotropic interactions of the spin moments located on different chains, which classifies the material as a quasi-one-dimensional magnetic system. The intrachain isotropic interactions between nearest neighbors are relatively large and ferromagnetic, while second-neighbor interactions along the chain have antiferromagnetic character and are about half the magnitude of the former. This frustration leads to a spiral spin structure, which can be subjected to electric polarization.

DOI: 10.1103/PhysRevB.86.024411 PACS number(s): 75.30.Et, 71.10.Li, 71.70.Gm, 75.10.Pq

An important class of multiferroics is formed by the materials that simultaneously exhibit (anti)ferromagnetism and ferroelectricity. Particularly interesting are those materials in which these properties are coupled, since this can lead to mechanisms to control ferroelectricity by external magnetic fields or vice versa, as demonstrated by Kimura *et al.* in $TbMnO_3$.[1] More recently, the $LiCu_2O_2$ ionic material has been studied by many scientists. Initially, attention was focused on its magnetic properties,[2–4] but later the compound gained even more interest when ferroelectric behavior was evidenced.[5] However, both the relative magnitude of the different magnetic interactions[2–4,6,7] and the origin of the ferroelectric properties[5,8–12] remain controversial. In particular, to what extent this material can be considered a single-chain one-dimensional system is still a subject of discussion.[9] Based on a combination of a local density approach with modified intra-atomic Coulomb interactions (LDA + U) calculations and nuclear magnetic resonance (NMR) measurements, Gippius and co-workers[2] concluded that the interchain interactions are significantly smaller than the intrachain ones, while Masuda *et al.* reported large interchain interactions based on inelastic neutron scattering data.[4,7] The latter picture gives rise to a double-chain frustrated model, where the frustration is due to interchain and next-nearest-neighbor intrachain antiferromagnetic interactions that compete with the ferromagnetic nearest-neighbor intrachain ones.

Different explanations for the origin of the spin current[13,14] leading to ferroelectricity in this spiral magnet can be envisaged, involving (i) the inverse Dzyaloshinskii-Moriya (DM) mechanism; (ii) the frustration in either the single or double chains, which leads to spiral-magnetic ferroelectrics;[5] or even (iii) the nonstoichiometry of the compound.[8] Here, we check the relevance of the mechanisms (i) and (ii) by addressing the magnitude of the magnetic interactions in the stoichiometric structure. Furthermore, we bring additional information on the orientation of the local classical spin and on the spiral ordering by determining the orientation of the DM pseudovectors. One should note that different orientations for the spiral ordering have been proposed in the literature[3,5,15] and that no consensus has been reached yet on this question. The theoretical determination of the magnetic interactions in a nonstoichiometric structure would be highly interesting to address the role of (iii) in the multiferroicity of this material. However, unfortunately this task is not easily doable in practice due to the lack of information on the (nonstoichiometric) structure, and therefore it is beyond the scope of the present work.

To provide detailed, unbiased information on the magnetic interactions in the stoichiometric $LiCu_2O_2$ structure, *ab initio* wave-function-based calculations are used within the embedded cluster approach. Due to the local character of the magnetic couplings, accurate J_{ij} values can be obtained from embedded cluster calculations[16] provided that the clusters and embedding are consistently chosen, and that accurate N-electron wave functions are used. To address the relevance of the clusters and their embedding schemes, it is useful to compare the results obtained with the embedded clusters with periodic calculations at a given level of theory. This comparison is usually done at the unrestricted Hartree-Fock (UHF) level with an Ising Hamiltonian ($\hat{H}_{\text{Ising}} = \sum_{ij} J_{ij}^{\text{Ising}} \hat{S}_i^z \hat{S}_j^z$). However, an accurate determination of the magnetic couplings requires a rigorous incorporation of the electron correlation in the theoretical treatment, as analyzed in detail by Calzado *et al.*[17–19] This requires a variational treatment of all the excited Slater determinants that contribute to the energy difference between the magnetic states at second order of perturbation, i.e., one has to invoke at least difference-dedicated configuration interaction (DDCI).[20] Once accurate energy differences between the magnetic states are obtained, the magnetic coupling parameters are extracted with the effective Hamiltonian theory[21] by mapping the energies and projected wave functions onto the Heisenberg-Dirac–van Vleck (HDVV) Hamiltonian ($\hat{H} = \sum_{ij} J_{ij} \hat{\mathbf{S}}_i . \hat{\mathbf{S}}_j$). The DM pseudovector can be computed in a similar way when the spin-orbit coupling is accounted for in the calculation.[22,23]

The experimental structure of the rhombohedral $LiCu_2O_2$ crystal[24] as shown in Fig. 1 is used in all the calculations. $LiCu_2O_2$ is a mixed-valence compound: double $LiCuO_2$ layers containing (formally) Cu(II) ions are separated by layers of nonmagnetic Cu(I) ions. The intrachain interactions occur

 ©2012 American Physical Society

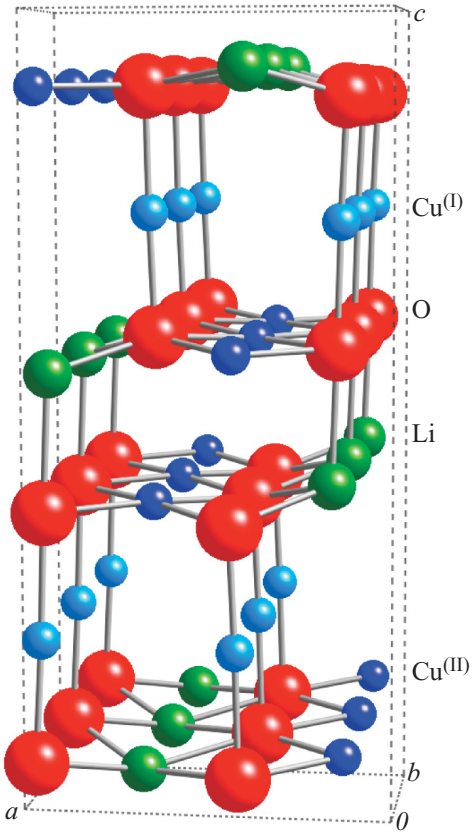

FIG. 1. (Color online) Crystal structure of $LiCu_2O_2$.[24]

along the b axis, as can be seen in Fig. 1. Intrachain and interchain clusters containing two and three copper centers have been considered to extract the magnetic interactions. Clusters 1 and 1b are intrachain clusters with two or three copper centers, respectively. They are depicted in Fig. 2. In cluster 1b, the three copper ions are effectively coupled through the nearest-neighbor interaction J_1 and the next-nearest-neighbor interaction J_2 (see Fig. 3). Clusters 2 and 2b are interchain clusters containing either two or three copper centers and are represented in Fig. 4. In this last cluster, the three copper ions occupy the corners of an isosceles triangle, interacting through J_1 along the chain and twice through J_{DC} among different chains, where DC stands for the "double-chain" interaction (see Fig. 5). In addition to the copper ions, the clusters contain all oxygen ions directly coordinated to the metal ions, as well as the first shell of lithium ions. The necessity of treating explicitly this shell of lithium ions was previously evidenced in the closely related Li_2CuO_2 system, for which it was shown that the quality of the treatment of the lithium ions affects the spin density on the bridging oxygen atoms, and hence strongly affects the next-nearest neighbor magnetic interactions while moderately affecting the nearest-neighbor ones.[25,26] The next shell of oxygen and copper ions is represented by *ab initio* model potentials (AIMPs) that have been optimized through the self-consistent field embedded ion (SCEI) procedure.[27] A large set of point charges located at lattice sites around the cluster has been optimized to accurately fit the Madelung potential on a grid centered in the cluster. This way of defining the clusters and their embeddings has been used successfully in many other works dealing with effective magnetic interactions, while only recently has it become possible to include anisotropic effective interactions.[23]

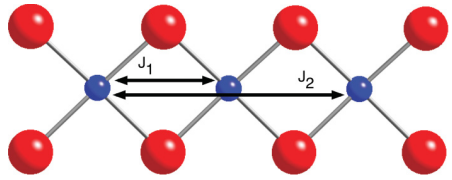

FIG. 3. (Color online) Magnetic interaction paths for J_1 and J_2 in cluster 1b. Explicitly treated copper atoms in blue and oxygen atoms in red; lithium ions are not shown for clarity.

It is good practice in embedded cluster studies to validate the employed clusters and embeddings. In the present study, this is done by comparing the outcomes of UHF and unrestricted density functional theory with the hybrid B3LYP functional, UDFT(B3LYP), obtained from periodic and cluster approaches. The periodic calculations are performed with the CRYSTAL09 program package.[28] The cluster calculations are performed with the MOLCAS code.[29] The same contracted Gaussian-type basis sets have been used for both types of calculations, i.e., Cu($6s5p2d$), O($3s2p$), and Li($2s1p$).[30] As expected, the periodic calculations confirm the mixed-valence character of the compound. We then considered different supercells and the above-described clusters to extract nearest

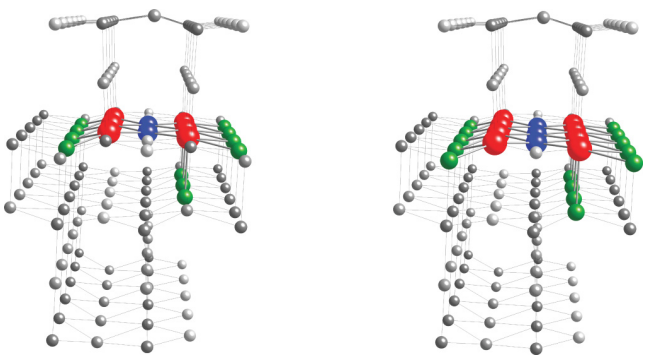

FIG. 2. (Color online) Cluster 1 (left) and cluster 1b (right). Explicitly treated atoms in blue (copper), red (oxygen), and green (lithium); other atoms in gray.

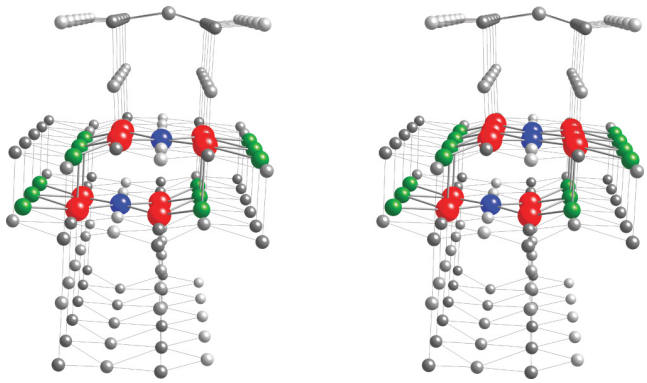

FIG. 4. (Color online) Cluster 2 (left) and cluster 2b (right). Explicitly treated atoms in blue (copper), red (oxygen), and green (lithium); other atoms in gray.

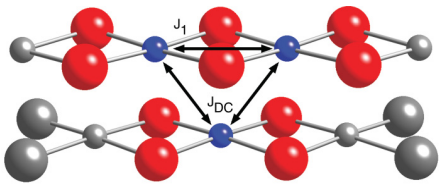

FIG. 5. (Color online) Magnetic interaction paths for J_1 and J_{DC} in cluster 2b. Explicitly treated copper atoms in blue and oxygen atoms in red; lithium ions are not shown for clarity; other atoms in gray.

intrachain (J_1^{Ising}) and interchain (J_{DC}^{Ising}) interactions (following the notations of Seki *et al.*[9]) of the Ising model. The results are presented in Table I. The magnetic coupling parameters extracted from the embedded cluster calculations closely reproduce the trends observed in the periodic calculations at both levels of theory. A large ferromagnetic intrachain nearest-neighbor interaction (i.e., a large negative J_1 value) is combined with a smaller antiferromagnetic interchain interaction (i.e., a small positive J_{DC} value). As expected, the B3LYP coupling parameters are much larger than the ones obtained at the UHF level.[31] The UHF and B3LYP results are known to give very different coupling parameters, and none of these levels of theory is expected to give sufficiently accurate descriptions of the magnetic couplings. Here, we present both UHF and B3LYP results to show that the reasonably good agreement of the cluster calculations with the periodic ones is independent of the levels of theory used in the calculation, although the computed magnetic couplings are strongly dependent on these. The use of other functionals than the B3LYP considered here could lead to important changes in the calculated magnitude of the couplings.[32] However, this does not affect the agreement found between periodic and embedded cluster calculations, since both approaches would suffer very similar variations upon changing the functional. It is then concluded at this stage that the clusters and embeddings are consistently built, and that embedded cluster calculations provide a good description of the magnetic interactions calculated at the same level of approximation in the $LiCu_2O_2$ crystal. Of course UHF and UDFT(B3LYP) results cannot be used to obtain quantitative estimates of the ratios between different (competing) interactions.[23]

To provide quantitative estimates of the magnetic coupling parameters, we give an accurate description of the N-electron wave functions in the clusters by applying the DDCI scheme.[20] This scheme, which is implemented in the CASDI code,[33] provides an efficient way to include electron correlation in the *ab initio* description of the electronic structure. It is similar to the method recently described by Hozoi and co-workers[34,35]

TABLE I. UHF and UDFT(B3LYP) magnetic coupling constants (in meV) obtained from cluster and periodic calculations. The Ising model Hamiltonian $\hat{H}_{\text{Ising}} = \sum_{ij} J_{ij}^{\text{Ising}} \hat{S}_i^z \hat{S}_j^z$ is used to extract J values from the energy eigenvalues.

UHF/UDFT(B3LYP)	Cluster	Periodic
J_1^{Ising}	−16.0/ −42.2	−10.4/ −33.6
J_{DC}^{Ising}	0.3/0.3	0.8/0.8

TABLE II. CASSCF magnetic coupling constants (in meV) obtained from embedded clusters with two and three Cu ions. The HDVV model Hamiltonian $\hat{H}_{\text{HDVV}} = \sum_{ij} J_{ij} \hat{\mathbf{S}}_i . \hat{\mathbf{S}}_j$ is used to extract J values from the energy eigenvalues.

	J_1	J_2	J_{DC}
Cluster 1	−4.8		
Cluster 1b	−4.8	1.1	
Cluster 2			−0.1
Cluster 2b	−4.8		0.0

to study the d-d transitions in related cuprate compounds. The applied basis set to describe the one-electron functions is especially designed to recover the semicore and valence electron correlation. We use atomic natural orbitals relativistic with core correlation (ANO-RCC) basis sets[36] with the following contractions: Cu($6s5p4d$), O($4s3p1d$), and Li($2s$). The complete active space self consistent field (CASSCF) and DDCI results are reported in Tables II and III, respectively. As expected, CASSCF only accounts for about 30% of the DDCI J_1 value, due to the lack of dynamic correlation. J_2 is even more drastically affected by the introduction of dynamic correlation (from 1.1 meV at the CASSCF level to 7.1 meV at the DDCI level), while J_{DC} is very small at both CASSCF and DDCI levels. Experience has shown that CASSCF usually accounts for 20–30 % of the J values, while the more accurate DDCI results usually account for 70–90 % of these values. Therefore, we will use the DDCI results in the rest of the discussion.

The cluster wave functions are spin eigenfunctions, and we map the energies on the Heisenberg Hamiltonian. In all the clusters where J_1 is accessible, a similar value of about −15 meV is obtained, confirming the large ferromagnetic intrachain nearest-neighbor interaction. The intrachain next-nearest-neighbor interaction, J_2, is found to be antiferromagnetic and of sufficient magnitude to compete with the ferromagnetic J_1, and its value is in agreement with experimental and previous theoretical estimates. Our results for the different magnetic couplings are indeed in good agreement with the LDA + U calculations of Gippius *et al.* ($J_1 = -13.9$ meV, $J_2 = 10.1$ meV, and $J_{DC} = 0.5$ meV).[2,4] The obtained ratio of J_2 and J_1 is expected to lead to a long-range spiral-type ordering of the spins in a classical picture.[37]

Due to the symmetry of the crystal,[24] no interchain DM interaction is expected, while it may be present for neighboring ions located on the same chain.[38,39] Following the strategy applied earlier in the CuO material,[23] we computed the DM pseudovector in cluster 1. In this cluster, a symmetry plane

TABLE III. DDCI magnetic coupling constants (in meV) obtained from embedded clusters with two and three Cu ions. The HDVV model Hamiltonian $\hat{H}_{\text{HDVV}} = \sum_{ij} J_{ij} \hat{\mathbf{S}}_i . \hat{\mathbf{S}}_j$ is used to extract J values from the energy eigenvalues.

	J_1	J_2	J_{DC}
Cluster 1	−17.6		
Cluster 1b	−14.8	7.1	
Cluster 2			0.1
Cluster 2b	−14.1		−0.1

is present in the *ac* direction, and this symmetry plane can transform one magnetic center into another one. As a consequence, the DM vector is expected to be along this *ac* plane. The determination of the orientation of the DM vector can give important information on the orientation of the local classical spins and hence on the spiral ordering: if the DM vector is found in the *a* direction, then the spins should be oriented within the *bc* plane; if the DM vector is found in the *c* orientation, the spins should be oriented within the *ab* place; and if the DM vector has nonzero components in both *a* and *c* orientations, then the spins are oriented in a tilted plane in between the *ab* and *bc* planes. However, our *ab initio* calculations show that the DM vector is extremely small ($|\bar{d}| < 0.02$ meV) and falls below the intrinsic numerical accuracy of the method. In fact, the structure is rather close to having inversion symmetry located between two adjacent Cu ions along the chains. Therefore, it is not unexpected that the DM vector almost vanishes and that the orientation of the DM vector cannot be used to give further information on the spiral ordering in this compound. At this stage, one could argue that the orientation of the local classical spins in this compound is still an open question, but one could also question the role played by the DM interaction on the properties of the compound given the smallness of the calculated DM vector.

Another important result concerns the magnitude of the interchain interactions, i.e., the magnitude of J_{DC}. As can be seen in Table III, in none of our calculations was a sufficiently large J_{DC} value obtained to induce competition with the intrachain interactions. According to our long-standing experience, this result is not sensitive to the extension of the clusters. The two orders of magnitude difference indicates that the compound is essentially a frustrated single-chain one-dimensional system, as suggested by Gippius *et al.*[2] The hypothesis of a frustrated double-chain system, as suggested by Masuda *et al.*,[3,4] is not supported by our calculations. Since the interchain interactions are negligible in this system, one would consider that the intrachain couplings are responsible for the multiferroicity. However, despite the frustration observed in this chain, the DM interaction is almost negligible. As a consequence, the DM interaction is not likely to cause any significant electric polarization and cannot be the main origin of the multiferroicity in $LiCu_2O_2$. The multiferroic behavior of $LiCu_2O_2$ can then come from the frustration along the *b* orientation and/or be linked to the nonstoichiometry of the crystal samples,[3,8,11] but not from direct DM interaction.

The authors thank N. Guihéry for her contribution in the development of the extraction method used in this work, and M. Mostovoy and S. Artyukhin for stimulating discussions. This work was supported by the Spanish ministry of Science and Innovation (Project CTQ2011-23140).

*r.broer@rug.nl

[1] T. Kimura, T. Goto, H. Shintani, K. Ishizaka, T. Arima, and Y. Tokura, Nature (London) **426**, 55 (2003).
[2] A. A. Gippius, E. N. Morozova, A. S. Moskvin, A. V. Zalessky, A. A. Bush, M. Baenitz, H. Rosner, and S.-L. Drechsler, Phys. Rev. B **70**, 020406 (2004).
[3] T. Masuda, A. Zheludev, A. Bush, M. Markina, and A. Vasiliev, Phys. Rev. Lett. **92**, 177201 (2004).
[4] T. Masuda, A. Zheludev, B. Roessli, A. Bush, M. Markina, and A. Vasiliev, Phys. Rev. B **72**, 014405 (2005).
[5] S. Park, Y. J. Choi, C. L. Zhang, and S.-W. Cheong, Phys. Rev. Lett. **98**, 057601 (2007).
[6] S.-L. Drechsler, J. Málek, J. Richter, A. S. Moskvin, A. A. Gippius, and H. Rosner, Phys. Rev. Lett. **94**, 039705 (2005).
[7] T. Masuda, A. Zheludev, A. Bush, M. Markina, and A. Vasiliev, Phys. Rev. Lett. **94**, 039706 (2005).
[8] A. S. Moskvin and S.-L. Drechsler, Phys. Rev. B **78**, 024102 (2008).
[9] S. Seki, Y. Yamasaki, M. Soda, M. Matsuura, K. Hirota, and Y. Tokura, Phys. Rev. Lett. **100**, 127201 (2008).
[10] C. Fang, T. Datta, and J. Hu, Phys. Rev. B **79**, 014107 (2009).
[11] A. S. Moskvin, Y. D. Panov, and S.-L. Drechsler, Phys. Rev. B **79**, 104112 (2009).
[12] S. Furukawa, M. Sato, and S. Onoda, Phys. Rev. Lett. **105**, 257205 (2010).
[13] H. Katsura, N. Nagaosa, and A. V. Balatsky, Phys. Rev. Lett. **95**, 057205 (2005).
[14] M. Mostovoy, Phys. Rev. Lett. **96**, 067601 (2006).
[15] L. Zhao, K.-W. Yeh, S. M. Rao, T.-W. Huang, P. Wu, W.-H. Chao, C.-T. Ke, C.-E. Wu, and M.-K. Wu, E. P. L. **97**, 37004 (2012).
[16] I. de P. R. Moreira, F. Illas, C. J. Calzado, J. F. Sanz, J.-P. Malrieu, N. B. Amor, and D. Maynau, Phys. Rev. B **59**, R6593 (1999).
[17] C. J. Calzado, J. Cabrero, J. P. Malrieu, and R. Caballol, J. Chem. Phys. **116**, 2728 (2002).
[18] C. J. Calzado, J. Cabrero, J. P. Malrieu, and R. Caballol, J. Chem. Phys. **116**, 3985 (2002).
[19] C. J. Calzado, C. Angeli, D. Taratiel, R. Caballol, and J.-P. Malrieu, J. Chem. Phys. **131**, 044327 (2009).
[20] J. Miralles, O. Castell, R. Caballol, and J.-P. Malrieu, Chem. Phys. **172**, 33 (1993).
[21] C. Bloch, Nucl. Phys. **6**, 329 (1958).
[22] R. Maurice, A. M. Pradipto, N. Guihéry, R. Broer, and C. de Graaf, J. Chem. Theor. Comput. **6**, 3092 (2010).
[23] A.-M. Pradipto, R. Maurice, N. Guihéry, C. de Graaf, and R. Broer, Phys. Rev. B **85**, 014409 (2012).
[24] R. Berger, P. Önnerud, and R. Tellgren, J. Alloys Comp. **184**, 315 (1992).
[25] C. de Graaf, I. de P. R. Moreira, and F. Illas, Int. J. Mol. Sci. **1**, 28 (2000).
[26] C. de Graaf, I. de P. R. Moreira, F. Illas, O. Iglesias, and A. Labarta, Phys. Rev. B **66**, 014448 (2002).
[27] Z. Barandiaran and L. Seijo, J. Chem. Phys. **89**, 5739 (1988).
[28] R. Dovesi, V. R. Saunders, C. Roetti, R. Orlando, C. M. Zicovich-Wilson, F. Pascale, B. Civalleri, K. Doll, N. M. Harrison, I. J. Bush *et al.*, *CRYSTAL09 package*, University of Torino, Italy.
[29] F. Aquilante, L. De Vico, N. Ferre, G. Ghigo, P. A. Malmqvist, P. Neogrady, T. B. Pedersen, M. Pitonak, M. Reiher, B. O. Roos *et al.*, J. Comp. Chem. **31**, 224 (2010).

[30]K. Doll and N. M. Harrison, Chem. Phys. Lett. **317**, 282 (2000).
[31]I. de P. R. Moreira and F. Illas, PhysChemChemPhys **8**, 1645 (2006).
[32]R. L. Martin and F. Illas, Phys. Rev. Lett. **79**, 1539 (1997).
[33]D. Maynau and N. Ben Amor, *CASDI Suite of Programs*, Université Paul Sabatier, Toulouse, France.
[34]L. Hozoi, L. Siurakshina, P. Fulde, and J. van den Brink, Nature Sci. Rep. **1**, 65 (2011).
[35]H.-Y. Huang, N. A. Bogdanov, L. Siurakshina, P. Fulde, J. van den Brink, and L. Hozoi, Phys. Rev. B **84**, 235125 (2011).
[36]B. O. Roos, R. Lindh, P. A. Målmqvist, V. Veryazov, and P. O. Widmark, J. Phys. Chem. A **109**, 6575 (2005).
[37]S. Blundell, *Magnetism in Condensed Matter* (Oxford University Press, Oxford, 2001).
[38]T. Moriya, Phys. Rev. **120**, 91 (1960).
[39]A. D. Buckingham, P. Pyykko, J. B. Robert, and L. Wiesenfeld, Mol. Phys. **46**, 177 (1982).

PCCP

PAPER

View Article Online
View Journal | View Issue

Cite this: *Phys. Chem. Chem. Phys.*, 2016, **18**, 32703

Unraveling the hydration-induced ground-state change of AtO^+ by relativistic and multiconfigurational wave-function-based methods†

Dumitru-Claudiu Sergentu,[ab] Florent Réal,[c] Gilles Montavon,[a] Nicolas Galland*[b] and Rémi Maurice*[a]

Received 19th July 2016,
Accepted 24th October 2016

DOI: 10.1039/c6cp05028j

www.rsc.org/pccp

Published on 26 October 2016. Downloaded on 09/12/2016 12:27:15.

The AtO^+ cation is one of the main chemical forms that appear in the astatine Pourbaix diagram. This form can react with closed-shell species in solution, while in the gas phase, it has a spin-triplet ground spin–orbit-free (SOF) state. Spin–orbit coupling (SOC) mixes its $M_S = 0$ component with the $^1\Sigma^+$ singlet-spin component, while keeping an essentially-spin-triplet SOC ground-state. Therefore, it was suggested that AtO^+ undergoes a hydration-induced ground-state change to explain its reactivity in solution with closed-shell species [*J. Phys. Chem. B*, 2013, **117**, 5206–5211]. In this work, we track the nature of the low-lying SOF and SOC states when the hydration sphere of AtO^+ is stepwise increased, using relativistic and multiconfigurational wave-function-based methods. This work clarifies previous studies by (i) giving additional arguments justifying a solvation-induced ground-state change in this system and (ii) clearly identifying for the first time the nature of the involved SOF and SOC many-electron states. Indeed, we find at the SOF level that AtO^+ undergoes a ground-state reversal between $^3\Sigma^-$ and the closed-shell component of $^1\Delta$, which leads to an essentially-spin-singlet and closed-shell SOC ground-state. This explains the observed reactivity of AtO^+ with closed-shell species in solution.

1 Introduction

In most cases, environmental effects only moderately affect the nature of the ground-state of molecular systems. This is why it is usually wise to study such systems in a vacuum to get a first picture on their ground-state electronic structures. However, in some peculiar cases, such a picture may be qualitatively incorrect, *e.g.* when an environment-induced ground-state reversal occurs. Molecular systems which are prone to such phenomena typically exhibit small energy gaps between their ground-state and one or more excited states in the gas phase, as in actinide-containing systems. For instance, CUO and UO_2 are notorious examples that exhibit ground-state reversals upon interaction within argon matrices.[1–4] In these cases two electronic states are reversed, which correlate with $^1\Sigma^+$ and $^3\Phi$ for CUO, and with $^3\Phi_u$ and ^3H_g for UO_2. We note that in these two cases, the electronic states involved in the reversal are separated by less than ~0.2 eV in a vacuum.

Recently, the AtO^+ cation was suggested to undergo a solvation-induced ground-state change in aqueous solution.[5,6] In the gas phase, this cation has a $^3\Sigma^-$ ground spin–orbit-free (SOF) state, separated by ~0.6 eV from the first singlet-spin state, $^1\Delta$.[7,8] Spin–orbit coupling (SOC) leads to an $X0^+$ ground-state that essentially consists of the $M_S = 0$ component of $^3\Sigma^-$ (~70%) and $^1\Sigma^+$ (~25%), another SOF singlet-spin state that appears ~1 eV above $^3\Sigma^-$ in the SOF spectrum.[7,8] However, in aqueous solution, the AtO^+ cation readily reacts with simple closed-shell anionic species such as Cl^-, Br^-, SCN^- and OH^-,[9–11] which implies that the involved reactions are not spin forbidden. Although SOC in the gas phase already leads to a noticeable singlet-spin character in the ground-state of AtO^+, a feature which was later found compatible with four-component calculations,[7] Ayed *et al.* extensively discussed the influence of hydration on the nature of the ground-state of this species by means of relativistic density functional theory (DFT).[5,6] They hypothesized that hydration induces a ground-state change in AtO^+, leading to an essentially-spin-singlet SOC ground state. Their work can be the subject of two main critics: (i) the use of single-determinental calculations may lead to incorrect nature of the obtained

[a] *SUBATECH, UMR CNRS 6457, IN2P3/EMN Nantes/Université de Nantes, 4 Rue A. Kastler, BP 20722, 44307 Nantes Cedex 3, France. E-mail: remi.maurice@subatech.in2p3.fr*

[b] *CEISAM, UMR CNRS 6230, Université de Nantes, 44322 Nantes Cedex 3, France. E-mail: nicolas.galland@univ-nantes.fr*

[c] *PhLAM, UMR CNRS 8523, Université de Lille 1, 59655 Villeneuve d'Ascq Cedex, France*

† Electronic supplementary information (ESI) available: Energies of the $S_0(^1\Delta)$ and $S_1(^1\Delta)$ electronic states of the AtO^+ (H_2O) system computed at the NEVPT2/AVTZ level of theory and compositions of the five lowest spin–orbit coupled states at the equilibrium spin-restricted-singlet AtO^+ $(H_2O)_n$ (n = 3–5) geometries. See DOI: 10.1039/c6cp05028j

Published on 26 October 2016. Downloaded on 09/12/2016 12:27:15.

electronic states and (ii) the choice of the exchange–correlation functional may not be the most appropriate one.[7] In this work, we thus aim at clarifying the origin of the non-spin-forbidden complexation that occurs in solution by assessing the respective roles of water molecules belonging to solvation shells and of SOC.

Actually, the AtO^+ cation is an important species in the astatine Pourbaix (*E*-pH) diagram,[10–13] since it can predominate,[12] and since it is the basic unit of the hydrolyzed AtO(OH) and $AtO(OH)_2^-$ species that also appear in this diagram.[10,11] Note that the exploration of the physico-chemical properties of astatine compounds hardly advanced in the last few decades due to the experimental difficulties that trigger the radioactive nature and the actual half-life times of its most stable isotopes.[14] Indeed, the ^{210}At ($t_{1/2}$ = 8.1 h) and ^{211}At ($t_{1/2}$ = 7.2 h) radionuclides can only be studied at ultra-trace scales, typically after artificial production by irradiation of bismuth targets with alpha beams.[15] However, since the ^{211}At isotope is recognized as a promising candidate for nuclear medicine,[16] a strong and recent interest appeared for more fundamental studies on the chemistry of astatine and its compounds.[14,17–19] In this context, it appears crucial and timely to (i) provide new arguments to justify the occurrence of a hydration-induced ground-state change in AtO^+ and (ii) properly characterize the nature of the involved many-electron states, which are the two main objectives of the present work. To avoid the potential issues of the previous studies,[5–7] we study the stepwise hydration of AtO^+ using relativistic and multiconfigurational wave-function-based approaches, which proved to be accurate enough to study the zero-field splittings (ZFSs) of various 6p diatomics,[8,20] as well as to properly discuss the influence of SOC on the chemical bonding in these systems.[8]

This paper is organized as follows: first, the computational details are given; then, the results are discussed in three steps, in which we deal with (i) the gas phase electronic structure of AtO^+, (ii) the influence of solvation on its SOF many-electron states, and (iii) its consequence on the SOC states; finally, conclusions are given.

2 Computational details

2.1 Spin–orbit-free calculations

The most stable AtO^+ $(H_2O)_n$ (n = 1–6) clusters were previously optimized with scalar-relativistic DFT (SR-DFT) and spin–orbit DFT by Ayed *et al.*[5,6] Two types of spin configurations were considered in the SR-DFT calculations, namely spin-restricted-singlet and spin-unrestricted-triplet ones. Note that these earlier studies were done using the M06-2X functional,[21] a choice that has been recently criticized in the literature.[7,22] In the present work, we consider the same types of clusters, which have however been optimized with the PBE0 hybrid generalized gradient approximation (GGA) functional.[23,24] We chose this functional since it was previously proven to provide very accurate geometries for various At-containing systems.[22,25]

The GAUSSIAN program package[26] was employed to perform all the SR-DFT calculations. The scalar-relativistic many-electron-fit effective core potential ECP60MDF[27] was used to mimic the role of the 60 core electrons of the At atom. The remaining valence electrons of the At atom were dealt with the aug-cc-pVDZ-PP basis set modified for two-component calculations,[9,27,28] while for the H and O atoms, the aug-cc-pVDZ basis sets were used.[29,30] For the sake of simplicity, these basis sets will be referred to as "AVDZ" in the remainder of the text. Harmonic vibrational frequencies were determined in order to establish the nature of the obtained structures.

The obtained geometries were used in subsequent wave-function-based calculations. The state-averaged complete active space self-consistent field (SA-CASSCF) method[31,32] has been used to build multiconfigurational SOF wave functions. As in previous studies of the AtO^+ free cation,[7,8] we have used an active space comprising 8 electrons and 6 molecular orbitals (generated by the 6p and 2p atomic orbitals of the At and O centers of AtO^+), leading to CASSCF(8/6) calculations. We determined that enlarging the active space by introducing some ligand-centred orbitals does not significantly improve the description of the SOF electronic states of interest. An equal-weighted orbital average between several states of different spin multiplicities has been done (6 spin-singlet states, 9 spin-triplet states and 2 spin-quintet states).[8] Note that, in view of subsequent SOC calculations, the state-averaging space cannot be restricted to just a few SOF states. In practice, this state-averaging space must be limited as much as possible, while maintaining a good representation of the SOC operator. To recover more electron correlation, we have employed the n-electrons valence state perturbation theory at second order (NEVPT2) method in the partially contracted formulation.[33] Note that the Dyall's Hamiltonian[34] is used as the zeroth-order Hamiltonian in NEVPT2, which limits the occurrence of intruder states (in comparison with other implementations of multireference second-order perturbation theories).

For all the wave-function-based calculations, we have retained the above-mentioned ECP60MDF effective core potential to mimic the effect of the 60 core electrons of the At atom. Its remaining electrons were dealt with the aug-cc-pVTZ-PP basis set,[27] while for the H and O centers we have used the aug-cc-pVTZ ones.[29,30] For the sake of simplicity, these basis sets will be referred to as "AVTZ". In the NEVPT2 calculations, we have frozen the 5s5p5d semicore shells of the At atom and the 1s core shell of the O one. All the CASSCF and NEVPT2 calculations were performed using the MOLPRO program package.[35]

2.2 Spin–orbit coupling calculations

The (relativistic) two-component DFT (2c-DFT) method[36] implemented in the TURBOMOLE program package[37] was employed to relax the geometries under the influence of SOC. The previously optimized AtO^+ $(H_2O)_n$ (n = 1–6) structures were used as the starting points for the 2c-DFT geometry optimizations. For these calculations, we have used the *a priori* calculated scalar-relativistic wave functions as initial guesses. Naturally, we have retained the aforementioned PBE0 hybrid GGA functional and the AVDZ basis sets. To avoid the treatment of the 60 core electrons of At, we have used the ECP60MDF spin-dependent potential,[27] such that scalar relativistic effects and SOC are both included in the calculations. Numerical frequencies were computed to determine the nature of the obtained 2c-DFT structures.

 This journal is © the Owner Societies 2016

Published on 26 October 2016. Downloaded on 09/12/2016 12:27:15.

The obtained 2c-DFT geometries were used in subsequent two-step wave-function-based calculations within a contracted spin–orbit configuration interaction (c-SOCI) scheme. SA-CASSCF(8/6) wave functions were built as zeroth-order wave functions for the SOC calculations, *i.e.* they are used to compute the off-diagonal matrix elements of the $E_{el} + \hat{H}_{SOC}$ interaction matrix. The diagonal of this matrix is "dressed" with calculated NEVPT2 energies. The c-SOCI wave functions are obtained by diagonalizing this interaction matrix, which is expressed in terms of the M_S components of the considered SOF SA-CASSCF(8/6) solutions. All the c-SOCI calculations were performed using MOLPRO, and the aforementioned ECP60MDF and AVTZ basis sets were used. Note that the SOC integrals have been determined using the spin-dependent part of the ECP60MDF pseudopotential.

3 Results and discussion

3.1 Comments on the AtO^+ free-cation electronic spectra

The AtO^+ free cation exhibits a $^3\Sigma^-$ SOF ground-state that is separated by ~0.6 eV from $^1\Delta$ and ~1 eV from $^1\Sigma^+$. Since in this work we use a different computational setup than the ones used in previous studies,[7,8] we start by briefly reviewing this case by means of single-point wave-function-based calculations. At the NEVPT2/AVTZ//2c-PBE0/AVDZ level of theory, the $^3\Sigma^- \rightarrow {}^1\Delta$ and $^3\Sigma^- \rightarrow {}^1\Sigma^+$ SOF excitation energies are 0.56 and 1.00 eV, respectively. When SOC is introduced, the $X0^+ \rightarrow \mathbf{a}1$ and $X0^+ \rightarrow \mathbf{a}2$ excitation energies are 0.42 and 0.98 eV, respectively. Since all these values are in good agreement with reference values that are available in the literature,[7,8] we conclude that no major basis set or geometrical artifact affects the present values, which validates the NEVPT2/AVTZ//2c-PBE0/AVDZ and c-SOCI/AVTZ//2c-PBE0/AVDZ levels of theory to study the AtO^+ free cation.

The following compositions of the SOF wave functions,‡

$$\begin{cases} |^3\Sigma^-\rangle &= 88\%|[\ldots]\sigma^2\pi^2\pi^2\pi^{*1}\pi^{*1}\sigma^{*0}\rangle + \ldots \\ |^1\Delta\rangle^{(1)} &= 42\%|[\ldots]\sigma^2\pi^2\pi^2\pi^{*1}\pi^{*1}\sigma^{*0}\rangle \\ & \quad + 42\%|[\ldots]\sigma^2\pi^2\pi^2\pi^{*1}\pi^{*1}\sigma^{*0}\rangle + \ldots \\ |^1\Delta\rangle^{(2)} &= 42\%|[\ldots]\sigma^2\pi^2\pi^2\pi^{*2}\pi^{*0}\sigma^{*0}\rangle \\ & \quad + 42\%|[\ldots]\sigma^2\pi^2\pi^2\pi^{*0}\pi^{*2}\sigma^{*0}\rangle + \ldots \\ |^1\Sigma^+\rangle &= 40\%|[\ldots]\sigma^2\pi^2\pi^2\pi^{*2}\pi^{*0}\sigma^{*0}\rangle \\ & \quad + 40\%|[\ldots]\sigma^2\pi^2\pi^2\pi^{*0}\pi^{*2}\sigma^{*0}\rangle + \ldots \end{cases} \quad (1)$$

and of the SOC wave functions,

$$\begin{cases} |X0^+\rangle &= 68\%|^3\Sigma^-\rangle_{M_S=0} + 26\%|^1\Sigma^+\rangle + \ldots \\ |\mathbf{a}1\rangle^{(1,2)} &= 43\%|^3\Sigma^-\rangle_{M_S=+1} + 43\%|^3\Sigma^-\rangle_{M_S=-1} + \ldots \\ |\mathbf{a}2\rangle^{(1)} &= 83\%|^1\Delta\rangle^{(1)} + \ldots \\ |\mathbf{a}2\rangle^{(2)} &= 83\%|^1\Delta\rangle^{(2)} + \ldots \end{cases} \quad (2)$$

‡ In the determinant expansion of the wave function corresponding to the $^1\Delta^{(2)}$ state, the second CSF that is shown carries a coefficient with an opposite sign.

have been obtained for the lowest-lying electronic states of interest. Again, we note a good agreement of the NEVPT2/AVTZ//2c-PBE0/AVDZ and c-SOCI/AVTZ//2c-PBE0/AVDZ wave functions with the reference ones that are available in the literature.[7,8] If AtO^+ undergoes a ground-state change in water, leading to a closed-shell singlet-spin ground-state as suggested by Ayed *et al.*,[5,6] two main hypotheses can be formulated from eqn (1) and (2), (i) a closed-shell configuration, correlating most likely with one component of $^1\Delta$, becomes the SOF ground-state and contributes most to the ground SOC state or (ii) a closed-shell configuration is stabilized in such a way that it does not become the SOF ground-state while being the most important contributor to the ground SOC state. We will first discriminate between these two hypotheses by monitoring the electronic states that correlate with $^3\Sigma^-$, $^1\Delta$ and $^1\Sigma^+$ in different $AtO^+(H_2O)_n$ (n = 1–6) clusters by means of NEVPT2/AVTZ calculations. After this, using c-SOCI/AVTZ calculations, we will scrutinize the SOC states to firmly justify the occurrence of a hydration-induced ground-state change in AtO^+.

3.2 Spin–orbit-free calculations

In this section we discuss the electronic structures of the $AtO^+(H_2O)_n$ (n = 1–6) systems by means of single-point NEVPT2/AVTZ calculations performed at the PBE0/AVDZ geometries. For each system, two geometries are considered, corresponding to the equilibrium structures of the lowest-energy spin-restricted-singlet and spin-unrestricted-triplet SR-DFT solutions (see Fig. 1). Note that more extensive discussions concerning these geometries can be found elsewhere.[5,6] We just recall briefly that the hydration spheres corresponding to different spin-symmetry solutions for each system significantly differ. For instance, in the spin-restricted-singlet clusters, the water molecules lead to charge transfer to At and may form hydrogen bonds with the O atom of the AtO^+ unit. In contrast, the conformation of the surrounding water molecules in the spin-unrestricted-triplet clusters is ruled by halogen bonding with At, while hydrogen bonds are only formed between water units. Moreover, the interatomic distances are different in both types of clusters, with shorter water–AtO^+ distances in the spin-restricted-singlet clusters. We will split the discussion into two parts, by first analyzing the $AtO^+(H_2O)$ system, and then discussing the $AtO^+(H_2O)_n$ (n = 2–6) cases. Note that SOF excitation energies corresponding to all the studied clusters are reported in Table 1.

3.2.1 The $AtO^+(H_2O)$ system. In agreement with the previous M06-2X/AVDZ studies,[5,6] we find that the equilibrium geometry for the spin-unrestricted-triplet cluster belongs to the C_{2v} symmetry point group, while the spin-restricted-singlet one has a C_s symmetry. At first, we check that these SR-DFT stationary points nearly correspond to stationary points of the NEVPT2/AVTZ potential energy surfaces. For this, we study the dependence of the energy of various states with respect to the two main coordinates that are at play, *i.e.* the H_2O–AtO^+ bond distance and the ∠OAtO bond angle. We fix all the other geometrical parameters to the values they have in the PBE0/AVDZ spin-unrestricted-triplet structure. As can be seen in Fig. 2 and Fig. S1 (ESI†) (where only S_0 and S_1 are displayed for the sake of clarity),

Published on 26 October 2016. Downloaded on 09/12/2016 12:27:15.

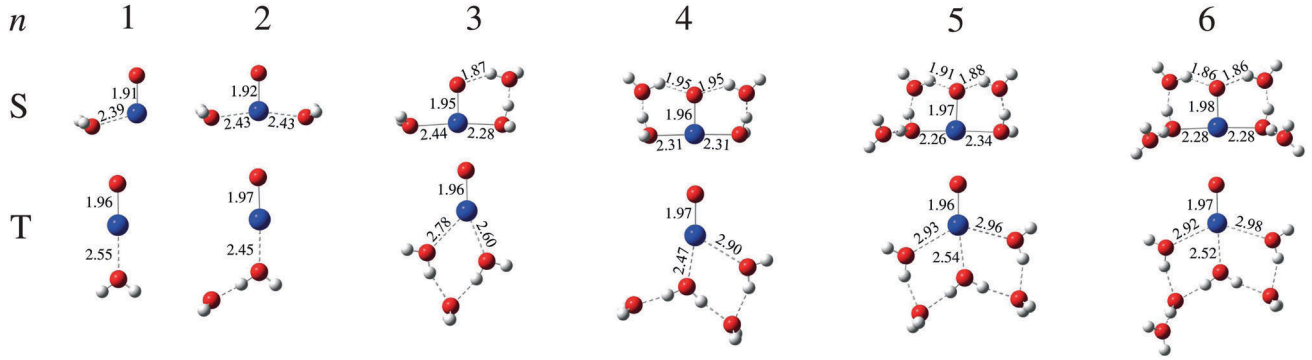

Fig. 1 PBE0/AVDZ lowest-energy structures for the spin-restricted-singlet (top) and spin-unrestricted-triplet (bottom) AtO^+ $(H_2O)_n$ clusters (n = 1–6). Interatomic distances are given in Angstroms. Color code: blue stands for At and red for O.

Table 1 Calculated scalar-relativistic excitation energies (in eV) for different equilibrium structures displayed in Fig. 1. The ΔE (non-adiabatic) energy difference between the spin-restricted-singlet state and the spin-restricted-triplet state is also given in each case (a positive value means that the spin-unrestricted-triplet cluster is more stable)

		AtO^+ (H_2O)	AtO^+ $(H_2O)_2$	AtO^+ $(H_2O)_3$	AtO^+ $(H_2O)_4$	AtO^+ $(H_2O)_5$	AtO^+ $(H_2O)_6$
Spin-unrestricted-triplet clusters							
NEVPT2/AVTZ	$T_0(^3\Sigma^-)$	0.00	0.00	0.00	0.00	0.00	0.00
	$S_0(^1\Delta)$	0.54	0.53	0.45	0.48	0.30	0.29
	$S_1(^1\Delta)$	0.55	0.54	0.54	0.54	0.54	0.54
	$S_2(^1\Sigma^+)$	0.97	0.96	1.09	1.02	1.24	1.25
Spin-restricted-singlet clusters							
NEVPT2/AVTZ	$T_0(^3\Sigma^-)$	0.17	1.09	1.76	2.26	2.45	2.71
	$S_0(^1\Delta)$	0.00	0.00	0.00	0.00	0.00	0.00
	$S_1(^1\Delta)$	0.70	1.58	2.25	2.80	3.00	3.40
	$S_2(^1\Sigma^+)$	2.08	4.01	$>4.97^a$	$>5.42^a$	$>5.60^a$	$>5.76^a$
Energy differences							
NEVPT2/AVTZ	ΔE	0.55 (0.57)^b	0.23 (0.26)^b	−0.02 (−0.03)^b	−0.26	−0.52	−0.64

^{a} When $S_2(^1\Sigma^+)$ is out of the state-averaging space, we only report a lower limit for the corresponding excitation energy. ^{b} The values in parenthesis are calculated at the NEVPT2/AVTZ//PBE0/AVTZ level of theory. These values show that there is no bias introduced by the use of equilibrium geometries calculated using the smaller AVDZ basis set.

we found a spin-restricted-triplet C_{2v} minimum, a spin-restricted-singlet C_{2v} minimum, and a spin-restricted-singlet C_s minimum, the latter being the global minimum for the singlet multiplicity.

Fig. 2A evidences that the lowest-energy electronic states correlate with the states of the free AtO^+ cation: one spin-restricted-triplet state correlate with $^3\Sigma^-$, two spin-restricted-singlet roots correlate with $^1\Delta$, and one spin-restricted-singlet state correlates with $^1\Sigma^+$. Therefore, we label these states as $T_0(^3\Sigma^-)$, $S_0(^1\Delta)$, $S_1(^1\Delta)$ and $S_2(^1\Sigma^+)$. Note that at the PBE0/AVDZ spin-unrestricted-triplet geometry, the degeneracy lift between $S_0(^1\Delta)$ and $S_1(^1\Delta)$ is very small ($\sim$0.01 eV), as expected. It can be seen from Fig. 2B that the $S_2(^1\Sigma^+)$ state is largely destabilized while going toward the equilibrium C_s geometry. Also, due to the degeneracy lifting of the frontier π^* orbitals, the $S_1(^1\Delta)$–$S_0(^1\Delta)$ energy gap increases when one considers a minimum energy path between the C_{2v} and C_s geometries. Indeed, while going to the spin-restricted-singlet geometry, the π^* orbital that belongs to the OAtO plane is relatively destabilized with respect to the other one because of the ligand-field created by the water molecule.

At the equilibrium PBE0/AVDZ C_s geometry, the $T_0(^3\Sigma^-)$, $S_1(^1\Delta)$ and $S_2(^1\Sigma^+)$ states lie 0.17, 0.70 and 2.08 eV above $S_0(^1\Delta)$, respectively (see Table 1). The CASSCF wave function of the $S_0(^1\Delta)$ state is essentially composed of the $[\ldots]\sigma^2\pi^2\pi^2\pi^{*2}\pi^{*0}\sigma^{*0}$ configuration (81%), the $T_0(^3\Sigma^-)$ state of the $[\ldots]\sigma^2\pi^2\pi^2\pi^{*1}\pi^{*1}\sigma^{*0}$ configuration (87%), the $S_1(^1\Delta)$ state of the $[\ldots]\sigma^2\pi^2\pi^2\pi^{*1}\pi^{*1}\sigma^{*0}$ configuration (81%), and the $S_2(^1\Sigma^+)$ state of the $[\ldots]\sigma^2\pi^2\pi^2\pi^{*0}\pi^{*2}\sigma^{*0}$ configuration (82%). Since at this geometry the $S_0(^1\Delta)$ state is the ground-state, the premise of the hydration-induced ground-state change is already observed in the AtO^+ (H_2O) system. However, the spin-unrestricted-triplet cluster is more stable than the spin-restricted-singlet one by 0.55 eV (see Table 1). Therefore, one has to pursue the micro-hydration in order to determine if AtO^+ undergoes an hydration-induced ground-state change at the scalar-relativistic NEVPT2/AVTZ level.

3.2.2 The AtO^+ $(H_2O)_n$ (n = 2–6) systems. We start by discussing the nature of the electronic states that correlate with the $^3\Sigma^-$, $^1\Delta$ and $^1\Sigma^+$ of the free AtO^+ cation. At the spin-unrestricted-triplet geometries, these states are not strongly perturbed by hydration since the water units tend to create a network between themselves through hydrogen bonding (see Fig. 1). For all these structures, we find that $T_0(^3\Sigma^-)$ is the ground-state. The corresponding CASSCF wave functions in each case reveal that

 This journal is © the Owner Societies 2016

Published on 26 October 2016. Downloaded on 09/12/2016 12:27:15.

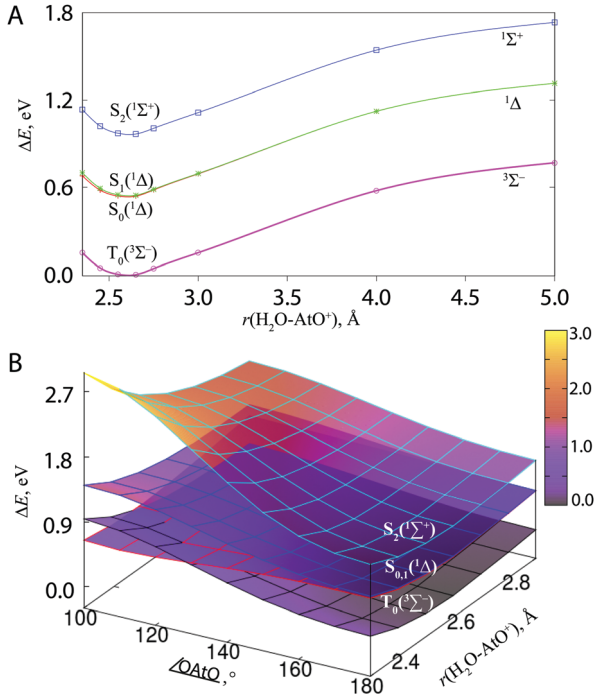

Fig. 2 Evolution of the relative energies of the lowest-lying electronic states of the AtO^+ (H_2O) system computed at the NEVPT2/AVTZ level of theory as a function of the H_2O–AtO^+ distance and the ∠OAtO angle: (A) the angle is fixed at 180°, while the distance is varied and (B) both the angle and the distance are varied.

they are mainly single-configurational, with weights of more than 80% on the $[\ldots]\sigma^2\pi^2\pi^2\pi^{*1}\pi^{*1}\sigma^{*0}$ configuration. In each case, we have identified three spin-restricted-singlet states right above $T_0(^3\Sigma^-)$. The first two of them are nearly degenerate in the $n = 2$ case, and the energy gap between them increases with increasing n, up to 0.25 eV in the $n = 6$ case (see Table 1). The CASSCF wave functions of the lowest-energy ones have, in all the cases, ∼80% weights on the closed-shell $[\ldots]\sigma^2\pi^2\pi^2\pi^{*2}\pi^{*0}\sigma^{*0}$ and $[\ldots]\sigma^2\pi^2\pi^2\pi^{*0}\pi^{*2}\sigma^{*0}$ configurations. When n is increased, due to the degeneracy lift of the π* orbitals, the weight of the former configuration increases up to 78% for these states, which thus becomes essentially single-configurational. The CASSCF wave functions of the second spin-restricted-singlet roots have ∼80% weight on the $[\ldots]\sigma^2\pi^2\pi^2\pi^{*1}\pi^{*1}\sigma^{*0}$ configuration. Thus, these sets of states clearly correlate with the $^1\Delta$ state of the free AtO^+ cation. The CASSCF wave functions corresponding to the third spin-restricted-singlet root have ∼80% weights on the closed-shell $[\ldots]\sigma^2\pi^2\pi^2\pi^{*2}\pi^{*0}\sigma^{*0}$ and $[\ldots]\sigma^2\pi^2\pi^2\pi^{*0}\pi^{*2}\sigma^{*0}$ configurations, with the weight of the latter configuration increasing with n. Therefore, these third spin-restricted-singlet roots correlate with $^1\Sigma^+$, and we note that these states are relatively destabilized with increasing n (see Table 1).

We now continue by analyzing the electronic states of the spin-restricted-singlet equilibrium structures. As in the AtO^+ (H_2O) spin-restricted-singlet case, the obtained spectra are expected to largely differ from the one of the AtO^+ free cation. Obviously, one cannot play with all the degrees of freedom that arise from the water positions to track states from the free AtO^+ cation to each AtO^+ $(H_2O)_n$ structure of interest. A simpler approach consists of calculating the lowest-lying electronic states at the equilibrium geometries corresponding to these spin-restricted-singlet clusters and to track them up to dissociating the water molecules from the AtO^+ unit. We monitored the evolution of the states correlating with $^3\Sigma^-$, $^1\Delta$, and $^1\Sigma^+$ while the 2(6) water molecules are moving away in the $C_{2v}(C_s)$ symmetry point group (see Fig. 3). Note that in the $n = 6$ case, the parameters which are scanned correspond to the two bonds between the water molecules and the At center (see the spin-singlet AtO^+ $(H_2O)_6$ cluster in Fig. 1), the 6 water molecules moving simultaneously away from the AtO^+ unit in a symmetric fashion. Notably, the closed-shell electronic state that correlates with $^1\Delta$, which we label as $S_0(^1\Delta)$, crosses $T_0(^3\Sigma^-)$ at distances below ∼3.0 Å and becomes the ground-state for shorter distances such that it reaches its minimum at distances smaller than ∼2.5 Å. Note that the differential stabilization of $S_0(^1\Delta)$ and $T_0(^3\Sigma^-)$ with increasing n can be easily explained: the energy gap between the two orbitals that correlate with π* increases with increasing n; therefore, it costs more energy to promote an electron to the other π* orbital than to pair two electrons in the lowest-energy π* orbital to form the closed-shell configuration.

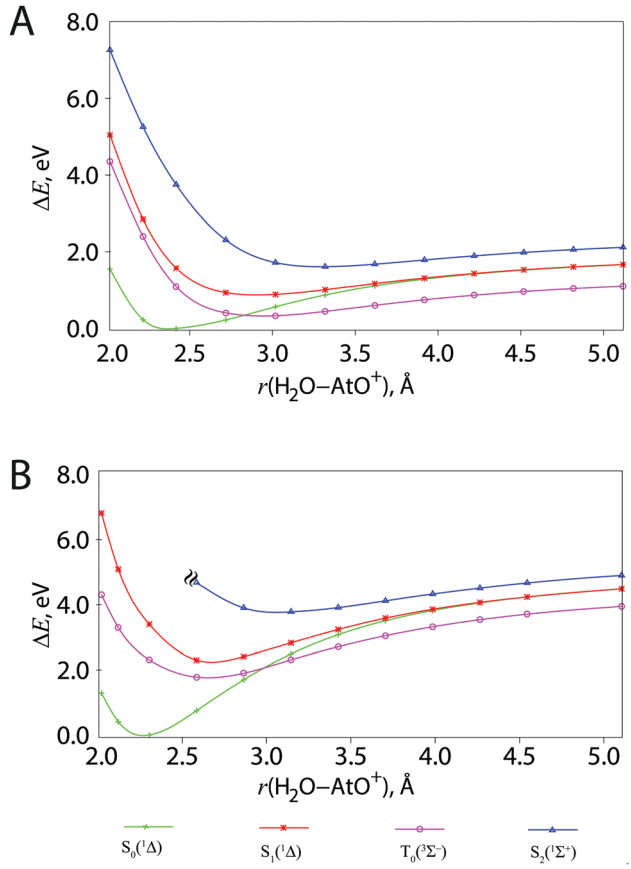

Fig. 3 Evolution of the energy of low-lying electronic states as a function of the main H_2O–AtO^+ distances: (A) in the AtO^+ $(H_2O)_2$ system (C_{2v} symmetry) and (B) in the AtO^+ $(H_2O)_6$ system (C_s symmetry). The geometries of the spin-restricted-singlet clusters are taken as references.

Published on 26 October 2016. Downloaded on 09/12/2016 12:27:15.

In all the AtO^+ $(H_2O)_n$ (n = 2–6) spin-restricted-singlet clusters, the CASSCF ground-state wave functions are dominated by the closed-shell $[\ldots]\sigma^2\pi^2\pi^2\pi^{*2}\pi^{*0}\sigma^{*0}$ configuration (with weights larger than 80%). The states labeled as $T_0(^3\Sigma^-)$ are always the first excited states and the corresponding excitation energies increase with increasing n (see Table 1). Their CASSCF wave functions are essentially single-configurational and have weights larger than 80% in the $[\ldots]\sigma^2\pi^2\pi^2\pi^{*1}\pi^{*1}\sigma^{*0}$ configuration. The $S_1(^1\Delta)$ states are also relatively destabilized with increasing n (see Table 1), as their CASSCF wave functions have weights larger than 82% in the $[\ldots]\sigma^2\pi^2\pi^2\pi^{*1}\pi^{*1}\sigma^{*0}$ configuration. We found that the $S_2(^1\Sigma^+)$ states are so much destabilized with increasing n starting from n = 3, and they go out of the used state-averaging space, which is not surprising since this root essentially corresponds to the $[\ldots]\sigma^2\pi^2\pi^2\pi^{*0}\pi^{*2}\sigma^{*0}$ configuration.

From Table 1, it is clear that the spin-restricted-singlet clusters quickly become more stable than the spin-unrestricted-triplet ones when n is increased. Therefore, at the SOF level, hydration induces a ground-state reversal between $T_0(^3\Sigma^-)$ and $S_0(^1\Delta)$, and therefore, one of the two aforementioned hypotheses can be dropped out. We thus conclude from this part that hydration induces a ground-state change at the SOF level, which supports the results of Ayed *et al.*[5,6]

3.3 Spin–orbit coupling calculations

In this section we discuss the influence of SOC on the geometries and electronic structures of the essentially-spin-triplet and essentially-spin-singlet AtO^+ $(H_2O)_n$ (n = 1–6) clusters. The geometries optimized for the AtO^+ $(H_2O)_n$ (n = 2–6) systems at the 2c-PBE0/AVDZ level of theory are shown in Fig. 4. The vertical excitation energies obtained at the NEVPT2/AVTZ//2c-PBE0/AVDZ and c-SOCI/AVTZ//2c-PBE0/AVDZ levels are gathered in Table 2. Note that the n = 1 case will be discussed separately as it deserves special attention. The influence of SOC on the geometries of the two types of clusters is different: while in the essentially-spin-singlet clusters the water–AtO^+ distances generally increase, in some of the essentially-spin-triplet clusters such water–AtO^+ distances can decrease (see Fig. 1 and 4). Therefore, SOC is susceptible to the strengthening of specific water–AtO^+ interactions in these clusters.

3.3.1 The AtO^+ (H_2O) system. In line with previous results,[6,7] we found at the 2c-PBE0/AVDZ level of theory that the equilibrium geometry of the essentially-spin-triplet AtO^+ (H_2O) cluster belongs to the C_{2v} symmetry point group, with a larger H_2O–AtO^+ distance than the one obtained at the SOF level (*i.e.* 2.63 Å). We have not identified a C_s-like equilibrium geometry for the essentially-spin-singlet cluster. Therefore, we performed c-SOCI calculations in order to study the dependence of the energy and the nature of the lowest-lying SOC states, with respect to the H_2O–AtO^+ distance and the ∠OAtO angle (see Fig. 5). In order to identify these states, we have tracked them while the water molecule approaches toward the essentially-spin-triplet equilibrium geometry (in a similar way as what was done at the scalar-relativistic level). As expected, they clearly correlate with the $X0^+$, **a**1 and **a**2 states of the free AtO^+ cation, and therefore, we label them accordingly. As can be seen in Fig. 5A, the five lowest-lying SOC states all raise in energy toward the region of the potential energy surface where the equilibrium scalar-relativistic spin-singlet geometry was found.

At first, we focus on the $\Psi(X0^+)$ SOC ground-state and the evolution of its composition as a function of the H_2O–AtO^+ distance and the ∠OAtO angle (see Fig. 5B). At the essentially-spin-triplet equilibrium geometry (C_{2v}), this state is very similar to the one of the free AtO^+ cation: it is essentially composed of the M_S = 0 component of $T_0(^3\Sigma^-)$ (68%) and $S_2(^1\Sigma^+)$ (25%). Since the $T_0(^3\Sigma^-)$ and $S_2(^1\Sigma^+)$ states are relatively destabilized when going toward the scalar-relativistic spin-singlet equilibrium geometry (see Fig. 2B), their contributions to the $\Psi(X0^+)$ ground-state wave function are diminished (see Fig. 5B). In contrast, as $S_0(^1\Delta)$ is at the same time relatively stabilized (see Fig. 2B), its contribution to $\Psi(X0^+)$ is enhanced (see Fig. 5B). At the scalar-relativistic spin-singlet equilibrium geometry (C_s), we find that the ground SOC state (Ψ_0) has a mixed singlet–triplet character, with 45% of $T_0(^3\Sigma^-)$, 5% of $S_2(^1\Sigma^+)$ and 41% of $S_0(^1\Delta)$.

The two Ψ(**a**1) states lie ∼0.40 eV above $\Psi(X0^+)$ at the essentially-spin-triplet geometry (C_{2v}) and are mainly composed of M_S = −1 (43%) and M_S = +1 (43%) components of $T_0(^3\Sigma^-)$. Toward the scalar-relativistic spin-singlet geometry (C_s), these states raise in energy and appear at 0.67 (Ψ_1) and 0.68 eV (Ψ_2) above the ground SOC state while retaining their compositions.

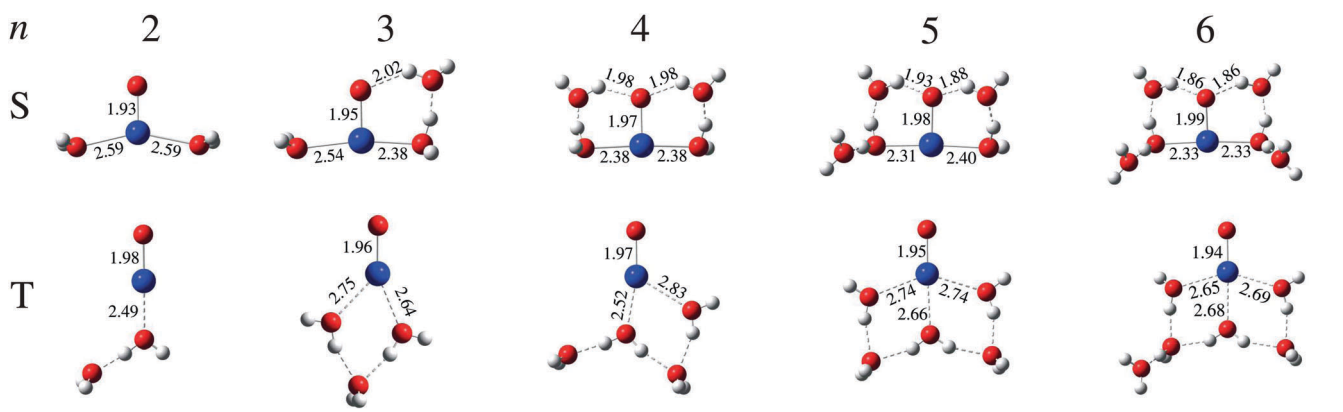

Fig. 4 2c-PBE0/AVDZ lowest-energy structures for the essentially-spin-singlet (top) and essentially-spin-triplet (bottom) AtO^+ $(H_2O)_n$ clusters (n = 2–6). Interatomic distances are given in Angstroms. Color code: blue stands for At and red for O.

 This journal is © the Owner Societies 2016

Published on 26 October 2016. Downloaded on 09/12/2016 12:27:15.

Table 2 Calculated electronic excitation energies (in eV) for different equilibrium structures displayed in Fig. 4. The ΔE (non-adiabatic) energy difference between the essentially-spin-singlet state and the essentially-spin-triplet state is also given in each case (a positive value means that the essentially-spin-triplet state is more stable)

		AtO^+ $(H_2O)_2$	AtO^+ $(H_2O)_3$	AtO^+ $(H_2O)_4$	AtO^+ $(H_2O)_5$	AtO^+ $(H_2O)_6$
Essentially-spin-triplet clusters						
NEVPT2/AVTZ	$T_0(^3\Sigma^-)$	0.00	0.00	0.00	0.01	0.21
	$S_0(^1\Delta)$	0.53	0.43	0.44	0.00	0.00
	$S_1(^1\Delta)$	0.54	0.54	0.54	0.54	0.74
	$S_2(^1\Sigma^+)$	0.95	1.10	1.06	1.63	2.08
c-SOCI/NEVPT2/AVTZ	Ψ_0	0.00	0.00	0.00	0.00	0.00
	Ψ_1	0.37	0.43	0.44	0.62	0.71
	Ψ_2	0.37	0.44	0.45	0.64	0.74
	Ψ_3	0.91	0.97	0.96	1.01	1.03
	Ψ_4	0.91	0.98	0.97	1.14	1.22
Essentially-spin-singlet clusters						
NEVPT2/AVTZ	$T_0(^3\Sigma^-)$	0.50	1.14	1.80	2.08	2.28
	$S_0(^1\Delta)$	0.00	0.00	0.00	0.00	0.00
	$S_1(^1\Delta)$	1.01	1.63	2.33	2.61	2.81
	$S_2(^1\Sigma^+)$	2.74	3.94	$>4.90^a$	$>5.16^a$	$>5.34^a$
c-SOCI/NEVPT2/AVTZ	Ψ_0	0.00	0.00	0.00	0.00	0.00
	Ψ_1	0.89	1.44	2.04	2.21	2.31
	Ψ_2	0.89	1.44	2.12	2.33	2.45
	Ψ_3	1.05	1.47	2.21	2.36	2.48
	Ψ_4	1.37	1.83	2.34	2.45	2.51
Energy differences						
c-SOCI/NEVPT2/AVTZ	ΔE	0.33 (0.32)^b	0.30 (0.30)^b	0.10	−0.10	−0.23

^{a} When $S_2(^1\Sigma^+)$ is out of the state-averaging space, we only report a lower limit for the corresponding excitation energy. ^{b} The values in parenthesis are calculated at the c-SOCI/NEVPT2/AVTZ//2c-PBE0/AVTZ2-2c level of theory. These values show that there is no bias introduced by the use of equilibrium geometries calculated using the smaller AVDZ basis set.

Since these states are not involved in the ground-state change under study, we continue by discussing the evolution of the $\Psi(\mathbf{a2})$ states. At the essentially-spin-triplet geometry, they lie $\sim$0.95 eV above $\Psi(X0^+)$. Their wave functions are essentially composed of the $S_0(^1\Delta)$ and $S_1(^1\Delta)$ states (82% and 83%, respectively). Toward the scalar-relativistic spin-singlet geometry, the energy gap between the two $\Psi(\mathbf{a2})$ states gradually increases (see Fig. 5A), these states being at 0.93 (Ψ_3) and 1.20 eV (Ψ_4) above Ψ_0 at this geometry. The composition of the Ψ_3 SOC state shows a decrease in its $S_0(^1\Delta)$ component from 82% in the essentially-spin-triplet geometry (C_{2v}) to 46% in the scalar-relativistic spin-singlet structure, while the weight of the M_S = 0 component of the $T_0(^3\Sigma^-)$ state increases from 0 to 31%. At the same time, the composition of the Ψ_4 state is almost unaffected. Note that the C_s geometry does not correspond to a minimum for neither Ψ_3 nor Ψ_4 (see Fig. 5A), which explains that we failed in optimizing an essentially-spin-singlet structure at the 2c-PBE0 level. As stated by Ayed *et al.*,[5,6] a fierce competition between SOC and hydration occurs, the former being dominant in the AtO^+ (H_2O) system. As a consequence, no essentially-spin-singlet structure can be obtained in this system.

3.3.2 The AtO^+ $(H_2O)_n$ (n = 2–6) systems. At first, we discuss the energy levels obtained at the essentially-spin-triplet geometries of the AtO^+ $(H_2O)_n$ (n = 2–6) clusters. While we noticed only little changes in the SOF states for $n \leq 4$, a ground-state reversal between $T_0(^3\Sigma^-)$ and $S_0(^1\Delta)$ occurs in the n = 5–6 cases. One should note that this ground-state reversal did not occur at the scalar-relativistic spin-triplet geometries, meaning that the geometrical changes induced by SOC matter. In Table 2 we have denoted as Ψ_n, n = 0–4, the lowest five SOC states. At the equilibrium geometry of the n = 2 essentially-spin-triplet cluster, the compositions of the c-SOCI wave functions of these states read:

$$\begin{cases} |\Psi_0\rangle &= 69\%\left|T_0\left(^3\Sigma^-\right)\right\rangle_{M_S=0} + 24\%\left|S_2\left(^1\Sigma^+\right)\right\rangle + \ldots \\ |\Psi_1\rangle &= 43\%\left|T_0\left(^3\Sigma^-\right)\right\rangle_{M_S=+1} + 43\%\left|T_0\left(^3\Sigma^-\right)\right\rangle_{M_S=-1} + \ldots \\ |\Psi_2\rangle &= 43\%\left|T_0\left(^3\Sigma^-\right)\right\rangle_{M_S=+1} + 43\%\left|T_0\left(^3\Sigma^-\right)\right\rangle_{M_S=-1} + \ldots \\ |\Psi_3\rangle &= 81\%\left|S_0\left(^1\Delta\right)\right\rangle + \ldots \\ |\Psi_4\rangle &= 82\%\left|S_1\left(^1\Delta\right)\right\rangle + \ldots \end{cases} . \quad (3)$$

In terms of composition, they clearly correlate with the lowest five SOC states of the free AtO^+ cation. Ψ_0 has a dominant spin-triplet character and correlates with the $X0^+$ state of AtO^+. The nearly-degenerate Ψ_1 and Ψ_2 states are placed 0.37 eV above Ψ_0; they have dominant spin-triplet characters and correlate with the two-fold degenerate **a1** state of AtO^+. The nearly-degenerate Ψ_3 and Ψ_4 states, 0.91 eV above Ψ_0, have dominant spin-singlet character and correlate with the two-fold degenerate **a2** state of AtO^+. We note that the vertical excitation energies of these Ψ_n (n = 1–4) states are very similar to the ones observed in the free AtO^+ cation, suggesting that the two water molecules do not perturb that much the AtO^+ unit. While n increases, the near

Published on 26 October 2016. Downloaded on 09/12/2016 12:27:15.

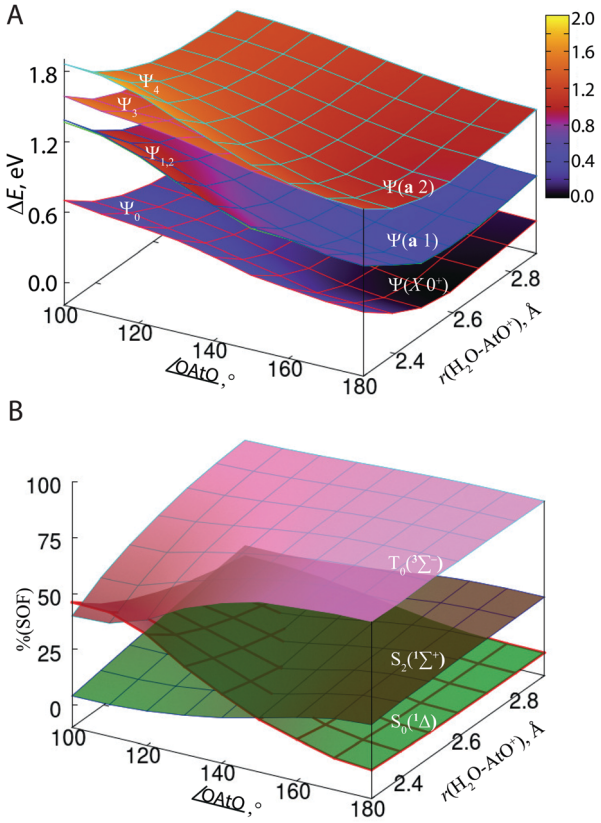

Fig. 5 Evolution of the lowest-lying energy levels of the AtO^+ (H_2O) system computed at the c-SOCI/AVTZ level of theory as a function of the H_2O–AtO^+ distance and the ∠OAtO angle: (A) relative energies (in eV) and (B) composition of Ψ_0 in terms of the M_S components of $T_0(^3\Sigma^-)$, $S_0(^1\Delta)$, and $S_2(^1\Sigma^+)$.

degeneracies between the states Ψ_1 and Ψ_2 and between the Ψ_3 and Ψ_4 states are more and more lifted, all these SOC states being destabilized with respect to the Ψ_0 states (see Table 2). Also, the composition of the corresponding SOC wave functions evolve with n. For the n = 6 essentially-spin-triplet cluster, the compositions of the c-SOCI wave functions are:

$$\begin{cases} |\Psi_0\rangle = 46\%|T_0(^3\Sigma^-)\rangle_{M_S=0} + 40\%|S_0(^1\Delta)\rangle + \ldots \\ |\Psi_1\rangle = 43\%|T_0(^3\Sigma^-)\rangle_{M_S=+1} + 43\%|T_0(^3\Sigma^-)\rangle_{M_S=-1} + \ldots \\ |\Psi_2\rangle = 44\%|T_0(^3\Sigma^-)\rangle_{M_S=+1} + 44\%|T_0(^3\Sigma^-)\rangle_{M_S=-1} + \ldots \\ |\Psi_3\rangle = 29\%|T_0(^3\Sigma^-)\rangle_{M_S=0} + 14\%|S_2(^1\Sigma^+)\rangle \\ \qquad + 46\%|S_0(^1\Delta)\rangle + \ldots \\ |\Psi_4\rangle = 84\%|S_1(^1\Delta)\rangle + \ldots \end{cases} \quad (4)$$

By comparing the c-SOCI wave functions shown in eqn (3) and (4), it is clear that the Ψ_1, Ψ_2 and Ψ_4 states are nearly unchanged while n is increased from 2 to 6. On the other hand, interesting changes appear in the compositions of the Ψ_0 and Ψ_3 states: with increasing n, the (M_S = 0) $T_0(^3\Sigma^-)$ contribution to the Ψ_0 wave function is decreased while that to Ψ_3 is increased, and the $S_0(^1\Delta)$ contribution to Ψ_3 is decreased while that to Ψ_0 is increased. In the n = 6 essentially-spin-triplet cluster, the Ψ_0 and Ψ_3 states have mixed singlet/triplet characters (see eqn (4)). The concerted change in the dominant compositions of the Ψ_0 and Ψ_3 wave functions is in line with the change in the relative energies of the corresponding SOF states (see Table 2).

Now, we discuss the energy levels obtained at the essentially-spin-singlet geometries. Following the geometrical changes induced SOC, we noticed that the SOF states are largely affected in terms of relative energies: the $S_0(^1\Delta)$ states remain the ground-states in each case while the vertical excitation energies from these states to the $T_0(^3\Sigma^-)$ and $S_1(^1\Delta)$ ones are significantly reduced (see Tables 1 and 2). The compositions of the c-SOCI wave functions for the n = 2 case read:

$$\begin{cases} |\Psi_0\rangle = 34\%|T_0(^3\Sigma^-)\rangle_{M_S=0} + 53\%|S_0(^1\Delta)\rangle + \ldots \\ |\Psi_1\rangle = 43\%|T_0(^3\Sigma^-)\rangle_{M_S=+1} + 43\%|T_0(^3\Sigma^-)\rangle_{M_S=-1} + \ldots \\ |\Psi_2\rangle = 43\%|T_0(^3\Sigma^-)\rangle_{M_S=+1} + 43\%|T_0(^3\Sigma^-)\rangle_{M_S=-1} + \ldots \\ |\Psi_3\rangle = 42\%|T_0(^3\Sigma^-)\rangle_{M_S=0} + 35\%|S_0(^1\Delta)\rangle + \ldots \\ |\Psi_4\rangle = 83\%|S_1(^1\Delta)\rangle + \ldots \end{cases} \quad (5)$$

The Ψ_1 and Ψ_2 states are degenerate in energy and they lie at 0.89 eV above the ground-state. In terms of composition, these states have dominant spin-triplet characters and clearly correlate with the two-fold degenerate **a1** state of AtO^+. Ψ_4 lies 1.37 eV above the ground-state, its wave function has a dominant spin-singlet character (it correlates with the open-shell component of **a2**). The wave functions of Ψ_0 and Ψ_3 have mixed singlet/triplet characters instead of dominant spin-triplet and spin-singlet characters, respectively, as was the case at the n = 2 essentially-spin-triplet equilibrium geometry (see eqn (2)). The compositions of the c-SOCI wave functions for the n = 6 case are:

$$\begin{cases} |\Psi_0\rangle = 84\%|S_0(^1\Delta)\rangle + \ldots \\ |\Psi_1\rangle = 28\%|T_0(^3\Sigma^-)\rangle_{M_S=+1} + 28\%|T_0(^3\Sigma^-)\rangle_{M_S=-1} \\ \qquad + 42\%|T_1(^3\Pi)\rangle_{M_S=0} + \ldots \\ |\Psi_2\rangle = 21\%|T_1(^3\Pi)\rangle_{M_S=+1} + 21\%|T_1(^3\Pi)\rangle_{M_S=-1} \\ \qquad + 42\%|T_0(^3\Sigma^-)\rangle_{M_S=0} + \ldots \\ |\Psi_3\rangle = 39\%|T_0(^3\Sigma^-)\rangle_{M_S=+1} + 39\%|T_0(^3\Sigma^-)\rangle_{M_S=-1} + \ldots \\ |\Psi_4\rangle = 35\%|S_1(^1\Delta)\rangle + 31\%|T_1(^3\Pi)\rangle_{M_S=+1} \\ \qquad + 31\%|T_1(^3\Pi)\rangle_{M_S=-1} + \ldots \end{cases} \quad (6)$$

As a consequence of the stabilization of the $S_0(^1\Delta)$ SOF state with respect to the $T_0(^3\Sigma^-)$ one, Ψ_0 has a dominant spin-singlet character, *i.e.* 84% of its wave function corresponds to the $S_0(^1\Delta)$ state. This Ψ_0 state clearly correlates with the closed-shell

 This journal is © the Owner Societies 2016

Published on 26 October 2016. Downloaded on 09/12/2016 12:27:15.

component of the **a**2 state of the free AtO^+ cation. The remaining SOC states, namely Ψ_1, Ψ_2, Ψ_3 and Ψ_4, are more and more destabilized with respect to Ψ_0 with increasing n (see Table 2). Actually, when going from the $n = 2$ to the $n = 6$ essentially-spin-singlet cluster, the composition of their wave functions gradually changes (see eqn (S1), ESI†). For instance, in the $n = 6$ case, the wave functions corresponding to Ψ_1, Ψ_2 and Ψ_3 exhibit mixtures of the M_S components of the lowest two SOF triplet states, $T_0(^3\Sigma^-)$ and $T_1(^3\Pi)$, while the one of Ψ_4 exhibits a mixture of $S_1(^1\Delta)$ and the $|M_S| = 1$ components of $T_1(^3\Pi)$.

Finally, we discuss the nature of the ground-states of the AtO^+ $(H_2O)_n$ (n = 2–6) systems. Clearly, beyond $n = 4$ water molecules in the first hydration sphere, the lowest-energy structures exhibit essentially-spin-singlet closed-shell ground-states. Therefore, when SOC is included in the calculations, AtO^+ undergoes a hydration-induced ground-state change, leading to an essentially closed-shell ground-state that can readily react in a spin-allowed fashion with closed-shell species. Note that in this work, we have not taken into consideration a continuum solvation model to introduce long-range bulk effects. Nonetheless, these effects have been lengthily discussed by Ayed *et al.*[5,6] and were shown to strongly stabilize the AtO^+–water species that exhibit (essentially-)spin-singlet ground-states relatively to the ones exhibiting (essentially-)spin-triplet ones. Our results are thus in qualitative agreement with this trend. Therefore, we confirm the recent M06-2X results of Ayed *et al.*[5,6] and complements them by clearly establishing the nature of the electronic states that are involved in this ground-state change.

4 Conclusions

Although recently suggested, the fact that AtO^+ undergoes a hydration-induced ground-state change was recently questioned in the literature.[7] In this work, we have used relativistic density functional theory and wave function theory methods to revisit this phenomenon. While in the gas-phase and in the absence of spin–orbit coupling, AtO^+ adopts a spin-triplet ground-state ($^3\Sigma^-$), we showed that hydration leads to a closed-shell ground-state, even when relatively small hydration spheres ($n = 3$ and beyond) are considered. We have determined for the first time the nature of these states, showing that they clearly correlate with the closed-shell component of the free-cation $^1\Delta$ state. When spin–orbit coupling is accounted for, AtO^+ adopts, in the gas-phase, an essentially-spin-triplet ground-state, $X0^+$, with a strong weight on the $M_S = 0$ component of the $^3\Sigma^-$ SOF state. As a consequence of the hydration effects, the AtO^+ $(H_2O)_n$ ($n \geq 5$) clusters adopt essentially-spin-singlet closed-shell ground-states. We have determined, for the first time, that these ground-states are dominated by the closed-shell $S_0(^1\Delta)$, originating from the closed-shell component of $^1\Delta$ of the free AtO^+ cation. We showed that this spin–orbit-coupled state correlates with one component of the **a**2 state of AtO^+, meaning that a hydration-induced ground-state change definitely occurs in AtO^+, which supports the studies of Ayed *et al.*[5,6]

The AtO^+ species is one of the cationic forms that appears to predominate under acidic conditions in the Pourbaix (E-pH) diagram of astatine. This species readily reacts with closed-shell species, which can be explained by the abovementioned hydration-induced ground-state change. The fact that it undergoes a ground-state change in aqueous solution is clearly a peculiarity which further shows once more that the chemistry of astatine and its species can be very different from those of the other halogens.[10,25,38–40] Therefore, it remains crucial and timely to pursue chemical studies concerning this "invisible" element.

Acknowledgements

This work has been supported by grants funded by the French National Agency for Research with "Investissements d'Avenir" (ANR-11-EQPX-0004, ANR-11-LABX-0018). This work was performed using HPC resources from CCIPL ("Centre de Calcul Intensif des Pays de la Loire").

References

1 L. Andrews, B. Liang, J. Li and B. E. Bursten, *Angew. Chem.*, 2000, **112**, 4739–4741.
2 J. Li, B. E. Bursten, B. Liang and L. Andrews, *Science*, 2002, **295**, 2242–2245.
3 J. Li, B. E. Bursten, L. Andrews and C. J. Marsden, *J. Am. Chem. Soc.*, 2004, **126**, 3424–3425.
4 I. Infante, L. Andrews, X. Wang and L. Gagliardi, *Chem. – Eur. J.*, 2010, **16**, 12804–12807.
5 T. Ayed, M. Seydou, F. Réal, G. Montavon and N. Galland, *J. Phys. Chem. B*, 2013, **117**, 5206–5211.
6 T. Ayed, F. Réal, G. Montavon and N. Galland, *J. Phys. Chem. B*, 2013, **117**, 10589–10595.
7 A. S. P. Gomes, F. Réal, N. Galland, C. Angeli, R. Cimiraglia and V. Vallet, *Phys. Chem. Chem. Phys.*, 2014, **16**, 9238–9248.
8 R. Maurice, F. Réal, A. S. P. Gomes, V. Vallet, G. Montavon and N. Galland, *J. Chem. Phys.*, 2015, **142**, 094305.
9 J. Champion, M. Seydou, A. Sabatié-Gogova, E. Renault, G. Montavon and N. Galland, *Phys. Chem. Chem. Phys.*, 2011, **13**, 14984–14992.
10 J. Champion, A. Sabatié-Gogova, F. Bassal, T. Ayed, C. Alliot, N. Galland and G. Montavon, *J. Phys. Chem. A*, 2013, **117**, 1983–1990.
11 D.-C. Sergentu, D. Teze, A. Sabatié-Gogova, C. Alliot, N. Guo, F. Bassal, I. Da Silva, D. Deniaud, R. Maurice, J. Champion, N. Galland and G. Montavon, *Chem. – Eur. J.*, 2016, **22**, 2964–2971.
12 J. Champion, C. Alliot, E. Renault, B. M. Mokili, M. Chérel, N. Galland and G. Montavon, *J. Phys. Chem. A*, 2010, **114**, 576–582.
13 A. Sabatié-Gogova, J. Champion, S. Huclier, N. Michel, F. Pottier, N. Galland, Z. Asfari, M. Cherél and G. Montavon, *Anal. Chim. Acta*, 2012, **721**, 182–188.
14 D. S. Wilbur, *Nat. Chem.*, 2013, **5**, 246.
15 M. R. Zalutsky and M. Pruszynski, *Curr. Radiopharm.*, 2011, **4**, 177–185.
16 D. S. Wilbur, *Curr. Radiopharm.*, 2008, **1**, 144–176.

Published on 26 October 2016. Downloaded on 09/12/2016 12:27:15.

17 S. G. DiMagno, *US Pat.*, US20140275539 A1, 2014.
18 M. Amaouch, G. Montavon, N. Galland and J. Pilmé, *Mol. Phys.*, 2016, **114**, 1326–1333.
19 T. Ayed, J. Pilmé, D. Tézé, F. Bassal, J. Barbet, M. Chérel, J. Champion, R. Maurice, G. Montavon and N. Galland, *Eur. J. Med. Chem.*, 2016, **116**, 156–164.
20 J.-B. Rota, S. Knecht, T. Fleig, D. Ganyushin, T. Saue, F. Neese and H. Bolvin, *J. Chem. Phys.*, 2011, **135**, 114106.
21 Y. Zhao and D. G. Truhlar, *Theor. Chem. Acc.*, 2008, **120**, 215–241.
22 D.-C. Sergentu, G. David, G. Montavon, R. Maurice and N. Galland, *J. Comput. Chem.*, 2016, **37**, 1345–1354.
23 J. P. Perdew, M. Ernzerhof and K. Burke, *J. Chem. Phys.*, 1996, **105**, 9982–9985.
24 C. Adamo and V. Barone, *J. Chem. Phys.*, 1999, **110**, 6158–6170.
25 D.-C. Sergentu, M. Amouch, J. Pilmé, N. Galland and R. Maurice, *J. Chem. Phys.*, 2015, **143**, 114306.
26 M. J. Frisch, G. W. Trucks, H. B. Schlegel, G. E. Scuseria, M. A. Robb, J. R. Cheeseman, G. Scalmani, V. Barone, B. Mennucci, G. A. Petersson, H. Nakatsuji, M. Caricato, X. Li, H. P. Hratchian, A. F. Izmaylov, J. Bloino, G. Zheng, J. L. Sonnenberg, M. Hada, M. Ehara, K. Toyota, R. Fukuda, J. Hasegawa, M. Ishida, T. Nakajima, Y. Honda, O. Kitao, H. Nakai, T. Vreven, J. A. Montgomery, Jr., J. E. Peralta, F. Ogliaro, M. Bearpark, J. J. Heyd, E. Brothers, K. N. Kudin, V. N. Staroverov, R. Kobayashi, J. Normand, K. Raghavachari, A. Rendell, J. C. Burant, S. S. Iyengar, J. Tomasi, M. Cossi, N. Rega, J. M. Millam, M. Klene, J. E. Knox, J. B. Cross, V. Bakken, C. Adamo, J. Jaramillo, R. Gomperts, R. E. Stratmann, O. Yazyev, A. J. Austin, R. Cammi, C. Pomelli, J. W. Ochterski, R. L. Martin, K. Morokuma, V. G. Zakrzewski, G. A. Voth, P. Salvador, J. J. Dannenberg, S. Dapprich, A. D. Daniels, Ö. Farkas, J. B. Foresman, J. V. Ortiz, J. Cioslowski and D. J. Fox, *Gaussian 09 Revision D.01*, Gaussian Inc., Wallingford, CT, 2009.
27 K. A. Peterson, D. Figgen, E. Goll, H. Stoll and M. Dolg, *J. Chem. Phys.*, 2003, **119**, 11113–11123.
28 M. K. Armbruster, W. Klopper and F. Weigend, *Phys. Chem. Chem. Phys.*, 2006, **8**, 4862–4865.
29 T. H. Dunning Jr, *J. Chem. Phys.*, 1989, **90**, 1007–1023.
30 R. A. Kendall, T. H. Dunning and R. J. Harrison, *J. Chem. Phys.*, 1992, **96**, 6796–6806.
31 B. O. Roos, P. R. Taylor and P. E. M. Siegbahn, *Chem. Phys.*, 1980, **48**, 157–173.
32 B. O. Roos, in *Theory and applications of computational chemistry: The first forty years*, ed. C. E. Dykstra, G. Frenking, K. S. Kim and G. E. Scuseria, Elsevier, Amsterdam, 2005, ch. 25, pp. 725–764.
33 A. Celestino, R. Cimiraglia and J.-P. Malrieu, *Chem. Phys. Lett.*, 2001, **350**, 297–305.
34 K. G. Dyall, *J. Chem. Phys.*, 1995, **102**, 4909–4918.
35 H. J. Werner, P. J. Knowles, R. Lindh, F. R. Manby, M. Schütz, P. Celani, T. Korona, A. Mitrushenkov, G. Rauhut, T. B. Adler, R. D. Amos, A. Bernhardsson, A. Berning, D. L. Cooper, M. J. O. Deegan, A. J. Dobbyn, F. Eckert, E. Goll, C. Hampel, G. Hetzer, T. Hrenar, G. Knizia, C. Köppl, Y. Liu, A. W. Lloyd, R. A. Mata, A. J. May, S. J. McNicholas, W. Meyer, M. E. Mura, A. Nicklass, P. Palmieri, K. Pflüger, R. Pitzer, M. Reiher, U. Schumann, H. Stoll, A. J. Stone, R. Tarroni, T. Thorsteinsson, M. Wang and A. Wolf, *MOLPRO, Version 2009.1, A Package of Ab Initio Programs*, 2009, see http://www.molpro.net.
36 M. K. Armbruster, F. Weigend, C. van Wullen and W. Klopper, *Phys. Chem. Chem. Phys.*, 2008, **10**, 1748–1756.
37 *TURBOMOLE V6.6 2014, A Development of University of Karlsruhe And Forschungszentrum Karlsruhe GmbH, 1989–2007*, TURBOMOLE GmbH, since 2007, available from http://www.turbomole.com.
38 J. Pilmé, E. Renault, T. Ayed, G. Montavon and N. Galland, *J. Chem. Theory Comput.*, 2012, **8**, 2985–2990.
39 A. Hermann, R. Hoffmann and N. W. Ashcroft, *Phys. Rev. Lett.*, 2013, **111**, 116404.
40 R. E. Vernon, *J. Chem. Educ.*, 2013, **90**, 1703–1707.

 This journal is © the Owner Societies 2016

Electronic Supplementary Material (ESI) for Physical Chemistry Chemical Physics.
This journal is © the Owner Societies 2016

Supporting Information for: Unraveling the hydration-induced ground-state change of AtO^+ with relativistic and multiconfigurational wave-function-based methods

Dumitru-Claudiu Sergentu,[a,b] Florent Réal,[c] Gilles Montavon,[a] Nicolas Galland,*[b] and Rémi Maurice*[a]
[a] SUBATECH, UMR CNRS 6457, IN2P3/EMN Nantes/Université de Nantes, 4 Rue A. Kastler, BP 20722, 44307 Nantes Cedex 3, France. E-mail: remi.maurice@subatech.in2p3.fr
[b] CEISAM, UMR CNRS 6230, Université de Nantes, 44322 Nantes Cedex 3, France. E-mail: nicolas.galland@univ-nantes.fr
[c] PhLAM, UMR CNRS 8523, Université de Lille 1, 59655 Villeneuve d'Ascq Cedex, France

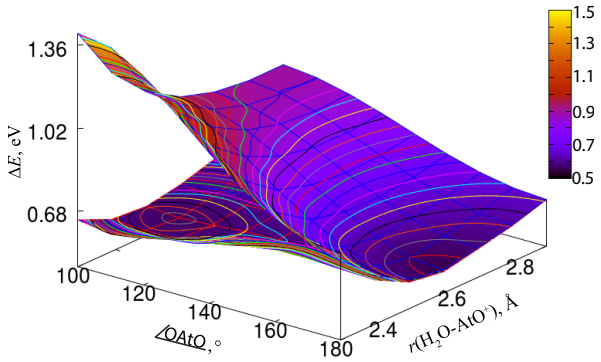

Figure S1 Evolution of the energies of the $S_0(^1\Delta)$ and $S_1(^1\Delta)$ electronic states of the $AtO^+(H_2O)$ system computed at the NEVPT2/AVTZ level of theory as a function of the H_2O–AtO^+ bond distance and of the ∠OAtO bond angle.

Equation S1 c-SOCI compositions of the five lowest spin-orbit coupled states at the equilibrium spin-restricted-singlet $AtO^+(H_2O)_n$ (n=3–5) geometries.

$$n=3\begin{cases}|\Psi_0\rangle = & 73\%\left|\mathrm{S}_0(^1\Delta)\right\rangle + ... \\ |\Psi_1\rangle = & 24\%\left|\mathrm{T}_0(^3\Sigma^-)\right\rangle_{M_S=+1} + 24\%\left|\mathrm{T}_0(^3\Sigma^-)\right\rangle_{M_S=-1} + 26\%\left|\mathrm{T}_0(^3\Sigma^-)\right\rangle_{M_S=0} + ... \\ |\Psi_2\rangle = & 18\%\left|\mathrm{T}_0(^3\Sigma^-)\right\rangle_{M_S=+1} + 18\%\left|\mathrm{T}_0(^3\Sigma^-)\right\rangle_{M_S=-1} + 33\%\left|\mathrm{T}_0(^3\Sigma^-)\right\rangle_{M_S=0} + ... \\ |\Psi_3\rangle = & 44\%\left|\mathrm{T}_0(^3\Sigma^-)\right\rangle_{M_S=+1} + 44\%\left|\mathrm{T}_0(^3\Sigma^-)\right\rangle_{M_S=-1} + ... \\ |\Psi_4\rangle = & 76\%\left|\mathrm{S}_1(^1\Delta)\right\rangle + ...\end{cases}$$

$$n=4\begin{cases}|\Psi_0\rangle = & 82\%\left|\mathrm{S}_0(^1\Delta)\right\rangle + ... \\ |\Psi_1\rangle = & 36\%\left|\mathrm{T}_0(^3\Sigma^-)\right\rangle_{M_S=+1} + 36\%\left|\mathrm{T}_0(^3\Sigma^-)\right\rangle_{M_S=-1} + 25\%\left|\mathrm{T}_1(^3\Pi)\right\rangle_{M_S=0} + ... \\ |\Psi_2\rangle = & 43\%\left|\mathrm{T}_0(^3\Sigma^-)\right\rangle_{M_S=+1} + 43\%\left|\mathrm{T}_0(^3\Sigma^-)\right\rangle_{M_S=-1} + ... \\ |\Psi_3\rangle = & 11\%\left|\mathrm{T}_1(^3\Pi)\right\rangle_{M_S=+1} + 11\%\left|\mathrm{T}_1(^3\Pi)\right\rangle_{M_S=-1} + 58\%\left|\mathrm{T}_0(^3\Sigma^-)\right\rangle_{M_S=0} + ... \\ |\Psi_4\rangle = & 55\%\left|\mathrm{S}_1(^1\Delta)\right\rangle + 21\%\left|\mathrm{T}_1(^3\Pi)\right\rangle_{M_S=+1} + 21\%\left|\mathrm{T}_1(^3\Pi)\right\rangle_{M_S=-1} + ...\end{cases}$$

$$n=5\begin{cases}|\Psi_0\rangle = & 83\%\left|\mathrm{S}_0(^1\Delta)\right\rangle + ... \\ |\Psi_1\rangle = & 32\%\left|\mathrm{T}_0(^3\Sigma^-)\right\rangle_{M_S=+1} + 32\%\left|\mathrm{T}_0(^3\Sigma^-)\right\rangle_{M_S=-1} + 33\%\left|\mathrm{T}_1(^3\Pi)\right\rangle_{M_S=0} + ... \\ |\Psi_2\rangle = & 41\%\left|\mathrm{T}_0(^3\Sigma^-)\right\rangle_{M_S=+1} + 41\%\left|\mathrm{T}_0(^3\Sigma^-)\right\rangle_{M_S=-1} + ... \\ |\Psi_3\rangle = & 16\%\left|\mathrm{T}_1(^3\Pi)\right\rangle_{M_S=+1} + 16\%\left|\mathrm{T}_1(^3\Pi)\right\rangle_{M_S=-1} + 50\%\left|\mathrm{T}_0(^3\Sigma^-)\right\rangle_{M_S=0} + ... \\ |\Psi_4\rangle = & 44\%\left|\mathrm{S}_1(^1\Delta)\right\rangle + 26\%\left|\mathrm{T}_1(^3\Pi)\right\rangle_{M_S=+1} + 26\%\left|\mathrm{T}_1(^3\Pi)\right\rangle_{M_S=-1} ...\end{cases}$$

SCIENTIFIC REPORTS

OPEN

Targeted radionuclide therapy with astatine-211: Oxidative dehalogenation of astatobenzoate conjugates

Received: 26 January 2017
Accepted: 13 April 2017
Published online: 31 May 2017

David Teze[1,2], Dumitru-Claudiu Sergentu[1,2], Valentina Kalichuk[3], Jacques Barbet[3,4], David Deniaud[2], Nicolas Galland[2], Rémi Maurice[1] & Gilles Montavon[1]

^{211}At is a most promising radionuclide for targeted alpha therapy. However, its limited availability and poorly known basic chemistry hamper its use. Based on the analogy with iodine, labelling is performed via astatobenzoate conjugates, but *in vivo* deastatination occurs, particularly when the conjugates are internalized in cells. Actually, the chemical or biological mechanism responsible for deastatination is unknown. In this work, we show that the C—At "organometalloid" bond can be cleaved by oxidative dehalogenation induced by oxidants such as permanganates, peroxides or hydroxyl radicals. Quantum mechanical calculations demonstrate that astatobenzoates are more sensitive to oxidation than iodobenzoates, and the oxidative deastatination rate is estimated to be about 6×10^6 faster at 37 °C than the oxidative deiodination one. Therefore, we attribute the "internal" deastatination mechanism to oxidative dehalogenation in biological compartments, in particular lysosomes.

Halogens are usually named according to ancient Greek words denoting one of their characteristics. The heaviest of these elements befell the name astatine, as a reference to its instability[1]. While this name was proposed from a physical perspective (*i.e.* the absence of any stable isotope), one might tend to consider that it is also suitable from a chemical point of view, since most bonds involving this atom are less stable than the ones involving its closest analogue, iodine. This affects the potential application of ^{211}At to medicine. Nevertheless, ^{211}At is considered as one of the most promising radionuclides for targeted alpha therapy, due to its favourable physical properties (notably its half-life time of 7.2 h and its α-particle emission yield of 100%)[2,3].

Clinical trials using either monoclonal antibodies (mAbs) or antibody fragments labelled by astatobenzoate conjugates afforded encouraging results against both recurrent brain tumours and recurrent ovarian cancers[2,4–6]. However, labelling with astatobenzoate conjugates suffers from *in vivo* dehalogenation, which diminishes the tumour uptake and leads to the release of free astatine and its accumulation in stomach and thyroid. Even if stomach and thyroid uptake can be mitigated[7–9], a more stable labelling is needed for systemic administration[8]. It is particularly interesting to note that when mAbs are labelled with astatobenzoates, deastatination is limited[10–14], while when antibody fragments are used, considerable dehalogenation occurs[10,11,15]. Unfortunately, the slow mAbs pharmacokinetics are not well-suited to be combined with the ^{211}At half-life time[7,16], and astatine-labelled antibodies have been so far limited to locoregional treatments. Moreover, this behaviour is remarkable, as it echoes the one of proteins, iodinated through direct labelling or using the Bolton-Hunter reagent[17]. In these cases the dehalogenation mechanism has been elucidated: the *2*-iodophenol moiety of the catabolites released through carrier metabolization undergoes dehalogenation catalysed by deiodinases. Thus, the deastatination mechanism is most probably initiated through internalization into cells and lysosomal degradation. To overcome deiodination, reagents such as the *N*-succinimidyliodobenzoate (SIB) have been synthesized by electrophilic radioiodination

[1]SUBATECH, UMR CNRS 6457, IN2P3/IMT Atlantique/Université de Nantes, 4 rue Alfred Kastler, BP 20722, 44307, Nantes Cedex 3, France. [2]CEISAM, UMR CNRS 6230, Université de Nantes, 2 rue de la Houssinière, BP 92208, 44322, Nantes Cedex 3, France. [3]Centre de Recherche en Cancérologie de Nantes-Angers, Inserm U892, CNRS UMR 6399, Université de Nantes, Institut de Recherche en Santé de l'Université de Nantes, 8 quai Moncousu, F-44007, Nantes Cedex 1, France. [4]GIP ARRONAX, 1 rue Aronnax, F-44817, Saint-Herblain, France. Correspondence and requests for materials should be addressed to D.T. (email: david.teze@gmail.com) or R.M. (email: remi.maurice@subatech.in2p3.fr)

of *N*-succinimidylaryltrialkylstannane derivatives[18,19]. Indeed, these reagents lack the phenolic hydroxyl group required in the catalytic mechanism of mammal deiodinases[18–21].

Therefore, an analogous astatination reagent, the *N*-succinimidylastatobenzoate (SAB), has been developed[10]. However, the aforementioned studies of astatobenzoate-labelled proteins showed that such labelling with ^{211}At is unstable, leading to dehalogenation, contrary to the iodine case. Hence, it is clear that carrier catabolism favours astatobenzoate deastatination via mechanisms that remain unknown. It should also be mentioned that besides proteins, the injection of small organic compounds such as astatobenzoate-labelled biotin derivatives[22] or simply 3-astatobenzoate itself[11] leads to a radioactivity biodistribution similar to that of astatide, and very dissimilar to the iodobenzoate one, denoting a fast deastatination. Alternatively, labelling with astatodecaborates instead of astatobenzoate conjugates was envisaged, leading to stable labelling even with small molecules and very encouraging preclinical results[23–25]. However, this approach seems hindered by high uptake in kidneys and liver[7,26]. Note that the study of such compounds is beyond the scope of the present work, which aims at revealing the mechanism(s) responsible for astatobenzoate dehalogenation.

Two explanations have been proposed so far to justify the astatobenzoate dehalogenation, (i) the action of unidentified enzymes that would catalyse the C−At bond cleavage (similarly to what happens to radioiodinated proteins by direct labelling)[27], and (ii) the relative weakness of the C−At bonds compared to the C−I ones. One may argue that since astatine is absent from the biosphere (it is the rarest naturally occurring element on Earth)[28,29], no At-specific enzyme that catalyses C−At bond breakages is likely to exist. However, some proteins such as the sodium-iodide symporter recognize both astatide and iodide[30,31], demonstrating that the presence of iodine-processing enzymes may also affect astatine compounds. Nevertheless, C−At bond cleavages induced by promiscuous enzymes are unlikely to happen since the analogous C−I bonds are not cleaved. The second and most often quoted justification, that the C−At bonds are weaker than the corresponding C−I ones, although true[32], is not sufficient to explain why astatobenzoate-labelled proteins are seemingly stable in blood and not when internalized inside living cells.

In order to explain the biodistribution observations from the literature, the sought *in vivo* deastatination mechanism(s) should satisfy the following criteria, (i) the analogous C−I bonds must remain stable under conditions that are sufficient for allowing C−At bond cleavages, (ii) these conditions could not be met in blood, but rather in other biological compartments such as the ones the carrier and its catabolites enter during the catabolism process, and (iii) the C−At bond breakage, should occur in the absence of any enzyme. This work aims at providing a satisfactory explanation that fully meets these criteria. One of the most striking differences between I and At lies in the astatine metalloid properties[33,34]: its Pourbaix (*E*−pH) diagram displays cationic species[35,36], contrarily to the iodine one[37], and the ionization potential of its free atom[28] is lower than the one of iodine by more than 1 eV. Therefore, one may hypothesize that astatinated compounds are more sensitive to oxidation than iodinated ones, which seems particularly relevant since carrier catabolism (which favours deastatination) exposes astatobenzoate moieties to critical changes in redox conditions. Indeed, internalization in cells will lead labelled carriers into lysosomes, where myriads of strong oxidants such as the so-called reactive oxygen species (ROS), a family of compounds including peroxides and oxygen radicals, are present.

Here, we report the stability of an astatobenzoate conjugate in the presence of various oxidants to assess if its oxidation is possible, and if it eventually leads to deastatination. Indeed, an extensive metabolic study has been made on a ^{125}I-iodobenzoate-labelled antibody fragment[38], showing the presence of iodobenzoate and of its lysine and glycine conjugates as main catabolites, free iodine being absent. One could thus assume that the astatobenzoate catabolites would be similar to the iodinated ones. Oxidants such as permanganates, peroxides or hydroxyl radicals have been tested. Also, we show that the Fenton reaction, which happens *in vivo* in lysosomes, leads to deastatination within seconds. Since astatine is only produced in minute quantities, no spectroscopic tool can be used to probe the nature of its chemical species. Therefore, we also present relativistic density functional theory (DFT) calculations to elucidate or at least get insight on the "microscopic" mechanism that eventually leads to deastatination. It is indeed of great interest to combine quantum calculations and experiments to obtain information on astatine species at the molecular scale[35,39–41]. Finally, we conclude by attributing the deastatination mechanism to oxidative dehalogenation.

Results

Oxidative dehalogenation of astatobenzoate conjugates. To probe the oxidative dehalogenation hypothesis, we have selected ethyl 3-astatobenzoate (**1a**) as a model compound for performing stability studies in presence of oxidants such as permanganates (Fig. 1a) or peroxides (Fig. 1b) by measuring the proportion of "intact" astatobenzoate conjugate by reverse-phase high-performance liquid chromatography (HPLC). The influence of acidity (up to pH = 1) and strong reductants was also briefly investigated, but did not result in any noticeable deastatination.

Figure 1a clearly evidences that, at pH = 4.7 (an average pH value for lysosomes), the presence of MnO_4^- ions leads to the deastatination of astatobenzoates, in a concentration-dependent way. This demonstrates for the first time that astatobenzoate conjugates can be altered by oxidative dehalogenation, contrarily to what was previously thought[43]. By contrast, no discernible deiodination is observed after 12 h incubation of ethyl 3-iodobenzoate (**1b**) in the presence of 2 mM $NaMnO_4$ (not shown). Figure 1b also shows that some peroxides (*tert*-butyl hydroperoxide, referred to as "TBHP" and peroxodisulfate) are also able to induce deastatination at the same pH value. This is particularly interesting since the most notorious oxidants occurring *in vivo* are the ROS, among which peroxides can be found. Also, one should note that oxidative dehalogenation induced by TBHP occurs at physiological pH, *i.e.* 7.4, with similar kinetics as observed at pH = 4.7.

Oxidative dehalogenation of astatobenzoate conjugates induced by Fenton and Fenton-like conditions. The most common *in vivo* ROS, namely hydrogen peroxide (H_2O_2), does not promote any

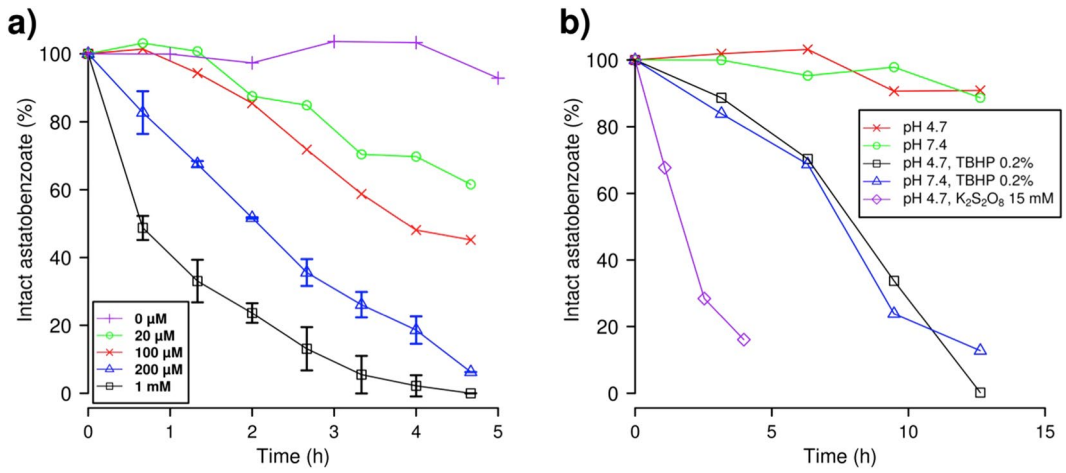

Figure 1. Influence of oxidants on the deastatination of ethyl 3-astatobenzoates. The proportion of intact ethyl 3-astatobenzoate is assessed by reverse-phase HPLC coupled to a dual-flow cell gamma detection system[42]. (**a**) Concentration-dependent deastatination promoted by permanganate. The $NaMnO_4$ concentration is varied between 0 and 1 mM while the pH value is fixed at 4.7 with a phosphate-acetate buffer (50 mM). (**b**) Effect of peroxodisulfate (purple) and *tert*-butyl hydroperoxide (TBHP, black and blue) on the ethyl 3-astatobenzoate stability (see text).

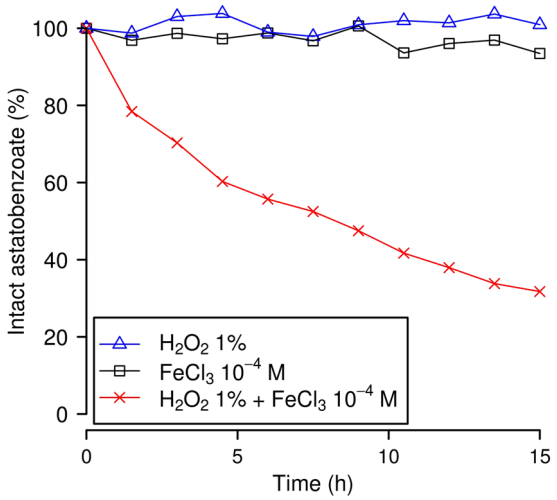

Figure 2. Influence of Fenton-like conditions on the deastatination of the 1a astatobenzoate. Amounts of intact ethyl 3-astatobenzoate are assessed by reverse-phase HPLC coupled to a dual-flow cell gamma detection system[42].

noticeable deastatination (see Fig. 2). By contrast, the combination of catalytic amount of ferrous iron with hydrogen peroxide (and other peroxides as well) was proven to be a powerful oxidant more than 120 years ago[44]. While radicals were not known at that time, it is now well-established that this combination produces hydroxyl radicals, which are highly reactive species[45]. When astatobenzoate conjugates are incubated under Fenton conditions (50 mM of the phosphate-acetate buffer – pH ≈ 3, 10^{-4} M of Fe^{2+} ions, and 1% H_2O_2), they undergo an extremely fast deastatination: within the few tens of seconds needed for the HPLC injection, most of the astatobenzoate moieties were dehalogenated, and the majority of the activity was found in a peak having a retention time that appears to match the one of an oxygen adduct of astatine (in particular an At (III) species).

Catalytic amounts of ferric iron (*i.e.* trivalent iron instead of divalent) coupled with hydrogen peroxide are also known to produce hydroxyl radicals, but at a much slower rate[45]. These conditions are often referred to as "Fenton-like". The dehalogenation kinetics of ethyl 3-astatobenzoate (**1a**) incubated under Fenton-like conditions is displayed on Fig. 2. Note that, for illustration purposes, the radiochromatograms obtained after 3 h with 1% H_2O_2 and 1% H_2O_2 plus 10^{-4} M of Fe^{3+} ions are displayed in Fig. S1. These experimental results prove that astatobenzoate conjugates are sensitive to oxidation via the Fenton reaction, that is actually at play in lysosomes[46,47]. They also indicate that the released astatine species should be an oxygen adduct, but they do not indicate how and why oxidation leads to deastatination. One should note that this part of the study has been performed at pH = 3 to favour the efficiency of the Fenton reaction in order to probe the effect of the presence of hydroxyl radicals

(which are produced in lysosomes) on the dehalogenation mechanism(s). Furthermore, one should note that no discernible deiodination of ethyl 3-iodobenzoate (**1b**) is observed after 12 h incubation under Fenton-like conditions. In order to gain more insight on the oxidative dehalogenation mechanism(s) and on the differences between the C−At and C−I bonds of interest, a quantum mechanical study was performed.

Accuracy of the computational approach. As no spectroscopic information can be obtained at ultratrace concentrations, it is necessary to consider quantum mechanical calculations to get any "microscopic" information on the deastatination mechanism(s). It is of particular importance to treat spin-orbit coupling (SOC), since this relativistic interaction has a strong influence on the geometries and properties of At compounds[40,48]. The B3LYP hybrid exchange-correlation functional was selected, owing to its "safe choice" label for investigating astatine species[48]. Before studying the bond energies of interest, it was worth checking the validity of the used level of theory on well-known systems for which experimental data are available[49]. In the case of astatobenzene and iodobenzene, the correct dissociation limit is the homolytic one (i.e. radical fission, $A-B \rightarrow A^{\cdot} + B^{\cdot}$), and test calculations confirmed that this dissociation limit is found to be favoured by more than a hundred kcal.mol^{-1} compared to ionic limits at the considered level of theory.

A good agreement between the experimental dissociation energies of astatobenzene and iodobenzene (44.9 ± 5.1 and 61.1 ± 4.7 kcal.mol^{-1}, respectively)[49] and the computed ones (44.7 and 59.6 kcal.mol^{-1}, respectively) was obtained. Furthermore, first ionisation potentials (IP_1s) were computed as a model descriptor for the oxidation propensity of halobenzoates. We obtained an IP_1 value of 195.5 kcal.mol^{-1} for iodobenzene, which fits well with the experimental value of 201.3 ± 0.7 kcal.mol^{-1} [50]. All these results provide a firm ground to the used level of theory prior to starting the study of the oxidation of halobenzoate conjugates. Note that for the interested reader, additional calculations to illustrate the importance of SOC on the computed quantities are reported in Tables S1 and S2. Since reliable values can only be obtained when SOC is accounted for, we only report in the main text results that do include this relativistic interaction.

Probing the sensitivity to oxidation of halobenzoates: first ionisation potentials. To probe the relative feasibility of the oxidation of **1a** and **1b**, we first computed their IP_1s. At first, we checked that these IP_1s were indeed related to electron removal at the halogen moiety of halobenzoates by computing the condensed-to-atom Fukui index, a quantity that resides in the realm of conceptual DFT. This index is computed through a finite difference approximation to the so-called Fukui function; for an electrophilic attack, it has the $f_k^- = q_k(N) - q_k(N-1)$ form, where k is an atom, $q_k(N)$ is the electron population of the k atom in the neutral system (N electrons) and $q_k(N-1)$ is the electron population of the k atom in the ionized system ($N-1$ electrons). Note that the electron populations are obtained in the present work from natural population analyses. We found that the condensed-to-atom Fukui index, f^- [51], is not only maximum for At in **1a**, and for I in **1b**, but is also at least four times larger for At or I, respectively, than for any other atom of the system. The corresponding f^- values are 0.7 and 0.5, meaning that the removed electron is more than 50% localized on the halogen moiety in each case.

It appears that the iodobenzoate compound **1b** presents a higher IP_1 (196.2 kcal.mol^{-1}) than the one computed for astatobenzoate **1a** (185.8 kcal.mol^{-1}). The important difference, 10.4 kcal.mol^{-1}, makes **1a** actually significantly easier to oxidize than its iodine counterpart. Indeed, the previous difference is greater than the one between iodobenzene and bromobenzene, and even the one between iodobenzene and chlorobenzene (5.8 and 7.8 kcal.mol^{-1} according to the experimental IP_1s)[50]. Thus, our calculations support the fact that astatobenzoates should be more prone to oxidation than their iodinated counterparts, since the first conceptual step of any potential oxidation, *i.e.* the withdrawal of one electron, is more favourable in the X = At case. Therefore, since we do not aim at fully elucidating the oxidation mechanism(s), we continue by directly studying the consequences of oxidation on the C−X bonds of interest.

The effect of oxidation on the C−X bond dissociation energies. As the immediate product of deastatination resulting from the Fenton reaction is attributed to an oxygen adduct of astatine, and since the **2b** species is known to exist, it seems reasonable to study the dissociation energies of the **2a** and **2b** compounds (see Fig. 3), where the halogen atoms formally bear a +III oxidation state, and to compare them with the ones of **1a** and **1b**. The bond dissociation energies are calculated considering the most favourable process, *i.e* a homolytic cleavage, by subtracting the energies of the two radical products (see Fig. 3), from the energy of the whole molecule. The obtained numerical results are displayed in Table 1.

By comparing the results obtained for **1a** and **1b** with the ones of the corresponding halobenzenes (44.7 and 59.6 kcal.mol^{-1}, respectively), one can first observe that the C−At and C−I bond energies are almost unchanged. Much more enthralling is the comparison between halobenzoates and their oxidized counterparts, as the bond dissociation energies drop in **2a** and **2b** by more than a third compared to **1a** and **1b**, respectively, *e.g.* diminishing the C−At bond energy from 44.6 to 28.2 kcal.mol^{-1}. While these energy decreases are of course noticeable, their significance may be further assessed with transition state theory in these undoubtedly kinetically controlled systems. As test calculations showed no energy barrier on the potential energy surfaces corresponding to the homolytic dissociations of the C−X bonds in **2a** and **2b**, as well as in **1a** and **1b**, these bond breakages are kinetically controlled by the corresponding bond dissociation energies. According to the Eyring equation[52], the ratio between the bond breakages rates in **2a** and **2b** is affected by the following temperature-dependent factor:

$$k(T) = e^{\frac{E_d(\mathbf{2b}) - E_d(\mathbf{2a})}{RT}} \quad (1)$$

where $E_d(\mathbf{2b})$ and $E_d(\mathbf{2a})$ are the bond dissociation energies of **2b** and **2a**, respectively, R is the universal gas constant and T is the temperature. Hence, the 9.6 kcal.mol^{-1} difference between $E_d(\mathbf{2b})$ and $E_d(\mathbf{2a})$ leads to a dissociation rate in **2a** larger by a factor of roughly 6×10^6 at 37 °C (human body temperature) than in **2b**, which

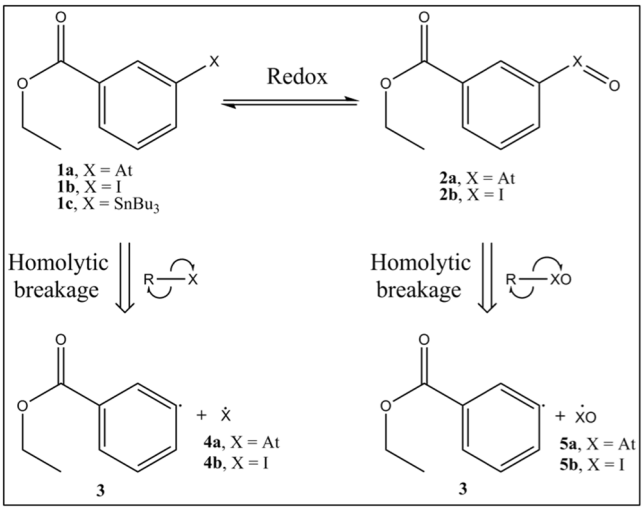

Figure 3. Scheme to assess the effect of oxidation on the C−X bond dissociation energies of halobenzoate compounds (X = At, I).

Compound	DFT
1a	44.6
2a	28.2
1b	59.4
2b	37.8

Table 1. C−X bond dissociation energies (kcal.mol^{-1}) of halobenzoates (X = At, I).

could explain the iodobenzoate relative stabilities towards oxidizing conditions compared to the astatobenzoate ones. Indeed, the iodosobenzoates will not only be produced much less efficiently than their astatinated counterparts, but also the astatosobenzoates are more prone to homolytic dehalogenation, unlike the iodosobenzoates for which the halogen will be more efficiently reduced back while proteins are oxidized[53]. On the other hand, the 16.4 kcal.mol^{-1} difference between E_d(**1a**) and E_d(**2a**) leads at 37 °C to an impressive relative increase of the dissociation rate for **2a**, by a factor of roughly 4×10^{11} with respect to **1a**. This difference is compatible with stable astatobenzoates in blood, given its antioxidant protections[54], and efficient dehalogenation of astatosobenzoates after the oxidation of astatine to its +II oxidation state.

Discussion

We report the first experiments of astatobenzoate dehalogenations, and shed light on the probable *in vivo* mechanism by which these therapeutically relevant compounds are catabolized. We propose that the *in vivo* C−At bond cleavage occurs through oxidative dehalogenation of the astatobenzoate moiety. This would explain the stability of the labelled carriers in blood, where the conjugates are protected from oxidative dehalogenation, notably by the thiolates of the human serum albumin (≈43 g.L^{-1}) in its mercaptalbumin form, and by the strong antioxidants properties of erythrocytes[54]. Also, no strong oxidant is known to be present in blood. On the other hand, after internalisation in cells, the halobenzoates moieties would no longer be shielded from encountering strong oxidants.

We propose reactions with ROS in lysosomes as the most likely path to oxidation. Indeed, lysosomes are the organelles that are responsible for protein degradation, and will be met in the first step of the carrier catabolism. They are known to be acidic (with average pH values ranging from 4.5 to 5)[46] and more oxidizing than other subcellular organelles[55,56]. However, the overall oxidation level is not the only parameter at play. Indeed, strong oxidants and reductants coexist in the lysosomes microdomains[56,57]. Similarly, the pH value experiences strong local variations, notably in the strict vicinity of proton pumps. Thus, when catabolized, the astatobenzoate conjugates will be exposed to strong oxidants, typically under acidic conditions in lysosomes. We have shown that the most common *in vivo* ROS, *i.e.* hydrogen peroxide (H_2O_2), does not intrinsically promote any noticeable deastatination. When coupled with ferrous (Fenton conditions) or even of ferric ("Fenton-like" conditions) ions, it promotes a fast cleavage of the C−At bond. It is thus clear that astatobenzoates undergo an extremely fast deastatination in the presence of hydroxyl radicals, ROS known to exist in lysosomes as products of the Fenton reaction. Indeed, due to the degradation of iron-containing macromolecules, many lysosomes are rich in redox-active iron compounds, which results in Fenton-type reactions in these organelles[46,47]. The ubiquity of lysosomes in mammalian cells is also consistent with the observed deastatination after cell internalisation regardless of the nature of the cells.

Alternatively, another possible oxidation path for halobenzoates is worth mentioning. Indeed, P-450 cytochromes (CYPs) catalyse the oxidation of iodobenzene into iodosobenzene[53], akin to the conversion of **1b**

into **2b**. Moreover, it has also been shown, within the halobenzene series, that, the heavier the halogen, the easier it is for CYPs to oxidize it ref. 58. Therefore, it seems possible that CYPs catalyses the oxidation of astatobenzoates as well. Note that even though iodosobenzene is formed *in vivo*, it could not be abundant, as it is reduced while it oxidizes proteins[53], and that no important dehalogenation of the iodosobenzene has been reported. It is therefore possible that following carrier metabolization, the astatobenzoates conjugates are released in the blood circulation, then captured by the liver, and later undergo oxidation catalysed by CYPs, which ultimately yields to deastatination.

The oxidative dehalogenation hypothesis nicely meets the criteria we proposed: deastatination by oxidation has been proven to be easily doable in the absence of any enzyme; it explains why the astatobenzoate conjugate stabilities must be very different in blood, where they are protected from oxidation, and within lysosomes where they are exposed to Fenton conditions (or alternatively after catabolization of the carrier and oxidation by CYPs in the liver). It is also consistent with the observed stability of the corresponding iodobenzoates under the same *in vivo* conditions: they are stable under conditions that are sufficient to provoke deastatination.

Besides experimental evidences and a proposed *in vivo* mechanism, we also aimed at giving an insight of the oxidative deastatination process at the molecular level, especially in regard to iodinated analogues of astatobenzoates. We hypothesized that the difference in *in vivo* stability between iodobenzoate- and astatobenzoate-labelled proteins with respect to dehalogenation is due to (i) the different sensitivities of the At and I atoms toward oxidation and (ii) the difference in the C−X bond strengths in the oxidized compounds. A plausible scenario is oxidative dehalogenation in which the At atom is oxidized to its +III oxidation state, which weakens enough the C−At bond and eventually leads to its breakage. Our DFT calculations show that it is much easier to start oxidizing astatobenzoates than their iodinated counterparts (by 10.4 kcal.mol^{-1} according to the calculated first ionization potentials). We also show that this oxidation results in a vast decrease of the C−X bond dissociation energies, illustrated by a drop of the C−At bond energy in the astatobenzoate from 44.6 to 28.2 kcal.mol^{-1}. Finally, to link this quantity to a more *in vivo* relevant one, we provide a rough estimate of the kinetic enhancement of the homolytic cleavage rate, showing that the reaction should be accelerated by a factor of about 4×10^{11} (a difference greater than the one between decades and milliseconds).

Finally, we deem that our results could be of interest to the conception of innovative ^{211}At-labelling agents, particularly in stimulating new ideas concerning their design and screening. Indeed, just as knowledge of the deiodinase involvement was a necessary step prior to designing SIB, our research demonstrates which types of mechanism should be inhibited for obtaining stable *in vivo* labelling with ^{211}At. Also, to speed up the quest for new compounds, as the *in vivo* experiments are costly, labour intensive, and time-consuming, we suggest that prior *in silico* screenings based on relativistic DFT calculations must be undertaken given both the accuracy and the cost-effective favour of this approach.

Methods

Radiolabelling. The synthesis of **1a** was done following the previously described methods for the synthesis of SAB[59,60]. Briefly, to 10 µL of acetic acid were added 25 µL of 2 mg/mL of *N*-chlorosuccinimide in methanol and 1,1 mg of ethyl 3-(tri-n-butylstannyl) benzoate (**1c**) in 25 µL of methanol in an HPLC vial. Then 50 µL of ^{211}At in chloroform were added (roughly corresponding to 5–10 MBq of activity). After 20 min incubation, **1a** was purified by HPLC using a Dionex Ultimate3000 HPLC device with an Interchrom C18 column piloted by the Chromeleon 6.80 software (ThermoFisher Scientific Inc.). It was coupled with a dual-flow cell gamma detection system[42] using a γ-ray detector (raytest GABI Star) piloted by the Gina software (raytest Isotopenmeßgeräte GmbH).

Kinetics of deastatination. 1.4 mL samples of **1a** (≃2–4 MBq of activity) were incubated in various media at 20 °C directly in the HPLC apparatus (same as described above), and 50 µL samples were injected onto column for analysis. The HPLC sequence was the following: 20 s of 100% acetonitrile (ACN) at 1.05 mL.min^{-1}, a 5 s gradient decrease from 100 to 0% ACN, 65 s of 0% ACN, a 90 s gradient from 0 to 60% ACN, a 720 s gradient from 60 to 72% ACN during which the flow is increased from 1.05 mL.min^{-1} to 1.3 mL.min^{-1} during 90 s after the first 6o s of the gradient, a 60 s gradient from 72 to 100% ACN, 300 s of 100% ACN, a 60 s gradient from 100 to 0% ACN during which the flow is decreased from 1.3 mL.min^{-1} to 1.05 mL.min^{-1} and 150 s of 0% CAN for a total run duration of 24.5 min. Two subsequent injections of 50 µL of $Na_2S_2O_3$ (50 mM) and of $NaMnO_4$ (2 mM) were run in a "short run mode" between two kinetic points to wash out any potential residual activity. The short run program consisted of 1 min of 100% H_2O, 1 min of 100% H_2O to 100% of CH_3CN (gradient) and 2 min of 100% CH_3CN. The sums of the counts in the "intact" astatobenzoate peak were corrected by the intrinsic decay of ^{211}At (considering its 7.21 h half-life time).

Computational methods. All the calculations have been performed in gas phase. The two-component (2*c*) DFT methods[61] relying on relativistic effective core potentials (namely ECP28MDF and ECP60MDF for I[62] and At[63], respectively) and implemented in the NWChem[64] and Turbomole[65] program packages were used. The hybrid B3LYP exchange-correlation functional[66] was selected, according to results of a recent benchmark study led on At compounds[48]. For treating the 25 valence electrons on both heavy atoms, we have selected triple zeta basis sets supplemented with 2*c* extensions, referred to as aug-cc-pVTZ-PP-2*c*[62,63,67]. The aug-cc-pVTZ basis sets[68,69] have been used for the remaining atoms (C, H and O).

References

1. Corson, D. R., Mackenzie, K. R. & Segre, E. Astatine: the element of Atomic Number 85. *Nature* **159**, 24–24, doi:10.1038/159024b0 (1947).
2. Zalutsky, M. R., Reardon, D. A., Pozzi, O. R., Vaidyanathan, G. & Bigner, D. D. Targeted alpha-particle radiotherapy with ^{211}At-labeled monoclonal antibodies. *Nucl. Med. Biol.* **34**, 779–85, doi:10.1016/j.nucmedbio.2007.03.007 (2007).

3. Vaidyanathan, G. & Zalutsky, M. Applications of ^{211}At and ^{223}Ra in Targeted Alpha-Particle Radiotherapy. *Curr Radiopharm* **4**, 283–294, doi:10.2174/1874471011104040283 (2011).
4. Zalutsky, M. R. *et al.* Clinical experience with alpha-particle emitting ^{211}At: treatment of recurrent brain tumor patients with ^{211}At-labeled chimeric antitenascin monoclonal antibody 81C6. *J. Nucl. Med.* **49**, 30–8, doi:10.2967/jnumed.107.046938 (2008).
5. Andersson, H. *et al.* Intraperitoneal alpha-particle radioimmunotherapy of ovarian cancer patients: pharmacokinetics and dosimetry of ^{211}At-MX35 F(ab')$_2$-a phase I study. *J. Nucl. Med.* **50**, 1153–60, doi:10.2967/jnumed.109.062604 (2009).
6. Aneheim, E. *et al.* Automated astatination of biomolecules–a stepping stone towards multicenter clinical trials. *Sci. Rep* **5**, 1–11, doi:10.1038/srep12025 (2015).
7. Steffen, A.-C. *et al.* Biodistribution of ^{211}At labeled HER-2 binding affibody molecules in mice. *Oncol. Rep.* **17**, 1141–1147, doi:10.3892/or.17.5.1141 (2007).
8. Vaidyanathan, G. & Zalutsky, M. R. Astatine Radiopharmaceuticals: Prospects and Problems. *Curr Radiopharm* **1**, 1–42, doi:10.2174/1874471010801030177 (2008).
9. Larsen, R. H., Slade, S. & Zalutsky, M. R. Blocking [^{211}At]Astatide Accumulation in Normal Tissues: Preliminary Evaluation of Seven Potential Compounds. *Nucl. Med. Biol.* **25**, 351–357, doi:10.1016/S0969-8051(97)00230-8 (1998).
10. Hadley, S. W., Wilbur, S. D., Gray, M. A. & Atcher, R. W. Astatine-211 Labeling of an Antimelanoma Antibody and Its Fab Fragment Using N-Succinimidyl p-Astatobenzoate: Comparisons *in Vivo* with the p-[^{125}I]Iodobenzoyl Conjugate. *Bioconjugate Chem* **2**, 171–179, doi:10.1021/bc00009a006 (1991).
11. Garg, P. K., Harrison, C. L. & Zalutsky, M. R. Comparative Tissue Distribution in Mice of the α-Emitter ^{211}At and ^{131}I as Labels of a Monoclonal Antibody and F(ab′)$_2$ Fragment. *Cancer Res.* **50**, 3514–3520 (1990).
12. Persson, M. I. *et al.* Astatinated trastuzumab, a putative agent for radionuclide immunotherapy of ErbB2-expressing tumours. *Oncol. Rep.* **15**, 673–80, doi:10.3892/or.15.3.673 (2006).
13. Gustafsson, A. M. E. *et al.* Comparison of therapeutic efficacy and biodistribution of ^{213}Bi- and ^{211}At-labeled monoclonal antibody MX35 in an ovarian cancer model. *Nucl. Med. Biol.* **39**, 15–22, doi:10.1016/j.nucmedbio.2011.07.003 (2012).
14. Zalutsky, M. R., Stabin, M. G., Larsen, R. H. & Bigner, D. D. Tissue distribution and radiation dosimetry of astatine-211-labeled chimeric 81C6, an alpha-particle-emitting immunoconjugate. *Nucl. Med. Biol.* **24**, 255–61, doi:10.1016/S0969-8051(97)00060-7 (1997).
15. Wilbur, D. S. *et al.* Reagents for Astatination of Biomolecules. 2. Conjugation of Anionic Boron Cage Pendant Groups to a Protein Provides a Method for Direct Labeling that is Stable to *in Vivo* Deastatination. *Bioconjugate Chem* **18**, 1226–1240, doi:10.1021/bc060345s (2007).
16. Orlova, A., Wållberg, H., Stone-Elander, S. & Tolmachev, V. On the selection of a tracer for PET imaging of HER2-expressing tumors: direct comparison of a ^{124}I-labeled affibody molecule and trastuzumab in a murine xenograft model. *J. nucl. med.* **50**, 417–25, doi:10.2967/jnumed.108.057919 (2009).
17. Bolton, A. E. & Hunter, W. M. The labelling of proteins to high specific radioactivities by conjugation to a ^{125}I-containing acylating agent. *Biochem. J.* **133**, 529–39, doi:10.1042/bj1330529 (1973).
18. Zalutsky, R. & Narula, A. S. A Method for the Radiohalogenation of Proteins Resulting in Decreased Thyroid Uptake of Radioiodine. *Appl. Radiat. Isot* **38**, 1051–1055, doi:10.1016/0883-2889(87)90069-4 (1987).
19. Vaidyanathan, G. & Zalutsky, M. R. Preparation of N -succinimidyl 3-[*I]iodobenzoate: an agent for the indirect radioiodination of proteins. *Nat. Protoc.* **1**, 707–713, doi:10.1038/nprot.2006.99 (2006).
20. Friedman, J. E., Watson, J. A. & Rokita, S. E. Iodotyrosine Deiodinase Is the First Mammalian Member of the NADH Oxidase/Flavin Reductase Superfamily. *J. Biol. Chem.* **281**, 2812–2819, doi:10.1074/jbc.M510365200 (2006).
21. Thomas, S. R., Mctamney, P. M., Adler, J. M., Laronde-leblanc, N. & Rokita, S. E. Crystal Structure of Iodotyrosine Deiodinase, a Novel Flavoprotein Responsible for Iodide Salvage in Thyroid Glands. *J. Biol. Chem.* **284**, 19659–19667, doi:10.1074/jbc.M109.013458 (2009).
22. Wilbur, D. S. *et al.* Biotin reagents in antibody pretargeting. 6. Synthesis and *in vivo* evaluation of astatinated and radioiodinated aryl- and nido-carboranyl-biotin derivatives. *Bioconjug. Chem* **15**, 601–616, doi:10.1021/bc034229q (2004).
23. Chen, Y. *et al.* Durable donor engraftment after radioimmunotherapy using alpha- emitter astatine-211 – labeled anti-CD45 antibody for conditioning in allogeneic hematopoietic cell transplantation. *Blood* **119**, 1130–1138, doi:10.1182/blood-2011-09-380436 (2012).
24. Orozco, J. J. *et al.* Anti-CD45 radioimmunotherapy using ^{211}At with bone marrow transplantation prolongs survival in a disseminated murine leukemia model. *Blood* **121**, 3759–3768, doi:10.1182/blood-2012-11-467035 (2013).
25. Green, D. J. *et al.* Astatine-211 conjugated to an anti-CD20 monoclonal antibody eradicates disseminated B-cell lymphoma in a mouse model. *Blood* **125**, 2111–2119, doi:10.1182/blood-2014-11-612770 (2015).
26. Wilbur, D. S., Chyan, M., Hamlin, D. K., Nguyen, H. & Vessella, R. L. Reagents for Astatination of Biomolecules. 5. Evaluation of Hydrazone Linkers in 211At- and 125I-Labeled closo-Decaborate(2-) Conjugates of Fab as a Means of Decreasing Kidney Retention. *Bioconjugate Chem* **22**, 1089–1102, doi:10.1021/bc1005625 (2011).
27. Orlova, A. *et al.* Targeting Against Epidermal Growth Factor Receptors. Cellular Processing of Astatinated EGF After Binding to Cultured Carcinoma Cells. *Anticancer Res.* **24**, 4035–4041 (2004).
28. Rothe, S. *et al.* Measurement of the first ionization potential of astatine by laser ionization spectroscopy. *Nat. Commun.* **4**, 1–6, doi:10.1038/ncomms2819 (2013).
29. Wilbur, D. S. Enigmatic astatine. *Nat. Chem.* **5**, 246–246, doi:10.1038/nchem.1580 (2013).
30. Carlin, S., Mairs, R. J., Welsh, P. & Zalutsky, M. R. Sodium-iodide symporter (NIS)-mediated accumulation of [^{211}At]astatide in NIS-transfected human cancer cells. *Nucl. Med. Biol.* **29**, 729–739, doi:10.1016/S0969-8051(02)00332-3 (2002).
31. Carlin, S., Akabani, G. & Zalutsky, M. R. *In Vitro* Cytotoxicity of ^{211}At-Astatide and ^{131}I-Iodide to Glioma Tumor Cells Expressing the Sodium/Iodide Symporter. *J. Nucl. Med.* **44**, 1827–1838 (2003).
32. Ayed, T. *et al.* ^{211}At-labeled agents for alpha-immunotherapy: On the *in vivo* stability of astatine-agent bonds. *Eur. J. Med. Chem.* **116**, 156–164, doi:10.1016/j.ejmech.2016.03.082 (2016).
33. Vernon, R. E. Which Elements Are Metalloids? *J. Chem. Educ.* **90**, 1703–1707, doi:10.1021/ed3008457 (2013).
34. Hermann, A., Hoffmann, R. & Ashcroft, N. W. Condensed astatine: Monatomic and metallic. *Phys. Rev. Lett.* **111**, 1–5, doi:10.1103/PhysRevLett.111.116404 (2013).
35. Sergentu, D.-C. *et al.* Advances on the Determination of the Astatine Pourbaix Diagram: Predomination of AtO(OH)$_2^-$ over At$^-$ in Basic Conditions. *Chem. Eur. J* **22**, 2964–2971, doi:10.1002/chem.201504403 (2016).
36. Champion, J. *et al.* Astatine Standard Redox Potentials and Speciation in Acidic Medium. *J. Phys. Chem. A* **3**, 576–582, doi:10.1021/jp9077008 (2010).
37. Tigeras, A., Bachet, M., Catalette, H. & Simoni, E. PWR iodine speciation and behaviour under normal primary coolant conditions: An analysis of thermodynamic calculations, sensibility evaluations and NPP feedback. *Prog. Nucl. Energy* **53**, 504–515, doi:10.1016/j.pnucene.2011.02.002 (2011).
38. Garg, P. K., Alston, K. L. & Zalutsky, M. R. Catabolism of Radioiodinated Murine Monoclonal Antibody F(ab')$_2$ Fragment Labeled Using N-Succinimidyl 3-Iodobenzoate and Iodogen Methods. *Bioconjugate Chem* **6**, 493–501, doi:10.1021/bc00034a020 (1995).
39. Champion, J. *et al.* Investigation of Astatine(III) Hydrolyzed Species: Experiments and Relativistic Calculations. *J. Phys. Chem. A* **117**, 1983–1990, doi:10.1021/jp3099413 (2013).

40. Champion, J. *et al*. Assessment of an effective quasirelativistic methodology designed to study astatine chemistry in aqueous solution. *Phys. Chem. Chem. Phys.* **13**, 14984–14992, doi:10.1039/c1cp20512a (2011).
41. Guo, N. *et al*. The Heaviest Possible Ternary Trihalogen Species, IAtBr −, Evidenced in Aqueous Solution: An Experimental Performance Driven by Computations. *Angew. Chem. Int. Ed.* **55**, 15369–15372, doi:10.1002/anie.201608746 (2016).
42. Lindegren, S., Jensen, H. & Jacobsson, L. A radio-high-performance liquid chromatography dual-flow cell gamma-detection system for on-line radiochemical purity and labeling efficiency determination. *J. Chromatogr. A* **1337**, 128–132, doi:10.1016/j.chroma.2014.02.043 (2014).
43. Milius, R. A. *et al*. Organoastatine Chemistry. Astatination via Electrophilic Destannylation. *Appl. Rad. Isot* **37**, 799–802, doi:10.1016/0883-2889(86)90274-1 (1986).
44. Fenton, H. J. H. Oxidation of tartaric acid in presence of iron. *J. Chem. Soc., Trans* **65**, 899–910, doi:10.1039/CT8946500899 (1894).
45. Walling, C. Fenton's reagent revisited. *Acc. Chem. Res.* **8**, 125–131, doi:10.1021/ar50088a003 (1975).
46. Kurz, T., Terman, A., Gustafsson, B. & Brunk, U. T. Lysosomes in iron metabolism, ageing and apoptosis. *Histochem. Cell Biol* **129**, 389–406, doi:10.1007/s00418-008-0394-y (2008).
47. Lin, Y., Epstein, D. L. & Liton, P. B. Intralysosomal iron induces lysosomal membrane permeabilization and cathepsin D-mediated cell death in trabecular meshwork cells exposed to oxidative stress. *Investig. Ophthalmol. Vis. Sci* **51**, 6483–6495, doi:10.1167/iovs.10-5410 (2010).
48. Sergentu, D., David, G., Montavon, G., Maurice, R. & Galland, N. Scrutinizing 'invisible' astatine: a challenge for modern density functionals. *J. Comput. Chem.* **37**, 1–16, doi:10.1002/jcc.v37.15 (2016).
49. Вашарош, Л, Норсеев, ЮВ & Халкин, ВА ОПРЕДЕЛЕНИЕ ЭНЕРГИИ РАЗРЫВА ХИМИЧЕСКОЙ СВЯЗИ УГЛЕРОД-АСТАТ. *Dokl Akad Nauk SSSR* **263**, 119–123 (1981).
50. Watanabe, K. Ionization Potentials of Some Molecules. *J. Chem. Phys.* **26**, 542–547, doi:10.1063/1.1743340 (1957).
51. Chattaraj, P. K., Sarkar, U. & Roy, D. R. Electrophilicity Index. *Chem. Rev.* **106**, 2065–2091, doi:10.1021/cr040109f (2006).
52. Eyring, H. The Activated Complex in Chemical Reactions. *J. Chem. Phys.* **3**, 107–115, doi:10.1063/1.1749604 (1935).
53. Burka, L. T., Thorsen, A. & Guengerich, F. P. Enzymatic Monooxygenation of Halogen Atoms: Cytochrome P-450 Catalyzed Oxidation of Iodobenzene by Iodosobenzene. *J. Am. Chem. Soc.* **102**, 7615–7616, doi:10.1021/ja00545a062 (1980).
54. Turell, L., Radi, R. & Alvarez, B. The thiol pool in human plasma: The central contribution of albumin to redox processes. *Free Radic. Biol. Med.* **65**, 244–253, doi:10.1016/j.freeradbiomed.2013.05.050 (2013).
55. Go, Y. M. & Jones, D. P. Redox compartmentalization in eukaryotic cells. *Biochim. Biophys. Acta* **1780**, 1273–1290, doi:10.1016/j.bbagen.2008.01.011 (2008).
56. Kaludercic, N., Deshwal, S. & Di Lisa, F. Reactive oxygen species and redox compartmentalization. *Front. Physiol* **5**, 1–15, doi:10.3389/fphys.2014.00285 (2014).
57. Kemp, M., Go, Y. & Jones, D. Nonequilibrium thermodynamics of thiol/disulfide redox systems: a perspective on redox systems biology. *Free Radic. Biol. Med.* **44**, 921–937, doi:10.1016/j.freeradbiomed.2007.11.008 (2008).
58. Burka, L. T., Plucinskit, T. & Macdonaldt, T. L. Mechanisms of hydroxylation by cytochrome P-450: Metabolism of monohalobenzenes by phenobarbital-induced microsomes. *Proc. Natl. Acad. Sci* **80**, 6680–6684, doi:10.1073/pnas.80.21.6680 (1983).
59. Vaidyanathan, G. & Zalutsky, M. R. Preparation of N-succinimidyl 3-[*I]iodobenzoate: an agent for the indirect radioiodination of proteins. *Nat. Protoc.* **1**, 707–13, doi:10.1038/nprot.2006.99 (2006).
60. Pozzi, O. R. & Zalutsky, M. R. Radiopharmaceutical chemistry of targeted radiotherapeutics, Part 3: alpha-particle-induced radiolytic effects on the chemical behavior of ^{211}At. *J. Nucl. Med.* **48**, 1190–6, doi:10.2967/jnumed.106.038505 (2007).
61. Armbruster, M. K., Weigend, F., van Wüllen, C. & Klopper, W. Self-consistent treatment of spin-orbit interactions with efficient Hartree-Fock and density functional methods. *Phys. Chem. Chem. Phys.* **10**, 1748–56, doi:10.1039/b717719d (2008).
62. Peterson, K. A., Shepler, B. C., Figgen, D. & Stoll, H. On the spectroscopic and thermochemical properties of ClO, BrO, IO, and their anions. *J. Phys. Chem. A* **110**, 13877–13883, doi:10.1021/jp065887l (2006).
63. Peterson, K. A., Figgen, D., Goll, E., Stoll, H. & Dolg, M. Systematically convergent basis sets with relativistic pseudopotentials. I. Correlation consistent basis sets for the post-d group 13–15 elements. *J. Chem. Phys.* **119**, 11099–11112, doi:10.1063/1.1622923 (2003).
64. Valiev, M. *et al*. NWChem: A comprehensive and scalable open-source solution for large scale molecular simulations. *Comput. Phys. Commun.* **181**, 1477–1489, doi:10.1016/j.cpc.2010.04.018 (2010).
65. R. Ahlrichs *et al*. 6.6, a development of University of Karlsruhe and Forschungszentrum Karlsruhe GmbH, TURBOMOLE GmbH (2014).
66. Stephen, P. J., Devlin, F. J., Chabalowski, C. F. & Frisch, M. J. Ab Initio Calculation of Vibrational Absorption. *J. Phys. Chem.* **98**, 11623–11627, doi:10.1021/j100096a001 (1994).
67. Armbruster, M. K., Klopper, W. & Weigend, F. Basis-set extensions for two-component spin-orbit treatments of heavy elements. *Phys. Chem. Chem. Phys.* **8**, 4862–5, doi:10.1039/b610211e (2006).
68. Kendall, Ra, Dunning, T. H. Jr. & Harrison, R. J. Electron affinities of the first-row atoms revisited. Systematic basis sets and wave functions. *J. Chem. Phys* **96**, 6796–6806, doi:10.1063/1.462569 (1992).
69. Dunning, T. H. Jr. Gaussian basis sets for use in correlated molecular calculations. I. The atoms boron through neon and hydrogen. *J. Chem. Phys.* **90**, 1007–1023, doi:10.1063/1.456153 (1989).

Acknowledgements

D.T. is thankful to Michel Chérel for helpful discussions. This work has been supported by grants funded by the French National Agency for Research with "Investissements d'Avenir" (ANR-11-EQPX-0004, ANR-11-LABX-0018). This work was performed using HPC resources from CCIPL ("Centre de Calcul Intensif des Pays de la Loire").

Author Contributions

D.T. and G.M. conceived and performed the experimental study. D.T., D.-C.S., N.G. and R.M. conceived and performed the computational studies. All authors jointly discussed the results and their interpretations and participated in writing the manuscript.

Additional Information

Supplementary information accompanies this paper at doi:10.1038/s41598-017-02614-2

Competing Interests: The authors declare that they have no competing interests.

Publisher's note: Springer Nature remains neutral with regard to jurisdictional claims in published maps and institutional affiliations.

Open Access This article is licensed under a Creative Commons Attribution 4.0 International License, which permits use, sharing, adaptation, distribution and reproduction in any medium or format, as long as you give appropriate credit to the original author(s) and the source, provide a link to the Creative Commons license, and indicate if changes were made. The images or other third party material in this article are included in the article's Creative Commons license, unless indicated otherwise in a credit line to the material. If material is not included in the article's Creative Commons license and your intended use is not permitted by statutory regulation or exceeds the permitted use, you will need to obtain permission directly from the copyright holder. To view a copy of this license, visit http://creativecommons.org/licenses/by/4.0/.

© The Author(s) 2017

Supporting Information for: "Targeted radionuclide therapy with astatine-211: Oxidative dehalogenation of astatobenzoate conjugates", by David Teze, Dumitru-Claudiu Sergentu, Valentina Kalichuk, Jacques Barbet, David Deniaud, Nicolas Galland, Rémi Maurice and Gilles Montavon.

Table S1 | SR-DFT and 2c-DFT C–X bond dissociation energies (kcal.mol^{-1}) of halobenzenes (X = At, I).

Compound	SR-DFT[a]	2c-DFT[b]	Expt.[1]
Astatobenzene	60.3	44.7	44.9 ± 5.1
Iodobenzene	67.4	59.6	61.1 ± 4.7

[a] Calculations performed with Gaussian09.[2]
[b] Reported from Table 1 for convenience.

Table S2 | SR-DFT and 2c-DFT first ionisation potentials (kcal.mol^{-1}) of halobenzoates and of iodobenzene.

Compound	SR-DFT[a]	2c-DFT
Astatobenzoate **1a**	208.3	185.8
Iodobenzoate **1b**	197.3	196.2
Iodobenzene	196.5	195.5[b]

[a] Calculations performed with Gaussian09.[2]
[b] Reported from the main text for convenience.

Comments:

These results are reported here to illustrate the importance of spin-orbit coupling (SOC) on the computed quantities, thus justifying the use of two-component relativistic DFT (2c-DFT) calculations for obtaining accurate results in this context. It is clear from Table S1 that the inclusion of SOC has a significant effect on the computed bond dissociation energies; typically scalar relativistic DFT (SR-DFT) calculations overestimate these quantities mainly because the SOC stabilizations of the ground state of the dissociated halogen radicals are missing, which is not compensated by the error done on the bound system. When SOC is accounted for, we obtain values in close agreement with the experiment (with less than 2 kcal.mol^{-1} of difference). From Table S2, we can see that SOC hardly affects the IPs of the iodinated species, while a significant effect is found for the astatinated one. Thus, even if the SR-DFT results for the IPs of iodinated species may be seen as reliable enough, we chose to report only 2c-DFT results in the main text to obtain reliable results for all the considered species at a same level of theory for the sake of comparison.

Figure S1 | Radiochromatograms of 1b obtained after 3 h with 1% H_2O_2 (top) and 1% H_2O_2 plus 10^{-4} M of Fe^{3+} ions (Fenton-like conditions, bottom). These radiochromatograms were used to generate data displayed in Fig. 2.

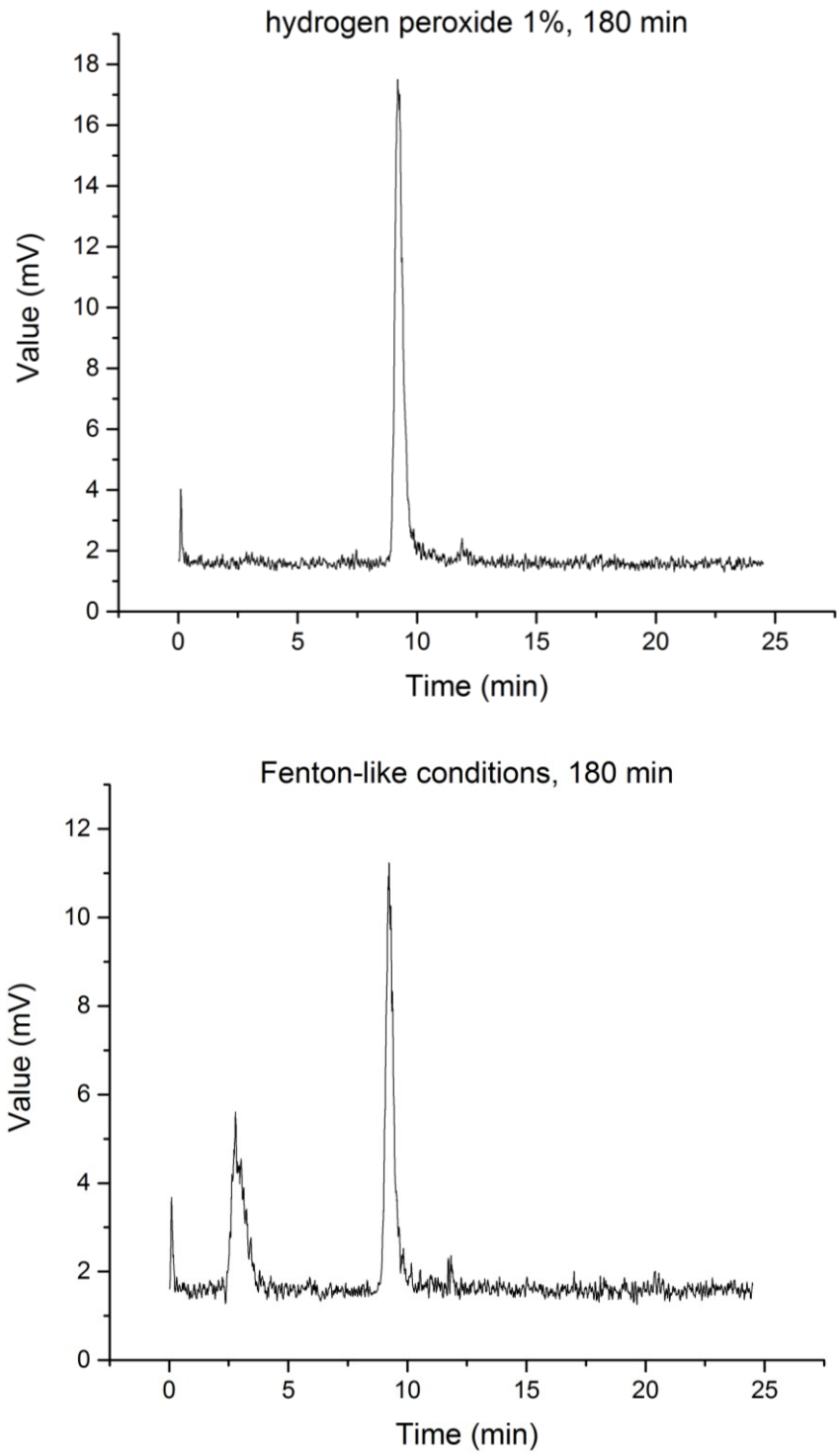

References

1. Вашарош, Л., Норсеев, Ю. В. & Халкин, В. А. ОПРЕДЕЛЕНИЕ ЭНЕРГИИ РАЗРЫВА ХИМИЧЕСКОЙ СВЯЗИ УГЛЕРОД-АСТАТ. *Dokl Akad Nauk SSSR* **263,** 119–123 (1981).
2. Gaussian 09, Revision D.01, M. J. Frisch, G. W. Trucks, H. B. Schlegel, G. E. Scuseria, M. A. Robb, J. R. Cheeseman, G. Scalmani, V. Barone, B. Mennucci, G. A. Petersson, H. Nakatsuji, M. Caricato, X. Li, H. P. Hratchian, A. F. Izmaylov, J. Bloino, G. Zheng, J. L. Sonnenberg, M. Hada, M. Ehara, K. Toyota, R. Fukuda, J. Hasegawa, M. Ishida, T. Nakajima, Y. Honda, O. Kitao, H. Nakai, T. Vreven, J. A. Montgomery, Jr., J. E. Peralta, F. Ogliaro, M. Bearpark, J. J. Heyd, E. Brothers, K. N. Kudin, V. N. Staroverov, R. Kobayashi, J. Normand, K. Raghavachari, A. Rendell, J. C. Burant, S. S. Iyengar, J. Tomasi, M. Cossi, N. Rega, J. M. Millam, M. Klene, J. E. Knox, J. B. Cross, V. Bakken, C. Adamo, J. Jaramillo, R. Gomperts, R. E. Stratmann, O. Yazyev, A. J. Austin, R. Cammi, C. Pomelli, J. W. Ochterski, R. L. Martin, K. Morokuma, V. G. Zakrzewski, G. A. Voth, P. Salvador, J. J. Dannenberg, S. Dapprich, A. D. Daniels, Ö. Farkas, J. B. Foresman, J. V. Ortiz, J. Cioslowski, and D. J. Fox, Gaussian, Inc., Wallingford CT, 2009.

THE JOURNAL OF CHEMICAL PHYSICS **142**, 094305 (2015)

Effective bond orders from two-step spin–orbit coupling approaches: The I_2, At_2, IO^+, and AtO^+ case studies

Rémi Maurice,[1,a)] Florent Réal,[2] André Severo Pereira Gomes,[2] Valérie Vallet,[2] Gilles Montavon,[1] and Nicolas Galland[3]
[1]*SUBATECH, CNRS UMR 6457, IN2P3/EMN Nantes/Université de Nantes, 4 rue Alfred Kastler, BP 20722, 44307 Nantes Cedex 3, France*
[2]*Laboratoire PhLAM, CNRS UMR 8523, Université de Lille, 59655 Villeneuve d'Ascq Cedex, France*
[3]*CEISAM, UMR CNRS 6230, Université de Nantes, 2 rue de la Houssinière, BP 92208, 44322 Nantes Cedex 3, France*

(Received 7 November 2014; accepted 17 February 2015; published online 4 March 2015)

The nature of chemical bonds in heavy main-group diatomics is discussed from the viewpoint of effective bond orders, which are computed from spin–orbit wave functions resulting from spin–orbit configuration interaction calculations. The reliability of the relativistic correlated wave functions obtained in such two-step spin–orbit coupling frameworks is assessed by benchmark studies of the spectroscopic constants with respect to either experimental data, or state-of-the-art fully relativistic correlated calculations. The I_2, At_2, IO^+, and AtO^+ species are considered, and differences and similarities between the astatine and iodine elements are highlighted. In particular, we demonstrate that spin–orbit coupling weakens the covalent character of the bond in At_2 even more than electron correlation, making the consideration of spin–orbit coupling compulsory for discussing chemical bonding in heavy (6*p*) main group element systems. © *2015 AIP Publishing LLC*. [http://dx.doi.org/10.1063/1.4913738]

I. INTRODUCTION

Relativistic effects play a key role on molecular structures and properties,[1] especially in the case of systems containing heavy atoms. Rationalizing the chemistry of such systems in terms of chemical bonding thus requires to introduce relativistic effects in the analysis. Our understanding of chemical bonding is usually based on atomic and molecular concepts. For instance, one can invoke molecular orbitals (MOs) expressed in terms of linear combinations of atomic orbitals (LCAOs), and assign for each MO a bonding, non-bonding, or anti-bonding character, which leads to the concept of bond order (BO) or effective bond order (EBO).[2] Population analyses defining atomic charges can also provide useful clues for rationalizing molecular structures and chemical bonds. Topological analyses of appropriately chosen functions are also particularly informative, namely, that of the electron density in the quantum theory of atoms in molecules (QTAIM) fashion,[3,4] or that of the electron localization function (ELF).[5–9] All these tools help in understanding the chemistry with intuitive models, which is especially important for compounds involving elements whose chemical properties are poorly known.

Although astatine (At) is a member of the halogen family, many of the characteristics of this radioelement and its compounds remain elusive since all of its radionuclides are very short-lived.[10] Understanding the chemical role of this element might not only be worthwhile from a fundamental viewpoint but also in view of the potential use of the ^{211}At isotope in radiotherapy.[11] Among the recent experimental highlights, it is worth quoting the determination of the ionization potential of the free atom,[12] or the determination of predominance domains in the Pourbaix diagram (E-pH) of At in aqueous solution.[13–15] One should also mention the theoretical prediction of a metallic behavior for condensed astatine, unlike the other halogens.[16] Furthermore, stable At cationic forms (At^+ and AtO^+) exist in aqueous solution and their coordination chemistry has been experimentally explored by reporting complexation constants with various inorganic ligands.[17,18] As the longest-lived radionuclides ^{210}At or ^{211}At can at present be produced only in trace quantities, it is not possible to obtain structural information from different spectroscopies. Therefore, the use of quantum chemical modeling methods offers the most promising way to shed light on astatine chemistry at a molecular scale.

Among the correlated relativistic electronic structure methods, contracted spin–orbit configuration interaction (c-SOCI) approaches are particularly interesting as they let us easily refer back to a spin–orbit free (SOF) picture of bonding while still providing accurate results, as attested by their success in computing zero-field splittings (ZFSs) and the electronic structure of *p*, *d* and *f* element containing systems.[19–24] However, for the open-shell 6*p* main group elements, treating spin–orbit coupling (SOC) *a posteriori* with a contracted scheme could be problematic[25] whenever differential spin polarization of the $6p_{1/2}$ and $6p_{3/2}$ spinors has a strong impact on the electronic structure, as it is the case for Tl or Bi^{3+} for instance.[26–29] In these cases, it is preferable to work with an uncontracted SOCI (uc-SOCI) correlated formalism rather than with the c-SOCI one, since we can retain the connection to the SOF picture while typically bringing the

a)Electronic mail: remi.maurice@subatech.in2p3.fr

 © 2015 AIP Publishing LLC

This article is copyrighted as indicated in the article. Reuse of AIP content is subject to the terms at: http://scitation.aip.org/termsconditions. Downloaded to IP: 134.158.25.87 On: Wed, 04 Mar 2015 16:04:50

results closer to either experiment or fully relativistic correlated results.

The objective of this paper is to characterize, using two-step SOCI methods, the nature of the chemical bonds in heavy-element systems. Illustrations of the SOC effects in the At_2 and AtO^+ molecules and in the lighter homologues I_2, and IO^+ are given to support the originality of the proposed approach. Prior to discussing bonding, it is necessary to assess the accuracy of the two-step SOCI scheme in determining spectroscopic constants, such as bond lengths, harmonic frequencies, and dissociation energies, by comparing the results to those obtained with fully relativistic methods. After having validated our methodology, the chemical bonding will be analyzed in terms of EBOs. Note that EBOs have so far been defined in the framework of multiconfigurational non-relativistic or scalar-relativistic calculations.[2] This work thus represents a first attempt to extend the concept of EBO to relativistic calculations including SOC. By using two-step SOC approaches, the EBOs can be directly derived from the analysis of the resulting spin–orbit coupled wave functions, which leads, in a straightforward way, to a qualitative picture of the bonding. The stabilities of the interatomic bonds will also be quantified by computing the bond dissociation energies.

II. THEORY AND METHODS

A. Effective bond orders

Defining a BO from an MO point of view requires to assign a bonding, non-bonding or anti-bonding character to each MO. When only one electronic configuration is considered, the bond order is thus directly obtained from the half-difference between the (total) occupation numbers of the bonding, n^{b}, and anti-bonding, n^{a}, orbitals,

$$\mathrm{BO} = \frac{n^{\mathrm{b}} - n^{\mathrm{a}}}{2}. \tag{1}$$

In such a case, both n^{b} and n^{a} are integers, leading to integer or half-integer BOs. A more refined definition, allowing notably the EBO to progressively tend to zero when the bond is weakened up to dissociation, requires the use of multiconfigurational wave functions.[2] One can thus define the EBO in terms of the natural orbital (NO) occupation numbers,

$$\mathrm{EBO} = \frac{\sum_b \eta^b - \sum_a \eta^a}{2}, \tag{2}$$

where the indices b and a refer to bonding and anti-bonding active orbitals, respectively, and where η^b and η^a are the occupation numbers of the corresponding bonding and anti-bonding active orbitals. In practice, it is equivalent to compute EBOs by determining the BO of each of the configuration state function (CSF), and then summing the weighted BOs,

$$\mathrm{EBO} = \sum_i \omega_i \frac{n_i^{\mathrm{b}} - n_i^{\mathrm{a}}}{2}, \tag{3}$$

where the index i refers to CSFs, ω_i is the weight of the CSF i in the wave function of interest, and where n_i^{b} and n_i^{a} are the number of bonding and anti-bonding electrons of the CSF i, respectively. In the general case, EBOs are neither integers nor half-integers. Note that the analysis only involves the active electrons, since it is assumed that the active space is properly chosen, such as bonding and anti-bonding orbitals are included pair-wise in the active space, and that the inactive electrons do not contribute directly to the bonding.

Defining σ, π, or δ type bonds also relies on a strict (or nearly ideal) separation of the σ, π, or δ type orbitals (by symmetry or by being close to a symmetrical situation). In a non-relativistic or scalar relativistic context, all these conditions can be fulfilled in diatomics, and also in some binuclear compounds (containing two relatively heavy atoms). In more complex situations, the nature of the active orbitals should be carefully checked, and it is not guaranteed that EBOs can be properly defined from a standard LCAO calculation. One may however transform the active orbitals to "localize" them in terms of bonding, non-bonding, and anti-bonding orbitals between the pair of atoms of interest. Such a discussion, although interesting, goes beyond the scope of the present work, aiming at introducing the concept of spin–orbit coupled EBO (SOC-EBO).

When two-step SOC calculations are performed, a set of SOF states is computed in the first step. A state-interaction (SI) matrix, built from the electronic energy matrix and the SOC matrix, can then be diagonalized within the basis of the spin components of the SOF states considered in the first step, i.e., a c-SOCI is often performed. Since the ground SOF and several excited SOF states are considered in the first step, state-averaged (SA) orbitals are usually built in order to ensure that the computed many-electron states are orthogonal. Of course, the determination of the spin–orbit free EBO (SOF-EBO) of a given SOF state cannot be obtained from the average occupation numbers of the SA orbitals, but it can in any case be done by using the CSF weights and BOs. Similarly, after the second step, one can obtain the SOC-EBO of a given spin–orbit (SO) state by computing the weighted sum of the SOF-EBOs of the spin components of each SOF state,

$$\text{SOC-EBO} = \sum_k \omega_k \left[\sum_i \omega_{i,K} \frac{n_{i,K}^{\mathrm{b}} - n_{i,K}^{\mathrm{a}}}{2} \right], \tag{4}$$

where k refers to the spin components of a given SOF state K, i refers to the CSFs used to express K, ω_k is the weight of the spin component of K in the SO wave function of interest, where $\omega_{i,K}$ is the weight of the CSF i in the SOF wave function of K. One should note that if an uc-SOCI is performed, the SO wave functions are directly expressed in terms of determinants. In such a case, the determination of the SOC-EBO of a given SO state can be obtained from Eq. (3) (the index i would refer in such a case to determinants and not to CSFs).

B. Computational details

To evaluate the sensitivity of the EBO analyses and spectroscopic constants to the atomic basis sets we have used two different types of relativistic atomic basis sets. The first one refers to the segmented all-electron relativistically contracted basis sets of valence triple-zeta quality with polarization functions adapted to the Douglas-Kroll Hess Hamiltonian[30–32] (SARC-DKH-TZVP).[33,34] For the oxygen and iodine atoms,

This article is copyrighted as indicated in the article. Reuse of AIP content is subject to the terms at: http://scitation.aip.org/termsconditions. Downloaded to IP: 134.158.25.87 On: Wed, 04 Mar 2015 16:04:50

the basis sets have been obtained by recontracting triple-zeta split-valence Karlsruhe non-relativistic basis sets[35,36] under the influence of scalar relativistic effects. The following contraction schemes are used: (29s21p15d11f)/22s14p9d4f for At, (19s15p10d)/12s10p6d for I, and (11s6p1d)/6s3p1d for O. Note that the addition of *f* polarization functions would slightly improve the computed spectroscopic constants of the iodine systems. Also, note that SARC-DKH basis sets are meant to be used for scalar relativistic calculations, or two-step SOC approaches, but not in two-component frameworks. The calculations with the SARC-DKH basis sets were performed with the ORCA program package.[37] The second type of basis sets we have used corresponds to the all-electron atomic natural orbitals relativistic core correlation basis sets of quadruple zeta quality (ANO-RCC-QZP),[38] with the following contraction schemes (25s22p16d12f4g)/9s8p6d4f3g, (22s19p13d5f3g)/8s7p5d4f2g, (14s9p4d3f2g)/5s4p3d2f1g, for At, I, and O, respectively. For these calculations we have used the MOLPRO (version 2012.1)[39] and MOLCAS (version 7.8)[40] quantum chemistry packages. As we shall discuss later, both SARC-DKH-TZVP and ANO-RCC-QZP basis sets lead to similar EBOs, but the ANO-RCC-QZP basis sets appears to perform better for spectroscopic constants in the studied cases, in particular, for bond dissociation energies and excitation energies.

In the first step of the calculation, SA complete active space self-consistent field (SA-CASSCF)[41,42] calculations are performed, in which the valence *p* electrons are active. For the free atoms, free ions, and homonuclear diatomics, all the SOF states that can be built with the corresponding active spaces were considered (see Table I). The SA space is built by considering the M_S(max) components of each SOF state, and equal weights are considered for all SOF roots. In the considered heteronuclear diatomics, IO^+ and AtO^+, this would lead to a too large number of SOF states, and potentially to averaging artifacts. Thus, we chose to restrict the set of states to the most important lowest-lying SOF states, that is including the singly excited SOF states with respect to the ground state, and consistently truncating both SA and SI spaces based on an energetic criteria. In this way, we ensure that the π symmetry is maintained, and the excited spin-components that couple most with the components of the ground SOF state are considered in the SI calculation. Note that the SI space is defined by the spin components of the SOF states considered in the first step. Contrary to a previous study on IO^+ and AtO^+,[43] two quintet spin roots are considered in the averaging and their spin components included in the SOC calculation (see Table I).

TABLE I. Active spaces, state-average (SA) and state-interaction (SI) spaces considered in the SOF and SOC calculations. For the SA and SI spaces, S refers to singlet, D to doublet, T to triplet, and Q to quintet spin states or their components, respectively.

X	Active space (electrons/orbitals)	SA/SI spaces
O	4/3	3T, 6S
I/At	5/3	3D
I^+/At^+	4/3	3T, 6S
I_2/At_2	10/6	15T, 21S
IO^+/AtO^+	8/6	2Q, 9T, 6S

However, since the quintet states appear at excitation energies of about 4–5 eV, they do not influence much the ZFS values between the X 0^+ and the *a* 1 SO states; the ZFS values reported in Table VIII are quite similar to the ones reported in Ref. 43.

In the second step of the calculation, the SOC is introduced by diagonalizing the SI matrix corresponding to the electronic energy plus SOC matrix (c-SOCI scheme). A mean-field SOC operator is considered.[44,45] As proposed by Teichteil *et al.*[46] and Llusar *et al.*[47] correlated electronic energies can be placed on the diagonal of the SI matrix. Here, *n*-electron valence states second-order perturbation theory (NEVPT2)[48] correlated energies are used (within the strongly contracted scheme with the SARC-DKH basis sets and the partially contracted one for the ANO-RCC basis sets). The NEVPT2 method uses the Dyall's zeroth-order Hamiltonian,[49] and (usually) does not suffer from intruder states. The core orbitals were kept frozen in the perturbative calculations with ANO-RCC basis sets, i.e., the 1*s* orbitals of the O centers, all the orbitals lower in energy than the 5s ones of the I centers (the 4*s*, 4*p*, and 4*d* orbitals being frozen), and all the orbitals lower in energy than the 6-shells of the At centers (the 5*s*, 5*p*, and 5*d* ones being frozen).

For the considered diatomics, the equilibrium distances and harmonic frequencies are computed using least-square fits of *ab initio* values obtained every 0.01 Å against an harmonic potential, following Hooke's law. The SOF and SOC electronic dissociation energies are computed considering the $X_2 \rightarrow X + X$ and $XO^+ \rightarrow X^+ + O$ dissociation reactions, for which all the species are considered in their ground SOF or SOC state, respectively. The C_1 symmetry point group is considered for the free atom and ion calculations to average the various spatially degenerate components of the atomic spin–orbit free states, while the D_{2h} and C_{2v} point groups are considered for the X_2 and XO^+ cases, respectively.

In some cases, due to the absence of available reference values in the literature, additional calculations have been performed to assess the accuracy of the results obtained with the aforementioned methods. In order to investigate the effect of SO polarization in the two-step SOC framework, we have used an uc-SOCI scheme, which diagonalizes the total relativistic Hamiltonian over a configurational space corresponding to the CAS plus all single-excitations (directly coupled by the effective one-electron mean-field spin–orbit operator[50]), projecting the effect of dynamic correlation, in the present case the (partially contracted) NEVPT2 scheme[51] onto that SOCI model space by an effective spin–orbit Hamiltonian.[28,47] The uc-SOCI calculations were performed with the EPCISO code,[28] interfaced to the MOLCAS quantum chemistry package (version 7.8).[40] To have a complete set of four-component correlated reference calculations we have used a development version of the DIRAC electronic structure code[52] to perform Dirac-Coulomb coupled cluster (DC-CC) or DC intermediate Hamiltonian Fock space coupled cluster (DC-IHFSCC) calculations, using the same basis sets and calculation settings as in a previous publication of some of us.[43]

The SOF-EBOs and SOC-EBOs are determined at the minimum of each method (CASSCF, NEVPT2, c-SOCI/CASSCF, c-SOCI/NEVPT2, and uc-SOCI/NEVPT2). Since we used internally contracted versions of NEVPT2, the reported CASSCF and NEVPT2 SOF-EBOs are equivalent in

This article is copyrighted as indicated in the article. Reuse of AIP content is subject to the terms at: http://scitation.aip.org/termsconditions. Downloaded to IP: 134.158.25.87 On: Wed, 04 Mar 2015 16:04:50

single-point calculations. When SOC is considered, there is an interplay between dynamic correlation and SOC. However, since only the diagonal of the SI matrix is affected by electron correlation (the off-diagonal SOC matrix elements are computed with the CASSCF wave functions in both cases), the EBOs computed at the c-SOCI/CASSCF and c-SOCI/NEVPT2 levels are expected to be very similar.

For the X_2 cases, the σ, π, π^*, and σ^* MOs are separated by symmetry (a_g, $b_{2u} + b_{3u}$, $b_{2g} + b_{3g}$, and b_{1u}, respectively). In the XO^+ cases, there is no symmetry distinction between bonding and anti-bonding orbitals, although the σ and π systems are strictly separated (the σ, π, π^*, and σ^* MOs have a_1, $b_1 + b_2$, $b_1 + b_2$, and a_1 symmetries, respectively). As a consequence, bonding and anti-bonding orbitals could (partly) rotate. However, since we only consider a limited set of SOF states, the bonding and anti-bonding orbitals are clearly separated in terms of average occupation numbers. Visualization of the active orbitals confirmed that each active orbitals have a clear bonding or anti-bonding character, and therefore there is no ambiguity in the determination of EBOs in the studied cases.

III. RESULTS AND DISCUSSIONS

A. Lowest energy levels of the free atoms and cations

When heavy atoms are considered, the calculation of dissociation energies of I_2, At_2, IO^+, and AtO^+ requires a proper determination of the electronic structure of free atoms or ions, to ensure that the energetic stabilization of the dissociated fragments induced by SOC is well estimated. Tables II and III gather the computed energies levels for the free atoms O, I, At and the cations I^+, and At^+.

As reported in Table II, the SO splitting of the ^3P state of the oxygen atom is well reproduced, as well as the $^3P_2 \rightarrow {}^1D_2$ excitation energy, both with CASSCF and NEVPT2 electronic energies. The $^3P_2 \rightarrow {}^1S_0$ excitation energy is overestimated by 0.85 eV, but since this excited state is very high in energy, it is not problematic for the discussion of chemical bonding and dissociation energies.

Iodine and astatine both have a ^2P SOF ground state. In c-SOCI calculations, as the effect of the dynamic correlation (projected on the diagonal of the SI matrix) is identical for all the six fine-structure components of the ^2P SOF state, the c-SOCI/CASSCF and c-SOCI/NEVPT2 results are strictly equivalent. The SO splitting of iodine appears to be underestimated by 0.08-0.10 eV with all the considered two-step approaches. This is in line with the result of Roos *et al.*[38] (0.863 eV), who used a similar approach, or with the value obtained by Fleig and Sadlej[55] using a four-component CI scheme (0.854 eV). At the c-SOCI level, the use of the ANO-RCC of quadruple zeta quality only slightly increases the $^2P_{3/2} \rightarrow {}^2P_{1/2}$ splitting with respect to the SARC basis of triple zeta quality. The contribution of spin-polarization effects is small for iodine, 0.014 eV, but sizable for astatine, 0.351 eV. While the uc-SOCI/NEVPT2 approach underestimates the SO splitting of iodine with respect to experiment or to the fully relativistic DC-IHFSCC calculations, the agreement is much better for astatine. Because they lack spin-polarization effects, c-SOCI results underestimate by 10% the SO splitting of both iodine and astatine atoms. Note that the two-component Kramers restricted CASSCF calculations of Kim and Lee[56] nicely corroborate with our fully relativistic values in both the iodine and astatine cases.

Regarding the I^+ and At^+ cations which have a p^4 valence configuration, the most interesting feature is related to the second-order SOC that introduces deviations to the Landé's rules that manifests itself by an inversion between $^3P_1$ and $^3P_0$ levels. This inversion has been experimentally determined decades ago for the I^+ ion,[58] but also in the isoelectronic Te atom.[59] Note that it is also the case for the Po atom,[60] which is isoelectronic with the At^+ ion. In the case of I^+, DC-IHFSCC is the only method that captures the correct state ordering, while all two-step SOC calculations (contracted and uncontracted) retain the Landé's ordering, but placing the $^3P_1$ and $^3P_0$ levels less than 0.05 eV apart from each other. It is thus not expected to be problematic for our semi-quantitative purposes.

As for At, the At^+ spectrum is not known experimentally. The comparison of the c-SOCI/CASSCF and c-SOCI/NEVPT2 results reveals a small interplay between electron correlation and SOC. The magnitude of the SO splitting is twice as large in astatine than in iodine. This larger SO splitting, which translates into a larger difference between the $\langle r \rangle$ values for the $p_{3/2}$ spinors over the $p_{1/2}$ spinors, implies that the contribution of spin-polarization effects is way stronger in At^+ than in I^+; this is the reason why the uc-SOCI/NEVPT2 results exhibit smaller deviations with respect to the DC-IHFSCC results than the c-SOCI/NEVPT2 ones. As in the case of At, the c-SOCI method underestimates by about

TABLE II. Excitation energies between spin–orbit levels of the O, I, and At free atoms obtained at various levels of theory and with different relativistic atomic basis sets.

		c-SOCI			uc-SOCI		
X	ΔE (eV)	CASSCF[a]	NEVPT2[a]	NEVPT2[b]	NEVPT2[b]	DC-IHFSCCSD	Expt.
O	$^3P_2 \rightarrow {}^3P_1$	0.018	0.018	0.019	0.019	...	0.020[53]
	$^3P_2 \rightarrow {}^3P_0$	0.027	0.027	0.028	0.028	...	0.028[53]
	$^3P_2 \rightarrow {}^1D_2$	2.182	2.092	1.955	1.955	...	1.967[53]
	$^3P_2 \rightarrow {}^1S_0$	5.442	5.045	5.040	5.040	...	4.190[53]
I	$^2P_{3/2} \rightarrow {}^2P_{1/2}$	0.844[c]		0.864[c]	0.878	0.941	0.943[54]
At	$^2P_{3/2} \rightarrow {}^2P_{1/2}$	2.461[c]		2.524[c]	2.875	2.888	...

[a]The SARC-DKH-TZVP basis sets are used.
[b]The ANO-RCC-QZP basis sets are used.
[c]c-SOCI/CASSCF and c-SOCI/NEVPT2 results are here equivalent.

This article is copyrighted as indicated in the article. Reuse of AIP content is subject to the terms at: http://scitation.aip.org/termsconditions. Downloaded to IP: 134.158.25.87 On: Wed, 04 Mar 2015 16:04:50

TABLE III. Excitation energies between spin–orbit levels of the I^+ and At^+ free ions obtained at various levels of theory with different relativistic atomic basis sets.

		c-SOCI			uc-SOCI		
X^+	ΔE (eV)	CASSCF[a]	NEVPT2[a]	NEVPT2[b]	NEVPT2[b]	DC-IHFSCCSD	Expt.
I^+	$^3P_2 \rightarrow {}^3P_0$	0.804	0.806	0.822	0.822	0.853	0.799[57]
	$^3P_2 \rightarrow {}^3P_1$	0.757	0.765	0.793	0.792	0.870	0.879[58]
	$^3P_2 \rightarrow {}^1D_2$	1.902	1.797	1.681	1.680	1.827	1.702[57]
	$^3P_2 \rightarrow {}^1S_0$	4.087	4.027	3.999	3.997	4.031	3.658[57]
At^+	$^3P_2 \rightarrow {}^3P_0$	1.353	1.334	1.347	1.347	1.324	...
	$^3P_2 \rightarrow {}^3P_1$	2.489	2.533	2.578	2.920	2.984	...
	$^3P_2 \rightarrow {}^1D_2$	3.443	3.298	3.346	3.676	3.780	...
	$^3P_2 \rightarrow {}^1S_0$	6.800	6.745	6.850	7.524	7.675	...

[a]The SARC-DKH-TZVP basis sets are used.
[b]The ANO-RCC-QZP basis sets are used.

10% the SO splittings, making (two-step) c-SOCI methods useful for semi-quantitative estimates of SOC consequences.

B. I_2 and At_2

1. Ground-state bond lengths, harmonic frequencies, and dissociation energies

The I_2 and At_2 systems have already been studied in the literature at various levels of theory.[4,9,18,61–66] The DC-CCSD(T) calculations of Visscher and Dyall[62] and recent two-component CCSD(T) calculations of Höfener *et al.*[66] are here taken as reference computational values.

In Table IV, we present the spectroscopic constants and bond dissociation energies of I_2 and At_2 computed without and with SOC and the ANO-RCC basis sets. Comparing first the results obtained at the SOF CASSCF and NEVPT2 levels, and at the corresponding c-SOCI ones, we note that the role of both dynamical electron correlation and SOC is larger in At_2 than in I_2. In both cases, dynamic correlation strengthens the bond, while SOC weakens it; for instance, in At_2, the bond lengths decreases from 2.913 Å to 2.849 Å under the effect of dynamic correlation, and increases from 2.913 Å to 3.108 Å under the effect of SOC. Note that these effects are not additive; the interplay between the dynamic correlation and the SOC leads to a clear stabilization of the I–I bond, while it destabilizes the At–At bond. This means that the role of SOC on the At_2 bond is at least as important as that of dynamic correlation. This highlights the growing influence of SOC on the strength of chemical bonds as the atomic number increases.

As can be seen from Table IV and Table SI in the supplementary material,[68] the SARC-DKH-TZVP basis set yields spectroscopic constants that tend to underestimate the bond strengths in terms of distance, harmonic frequency, and dissociation energy, as were also found by other authors with various methods.[9,61–65] However, the use of the ANO-RCC basis set on iodine centers yields data in excellent agreement not only with the experimental data[67] but also the latest reference calculations reported by Höfener *et al.*[66] with the two-component X2C-CCSD(T) method, and extrapolating the correlation energies to the complete basis set (CBS) limit. Therefore, we conclude that the ANO-RCC-QZP basis set tends to perform better than the SARC-DKH-TZVP one for our purposes, although such a good agreement obtained with respect to the reference values with the ANO-RCC-QZP basis set was not expected at the c-SOCI/NEVPT2 level.

In order to assess the role of the interplay between electron correlation and SOC on the I_2 and At_2 spectroscopic constants, these quantities are also determined with uc-SOCI calculations (see Table IV). The effect of SO polarization is expected to be negligible for I_2, contrary to the At_2 case. The computed uc-SOCI spectroscopic data are in excellent agreement with the DC-CCSD(T) and X2C-CCSD(T) results, noting however that the uc-SOCI/NEVPT2 bond dissociation energy is 0.16 eV lower than the X2C-CCSD(T)/CBS value in At_2. However,

TABLE IV. Ground-state bond lengths, harmonic frequencies, and dissociation energies of I_2 and At_2 obtained at various levels of theory with the ANO-RCC-QZP basis sets.

	I_2			At_2		
Method	r_e (Å)	ω_e (cm^{-1})	D_e (eV)	r_e (Å)	ω_e (cm^{-1})	D_e (eV)
CASSCF	2.792	196	1.25	2.913	140	1.10
NEVPT2	2.667	224	2.07	2.849	160	1.86
c-SOCI/CASSCF	2.748	185	0.77	3.108	81	0.17
c-SOCI/NEVPT2	2.679	216	1.57	2.957	124	0.85
uc-SOCI/NEVPT2	2.679	216	1.56	2.971	118	0.64
DC-CCSD(T)[62]	2.717	206	1.28	3.046	108	0.63
X2C-CCSD(T)[66 a]	2.692	206	1.54	3.006	110	0.79
Expt.[67]	2.666	214	1.56	...	...	...

[a]Complete basis set extrapolations were performed.

This article is copyrighted as indicated in the article. Reuse of AIP content is subject to the terms at: http://scitation.aip.org/termsconditions. Downloaded to IP: 134.158.25.87 On: Wed, 04 Mar 2015 16:04:50

with respect to the discussion of the At–At chemical bond, the fact that the uc-SOCI/NEVPT2 computed bond lengths (Δr_e = 0.014 Å) are not very different from the c-SOCI ones, suggests that the interplay between SOC and electron correlation is not crucial for the description of the chemical bonding in this molecule. Also, the effect of SO polarization on D_e is about −0.21 eV, which almost matches twice the effect on the free atom (−0.23 eV). Therefore, we conclude that the SO polarization is almost quenched in the molecule. This leads us to expect that the c-SOCI/NEVPT2 approach is sufficient for EBO analyses. The discrepancy between the two-step SOCI approaches and the two-component correlated value in At_2 is thus not expected to be essentially related to SOC, but most probably origins from the limitations in the treatment of dynamic correlation associated with the second-order perturbation theory treatment.

2. Effective bond orders

Having validated our methodology, we now focus our analysis on EBOs for the I_2 and At_2 systems. The effective bond orders have been determined at the minimum of each method (see Table V). Since two-step approaches are usually used for single-point calculations at given references geometries, it may be informative to compare the values obtained at different internuclear distances. For I_2, all the considered geometries differ by less than 0.1 Å, which does not lead to noticeable changes in the SOF and SO ground-state wave-functions. Therefore, using equilibrium or fixed geometries does not significantly affect the EBO value. It is interesting to note that, while the SARC-DKH-TZVP basis yielded a slightly smaller bond strength for I_2 with respect to the ANO-RCC-QZP one, the resulting EBOs are very much the same (see Table V and Table SII in the supplementary material[68]). One can note that the non-dynamic correlation within the active space decreases the EBO from the single-determinantal picture (the lowest-energy electronic configuration is $\sigma^2\pi^4\pi^{*4}$, leading to a BO of one) by one order of magnitude more than the SOC. Thus, SOC has not much effect on EBOs in this case. On the contrary, SOC has a (twice) stronger effect than non-dynamic correlation in At_2. The c-SOCI EBOs in At_2, 0.78, is significantly smaller than in I_2 (0.93).

In Table V, we have divided the EBO values into contributions arising from the σ and π systems. We can scrutinize the influence of SOC on the EBO of the homonuclear diatomics by noting that SOC makes the ground state of these molecules (especially for At_2) less σ bonding and slightly π anti-bonding. This behavior can be rationalized by analyzing the dominant configurations of the relevant SOF and SO wave functions. The ground-state SOF wave function is dominated by the $\sigma^2\pi^4\pi^{*4}$ configuration (which, as mentioned previously, corresponds to the ground state in a single-determinantal picture). Since this SOF ground state is a spin-singlet state and only singlet and triplet spin states can be built with the considered active space, the SO stabilization of the ground state is here essentially related to the coupling with spin components of singly excited triplet configurations with respect to the dominant SOF configuration of the ground state. Moreover, the SOC cannot break the inversion symmetry, i.e., only $g \rightarrow g$ and $u \rightarrow u$ excitations are symmetry allowed. Only four configurations fulfill these requirements, all of them belonging to the $\sigma^2\pi^3\pi^{*4}\sigma^{*1}$ electronic configuration, and have an $|M_S|$ value of 1. These (non-bonding) configurations are less σ bonding than the ground SOF configuration (their σ BO being 0.5), while being π anti-bonding (their π BO being −0.5). Therefore, the ground SO state becomes significantly less bonding in terms of EBO than the ground SOF state. In other words, SOC weakens the covalent character of the bond in At_2.

This result is in agreement with previous analyses based on the topological analyses performed on top of two-component density functional theory (DFT) calculations,[4,9] and also discussions based on the concept of orbital hybridizations or of coupled molecular spinors.[62,65] Note that the contraction partly inhibits the mixing of the $\sigma^2\pi^4\pi^{*4}$ and $\sigma^2\pi^3\pi^{*4}\sigma^{*1}$ configurations, and therefore uc-SOCI calculations lead to slightly smaller EBOs in I_2 (0.89) and At_2 (0.66) than the c-SOCI ones. However, the qualitative difference between the iodine and astatine compounds can already be quantified at the c-SOCI level. Therefore, we conclude that the comparison of SOF-EBOs and SOC-EBOs is also another way of highlighting the important role of SOC on the chemical bond in At_2.

C. IO^+ and AtO^+

1. Ground-state bond lengths, harmonic frequencies, and dissociation energies

Depending on the pH and the potential E, the AtO^+ species can be thermodynamically stable in aqueous solution.[13] The ground state in the gas phase is expected to have a dominant

TABLE V. Ground-state EBOs of I_2 and At_2 computed at various levels of theory at the corresponding equilibrium geometries with the ANO-RCC-QZP basis sets, unless specified otherwise.

	I_2				At_2			
Method	r_e (Å)	EBO_σ	EBO_π	EBO	r_e (Å)	EBO_σ	EBO_π	EBO
CASSCF	2.729	0.93	0.00	0.92	2.913	0.92	0.00	0.92
NEVPT2	2.667	0.93	0.00	0.93	2.849	0.93	0.00	0.93
c-SOCI/CASSCF	2.748	0.91	−0.01	0.90	3.108	0.75	−0.07	0.68
c-SOCI/NEVPT2[a]	2.732	0.91	0.00	0.91	2.916	0.83	−0.05	0.78
c-SOCI/NEVPT2	2.679	0.93	0.00	0.93	2.957	0.82	−0.04	0.78
uc-SOCI/NEVPT2	2.679	0.89	0.00	0.89	2.971	0.75	−0.08	0.66

[a]Results obtained with the SARC-DKH-TZVP basis sets.

This article is copyrighted as indicated in the article. Reuse of AIP content is subject to the terms at: http://scitation.aip.org/termsconditions. Downloaded to IP: 134.158.25.87 On: Wed, 04 Mar 2015 16:04:50

TABLE VI. Ground-state bond lengths, harmonic frequencies, and dissociation energies of IO^+ and AtO^+ computed at various levels of theory with the ANO-RCC-QZP basis sets.

	IO^+			AtO^+		
Method	r_e (Å)	ω_e (cm^{-1})	D_e (eV)	r_e (Å)	ω_e (cm^{-1})	D_e (eV)
CASSCF	1.869	708	2.10	1.970	638	1.74
NEVPT2	1.797	877	3.60	1.892	792	3.15
c-SOCI/CASSCF	1.872	695	1.79	1.979	605	1.08
c-SOCI/NEVPT2	1.799	870	3.26	1.900	786	2.43
uc-SOCI/NEVPT2	1.798	874	3.25	1.893	799	2.30
DC-CCSD(T)[43]	1.829	763	...	1.930	676	...

spin-triplet character, while the ground state in solution was predicted to be dominated by a spin-singlet character based on two-component DFT calculations.[69,70] Very recently, gas-phase reference calculations were also reported,[43] providing us with reference values to compare with. In Ref. 43, multireference calculations DC-IHFSCC calculations were performed on IO^+ and AtO^+, confirming that both molecules have a (relativistic) ground state dominated by one single configuration. For consistency, we only report in Table VI the DC-CCSD(T) values, which are very similar to the DC-IHFSCC ones. Note that, since DC-CCSD(T) energies for the free O atom cannot be properly computed with the current implementation of DIRAC, no reference D_e values exist for IO^+ and AtO^+.

As can be seen in Table VI, the r_e and ω_e values computed with the c-SOCI/NEVPT2 method agree well with the DC-CCSD(T) results. It is interesting to note that in both the IO^+ and AtO^+ cases, dynamic correlation significantly strengthens the bond. Although SOC induces minor changes to the bond lengths and harmonic frequencies, it significantly reduces the dissociation energies for IO^+ and AtO^+ by 0.34 eV and 0.72 eV, respectively. These contributions are of the same magnitude as those estimated for I_2 and At_2. The SOC contribution to the dissociation energy arises from the difference of the SO energetic stabilizations of (i) the diatomics of interest and (ii) the corresponding free heavy atoms and ions. In the iodine molecules, the SOC is essentially quenched at the equilibrium geometry, thus the decrease of the dissociation energies arises only from the atomic fragments. In astatine molecules, SOC coupling also contributes to the total ground-state equilibrium energy: if one neglects that contribution, At_2 would, for instance, be only weakly bound, by no more than 0.2 eV, while it is actually bound by about 0.85 eV at the c-SOCI/NEVPT2 level. In AtO^+, the SOC stabilization of the ground state at the c-SOCI/NEVPT2 equilibrium geometry accounts for about half of D_e. As in the I_2 and At_2 homonuclear molecules, changing the atomic basis set to the SARC-DKH-TZVP one has a minor effect on the bond distances and frequencies, but significantly decreases the XO^+ dissociation energies, by 0.93 eV and 0.39 eV, respectively, at the c-SOCI/NEVPT2 level (see Table SIII in the supplementary material[68]). The good accuracy of the results obtained with the ANO-RCC-QZP basis sets for the homonuclear molecules makes us think that the ANO-RCC-QZP basis sets may also yield (very) accurate dissociation energies for the IO^+ and AtO^+ systems. However, in the absence of experimental or reference data, one cannot definitely conclude on the quality of the obtained results.

2. Effective bond orders

EBOs are presented for the ground SOF state ($^3\Sigma^-$) and the ground SO state (X 0^+) at the minimum of each method in Table VII (see Table SIV in the supplementary material[68] for the results obtained with the SARC-DKH-TZVP basis sets). Note that Table VIII also provides EBOs for the lowest-energy excited SOF and SO states at the uc-SOCI geometries. By comparing these two tables, we conclude that the ground-state EBOs are not much affected by geometrical effects. Therefore, for the sake of simplicity, our analysis is essentially focussed on the results presented in Table VIII.

In order to understand the EBOs of the lowest-lying SO states, it is important to discuss their dominant components in terms of the lowest-lying SOF states. The X 0^+ SO state is

TABLE VII. Ground-state EBOs of IO^+ and AtO^+ obtained at various levels of theory at the corresponding equilibrium geometries with the ANO-RCC-QZP basis sets, unless specified otherwise.

	IO^+				AtO^+			
Method	r_e (Å)	EBO_σ	EBO_π	EBO	r_e (Å)	EBO_σ	EBO_π	EBO
CASSCF	1.869	0.92	0.84	1.76	1.970	0.90	0.82	1.72
NEVPT2	1.797	0.92	0.86	1.80	1.892	0.92	0.85	1.77
c-SOCI/CASSCF	1.872	0.91	0.83	1.74	1.979	0.86	0.78	1.64
c-SOCI/NEVPT2[a]	1.844	0.91	0.84	1.75	1.921	0.89	0.82	1.70
c-SOCI/NEVPT2	1.799	0.93	0.85	1.78	1.900	0.87	0.79	1.66
uc-SOCI/NEVPT2	1.789	0.90	0.89	1.78	1.893	0.86	0.87	1.73

[a]Results obtained with the SARC-DKH-TZVP basis sets.

This article is copyrighted as indicated in the article. Reuse of AIP content is subject to the terms at: http://scitation.aip.org/termsconditions. Downloaded to IP: 134.158.25.87 On: Wed, 04 Mar 2015 16:04:50

TABLE VIII. Lowest-energy states vertical transition energies (T_v) and EBOs of IO^+ and AtO^+ obtained at various levels of theory with the ANO-RCC-QZP basis sets at the uc-SOCI/NEVPT2 equilibrium geometries ($r(IO^+) = 1.789$ Å and $r(AtO^+) = 1.893$ Å).

		IO^+				AtO^+			
Method	State	T_v (eV)	EBO_σ	EBO_π	EBO	T_v (eV)	EBO_σ	EBO_π	EBO
NEVPT2[a]	$^3\Sigma^-$	0.00	0.93	0.87	1.80	0.00	0.92	0.85	1.76
	$^1\Delta$	0.57	0.94	0.80	1.74	0.58	0.92	0.77	1.69
	$^1\Sigma^+$	1.05	0.94	0.74	1.68	1.05	0.92	0.70	1.62
c-SOCI/NEVPT2	X 0^+	0.00	0.93	0.86	1.79	0.00	0.89	0.82	1.71
	a 1	0.08	0.93	0.86	1.79	0.43	0.89	0.77	1.66
	a 2	0.72	0.93	0.78	1.72	0.99	0.89	0.69	1.58
uc-SOCI/NEVPT2	X 0^+	0.00	0.90	0.89	1.78	0.00	0.86	0.87	1.73
	a 1	0.10	0.90	0.88	1.78	0.56	0.86	0.83	1.69
	a 2	0.74	0.87	0.87	1.74	1.09	0.84	0.79	1.63

[a]CASSCF and NEVPT2 EBOs are here equivalent.

essentially composed of the $|M_S| = 0$ component of $^3\Sigma^-$ and of $^1\Sigma^+$ SOF states (about 92% and 7%, respectively, for IO^+, and about 69% and 26%, respectively, for AtO^+). Since $^3\Sigma^-$ and $^1\Sigma^+$ have similar SOF-EBOs, SOC does not drastically change the EBO of the ground state. The doubly degenerate *a* 1 SO state is dominated by the $|M_S| = 1$ components of $^3\Sigma^-$, and also mix with some excited triplet configurations that exhibit a π non-bonding character. Note that these $\pi \rightarrow \pi^*$ excitations are symmetry allowed, due to the absence of a symmetry center. The *a* 2 SO state is dominated by the $^1\Delta$ components (by more than 98% for IO^+, and by about 85% for AtO^+); as a result the EBOs values are marginally changed by SOC. Therefore, the contraction in SOCI calculations is in this case not expected to significantly modify the computed EBOs. We note that the SOF-EBOs and SOC-EBOs are consistent with the relative stabilities of the states: the larger the EBO, the more stable the state is. For instance, at the c-SOCI/NEVPT2 level, the SOC-EBO values of the X 0^+, *a* 1, and *a* 2 states of AtO^+ are 1.71, 1.66, and 1.58, respectively. Since the X 0^+ and *a* 1 states essentially originate from the same SOF state ($^3\Sigma^-$) it is not surprising to see that they exhibit close EBO values, in contrast to the *a* 2 state which originates from the higher-energy $^1\Delta$ SOF state. It is also important to stress that SOC diminishes the EBOs, notably for the ground state, which pairs with the lengthening of interatomic distance and the decrease of the harmonic frequency upon inclusion of SOC. This detailed analysis leads us to the conclusion that the EBO is a good quantitative probe of the bond nature and strength in molecules and of the factors that act on it.

One can now distinguish the two sets of case studies; in I_2 and At_2, the SOC could significantly lower the EBOs since it could strongly mix the ground SOF spin components with spin components of excited SOF configurations that are less bonding, while in the IO^+ and AtO^+ cases, SOC essentially mixes the ground SOF configuration components with excited SOF components having similar EBOs. Also, the heavier the atom, the more important are SOC effects. Therefore, in iodine compounds, the SOC is not expected to drastically affect chemical bonding, contrary to what may happen in At compounds. In any case, SOC significantly affects the vertical energy excitations, and accurate determination of energy levels requires to account for spin-dependent relativistic effects.

IV. CONCLUDING REMARKS

In this work, we have shown the suitability of two-step SOCI approaches to both extend the definition of effective bond order and obtain the energetics and spectroscopic constants for species in which SOC is important. While SOC-EBOs can safely be obtained with both c-SOCI and uc-SOCI, since for the systems under consideration we have observed that both approaches yield the same qualitative picture, it should be stressed that uc-SOCI typically leads to more accurate results concerning energetics and spectroscopic data for 6*p*-containing species. The c-SOCI scheme is nevertheless appealing from the viewpoint of the EBO analysis, which allows one to easily quantify the role of SOC on chemical bonding.

For instance, for At_2 the c-SOCI EBOs clearly show that SOC significantly weakens the covalent character of the chemical bond, an effect that is paired with a weakening of the bond strength. Actually, the reduction of the EBO induced by SOC is larger than the one induced by electron correlation. This emblematic case therefore demonstrates that SOC can play a more important role than electron correlation on chemical bonding. Furthermore, while it is beyond dispute that one has to go beyond the Hartree-Fock picture to determine EBOs, our results show that SOC must be considered as well to determine EBOs when heavy atoms are involved.

One should also stress that, for the diatomics under consideration, the SOC-EBO analysis was found to be relatively insensitive to the bond lengths, something that opens the perspective of using different levels of approximation when treating larger systems—for instance, one could perform geometry optimizations with one- or two-component DFT and perform the SOC-EBO analysis at the resulting geometries with a more sophisticated electronic structure approach.

ACKNOWLEDGMENTS

This work has been supported by grants funded by the French National Agency for Research (ANR-2010-BLAN-0807), with "Investissements d'Avenir" (ANR-11-EQPX-0004, ANR-11-LABX-0018-01, ANR-11-LABX-0005), and by the "Région Pays de la Loire" (NUCSAN project). This work was performed using HPC resources from CCIPL ("Cen-

This article is copyrighted as indicated in the article. Reuse of AIP content is subject to the terms at: http://scitation.aip.org/termsconditions. Downloaded to IP: 134.158.25.87 On: Wed, 04 Mar 2015 16:04:50

tre de Calcul Intensif des Pays de la Loire"), from IDRIS-CNRS ("Institut de Développement et de Ressources en Informatique Scientifique du Centre National de la Recherche Scientifique;" contract 71859) and from CCRT-CEA ("Centre de Calcul et de Recherche Technologique," Grant Nos. 2013-081859 and 2014-081859).

[1]K. G. Dyall and K. Faegri, Jr., *Introduction to Relativistic Quantum Chemistry* (Oxford University Press, New York, 2007).
[2]B. O. Roos, A. C. Borin, and L. Gagliardi, Angew. Chem., Int. Ed. **46**, 1469 (2007).
[3]R. F. W. Bader, Chem. Rev. **91**, 893 (1991).
[4]J. Pilmé, E. Renault, F. Bassal, M. Amaouch, G. Montavon, and N. Galland, J. Chem. Theory Comput. **10**, 4830 (2014).
[5]A. Becke and K. E. Edgecombe, J. Chem. Phys. **92**, 5397 (1990).
[6]B. Silvi and A. Savin, Nature **371**, 683 (1994).
[7]M. Kohout and A. Savin, Int. J. Quantum Chem. **60**, 875 (1996).
[8]F. Feixas, E. Matito, M. Duran, M. Solà, and B. Silvi, J. Chem. Theory Comput. **6**, 2736 (2010).
[9]J. Pilmé, E. Renault, T. Ayed, G. Montavon, and N. Galland, J. Chem. Theory Comput. **8**, 2985 (2012).
[10]D. S. Wilbur, Nat. Chem. **5**, 246 (2013).
[11]D. S. Wilbur, Curr. Radiopharm. **1**, 144 (2008).
[12]S. Rothe, A. N. Andreyev, S. Antalic, A. Borschevsky, L. Capponi, T. E. Cocolios, H. De Witte, E. Eliav, D. V. Fedorov, V. N. Fedosseev, D. A. Fink, S. Fritzche, L. Ghys, M. Huyse, N. Imai, U. Kaldor, Y. Kudryavtsev, U. Köster, J. F. W. Lane, J. Lassen, V. Liberati, K. M. Lynch, B. A. Marsh, K. Nishio, D. Pauwels, V. Pershina, L. Popescu, T. J. Procter, D. Radulov, S. Raeder, M. M. Rajabali, E. Rapisarda, R. E. Rossel, K. Sandhu, M. D. Seliverstov, A. M. Sjödin, P. Van den Bergh, P. Van Duppen, M. Venhart, Y. Wakabayashi, and K. D. A. Wendt, Nat. Commun. **4**, 1835 (2013).
[13]J. Champion, C. Alliot, E. Renault, B. M. Mokili, M. Chérel, N. Galland, and G. Montavon, J. Phys. Chem. A **114**, 576 (2010).
[14]A. Sabatié-Gogova, J. Champion, S. Huclier, N. Michel, F. Pottier, N. Galland, Z. Asfari, M. Chérel, and G. Montavon, Anal. Chim. Acta **721**, 182 (2012).
[15]J. Champion, A. Sabatié-Gogova, F. Bassal, T. Ayed, C. Alliot, N. Galland, and G. Montavon, J. Phys. Chem. A **117**, 1983 (2013).
[16]A. Hermann, R. Hoffmann, and N. W. Ashcroft, Phys. Rev. Lett. **111**, 116404 (2013).
[17]J. Champion, C. Alliot, S. Huclier, D. Deniaud, Z. Asfari, and G. Montavon, Inorg. Chim. Acta **362**, 2654 (2009).
[18]J. Champion, M. Seydou, A. Sabatié-Gogova, E. Renault, G. Montavon, and N. Galland, Phys. Chem. Chem. Phys. **13**, 14984 (2011).
[19]C. de Graaf and C. Sousa, Int. J. Quantum Chem. **106**, 2470 (2006).
[20]R. Maurice, R. Bastardis, C. de Graaf, N. Suaud, T. Mallah, and N. Guihéry, J. Chem. Theory Comput. **5**, 2977 (2009).
[21]J.-B. Rota, S. Knecht, T. Fleig, D. Ganyushin, T. Saue, F. Neese, and H. Bolvin, J. Chem. Phys. **135**, 114106 (2011).
[22]L. F. Chibotaru and L. Ungur, J. Chem. Phys. **137**, 064112 (2012).
[23]F. Gendron, D. Páez-Hernández, F.-P. Notter, B. Pritchard, H. Bolvin, and J. Autschbach, Chem. Eur. J. **20**, 7994 (2014).
[24]F. Gendron, B. Pritchard, H. Bolvin, and J. Autschbach, Inorg. Chem. **53**, 8577 (2014).
[25]M. Reiher and A. Wolf, *Relativistic Quantum Chemistry* (Wiley-VCH, Weinheim, 2009).
[26]B. A. Hess, C. M. Marian, and S. D. Peyerimhoff, *Modern Structure Theory Part I*, Advanced Series in Physical Chemistry Vol. 2 (World Scientific, Singapore, 1995), pp. 152–278.
[27]F. Rakowitz and C. M. Marian, Chem. Phys. **225**, 223 (1997).
[28]V. Vallet, L. Maron, C. Teichteil, and J.-P. Flament, J. Chem. Phys. **113**, 1391 (2000).
[29]F. Réal, V. Vallet, J.-P. Flament, and J. Schamps, J. Chem. Phys. **125**, 174709 (2006).
[30]N. Douglas and N. M. Kroll, Ann. Phys. **82**, 89 (1974).
[31]B. A. Hess, Phys. Rev. A **33**, 3742 (1986).
[32]G. Jansen and B. A. Hess, Phys. Rev. A **39**, 6016 (1989).
[33]D. A. Pantazis, X.-Y. Chen, C. R. Landis, and F. Neese, J. Chem. Theory Comput. **4**, 908 (2008).
[34]D. A. Pantazis and F. Neese, Theor. Chem. Acc. **131**, 1292 (2012).
[35]R. Ahlrichs and K. May, Phys. Chem. Chem. Phys. **2**, 943 (2000).
[36]F. Weigend and R. Ahlrichs, Phys. Chem. Chem. Phys. **7**, 3297 (2005).
[37]F. Neese, ORCA—An *Ab Initio*, Density Functional and Semiempirical Program Package, version 3.0.1, Max-Planck-Institut für Bioanorganische Chemie, Mülheim an der Ruhr, 2013.
[38]B. O. Roos, R. Lindh, P.-Å. Malmqvist, V. Veryazov, and P.-O. Widmark, J. Phys. Chem. A **108**, 2851 (2004).
[39]H.-J. Werner, P. J. Knowles, G. Knizia, F. R. Manby, M. Schütz, P. Celani, T. Korona, R. Lindh, A. Mitrushenkov, G. Rauhut, K. R. Shamasundar, T. B. Adler, R. D. Amos, A. Bernhardsson, A. Berning, D. L. Cooper, M. J. O. Deegan, A. J. Dobbyn, F. Eckert, E. Goll, C. Hampel, A. Hesselmann, G. Hetzer, T. Hrenar, G. Jansen, C. Köppl, Y. Liu, A. W. Lloyd, R. A. Mata, A. J. May, S. J. McNicholas, W. Meyer, M. E. Mura, A. Nicklass, D. P. O'Neill, P. Palmieri, D. Peng, K. Pflüger, R. Pitzer, M. Reiher, T. Shiozaki, H. Stoll, A. J. Stone, R. Tarroni, T. Thorsteinsson, and M. Wang, , version 2012.1, a package of *ab initio* programs, 2012, see http://www.molpro.net.
[40]F. Aquilante, L. De Vico, N. Ferré, G. Ghigo, P.-Å. Malmqvist, P. Neogrády, T. B. Pedersen, M. Pitonak, M. Reiher, B. O. Roos, L. Serrano-Andrés, M. Urban, V. Veryazov, and R. Lindh, J. Comput. Chem. **31**, 224 (2010).
[41]B. O. Roos, P. R. Taylor, and P. E. M. Siegbahn, Chem. Phys. **48**, 157 (1980).
[42]B. O. Roos, in *Theory and Applications of Computational Chemistry: The First Forty Years*, edited by C. E. Dykstra, G. Frenking, K. S. Kim, and G. E. Scuseria (Elsevier, Amsterdam, 2005), Chap. 25, pp. 725–764.
[43]A. S. P. Gomes, F. Réal, N. Galland, C. Angeli, R. Cimiraglia, and V. Vallet, Phys. Chem. Chem. Phys. **16**, 9238 (2014).
[44]B. A. Hess, C. M. Marian, U. Wahlgren, and O. Gropen, Chem. Phys. Lett. **251**, 365 (1996).
[45]F. Neese, J. Chem. Phys. **122**, 034107 (2005).
[46]C. Teichteil, M. Pélissier, and F. Spiegelmann, Chem. Phys. **81**, 273 (1983).
[47]R. Llusar, M. Casarrubios, Z. Barandiarán, and L. Seijo, J. Chem. Phys. **105**, 5321 (1996).
[48]C. Angeli, R. Cimiraglia, S. Evangelisti, T. Leininger, and J.-P. Malrieu, J. Chem. Phys. **114**, 10252 (2001).
[49]K. G. Dyall, J. Chem. Phys. **102**, 4909 (1995).
[50]"AMFI, an atomic mean-field integral program," 1996, written by B. Schimmelpfennig.
[51]C. Angeli, S. Borini, M. Cestari, and R. Cimiraglia, J. Chem. Phys. **121**, 4043 (2004).
[52]"DIRAC, a relativistic *ab initio* electronic structure program," 2011, release DIRAC11, revision ab65b36, written by R. Bast, H. J. Aa. Jensen, T. Saue, and L. Visscher, with contributions from V. Bakken, K. G. Dyall, S. Dubillard, U. Ekström, E. Eliav, T. Enevoldsen, T. Fleig, O. Fossgaard, A. S. P. Gomes, T. Helgaker, J. K. Lærdahl, J. Henriksson, M. Iliaš, Ch. R. Jacob, S. Knecht, C. V. Larsen, H. S. Nataraj, P. Norman, G. Olejniczak, J. Olsen, J. K. Pedersen, M. Pernpointner, K. Ruud, P. Sałek, B. Schimmelpfennig, J. Sikkema, A. J. Thorvaldsen, J. Thyssen, J. van Stralen, S. Villaume, O. Visser, T. Winther, and S. Yamamoto (see http://dirac.chem.vu.nl).
[53]*Tables of Spectra of Hydrogen, Carbon, Nitrogen, and Oxygen Atoms and Ions*, edited by C. E. Moore and J. Gallagher (CRC Press, Boca Raton, 1993).
[54]E. Luc-Koenig, C. Morillon, and J. Vergès, Phys. Scr. **12**, 199 (1975).
[55]T. Fleig and A. J. Sadlej, Phys. Rev. A **65**, 032506 (2002).
[56]I. Kim and Y. S. Lee, J. Chem. Phys. **139**, 134115 (2013).
[57]W. C. Martin and C. H. Corliss, J. Res. Natl. Bur. Stand., Sect. A **64**, 443 (1960).
[58]C. Morillon and J. Vergès, Phys. Scr. **12**, 145 (1975).
[59]C. Morillon and J. Vergès, Phys. Scr. **12**, 129 (1975).
[60]G. W. Charles, J. Opt. Soc. Am. **56**, 1292 (1966).
[61]C. Teichteil and M. Pelissier, Chem. Phys. **180**, 1 (1994).
[62]L. Visscher and K. G. Dyall, J. Chem. Phys. **104**, 9040 (1996).
[63]O. Fossgaard, O. Gropen, M. C. Valero, and T. Saue, J. Chem. Phys. **118**, 10418 (2003).
[64]T. Nakajima and K. Hirao, J. Chem. Phys. **119**, 4105 (2003).
[65]A. V. Mitin and C. van Wüllen, J. Chem. Phys. **124**, 064305 (2006).
[66]S. Höfener, R. Ahlrichs, S. Knecht, and L. Visscher, ChemPhysChem **13**, 3952 (2012).
[67]K. P. Huber and G. Herzberg, *Constants of Diatomic Molecules* (Nostrand Reinhold, New York, 1979).
[68]See supplementary material at http://dx.doi.org/10.1063/1.4913738 for spectroscopic constants and effective bond orders computed with the SARC-DKH-TZVP basis sets.
[69]T. Ayed, M. Seydou, F. Réal, G. Montavon, and N. Galland, J. Phys. Chem. B **117**, 5206 (2013).
[70]T. Ayed, F. Réal, G. Montavon, and N. Galland, J. Phys. Chem. B **117**, 10589 (2013).

This article is copyrighted as indicated in the article. Reuse of AIP content is subject to the terms at: http://scitation.aip.org/termsconditions. Downloaded to IP: 134.158.25.87 On: Wed, 04 Mar 2015 16:04:50

Supplementary material for:

Effective bond orders from two-step spin-orbit coupling approaches: The I_2, At_2, IO^+, and AtO^+ case studies

Rémi Maurice,[1] Florent Réal,[2] André Severo Pereira Gomes,[2] Valérie Vallet,[2] Gilles Montavon,[1] and Nicolas Galland[3]

[1)] *SUBATECH, CNRS UMR 6457, IN2P3/EMN Nantes/Université de Nantes, 4 rue Alfred Kastler, BP 20722, 44307 Nantes Cedex 3, France*[a)]

[2)] *Laboratoire PhLAM, CNRS UMR 8523, Université de Lille, 59655 Villeneuve d'Ascq Cedex, France*

[3)] *CEISAM, UMR CNRS 6230, Université de Nantes, 2 rue de la Houssinière, BP 92208, 44322 Nantes Cedex 3, France*

[a)] Electronic mail: remi.maurice@subatech.in2p3.fr

TABLE SI. Ground-state bond lengths, harmonic frequencies, and dissociation energies of I_2 and At_2 obtained at various levels of theory with the SARC-DKH-TZVP basis sets.

Method	I_2			At_2		
	r_e (Å)	ω_e (cm^{-1})	D_e (eV)	r_e (Å)	ω_e (cm^{-1})	D_e (eV)
CASSCF	2.775	188	1.07	2.924	138	1.09
NEVPT2	2.718	208	1.69	2.818	158	2.01
c-SOCI/CASSCF	2.796	174	0.60	3.114	84	0.18
c-SOCI/NEVPT2	2.732	201	1.21	2.916	130	0.99

TABLE SII. Ground-state EBOs of I_2 and At_2 computed at various levels of theory with the SARC-DKH-TZVP basis sets at the corresponding equilibrium geometries, or at a fixed geometries ($r(I_2)$ = 2.717 Å and $r(At_2)$ = 3.046 Å[1]).

Method	I_2			At_2		
	EBO_σ	EBO_π	EBO	EBO_σ	EBO_π	EBO
			Equilibrium geometry			
CASSCF	0.92	0.00	0.92	0.91	0.00	0.92
NEVPT2	0.93	0.00	0.93	0.93	0.00	0.94
c-SOCI/CASSCF	0.90	-0.01	0.89	0.75	-0.06	0.69
c-SOCI/NEVPT2	0.91	0.00	0.91	0.83	-0.05	0.78
			Fixed geometry			
NEVPT2[a]	0.93	0.00	0.93	0.89	0.00	0.89
c-SOCI/CASSCF	0.92	0.00	0.91	0.78	-0.05	0.73
c-SOCI/NEVPT2	0.92	0.00	0.91	0.78	-0.05	0.72

[a] CASSCF and NEVPT2 EBOs are here equivalent.

TABLE SIII. Ground-state bond lengths, harmonic frequencies, and dissociation energies of IO^+ and AtO^+ computed at various levels of theory with the SARC-KH-TZVP basis sets.

Method	IO^+			AtO^+		
	r_e (Å)	ω_e (cm^{-1})	D_e (eV)	r_e (Å)	ω_e (cm^{-1})	D_e (eV)
CASSCF	1.911	659	1.65	1.984	630	1.59
NEVPT2	1.841	741	2.65	1.913	744	2.76
c-SOCI/CASSCF	1.915	610	1.34	1.998	581	0.94
c-SOCI/NEVPT2	1.844	733	2.33	1.921	729	2.04

TABLE SIV. Lowest-energy states vertical transition energies (T_v) and EBOs of IO^+ and AtO^+ obtained at various levels of theory at the reference DC-CCSD(T) geometries ($r(IO^+) = 1.829$ Å and $r(AtO^+) = 1.930$ Å[2]) computed with the SARC-DKH-TZVP basis sets.

Method	State	IO^+				AtO^+			
		T_v (eV)	EBO_σ	EBO_π	EBO	T_v (eV)	EBO_σ	EBO_π	EBO
NEVPT2[a]	$^3\Sigma^-$	0.00	0.92	0.85	1.78	0.00	0.91	0.84	1.74
	$^1\Delta$	0.63	0.93	0.78	1.70	0.58	0.91	0.74	1.66
	$^1\Sigma^+$	1.08	0.92	0.71	1.63	1.00	0.91	0.67	1.58
c-SOCI/CASSCF	X 0^+	0.00	0.92	0.84	1.76	0.00	0.88	0.80	1.68
	a 1	0.08	0.92	0.85	1.76	0.39	0.89	0.77	1.65
	a 2	0.68	0.92	0.76	1.69	0.94	0.89	0.67	1.56
c-SOCI/NEVPT2	X 0^+	0.00	0.92	0.84	1.76	0.00	0.88	0.80	1.68
	a 1	0.08	0.92	0.85	1.76	0.38	0.88	0.77	1.65
	a 2	0.70	0.92	0.76	1.69	0.96	0.89	0.67	1.56

[a] CASSCF and NEVPT2 EBOs are here equivalent.

REFERENCES

[1]L. Visscher and K. G. Dyall, J. Chem. Phys. **104**, 9040 (1996).

[2]A. S. P. Gomes, F. Réal, N. Galland, C. Angeli, R. Cimiraglia, and V. Vallet, Phys. Chem. Chem. Phys. **16**, 9238 (2014).